Experimental and Numerical studies of granular platforms reinforced by geosynthetics laid over soft subgrade soil

Nisrine Abou Chaz

THÈSE

Pour obtenir le grade de

DOCTEUR DE L'UNIVERSITÉ GRENOBLE ALPES

École doctorale : I-MEP2 - Ingénierie - Matériaux, Mécanique, Environnement, Energétique, Procédés, Production
Spécialité : 2MGE - Matériaux, Mécanique, Génie civil, Electrochimie
Unité de recherche : Laboratoire Sols, Solides, Structures et Risques

Etudes expérimentale et numérique des plateformes granulaires renforcées par géosynthétiques sur sol mou

Experimental and Numerical studies of granular platforms reinforced by geosynthetics laid over soft subgrade soil

Présentée par :

Nisrine ABOU CHAZ

Direction de thèse :

Pascal VILLARD PROFESSEUR DES UNIVERSITES, Université Grenoble Alpes	Directeur de thèse
Laurent BRIANCON INSA Lyon	Co-directeur de thèse
Claire SILVANI INSA LYON	Co-encadrante de thèse

Rapporteurs :

Pierre BREUL
PROFESSEUR DES UNIVERSITES, Université Clermont Auvergne
Nicola MORACI
FULL PROFESSOR, Università degli Studi Mediterranea di Reggio Calabria

Thèse soutenue publiquement le **4 avril 2024**, devant le jury composé de :

Frederic Victor DONZE, PROFESSEUR DES UNIVERSITES, Université Grenoble Alpes	Président
Pascal VILLARD, PROFESSEUR DES UNIVERSITES, Université Grenoble Alpes	Directeur de thèse
Laurent BRIANÇON, MAITRE DE CONFERENCES HDR, INSA Lyon	Co-directeur de thèse
Pierre BREUL, PROFESSEUR DES UNIVERSITES, Université Clermont Auvergne	Rapporteur
Nicola MORACI, FULL PROFESSOR, Università degli Studi Mediterranea di Reggio Calabria	Rapporteur
Philippe DELMAS, PROFESSEUR DES UNIVERSITES, CNAM Paris	Examinateur
Christelle ABADIE, CHARGEE DE RECHERCHE, Université Gustave Eiffel	Examinatrice

Invités :

Alain NANCEY
INGENIEUR DOCTEUR,
Claire SILVANI
MAITRESSE DE CONFERENCE, Institut National des Sciences Appliquées de Lyon

Acknowledgments

Abstract

Poor subgrade quality is a pervasive challenge in the construction of unpaved roads. Geosynthetics (GSYs) have emerged as innovative solutions since their initial usage in the late 1970s. Depending on the type of GSY employed, they can fulfil one or several roles, including separation, reinforcement by tensioned membrane effects, and stabilization by interlocking and/or friction at the soil-GSY interface. Few design methods exist in the literature to quantify these mechanisms, but they have limitations due to their calibration on specific GSY and soil parameters and, at times, under static rather than cyclic loading conditions. The various factors and parameters that influence the dominant mechanism and its corresponding contribution to platform enhancement underscore the necessity for further exploration in this area.

To address this persistent issue, a series of experimental and numerical studies were conducted. The experimental part studied the performance of reinforcement under cyclic vertical and traffic loadings using two woven geotextiles (GTXs) with two different tensile stiffnesses and two base course thicknesses. Additionally, alongside the experimentation, a numerical model coupling the discrete element method and the finite element method (using Software-Defined Edge Computing) was employed. This model aimed to showcase the impact of GSY and soil parameters on reinforcement performance and provide insights into aspects challenging to measure through experimentation.

The tested unpaved road sections are composed of a subgrade layer with a CBR around 1% covered by a compacted base course layer with thickness of 300 mm or 500 mm. The GTXs are placed at the interface between the subgrade and the base course layers. The results showed that the 500 mm base course reinforced platform did not exhibit reinforcement effects under vertical cyclic loading. However, the use of a 300 mm base course with GTX significantly reduced settlement compared to an unreinforced base course of the same thickness (300 mm) and to the thicker base course (500 mm). The most important improvement was observed with the highest-stiffness GTX. Moreover, three tests were performed under traffic loading applying by the Simulator Accelerator of Traffic (SAT). It was shown that traffic loading exerted greater deformation in the base course layer compared to vertical loading, but definitive conclusion can hardly be reached about the comparison between reinforced and unreinforced platform.

In the numerical model, a behavioural law (1D) was integrated, considering the variation of the subgrade reaction modulus during loading and unloading phases and with cycles, and describing the transition of the soil from plastic to quasi-elastic behavior. In addition, the purely frictional base course layer revealed its incapacity to sustain the loading applied in the experimental. This inherent limitation prompted the incorporation of adhesion between soil particles to rectify this shortcoming in load-bearing capacity. Once calibrated the numerical model proved capable of accurately replicating the behavior of GTX-reinforced platforms in the first cycle and with cycles. It facilitated a quantification of the GTX friction effort and GTX tension effort with cycles. Initially, frictional forces outweighed the tensioned membrane effect, but as deflection increased with cycles, the latter became more prominent. This dynamic highlighted a diminishing dominance of the soil confinement mechanism with cycles, giving way to the increasing significance of the membrane effect. Furthermore, a parametrical study has been performed to study the influence of the subgrade softness, the GTX rigidity, the mattress-GTX interface parameters and the base course mechanical parameters on the behavior of the model.

Resumé

La mauvaise qualité de la couche de fondation est un défi important dans la construction de routes non revêtues. Les géosynthétiques (GSY) sont des solutions innovantes développés à partir des années 70. Selon le type de GSY utilisé, ils peuvent assurer un ou plusieurs rôle (s), notamment la séparation, le renforcement par les effets membrane et la stabilisation par l'imbrication des grains de sol dans le GSY (quand une géogrille est utilisée) et/ou le frottement à l'interface sol-GSY. Il existe dans la littérature peu de méthodes de dimensionnement pour quantifier ces mécanismes, et elles présentent des limites en raison de leur calibration sur des paramètres spécifiques aux GSYs et au sol utilisé et, parfois, dans des conditions de charge statique plutôt que cyclique. La complexité des mécanismes et le nombre importants de paramètres qui interviennent dans leur mise en place requirent une analyse plus poussée dans ce domaine.

Pour répondre à ce problème persistant, une série d'études expérimentales et numériques a été menée. Le volet expérimental a étudié la performance du renforcement sous des charges cycliques verticales et de circulation en testant deux GTX tissés avec deux rigidités de traction différentes et deux épaisseurs de plateformes granulaires. En parallèle à l'expérimentation, un modèle numérique couplant couplant la méthode des éléments discrets et la méthode des éléments finis (à l'aide du logiciel SDEC) a été utilisé. Ce modèle visait à mettre en évidence l'impact du GSY et des paramètres du sol sur le rôle du renforcement et à fournir des données sur des phénomènes difficiles à mesurer expérimentalement.

Les plots expérimentaux sont formés d'une couche de sol de fondation avec un CBR d'environ 1 %, recouverte par une plateforme granulaire compactée d'une épaisseur de 300 mm ou 500 mm. Le GTX est placé à l'interface entre la couche de fondation et la couche de base. Les résultats ont montré que, sous des charges verticales cycliques, le GTX n'apportaient pas de gain d'efficacité des plateformes de 500 mm d'épaisseur. Pour une plateforme de 300 mm d'épaisseur, les deux GTXs ont réduit de manière significative le tassement par rapport à une plateforme non renforcée de la même épaisseur (300 mm) et à une plateforme plus épaisse (500 mm). L'amélioration la plus importante a été observée avec le GTX le plus rigide. Trois essais ont été réalisés avec une charge de circulation appliquée par le Simulateur Accélérateur de Trafic (SAT). Il a été démontré que la charge de circulation exerçait une plus grande déformation dans la plateforme par rapport à la charge verticale, mais il était difficile d'arriver à une conclusion définitive sur la comparaison entre une plateforme renforcée et non renforcée.

Dans le modèle numérique, une loi de comportement (1D) a été intégrée prenant en compte les variations du module de réaction du sol pendant les phases de chargement et de déchargement ainsi qu'avec les cycles, et décrivant la transition d'un comportement plastique à un comportement quasi-élastique du sol compressible. Par ailleurs, la plateforme granulaire purement frottante a montré son incapacité à supporter la charge cyclique verticale appliquée sur une plaque circulaire placée au centre du modèle. Cette limitation « numérique » a nécessité l'ajout d'une cohésion entre les particules de sol. Une fois calibré, le modèle numérique s'est avéré capable de reproduire avec précision le comportement des plates-formes renforcées par GSYs sur sol mou au cours du premier cycle et au fur et à mesure des cycles. Il a permis de quantifier les efforts de frottement exercés sur le GTX et de traction exercée par le GTX en fonction des cycles. Initialement, les efforts de frottement dépassaient l'effet membrane, mais à mesure que la déflexion augmentait avec les cycles, l'effet membrane devenait plus important. Cette dynamique a mis en évidence une diminution de la prédominance du mécanisme de confinement du sol avec les cycles, cédant la place à l'effet de membrane. Une étude paramétrique sur la compressibilité de la couche de fondation, la rigidité du GSY, le frottement à l'interface sol granulaire-GTX et les paramètres mécaniques de la couche a permis de mettre en évidence l'influence de ces différents paramètres sur les mécanismes.

Table of contents

List of figures

List of tables

Abreviation

a: adhesion between the spheres of the mattress (kPa)
α: Contact rigidity coefficient (kn/kt)
Ang: angularity
B: loading plate diameter in Terzaghi equation
c: cohesion within the mattress (kPa)
D: Loading plate diameter in the experimental and numerical model (m)
d_i: spheres diameter (m)
$D_{local,init}$: densities within the calculation volume at the initial state
$D_{local,N}$: densities within the calculation volume at the current cycle
δ: the friction angle between the soil particle and the geosynthetic sheet (°)
ΔF: Force increment in the time increment (N)
ΔF_t: incremental tangential force between the spheres of the mattress (kN)
Δt: Time increment (s)
Δv: incremental relative tangential displacement (m)
$d_{n\_average}$: Sphere average diameter in the mattress (m)
d_{n_max}: maximum sphere diameter in the mattress (m)
d_{n_min}: minimum sphere diameter in the mattress (m)
e: thickness of the geosynthetic element (in m)
E: modulus of compressibility of the geosynthetic sheet (in N/m²)
ε: deformation of the fibres (%)
F_l: Loading force applied to the model (kN)
F_n: normal contact force between the spheres of the mattress
f_β^i: projection onto axis i of the contact force at contact β
F_t: Tangential contact force between the spheres of the mattress (kN)
F_{tmax}: Maximum tangential contact force between the spheres of the mattress (kN)
F_u: Unloading force applied to the model (kN)
J: Geosynthetic's fibres stiffness
J_x: stiffness at 2% of strain along the longitudinal direction parallel to x-axis (kN/m)
J_y: stiffness at 2% of strain along the transverse direction parallel to the y-axis (kN/m)
k_a: damping factor
k_1: Subgrade reaction moduli at the 1st loading cycle
k_n: Normal contact stiffness
k_{ni}: normal contact stiffness between a particle of radius r_i and a geosynthetic sheet element (N/m)
k_t: Tangential contact stiffness
k_{ti}: Tangential contact stiffness between a particle of radius r_i and a geosynthetic sheet element (N/m)
K_{ic}: critical integration factor
K_n: Sphere normal rigidity
K_t: Sphere tangential rigidity
k_u: the subgrade reaction moduli of all the unloading cycle
$l_{n\text{-}average}$: average cluster length
$l_{n\text{-}max}$: maximum cluster length
$l_{n\text{-}min}$: minimum cluster length
m: mass of the particle
n: porosity

$n_{local,init}$: the initial local porosity of the calculation point
$n_{local,N}$: the local porosity of the point at the cycle N
n_{max}: maximum numerical porosity value
n_{min}: minimum numerical porosity value
N_C: the number of contacts within the calculation volume V
N: the number of the applied cycle
N_0: the number of cycles at which the subgrade soil became elastic
φ_{int}: Intergranular friction angle (°)
φ_{peak}: macroscopic friction angle (°)
q_u: allowable bearing capacity according to Terzaghi equation (kPa)
r_i and r_j: respective radii of spheres i and j that interact with each other (m)
s_{int}: contact influence area between the soil particle and the sheet element (πr_i^2 in m^2)
τ_{max}: the maximum tangential stress (kPa)
T: the tensile force of the geosynthetic fibres (KN)
u: normal overlap between the grains of the mattress (m)
U_0: represents the relative displacement needed to fully mobilize friction (m)
$\{F_e\}$: Forces acting on the nodes of a geosynthetic element (kN)
$\{K_e\}$: Elementary matrix of rigidity of a geosynthetic element (kN/m)
$\{R_e\}$: Corrective vector force resulting from the large displacement of a geosynthetic element
$\{U_{ni}\}$: Overlap between the geosynthetic sheet element and the soil particle (m)

1. Chapter 1. General Introduction

Transportation and infrastructure networks are pivotal drivers of economic development. In the United States, the road network facilitates freight transport by trucks, amounting to a staggering $12,906 billion or 63% of the total value of freight transport in 2023, as reported by the U.S. Department of Transportation. Notably, 32% of the road network in the United States is unpaved. The imperative need for an expansive road network to sustain overland freight transport has led to a surge in road construction on soft ground. However, the resultant unpaved roads on soft ground often develop deep ruts under heavy traffic, posing a significant risk to road safety. Traditional soil replacement methods have proven economically inefficient in addressing this issue, prompting the ascendancy of alternative stabilization solutions such as geosynthetic (GSY). Various GSYs, including woven and nonwoven geotextiles (GTXs), different geometries of geogrids (GGRs) and geocells (GCEs) have gained prominence in road applications. According to Giroud et al. (2023), GSYs initially found use in the 1930s with cotton fabrics in paved roads, evolving into nonwoven fabrics in the 1940s for military equipment traffic. A breakthrough occurred in the late 1960s with the successful construction of access roads at construction sites using nonwoven fabrics, while the introduction of GGRs in the 1980s marked another milestone in GSYs' utilization in road construction.

The behavior of unpaved roads is governed by intricate mechanisms, primarily due to the heterogeneous nature of the platform, comprising a cohesive and loose subgrade supporting a granular layer. GSYs add complexity by altering the properties of the road structure and underlying mechanisms. However, GSYs have proven effective over the years in reducing rutting and aggregate thickness on unpaved platforms, with research distinguishing mechanisms like the separation between the subgrade layer and the granular platform, the aggregate lateral restraint, and the tensioned membrane effect mechanisms. However, due to the complexity of the problem and numerous influencing parameters, the dominant mechanism remains unclear, warranting further research.

This study emerges from a collaboration between the 3SR laboratory at Grenoble Alpes University, the GEOMAS laboratory at INSA de Lyon, and Solmax Group through a Cifre agreement. The research aims to enhance understanding and clarity regarding the developed mechanisms and their contributions to platform behavior. The thesis comprises both experimental (conducted at GEOMAS laboratory) and numerical (collaboration with 3SR laboratory) components.

The experimentation (1:1 scale) investigates the performance of the granular platform reinforced by GSY over soft soil under cyclic vertical and traffic loadings using different GTXs and base course thicknesses. In addition, a DEM-FEM numerical model using Spherical Discrete Elements Code (SDEC) is used to simulate the experiments. This model facilitates the study of phenomena that are challenging to quantify through experiments.

Chapter 1 (this chapter) introduces the problematic behavior of the granular platform reinforced with GSY on a soft subgrade, for which this thesis was proposed, and outlines the subsequent chapters of this report.

Chapter 2 provides a comprehensive literature review on the unpaved road reinforced by GSY detailing laboratory tests subjected to vertical loading or traffic loading by Accelerated Pavement Tests Facilities, and in-situ tests, and various empirical and analytical design methods. It also discusses continuous and discrete elements models, emphasizing their limitations and the need for further research.

Chapter 3 presents the experimental study and describes the test protocol, the devices and the materials used, the instrumentation and the quality control tests. A detailed description of the vertical and the traffic load tests carried out is also given. The materials used for the subgrade, the base course and the two woven GTXs employed in the tests are also presented. In addition, the protocol followed for the installation and compaction of the subgrade and base course is detailed. The protocol includes special focus on the repeatability of soil preparation. Indeed, numerous quality control tests are established and detailed in this

chapter to verify the homogeneity and properties of the subgrade and the base course layers prior to each test performed. Finally, the platform instrumentation for plate and traffic load tests is presented.

Chapter 4 presents the results of the quality control tests carried out on each prepared test section. In the plate load testing: 10,000 vertical cyclic loads are applied to a circular plate (diameter = 320 mm) with a maximum load of 45 kN equivalent to a contact pressure of 560 kPa at a frequency of 0.77 Hz. Two woven GTXs placed at the interface between the base layer and the subgrade, and two base course layer thicknesses are tested. The plate load test results, including two repeatability tests, are presented in terms of vertical stress at the subgrade surface, base course settlement and subgrade settlement. The results of the tests are compared and analyzed to show the impact of reinforcement using two base layer thicknesses. This chapter also presents the results of the tests subjected to traffic loading using the SAT until 100 mm of rutting is achieved at the surface of the base course. In this test, the load applied to the wheel is equal to 28 kN at a speed of 4 km/h over an effective traffic length of 2 m. A woven GTX placed at the interface between the base course and the subgrade, and two base course thicknesses are tested.

Chapter 5 delves into an elucidation of the FEM-DEM coupling method, providing an intricate characterization of the model encompassing soil layers, GSYs, and their interfaces. Indeed, a behavioral law based on cyclic plate tests was introduced to simulate the response of the subgrade subjected to cyclic loading. Moreover, a sensitivity study is performed to select the optimal load increment and damping factor. Additionally, the calibration process employed is detailed. Furthermore, an exhaustive analysis of the performance of the model under cyclic plate load tests is showed. The results include the vertical and horizontal particle movements within the granular mattress, the particles rearrangement, the principal stress orientations, and the contact forces operational within the mattress. The GSY displacement, deflection, and strain under cyclic loading are also presented. The investigation extends to scrutinize the frictional interaction between the GSY and the granular mattress grains and the tensioned effort.

Chapter 6 delves into a parametric study through a series of numerical simulations, examining key parameters such as the number of mattress clusters, GSY rigidity, subgrade softness, friction angle at the granular mattress and the GTX interface, as well as the mechanical parameters of the granular mattress (including adhesion and friction).

Chapter 7 concludes with the most important findings of the thesis and presents future perspectives.

2. Chapter 2. State of the art

2.1. Introduction

Geosynthetics (GSYs) cover a diverse range of products, including geotextiles (GTXs), geogrids (GGRs), geocells (GCE), geocomposites, geomembranes, geonets and geofoams, among others. These versatile products have a wide range of applications in civil engineering, particularly in geotechnical engineering. The versatility of GSY lies in their ability to perform a variety of functions, each type being designed to address one or more specific problems depending on the application envisaged. These functions include separation, stabilization, reinforcement, drainage, filtration, protection, sealing and erosion control.

Road networks are increasing, and with them, the number of unpaved roads on soft subgrades. These roads are prone to quick degradation that poses a risk to road traffic. Some GSY have significant mechanical properties and are considered one of the most innovative solutions. Giroud et al. (2023) report two major steps in the modern development of the use of GSY in roads. The first was the introduction of non-woven textiles in the late 1960s to provide access roads on construction sites where it was not possible to operate trucks. The second step in developing GSY for roads was the introduction of GGRs in the 1980s. Subsequently, GCEs were introduced in the unpaved roads; however, their usage remains relatively limited, with observed applications in a modest number of cases.

The GSYs provide better performance in reducing the unpaved road surface rutting and increased service life. Alternatively, GSY can be used to allow a smaller thickness of the granular platform thickness or the use of lower quality construction materials. In addition to their beneficial impact on road design and performance, GSY facilitates the granular platform compaction where the subgrade is so soft that it would be impossible to start construction of a road without first placing a GSY on the subgrade.

Depending on the type of the GSY used, one or many functions among the separation, reinforcement through the tensioned membrane effect mechanism, and stabilization via the aggregate lateral restraint mechanism. The contribution of each mechanism to the overall reinforcement is influenced by numerous factors, and despite over 60 years of research, a clear understanding of this relationship has not yet been achieved. A few design methods have been presented in the literature and quantify either the tensioned membrane effect or the confinement mechanism by friction or interlocking between the GSY and the base course material. However, all these methods have limitations because they have been calibrated on limited GSY and soil parameters and sometimes under static loading rather than cyclic loading. Each method is validated in a range of rut depth which is linked to the mechanism quantified.

To underscore the existing limits in the unpaved roads over soft subgrade, this chapter provides an overview of the involved mechanisms and influencing parameters. Additionally, it reviews experimental tests, empirical and analytical design methods, and numerical simulations in the literature to characterize the impact of GSY parameters, soil parameters, and soil-GSY interaction on the road structure's behavior. Through this research, the goal is to further elucidate the complexities of the mechanisms developed in this specific application.

2.2. Geosynthetics types

The GSY is a polymeric (synthetic or natural) material used in contact with soil/rock and/or any other geotechnical material in civil engineering applications (International Geosynthetic Society). They encompass a wide range of types (Figure 2-1):

1. Geotextile (GTX)

The GTX is a planar, permeable, polymeric (synthetic or natural) textile material, which may be nonwoven, woven or knitted. Nonwoven GTXs are made from mechanically and/or thermally and/or chemically

bonded fibers, filaments or other directionally or randomly oriented elements. Woven GTXs are produced by interlacing, usually at right angles, two or more sets of yarns, fibres, filaments, tapes or other elements are produced by weaving fibers together at right angles in various patterns. Knitted GTXs are produced by interlooping one or more yarns, fibres, filaments or other elements. Commonly used polymers in GTX manufacturing include polypropylene (PP), polyester (e.g., polyethylene terephthalate or PET), polyethylene (PE), and polyamide (nylon).

2. Geogrid (GGR)

The GGR is a planar, polymeric structure consisting of a regular open network of integrally connected tensile elements, which may be linked by extrusion, bonding, knitting or weaving. The main difference between GTX and GGR is that GTX is continuous, while GGR takes the form of grids. According to the manufactural way the GGR can be woven, extruded, knitted or woven. These GGRs are further classified into uniaxial, biaxial, or triaxial categories, each exhibiting strength in one, two, or three principal directions, respectively. Notably, high-density polyethylene (HDPE), polyethylene terephthalate (PET), and polypropylene (PP) are commonly used polymers in GGR manufacturing.

3. Geomembrane

The Geomembrane is a planar, relatively impermeable, polymeric (synthetic or natural) sheet used in civil engineering applications. Depending on its material composition, it can take the form of a bituminous geomembrane when crafted from natural bituminous materials, an elastomeric geomembrane if manufactured with elastomeric polymers, or a plastomeric geomembrane if produced from plastomeric polymers.

4. Geocell (GCE)

The GCE is a three-dimensional, permeable, polymeric (synthetic or natural) honeycomb or web structure, made of strips of GTXs, GGRs or geomembranes linked alternatingly. These structures are constructed from materials such as HDPE, PET, and various other polymers.

5. Geocomposite

A geocomposite is a composite material that combines various GSY products, such as GTX, GGR, or geomembranes, to serve specific functions in geotechnical applications.

6. Geonet

Geonet is a planar, polymeric structure consisting of a regular dense network, whose constituent elements are linked by knots or extrusions and whose openings are much larger than the constituents, used in civil engineering applications.

7. Geofam

Geofam is a polymeric material which has been formed by the application of the polymer in semi-liquid form, through the use of a foaming agent, and results in a lightweight material with high void content, used in civil engineering applications.

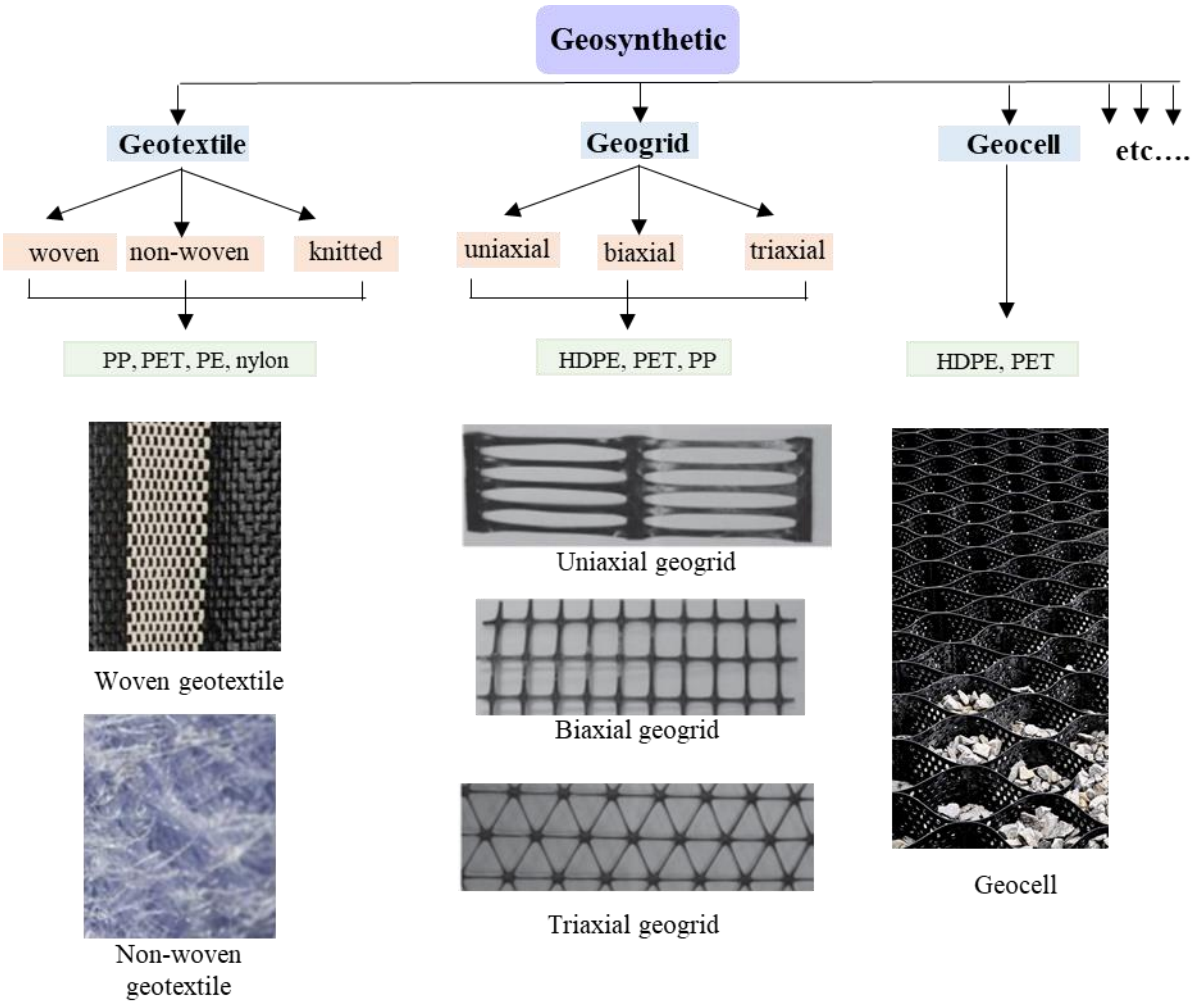

Figure 2-1: GSY types

2.3. Geosynthetic in unpaved roads

An unpaved road is characterized by the absence of a conventional paved or asphalt surface, featuring a typical cross-section comprising two distinct layers: the base course layer, constructed with aggregate materials, laid over a subgrade layer (Figure 2-2). These roads play a vital role in facilitating freight transportation, granting access to construction sites, supporting agricultural activities, and providing routes for recreational use. The urban expansion and subsequent increase in freight traffic, construction, and agricultural activities have led to construction of the unpaved roads on soft subgrade soils with low bearing capacity. The construction of unpaved roads on soft subgrade poses a challenge, resulting in the development of ruts and surface irregularities, making navigation challenging and, in some instances, impassable.

Over the years, various solutions have been envisioned to improve the characteristics of such soft soil. GSY has emerged as one of the most innovative solutions, technically, economically, and environmentally. According to FHWA (2008), GSYs are recommended when the supporting soil has a CBR less than 3%. The presence of a GSY can yield several benefits, including the reduction of rutting (Hufenus et al., 2006;

Khoueiry, 2020), increased bearing capacity of the granular platform (Sun et al., 2015; Akond, 2012), decreased thickness of the fill layer (Giroud and Han, 2004a), extended service life of the structure (Palmeira and Antunes, 2010), and enhanced compaction of the granular fill material (Hufenus et al., 2006).

The incorporation of GSY in unpaved roads aims to fulfil multiple functions, including reinforcement, stabilization, and separation. The contributions of GSY to improve road structure behavior depend on different mechanisms developed in this type of structure, such as separation between the soft soil layer and the gravel layer, the lateral restraint aggregates composed the base course (confinement), and the tensioned membrane effect of the GSY. Despite advancements, understanding the contribution of each mechanism to overall reinforcement remains a challenge. In fact, the part of each mechanism to overall reinforcement is contingent on numerous influencing parameters, including the type of GSY used and its strain level within the soil. This section provides a comprehensive discussion of the involved mechanisms in unpaved roads to address them and highlight existing gaps.

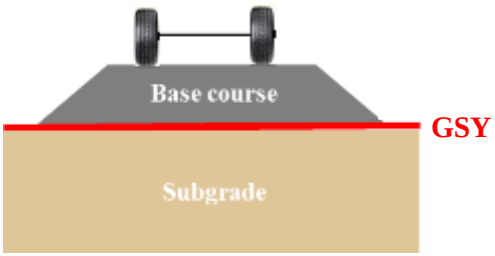

Figure 2-2: Unpaved road section

2.3.1. Separation

The separation function is ensured by preventing the intermixing of materials from the two distinct layers under repeated loads. In road construction, GTX is typically positioned between the subgrade and the overlying granular material, effectively preventing both the loss of aggregates into the subgrade and the migration of fines from the subgrade into the pore space of the aggregate (Figure 2-3). While a GGR or GCE can prevent aggregate loss in the subgrade layer but lacks the capacity to hinder the migration of fines into the aggregate pore space.

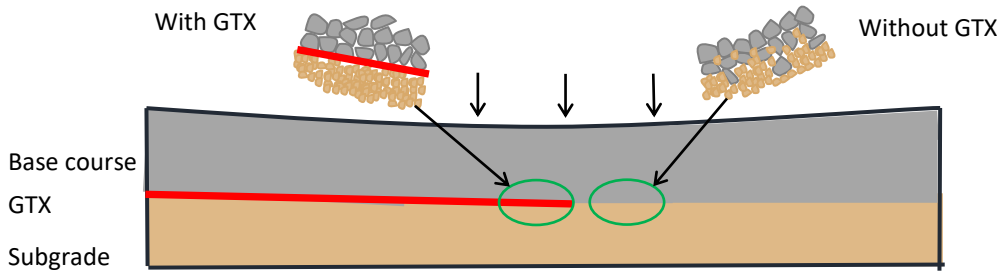

Figure 2-3: Separation

2.3.2. Lateral restraint

GSY stabilization involves minimizing the movement of particles through particle lateral restraint (particle confinement). For a GTX, soil confinement arises from soil/GTX friction (Figure 2-4 a), whereas for a

GGR, it results from both the interlocking of soil into the GGR apertures and soil/GGR strand friction (Figure 2-4 b). This interaction results in the formation of a GSY/soil composite material that exhibits greater resistance to deformation than the soil alone.

To effectively provide particle restraint, GSY typically require sufficient tensile stiffness and interaction with the soil. Specifically, in the case of a GGR, the soil should consist of aggregates, and their grading should align with the GGR aperture for optimal interlocking. During loading, additional shear stress is transmitted from the aggregate to the GSY, inducing strain in the GSY. Friction and mechanical interlock contribute to shear resistance, physically restraining the aggregate particles. The stiffness offered by the GSY minimizes the development of lateral tensile strain and stress in the base aggregate over a specified height above the GSY in a region known as the stabilized or 'confined zone'. Beyond this zone, a transition zone emerges until there is no further influence on the granular layer from the GSY (unconfined zone).

GCE controls horizontal infill soil movement by confining it within the GCE walls (Figure 2-4 c). This minimization of the horizontal movement depends on three factors: 1) hoop tension forces in the cell walls, 2) resistance from surrounding cells, and 3) friction between cell walls and infill material. Under vertical loads, cell walls restrain horizontal earth pressure by activating hoop tension forces. The resulting strains in the cell wall mobilize hoop stresses within the loaded cell, restricting lateral deformation of the fill through the generation of confining stresses (σ_{3D}). The thickness of the confined zone aligns with the height of the GCE. It's important to mention that GCE can accommodate a range of local soil types, provided that the filling process ensures proper compaction.

The effectiveness of the lateral restraint mechanism relies on both the strain within the GSY and the thickness of the base course. This mechanism exhibits optimal performance when the strain in the GSY is kept below 1%, in accordance with the guidelines set by ISO/TC 221/WG 6 (2019). Additionally, findings from Qian et al. (2013) emphasize the prominence of the particle lateral restraint mechanism when dealing with granular layers of thickness exceeding 300 mm. In such cases, the thickness of the granular layer acts to minimize the strain experienced by the GGR, further enhancing the efficacy of the lateral restraint mechanism.

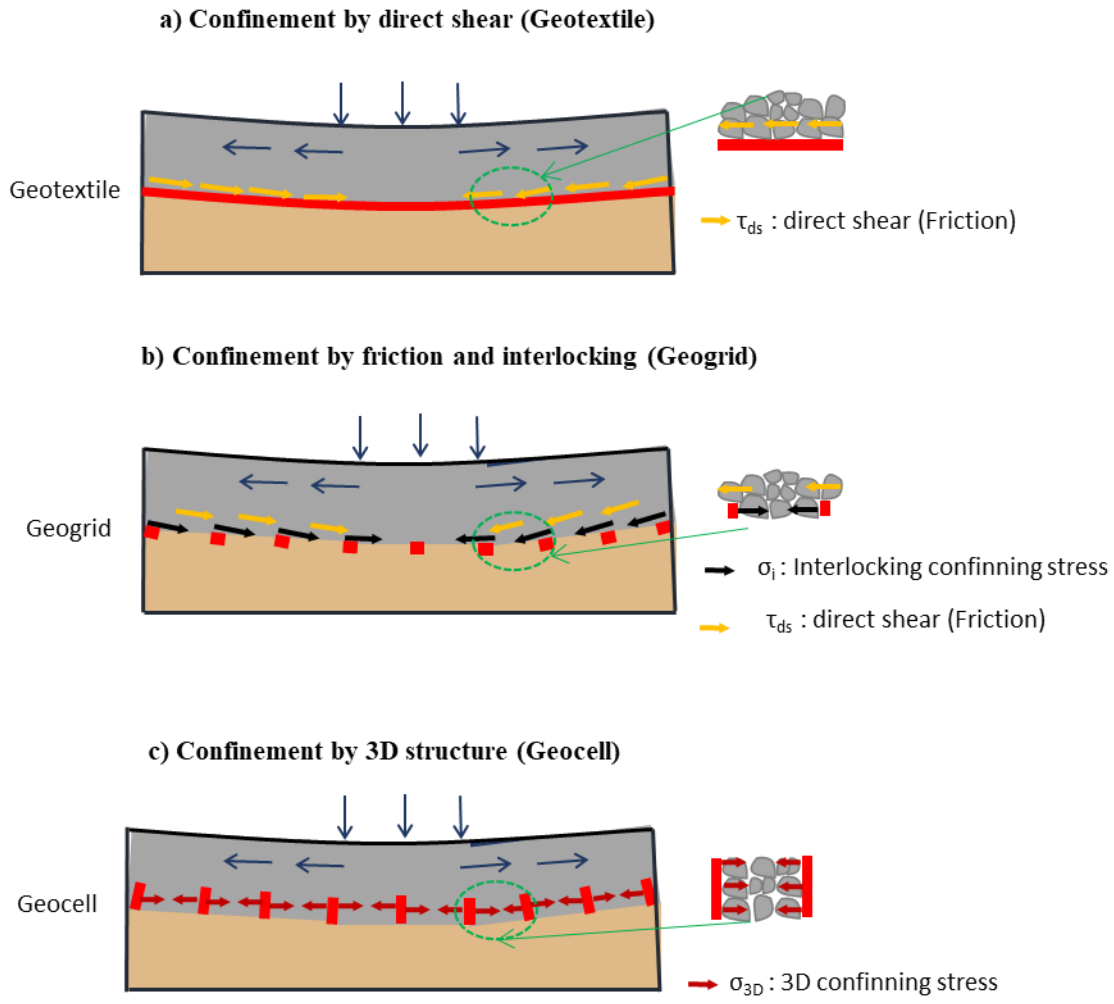

Figure 2-4: Particle lateral restraint (confinement)

2.3.3. Tensioned membrane effect

Reinforcement is achieved by activating an appropriate level of GSY tensile strength, responding to the tensile forces generated in the interaction between the GSY soil and the adjacent soil. In the case of an unpaved road, tensile forces arise within the GSY due to out-of-plane deformation induced by a load applied approximately perpendicular to its plane. A tensioned GSY redistributes tensile forces from the loaded zone to another zone where the GSY is anchored (Figure 2-5), effectively strengthening the unpaved road. At the GSY-soil interface, the tensioned GSY serves to disperse the load over a larger area, mitigating the load transferred to the subgrade layer and, consequently, reducing the subgrade deformation (Giroud et al., 2023).

The tensioned membrane effect is prominent for small fill material thickness, low base course shear stiffness (Ghosh & Madhav, 1994) out-of-plane soil displacement exceeding one-third of the base thickness (Qian et al., 2013), and high GSY stiffness (Perkins & Ismeik, 1997).

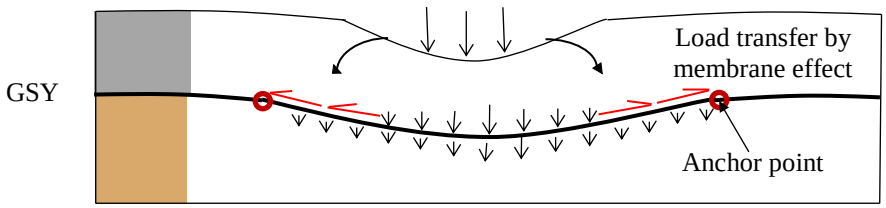

Figure 2-5: Tensioned membrane effect

2.3.4. Transition from lateral restrain to tensioned membrane effect

Cuelho et al. (2014) elucidated the transition from a lateral confinement mechanism to a tensioned membrane, drawing insights from displacement and strain analyses. When subjected to traffic loads, the gravel particles at the base layer initially tended to spread laterally under the load. However, GSY countered this lateral spreading by confining the aggregate movement, primarily through interaction with the intersecting members of the grid structure or via surface friction with the textile materials. The repeated passage of trucks contributed to both the enlargement and distortion of the rutted area (Figure 2-6). Consequently, the gravel gradually lost its ability to spread laterally, causing stresses direction within the base course particle to shift more vertically. This alteration in stress distribution increased stresses on the top of the subgrade, as the subgrade and base course continually shifted away from the rutted area under ongoing traffic loading. The primary support mechanism provided by the GSYs thus transitioned from lateral confinement to the tensioned membrane.

Cuelho et al. (2014) tried to correlate this explanation with data from LVDT sensors placed at various locations in the cross-machine direction (Figure 2-6). In the early truck passes, a noticeable global movement of the GSY away from the rutted area was observed. However, as the developed ruts attained a depth of approximately 50 mm, a significant change was detected in the direction of GSY displacement, now moving toward the rutted area. This observed shift implies a dynamic evolution in the response of the GSY signifying a transition to a tensioned-membrane effect as the rutting conditions intensified.

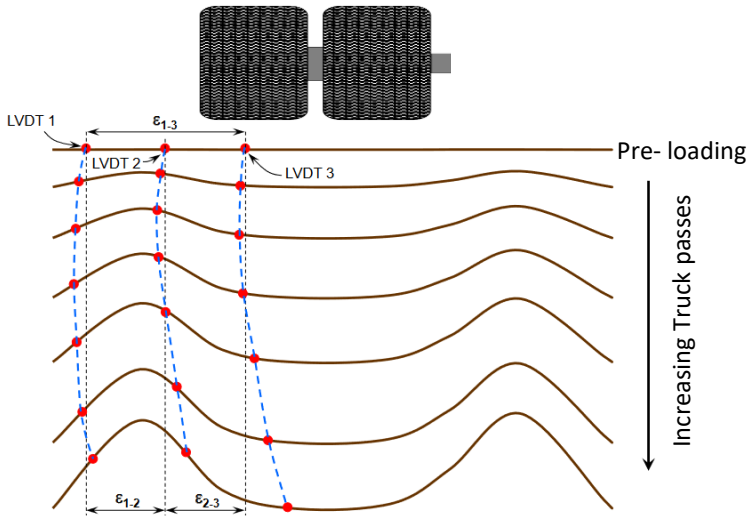

Figure 2-6: Distortion of the instrumented area due to rut formation (Cuelho et al., 2014)

Despite considerable research in this field, definitively establishing the clear dominance of one mechanism over another remains challenging. An alternative approach entails examining the parameters related to soil and GSY properties that influence the behaviour of GSY reinforcement in unpaved roads in the subsequent section.

2.4. Influencing parameters

To elucidate the implemented mechanisms, several authors in the literature have attempted to define the parameters influencing the behaviour of reinforcement through experimental tests in both laboratory and in situ conditions. The applied loads on the tested platforms were mainly vertical plate loads (cyclic or static) or traffic loads (traffic simulators or truck passages). Among these parameters, the thickness of the granular layer, the bearing capacity of the supporting soil, the type of GSY, the number of GSYs, and their positioning are discussed.

2.4.1. Base course layer thickness and subgrade bearing capacity

Optimal functionality of the GSY is contingent upon both the thickness of the base course layer (h) and the softness of the subgrade. In the context of unpaved roads, the use of GSY is recommended when the supporting soil exhibits a California Bearing Ratio (CBR) below 3%, as per FHWA (2008) guidelines.

Hufenus et al. (2006) noted that, for a subgrade with CBR ≤ 3, the presence of a GSY located at the interface between the subgrade and the granular layer under traffic load proves effective up to h ≤ 500 mm. Conversely, Sun et al. (2015) and Khoueiry (2020) concluded that placing the GSY at the interface between a subgrade with CBR=2 and h= 300 mm and h= 350 mm, respectively, did not yield additional effectiveness under cyclic loading. For thinner base course layers, approximately 220 mm, Khoueiry (2020) and Palmeira and Antunes (2010) observed the efficacy of the GSY for CBR values of the lower layer equal to 3 and 8.5, respectively.

2.4.2. GSY properties

Hufenus et al. (2006) concluded from their full-scale tests that each reinforcement GSY should have a stiffness at 2% axial strain ($T_{2\%}$) in both the longitudinal and transverse directions greater than 8 kN/m.

Cuelho and Perkins (2009) and Cuelho et al. (2014) attempted to correlate the mechanical properties of some GSYs to their performance in unpaved road applications. Specifically, they demonstrated that $T_{2\%}$ and $T_{5\%}$ in the transverse direction of the GGR controls its behavior under relatively high rutting development in granular platforms of low thickness. In a comparable case, Khoueiry (2020) tested two knitted GGRs reinforcements characterized by elevated tensile stiffness at 2% of strain and positioned at the interface between a granular platform with a low thickness (h = 22 cm) and the supporting soil (CBR = 2). The knitted GGR possessing the highest $T_{2\%}$ (2500 kN/m), exhibited superior effectiveness in mitigating the settlement of the granular platform under cyclic loading, surpassing the performance of a GGR with a lower $T_{2\%}$ (1000 kN/m).

Qian et al. (2013) concluded that the triaxial GGR, possessing the highest mechanical properties (aperture stability modulus, radial stiffness at 0.5% of strain), demonstrated its superiority in improving the performance of the granular platform compared to other granular platforms (h=15, h=20, and h=30 cm) reinforced by GGRs with lower resistance or unreinforced. In a comparable case Cuelho et al. (2014) attributed the improvement in the performance of the granular platform to the stiffness of the transverse strands and junction points of the GGR when the base layer is relatively thick, and the rut development is relatively slow.

2.4.3. GSY position and number

GTXs are commonly positioned at the interface between the subgrade layer and the base course layer, serving the dual purposes of separation and reinforcement.

For granular platforms with thin to medium thickness ($h \leq 30$ cm), various studies [Hufenus et al. (2006), Cuelho and Perkins (2009), Palmeira and Antunes (2010), Akond (2012), Qian et al. (2013), Cuelho et al. (2014), and Khoueiry (2020)] have highlighted the efficacy of a single GSY, whether it be a GGR or GTX, when placed at the interface between the supporting soil and the granular platform. However, Khoueiry (2020) demonstrated that a single knitted GGR, when positioned at mid-height in a thin granular platform (22 cm) atop compressible soil (CBR=2), exhibited less effectiveness compared to its placement between the two layers.

Furthemore, for thick granular platforms ($h \geq 450$ mm), Akond (2012) determined that the optimal position for a GGR is in the upper third of the granular platform. Additionaly, the most efficient configuration for thick granular platforms involved placing a GTX between the two layers and a GGR in the upper third of the granular layer (Akond, 2012). Recently, Khoueiry (2020) demonstated that the GGR placed at the interface between the granulr platform (h=350 mm) and the subgrade (CBR =2) didn't apport any inprovement to the structure performance.

To provide more knowledge regarding these impacting parameters, various authors have developed an experimental testing system on unpaved roads, and these tests are presented in the next section.

2.5. State of the art on the experimentation

Within the GSY granular platform laid over soft subgrade, the performance of reinforcement is subject to various influencing factors. Extensive research in literature aims to delineate the influence of reinforcement and the nuanced effects of each parameter. The large-scale investigations can be classified into three distinct categories:

1. Large-scale and small-scale laboratory plate load tests
2. Large-scale in situ tests
3. Large-scale laboratory cyclic traffic load tests

2.5.1. Large-scale and small-scale laboratory plate load tests

Two distinct approaches have been employed in previous studies to conduct plate load tests: the static load approach and the cyclic load approach. In this section, a variety of static plate load tests and cyclic plate load tests conducted on constructed unpaved road sections within experimental boxes are presented. Furthermore, a comprehensive comparison between these two loading approaches is discussed in the literature and presented in this section.

Akond (2012) performed a series of small-scale laboratory static plate load tests on both unreinforced and reinforced unpaved sections within a steel box (1.5 m in length, 0.91 m in width, and 0.91 m in height) illustrated in Figure 2-7a. The subgrade was constituted of silty clay and classified as CL according to the Unified Soil Classification System (USCS) with a CBR of around 1%. The base course was constructed using Kentucky crushed limestone, with tested thicknesses of 200 mm, 305 mm, and 460 mm. Additionally, three types of GSYs were subjected to testing: biaxial GGRs (BX), triaxial GGRs (TX), and woven GTXs (RS). Each type of GSY included variations with distinct stiffness levels, contributing to a comprehensive evaluation. Quality control during installation and compaction of the soil layers was ensured through the implementation of various tests, including: the nuclear density gauge, geo-gauge stiffness device, dynamic

cone penetrometer, and light falling weight deflectometer. Vertical stress distribution within the subgrade layer was monitored through pressure cells, while strain gauges strategically placed along the reinforcements provided additional insights. The study encompassed the evaluation of a single GSY sheet, positioned either at the base course-subgrade interface or within the base course. Additionally, the examination included the testing of double GSYs, with one placed at the interface and the other within the base course. The testing procedure involved incrementally applying vertical loads to a circular steel plate with a diameter of 0.19 m after reaching a settlement of 0.508 mm at the base course surface. The static plate load continued until the predetermined total deflection was achieved, with a ring load cell measuring applied pressure and two dial gauges measuring plate deflection. The comparison between the results of the performed tests revealed the following findings:

- The higher GSY tensile stiffness resulted in a wider stress distribution angle (Figure 2-7b). However, potential uncertainties associated with the use of earth pressure cells in soft subgrade, such as sensor settlement and rotation, were not considered noted. Additionally, the presence of non-negligible vertical pressure at the box borders indicated potential boundary effects, though these uncertainties were not addressed by the authors.
- In the case of thin base course layers (200 mm), the study emphasized the effectiveness of a single GSY reinforcement (GGR or GTX) at the subgrade-base course interface. For thick base course layers, optimal placement of a single GGR reinforcement was found to be at the upper one-third position of the base course layer.
- Positioning a biaxial GGR at the upper one-third of the base course layer, coupled with a GTX at the subgrade-base course interface, outperformed the configuration where the same biaxial GGR was placed at the upper one-third of the base course layer, coupled with another biaxial GGR at the interface.

It is crucial to emphasize that the study highlighted potential uncertainty arising from variations in subgrade layer thickness with changes in base course thickness due to the limited height of the box. This limitation could impact results with the absence of studies demonstrating the minimum subgrade thickness that doesn’t affect the results of the tests.

a) b)

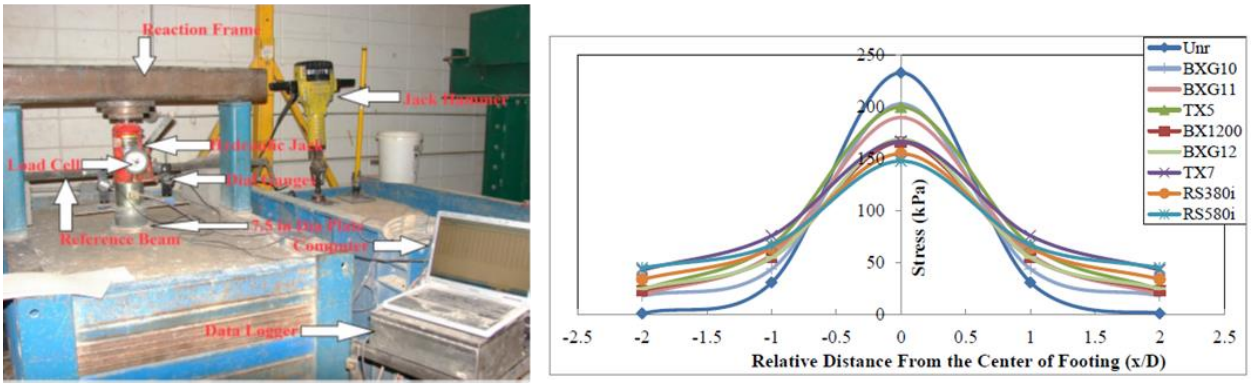

MD : Machine direction , **XMD** : Cross machine direction, $\mathbf{J_{2\%}}$: Tensile modulus at 2 % of strain for GTX and biaxial GGR, $\mathbf{J_{0.5\%}}$: Tensile modulus at 0.5 % of strain for triaxial GGR, **BX** : Biaxial GRR, **TX**: Triaxial GGR, **RS** : Woven GTX, **Unr**: Unreinforced.

	$J_{2\%}$ (kN/m)	
	MD	XMD
BXG10	205	330
BXG11	455	
BXG12	455	615
BX1200	300	450

	$J_{0.5\%}$ (kN/m)	
TX5	375	
TX7	475	

	$J_{2\%}$ (kN/m)	
	MD	XMD
RS380i	350	750
RS580i	350	1313

Figure 2-7: Akond (2012): a) Instrumentation system set-up; b) Vertical stress distributions on the subgrade layer along the centre line of the plate at 1206 kPa plate applied pressure at 200 mm thick base course

Demir et al. (2013) conducted a series of large scale in situ tests in a test pit measuring 30 m in length, 11.6 m in width, and 2 m in height. Each plate load test took place in a field test pit measuring 2.8 m in width, 2.8 m in length, and 2 m in depth (Figure 2-8). The subgrade layer, identified as clay (CH) by the Unified Soil Classification System (USCS), showed shear strengths (CBR) ranging from 60 kN/m^2 (2%) to 75 kN/m² (2.5%). Biaxial GGR with a tensile stiffness at 2% strain ($T_{2\%}$) of approximately 1,100 kN/m was tested. The base layer consisted of granular fill with four base course thicknesses: 200 mm, 300 mm, 400 mm and 600 mm. A proportional relationship between plate load diameter (D) and granular fill thickness (h) was maintained as h = 0.67D. Hence, the four plate load diameters were: 300 mm, 450 mm, 600 mm, and 900 mm. The static loads were applied until ultimate vertical deformation occurred with surface settlement reaching up to 45 mm and contact plate pressure reaching 1,000 kPa. The testing procedure adhered to ASTM D 1196-93 (ASTM, 1997), with load increments maintained until the settlement rate was less than 0.03 mm/min over three consecutive minutes. Pressure and plate settlement were measured using a pressure gauge and two LVDTs respectively. Various configurations were tested, including sections with only clay layers without granular fill, sections with granular fill layers over clay layers, sections with granular fill layers over clay layers reinforced by a single GGR at the interface, and sections with granular fill layers over clay layers reinforced with a double GGR, one at the interface and the other at the upper one-third of the granular fill. The key findings from the study include:

- The bearing capacity of the loading plate increased by 40% with the installation of a granular fill over the subgrade layer.
- A single GGR located at the base course-subgrade interface did not show any additional improvement in plate bearing capacity.

- The setup featuring a single GGR at the interface between the subgrade and the granular fill, coupled with another GGR at the upper one-third of the compacted granular fill, elevated the plate's bearing capacity by 70% at a 10 mm settlement and an impressive 130% at a 30 mm settlement. This suggests that the GGR layers are effectively mobilized in succession with increasing strain.

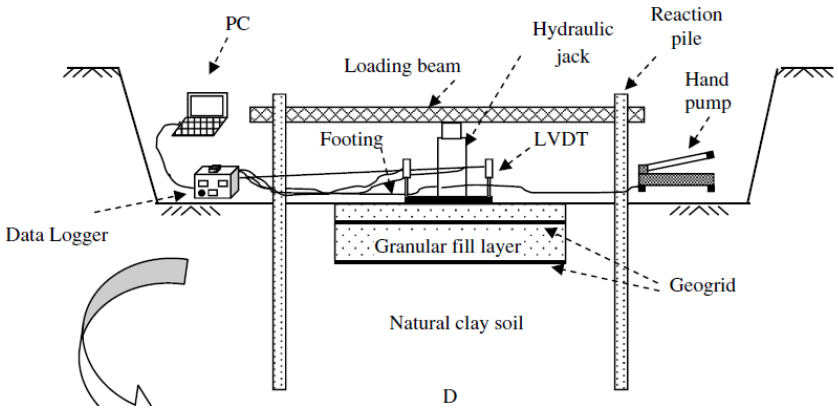

Figure 2-8: Schematic view of test setup (Demir et al., 2013)

Abu-Farsakh et al. (2016) performed a series of small-scale laboratory static plate load tests conducted within a steel box measuring 1.5 m in length, 0.91 m in width, and 0.91 m in height. The subgrade layer, characterized as CL soil (USCS), was a silty clay with a targeted CBR of 1%. The base course layer comprised crushed limestone with a thickness of 305 mm. The tested GSYs were woven GTXs and extruded biaxial and triaxial GGRs with varying stiffness. A range of configurations underwent testing, encompassing unreinforced sections, reinforced sections featuring a single GSY at different positions-either at the base course-subgrade interface, within the middle depth of the base course, or positioned at the upper one-third depth of the base course. Additionally, sections were examined with double GSY reinforcement: one at the interface and the other situated at the upper one-third of the granular fill. To assess soil properties, a nuclear density gauge, Light Falling Weight Deflectometer (LFWD), and Dynamic Cone Penetrometer (DCP) were employed. Earth pressure cells were positioned on the subgrade surface, while strain gauges were affixed to the GSYs. Tests were executed following ASTM D1196-93 standards, utilizing a 190 mm diameter plate. The primary objectives of Abu-Farsakh et al. (2016) study were to evaluate the impact of GSY reinforcement, the GSY stiffness, the placement of GSY, and the number of GSY layers. Their conclusions, drawn from the bearing capacity and the deformation analyses, include:

- The GSY reinforcement significantly reduced surface deformation and increased bearing capacity.
- Sections with double reinforcement consistently demonstrated superior results, showing a more substantial reduction in surface deformation and a corresponding increase in bearing capacity.
- A clear correlation emerged between higher tensile modulus of GSYs and elevated bearing capacity, highlighting the positive impact of increased tensile modulus on overall performance.

Gallage et al. (2023) conducted a series of 14 laboratory plate load tests on working platforms constructed within a steel box measuring 1 m in length, 1 m in width, and 1.2 m in height (Figure 2-9a). The subgrade comprised of high plastic silt (MH) clay according to the Unified Soil Classification System (USCS) and a CBR of 2.5%. The base course, composed of high-quality quarry materials, was classified as Type 2.1 road base material according to QDTMR specifications (QDTMR 2019). Three base course

thicknesses (200 mm, 300 mm, and 400 mm) were tested. The GSYs tested included welded biaxial GGR, extruded biaxial GGR, geocomposite of non-woven GTX with welded GGR, and geocomposite of non-woven GTX with extruded GGR. All GGRs exhibited ultimate tensile strength greater than or equal to 40 kN/m in both machine and cross-machine directions. Pressure cells were placed at the subgrade layer surface to measure vertical stresses, Linear Variable Displacement Transducers (LVDTs) were positioned at the base course surface to measure surface deformation, and foil-type strain gauges were affixed to two GGR products to monitor strain in the GSY. Monotonic loading was applied in two cycles at a rate of 1.0 mm/min through a steel plate of 200 mm diameter. The first load cycle was executed to 550 kPa surface stress and the second cycle continued until the state of ultimate failure. To investigate the effectiveness of base course and the GSYs in enhancing the bearing capacity of weak subgrades, various configurations were tested. The configurations included sections with only clay layers, sections with granular fill layers over clay layers, and sections with base course layers over clay layers reinforced by a single GGR or geocomposite at the subgrade-granular fill interface. The study yielded the following key findings (Figure 2-9b):

- The ultimate bearing capacity of the weak subgrade improved with increasing the granular cover thickness.
- The single reinforcement placed at the interface between the weak subgrade and the base course increased the ultimate bearing capacity by 60% and 37% when the base course equal to 200 mm and 300 mm respectively.
- The impact of the reinforcement on improving the subgrade bearing capacity was negligible when the it was positioned when the base course thickness equal to 400 mm (2D).

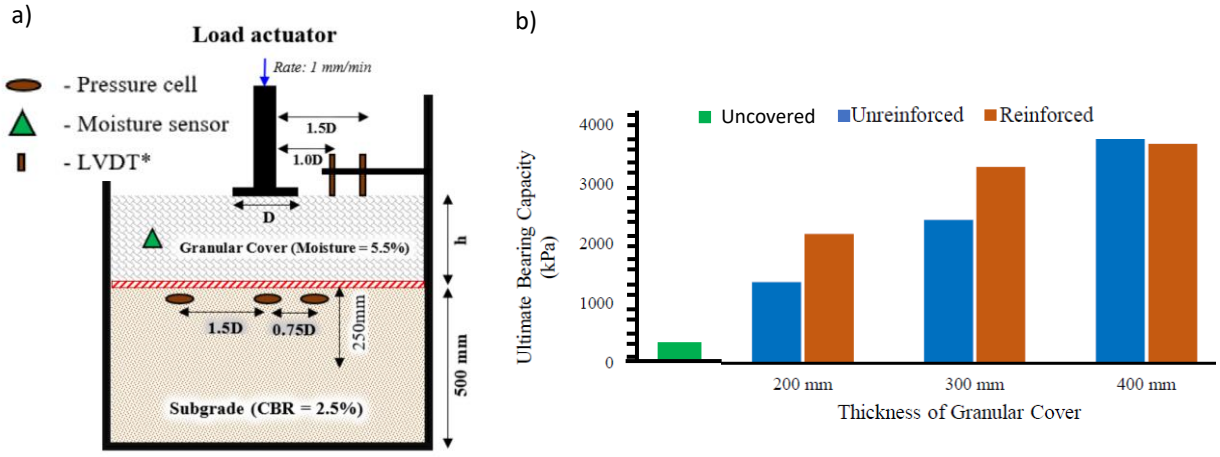

Figure 2-9: a) Schematic diagram of a reinforced section (Wimalasena et al. 2022); b) Comparison of the average values of ultimate bearing capacity of uncovered subgrade, covered subgrade, and reinforced covered subgrade at 60 mm of surface settlement (Gallage et al., 2023)

Palmiera and Antunes (2010) studied the transition from monotonic loading to cyclic loading in unpaved sections. One of the aims of their research was comparing the effectiveness of GSY under these loading conditions, utilizing a large-scale experimental box measuring 1.6 m in length, 1.6 m in width, and 1.2 m in height (Figure 2-10). The subgrade soil consisted of fine-grained tropical soil and classified as CH according to the Unified Soil Classification System (USCS). The subgrade layers had a CBR of 8%, exceeding the threshold recommended by the Federal Highway Administration (FHWA) in 2008 for the

use of GSYs. The fill material comprised well-graded aggregate with a base thickness of 200 mm. A knitted biaxial GGR and woven GTX were tested with each of them positioned at the interface between the base course and the subgrade. Measurement instruments, including LVDTs and load cells, were employed to measure vertical displacements of the loading plate and vertical loads applied to the plate, respectively. Total pressure cells were placed along the soil layers depth to measure stress increments during the tests, while strain gauges provided valuable data at various locations within the subgrade soil. The vertical stress on the fill surface is applied through a 300 mm diameter steel plate, situated beneath a jack connected to a hydraulic system. Cyclic loading tests were conducted with a frequency of 1 Hz and a plate stress of 566 kPa, representing a typical truck axle load of 80 kN, until a surface settlement of 25 mm is reached. Meanwhile, vertical monotonic loading steadily increased until a similar 25 mm plate settlement is attained. It is noteworthy that the loading rate was not specified in the published study. The authors revealed that tests conducted under monotonic loading conditions underestimated the beneficial effects of reinforcement compared to tests conducted under cyclic loading conditions. Furthermore, the study highlighted a significant reduction in breakage in gravel under monotonic loading, in contrast to the more challenging conditions posed by cyclic loading tests.

Furthermore, beyond the primary insights gleaned from the comparison between monotonic and cyclic loading, additional findings emerged from the cyclic loading tests, which encompassed two subsequent loading stages following the initial one where a settlement of 75 mm occurred:

- A notable augmentation in the number of load cycles required to achieve a specific rut depth was attributed to the presence of the reinforcement layer.
- The GGR reinforced platform exhibited superior performance not only in terms of rut development but also in effectively mitigating stress and strain within the subgrade, outperforming the GTX-reinforced platforms.
- The efficiency of GGR reinforcement surpassed that of GTX reinforcement in restraining lateral movement of the fill material, leading to a consequential increase in fill passive resistance.

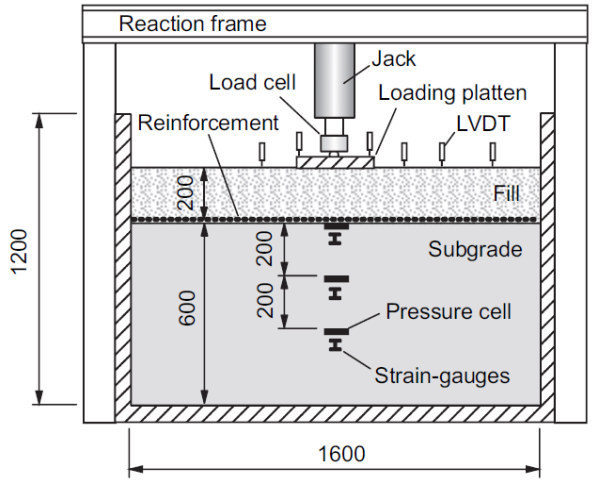

Figure 2-10: Schematic view of test setup
Palmiera and Antunes (2010)

Furthermore, Kiptoo et al. (2017) undertook an investigation involving static and cyclic plate loading tests to evaluate the effectiveness of reinforcement in unpaved sections. Utilizing a steel box (1 m in length and 1m in large), the authors asserted their efforts to minimize boundary effects and maintain a sufficient

sample size, yet the publication lacks explicit verification of these considerations. The soft subgrade layer, comprised of Kaolin Clay with a CBR of approximately 2%, exhibited a thickness of 500 mm. The underlying base material, classified as SC (Clayey sand) according to the Unified Soil Classification System (USCS), possessed a thickness of 300 mm. Two types of GSY were employed in the study: 1) an extruded biaxial GGR with a square grid measuring 38x38 mm and a tensile strength of 20 kN/m in both machine and cross-machine directions, and 2) a woven GTX with a tensile strength of 50 kN/m in both directions. While the GSY strain does not exceed 2% in unpaved applications, the publication omitted specific details regarding tensile stiffness values at this strain for either the GGR or GTX. Notably, details regarding sensor usage and soil installation and compaction were absent from the publication. Static and cyclic loads were applied using a 305 mm diameter steel plate, with static loading executed at a rate of 1.2 mm/min. Dynamic loading involved a sinusoidal load superimposed atop a static hold-down force of 4 kN. The dynamic load linearly increased with an incremental load of 4 kN for every 8 cycles at a frequency of 0.2 Hz. The settlement failure of the composite system was assessed at a deformation of 75 mm. However, testing persisted even after surpassing this failure point. Both static and cyclic plate loading tests revealed significant improvements in pavement performance due to inclusion GSY. Notably, the assessments under cyclic loading demonstrated a more pronounced effectiveness of the reinforcement when compared to static loading. This observation is consistent with the findings of Palmeira and Antunes (2010). The section reinforced with a single GTX at the base course-subgrade, and the section reinforced with a single GGR at the base-subgrade interface, demonstrated comparable effectiveness in reducing settlement compared to the unreinforced section. The revelation that the tensile strength of the GTX is 2.5 times the tensile strength of the GGR implies that tensile strength alone does not emerge as the dominant performance indicator. The inherent ability of GGR to interlock with soil results in a performance comparable to that of a GTX with 2.5 times the ultimate strength of the GGR. This underscores the intricate relationship between GSY properties and their impact on pavement performance, emphasizing the significance of factors beyond tensile strength in influencing overall effectiveness. Furthermore, employing double GSYs, with one GTX placed at the base-subgrade interface and one GGR positioned at the upper one-third of the base layer, exhibited superior performance in reducing settlement and increasing bearing capacity compared to sections with a single GSY.

Qian et al. (2011 and 2013) conducted a study involving 12 cyclic plate load tests using a box measuring 2.2 m in length, 2 m in width, and 2 m in height. The investigation focused on the performance of granular fill layers over a weak subgrade in the presence of a single triaxial GGR at the base course-subgrade interface. The weak subgrade consisted of an artificial soil blend, comprising 75% Kansas River sand and 25% kaolinite by weight, with a CBR of 2%. To assess the impact of different triaxial GGRs, characterized by radial stiffness and aperture stability (T_1: light-duty, T_2: medium-duty, and T_3: heavy-duty grades), the GGRs were placed at the interface between the subgrade and the base course. The base course layer consisted of well-graded aggregates with three different thicknesses of 150 mm, 230 mm, and 300 mm. Instrumentation of the testing platform included earth pressure cells at different positions at the interface between the subgrade and base course, as well as displacement transducers (LVDTs) at the plate surface and the base course surface. Cyclic loading, applied on a 300 mm circular plate diameter at a frequency of 0.77 Hz, featured a maximum load of 40 kN, equivalent to half of a truck axle load as per AASHTO (1993) standards. Testing concluded upon reaching a 75 mm plate displacement, in accordance with FHWA (2008) standards. Upon scrutinizing the collected sensor data, the authors showed that sections reinforced with triaxial GGR exhibited a significantly higher capacity for supporting loading cycles compared to their unreinforced counterparts, both at 25 mm and 75 mm plate settlements. Furthermore, the heavy-duty GGR-reinforced base sections demonstrated an ability to endure a greater number of loading cycles compared to their light-duty GGRs. Additionally, the use of triaxial GGR led to a reduction in the maximum vertical stress on the subgrade, resulting in a more uniform stress distribution when contrasted with unreinforced bases. Furthermore, the study delved into the manifestation of the tensioned membrane effect and the particle restraint mechanism, exploring their correlation with the permanent settlement of the base course thickness. The diminished maximum vertical stress was a direct outcome of the tensioned membrane effect. Figure 2-11a revealed a decrease in maximum vertical stress when the range of settlement was 33% to 40%

of the 150 mm thickness of the base course, indicating the initiation of the tensioned membrane effect. In contrast, when the permanent deformation equalled 25% of the 300 mm thickness (Figure 2-11b) of the base course, no reduction in maximum vertical stress was observed. Consequently, the absence of the tensioned membrane effect underscored the GGR -aggregate interlocking as the singular mechanism responsible for the enhanced performance in the reinforced base courses.

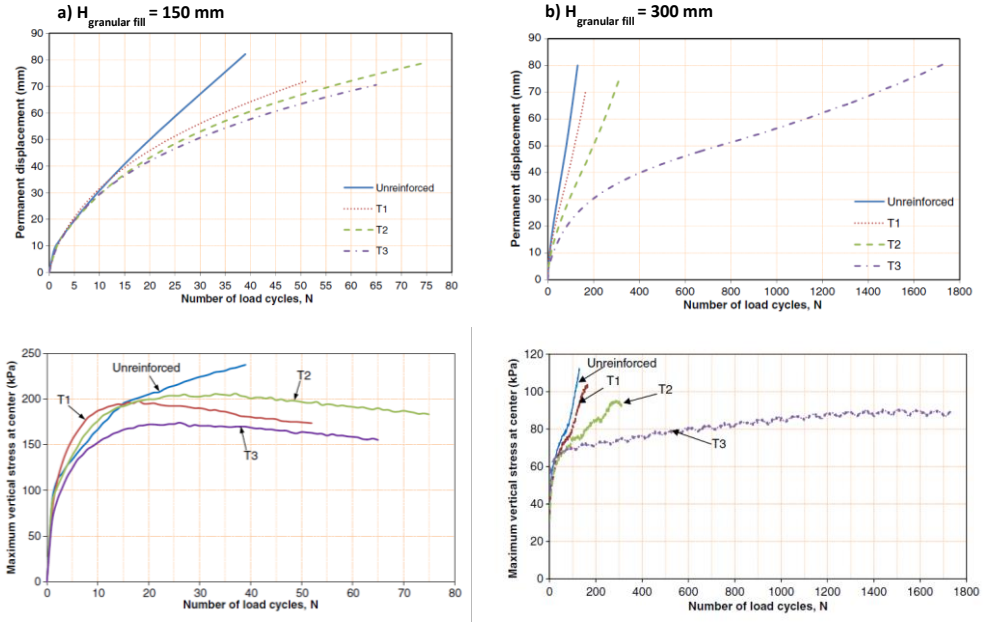

Figure 2-11: Surface permanent displacement / Maximum vertical stresses at the interface between subgrade and base course versus the number of load cycles for (a) 150-mm-thick; (b) 300-mm-thick

Another series of cyclic plate load test have been performed by Palmeira et al. (2016) to investigate the impact of soil–reinforcement interaction properties on the performance of low thickness reinforced fills on soft soil. The experimental setup involved a rigid tank with a diameter of 1.2 m and a height of 0.52 m (Figure 2-12). The instrumentation included a load cell and LDVTs to measure vertical loads and displacements. The fill layer, with a thickness of 300 mm, comprised gravel with particles ranging from 1.5 to 21 mm, and an average particle diameter (D_{50}) of 10.5 mm. A compressible layer of loose sand, 220 mm thick, served as a subgrade underneath the gravel to mimic conditions found in unpaved roads. The sand layer was prepared using the sand rain technique, achieving a relative density of 30% and a CBR value of 1.6%. Twelve GGRs (including two uniaxial and ten biaxial) and a woven GTX were employed in the tests. All reinforcements had their extremities folded into the fill material for improved anchorage conditions. Total pressure cells were placed to measure vertical stress at various points across the subgrade depth, and data acquisition was performed using a Lynx ADS 2000 data logger and a microcomputer. Vertical cyclic loading, applied to a 200 mm diameter loading plate, featured a frequency of 1 Hz and a maximum vertical stress of 560 kPa. The testing phase concluded upon achieving a vertical displacement of 75 mm. The woven GTX exhibited an enhancement in fill performance compared to the unreinforced fill layer, albeit with a performance level lower than that of the GGR possessing similar tensile stiffness at 5% strain. The interaction between the GGR and the surrounding soils emerged as a pivotal factor influencing reinforcement performance. The study highlighted that the ratio between the GGR's equivalent aperture dimension and the maximum fill particle diameter was optimal at 0.94. Similarly, the ratio between the GGRs equivalent aperture dimension and the average fill particle diameter was found to be optimal at 1.8.

Additionally, the thickness of the grid demonstrated a discernible impact on the overall performance of the fill material. Interestingly, while GGR aperture stability, considered a key characteristic in the Giroud and Han (2004a) method, did not significantly influence the performance of the fill layer in this study.

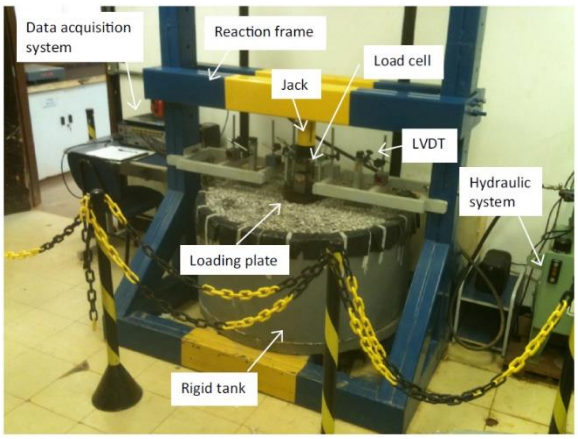

Figure 2-12: View of the equipment.
Palmeira et al. (2016)

Bräu and Vogt (2018) conducted a comprehensive series of cyclic plate load tests within a substantial test pit, boasting dimensions of 3.3 m by 5.0 m, as depicted in Figure 2-13a. A circular and rigid steel plate, featuring a diameter (D) of 300 mm, underwent an exhaustive 100,000 loading-unloading cycles. Stresses ($\sigma_{c,max}$) of 350 kPa, 450 kPa, and 550 kPa were applied at a frequency of 0.3 Hz. The subgrade soil layer, comprising a low-plasticity clay with a thickness of 900 mm, underwent vane shear tests after compaction. These tests measured undrained shear strength (c_u) ranging between 30 kPa and 60 kPa, equivalent to CBR values spanning 1% and 2%. Various GSYs were subjected to testing at the subgrade-base course interface, including a non-woven GTX (GT-3) characterized by low stiffness (6.5 kN/m in the machine direction and 10 kN/m in the cross-machine direction), a GGR (GT-4) exhibiting a stiffness of 40 kN in both directions, and a geocomposite (GT-5) comprising the GT-3 and the GT-4. The base course material, consisting of well-graded gravel with rounded grains, was layered with three distinct thicknesses: 150 mm (0.5 D), 300 mm (1.0 D), and 450 mm (1.5 D). The investigation unveiled a direct correlation between the effectiveness of GSYs (GT-3, GT-4, and GT-5) and both the subgrade strength and the thickness of the base course layer. In sections characterized by a weak subgrade and a thin base course layer, GSYs demonstrated notable efficacy in reducing soil settlement. However, as subgrade strength increased and the granular layer thickness expanded, the impact of the GSYs became less pronounced. Moreover, in the case of a low-strength subgrade (with a shear strength of 30 kPa), the integration of GSYs (GT-3, GT-4, and GT-5) resulted in substantial savings in base course thickness (Figure 2-13b). Sections reinforced with a 150 mm base course thickness (0.5 D) exhibited surface settlements comparable to those of the unreinforced section with a thicker base course measuring 300 mm (D), under a maximum cyclic stress ($\sigma_{c,max}$) of 450 kPa. Similarly, sections reinforced with a 300 mm base course thickness (D) displayed surface settlements closely resembling those of the unreinforced section with an even thicker base course measuring 450 mm (1.5 D) under $\sigma_{c,max}$ of 550 kPa.

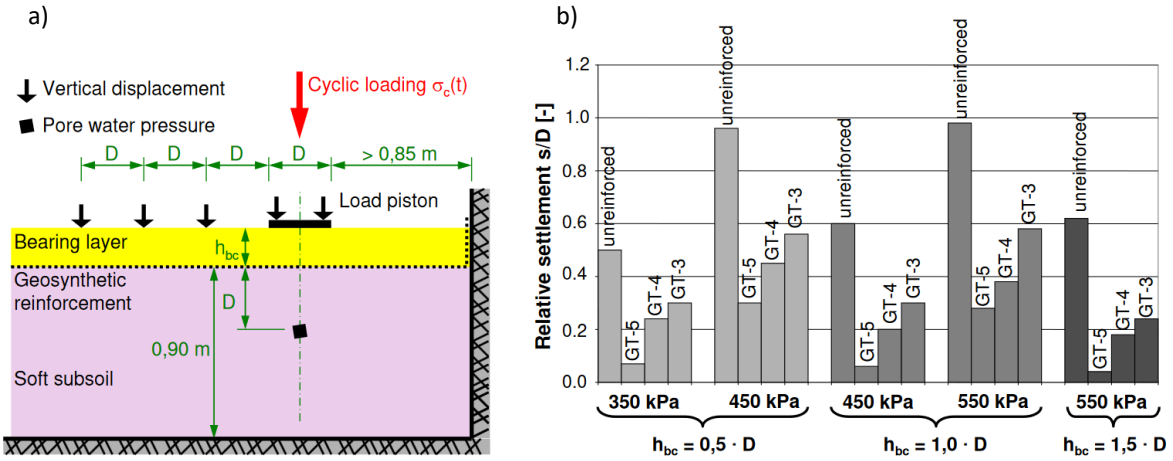

Figure 2-13: Schematic diagram of the experimental setup; b) Summary of the relative settlements (s/D) after n = 1000 cycles with a subsoil undrained shear strength s_u = 30 kPa

Khoueiry (2020) conducted a series of cyclic plate load tests on an unpaved road platform within a geotechnical box measuring 1.8 m in width, 1.9 m in length, and 1.1 m in height (Figure 2-14). The subgrade, comprising 20% kaolinite clay and 80% Hostun sand, exhibited a CBR of approximately 2% and a thickness of 600 mm. The base course layer utilized untreated aggregates at two distinct thicknesses, namely 350 mm and 220 mm. The study evaluated three GGRs: one extruded GGR with 80 mm hexagonal apertures of length and a tensile stiffness at 2% strain ($T_{2\%}$) of 360 kN/m and two knitted GGRs with high stiffness values ($T_{2\%}$ = 1000 kN/m and $T_{2\%}$ = 2500 kN/m) featuring rectangular apertures of 40 mm of length each. In the reinforced sections, the GGR was positioned either at the base-subgrade interface or at the middle depth of the base layer. Various instruments, including earth pressure cells and settlement sensors placed atop the subgrade surface, were employed to measure vertical stress and settlement, respectively. Displacement laser sensors were utilized to gauge surface settlement in the base course. Detailed descriptions of soil layer installation and compaction procedures are outlined in the report. Quality control tests, encompassing a water content profile, shear vane tests, as well as static and dynamic penetrometer tests, were conducted on each soil layer to ensure uniform testing conditions. Cyclic loading was applied using a circular plate with a diameter of 300 mm and a maximum load of 40 kN (566 kPa), equivalent half-axle load (ESAL). The loading frequency was maintained at a constant 0.77 Hz, with the testing concluding after 10,000 cycles. For the thicker base course (350 mm), the incorporation of a single GGR at the subgrade-base course interface proved ineffective, as surface settlement did not surpass 40 mm after 10,000 loading cycles for both reinforced and unreinforced platforms, falling below the maximum allowable rut depth of 75 mm. In the case of the thinner base course (220 mm), the knitted GGR with the highest stiffness reduced maximum surface settlement after 10,000 cycles by 35%, followed by the knitted GGR with the lower stiffness at 25%, and the extruded GGR at 12%, as compared to the unreinforced base course. Findings indicated that the extruded GGR significantly contributed to platform improvement, primarily through lateral restraint mechanisms during initial cycles with relatively small displacements (<50 mm). This can be attributed to its unique manufacturing characteristics and rigid nodes. Knitted GGRs, while not impactful initially, exhibited a tension membrane effect after reaching a certain displacement threshold (>50 mm) due to their high stiffness. Moreover, the knitted GGR placed at the middle depth of the base

course (h = 220 mm) demonstrated a limited effect on platform improvement when compared to the knitted GGR placed at the subgrade-base course interface.

Figure 2-14: Test setup (Khoueiry, 2020)

Jayalath et al. (2021) conducted six cyclic plate load tests to scrutinize the efficacy of composite GGR reinforcement (CGG) composed of GGR attached to a GTX in unpaved sections. Employing a robust steel box measuring 1.0 m in length, 1.0 m in width, and 1.2 m in height (Figure 2-15a), the researchers investigated both CGG-reinforced and unreinforced sections. The subgrade, comprised of high-plasticity silt (MH) classified under the Unified Soil Classification System (USCS), exhibited a thickness of 500 mm, with a targeted CBR of 2.5%. The base material, categorized as Type 2.3 granular material according to Transport and Main Roads Specifications (TMR, 2017), underwent experimentation with three different base course thicknesses: 200 mm, 300 mm, and 400 mm. The CGG, positioned at the subgrade-base course interface, possessed a tensile stiffness at 2% strain ($T_{2\%}$) of 16 kN/m. To gather comprehensive data, the researchers installed two pressure mapping sensors to measure lateral pressure on the soil box's wall surfaces, LVDTs, and soil pressure transducers at the granular base and subgrade layer for vertical soil displacement and stress measurements, respectively. Additionally, twenty placed strain gauges on the GGR provided insight into the strain distribution throughout the CGG. Cyclic loading, applied to a 200 mm rigid plate diameter (D), featured a maximum contact pressure of 550 kPa and a frequency of 0.33 Hz. Loading persisted until a 75 mm permanent deformation at the surface center, delineated by the failure criterion, or after 150,000 loading cycles. Negligible pressure was observed on the inner walls of the soil box, indicating the absence of a boundary effect. The results revealed that the effectiveness of CGG reinforcement varied with base course thickness. In instances of a thin granular base (200 mm), CGG at the base-subgrade interface proved effective, yielding a 45% reduction in rut depth at the base surface and a 40% reduction in settlement at the subgrade surface compared to unreinforced section. Contrarily, for thicker base courses (300 mm and 400 mm), placing CGG at the base-subgrade interface proved ineffective. The reinforced section generated higher rut depths compared to unreinforced sections due to shear failure, attributed to the rigid boundary effect formed in the confined zone where CGG and the aggregate of the base course are in contact through friction and/or interlocking (Figure 2-15b). Furthermore, the study revealed that thinner granular bases contribute to higher strains in the CGG reinforcement at the base course-subgrade interface. Consequently, the gravel lateral restraint and tension membrane effect's role in reinforcing the base-subgrade interface are more pronounced for unpaved sections with thinner granular bases.

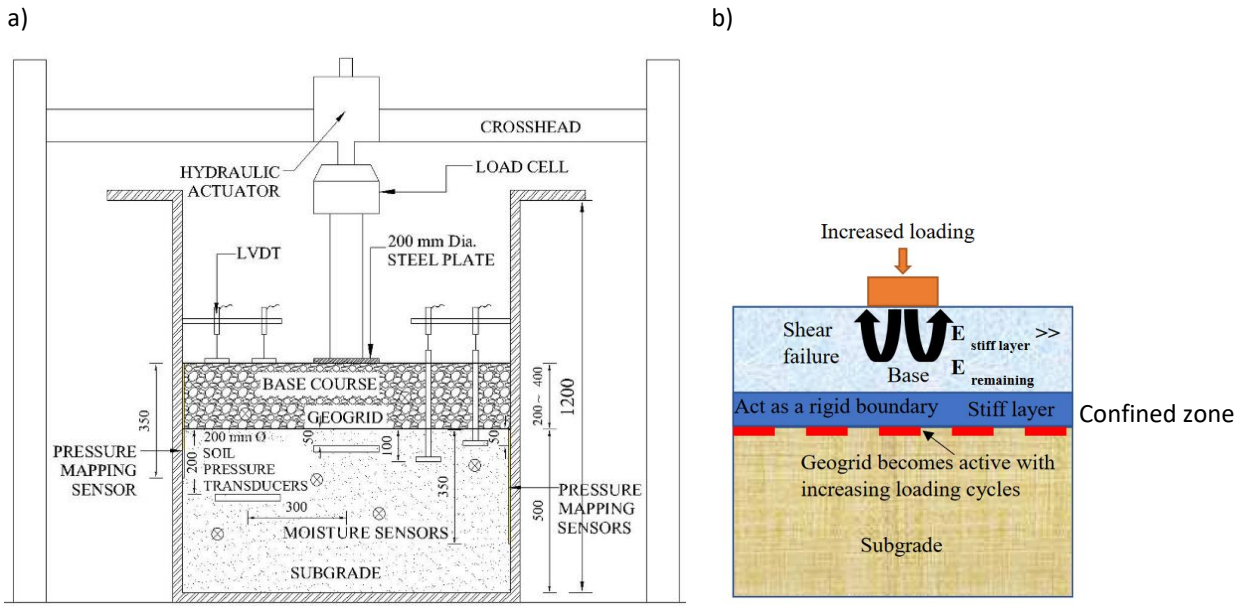

Figure 2-15: Jayalath et al. (2021): a) Schematic diagram of the experimental setup (dimension in mm); b) Rigid boundary effect

Plate loading tests review

This literature review on plate load tests, presented in Table 2-1, encompassed a range of experiments with diverse configurations aimed at simulating circulation traffic on unpaved roads. The plate load tests employed vertical loading on a plate, initially utilizing static loading in the early stages of research and later transitioning to cyclic loading to better emulate real loading scenarios. The significance of plate load tests lies in their pivotal role, offering a streamlined and controlled approach to assess the performance of reinforced platforms over soft soil. In most cyclic plate loading tests, a standardized maximum load of 40 kN (equivalent to the half-axle load or ESAL applied by a hydraulic jack) was consistently employed, facilitated by the automation of loading cycles, enabling the efficient execution of a high number of cycles. The tests, conducted within controlled laboratory settings, yielded several notable benefits:

- Resource efficiency: the quantity of soil required for these tests, along with associated preparation and installation efforts, was significantly reduced compared to in situ tests, saving both time and material resources.
- Laboratory control: testing in a controlled laboratory environment minimized the impact of external environmental factors, enhancing the reliability and repeatability of results, ensuring a more accurate evaluation of reinforced platform performance over soft soil.
- Influencing parameter exploration: Various authors conducting these tests uncovered crucial insights into influencing parameters impacting the behavior of reinforced platforms, including the optimal location of the GSY, base course thickness, subgrade softness, number of GSY used, and GSY properties.

To simplify time and effort and test numerous configurations involving two base course thicknesses and two GSYs, we opted to perform plate load tests in our experimental works. However, the literature also reveals several limitations in conducted plate load tests. Firstly, there is a lack of emphasis on illustrating installation procedures in the reviewed works, despite their critical importance. In response, our

experimental work will establish a protocol for soil preparation and installation, ensuring uniform platform properties for each test, controlled through a series of quality control tests. The quality control tests include static cone penetration tests and vane shear tests to control the properties of the subgrade and dynamic cone penetration tests and clegg impact soil test to control the bearing of the base course. Additionally, the soil water content is controlled before and after the testing. Secondly, recognizing the underestimation of GSY Reinforcement impact in monotonic plate load tests, we have chosen to implement cyclic loading in our experiments. Thirdly, numerous studies reported reaching failure criteria after a relatively small number of cycles, deviating from the proposed 10,000 cycles for designing structures. In the testing of GSY products, GGRs are commonly tested with less emphasis on GTXs. Therefore, our testing experiments will specifically focus on evaluating GTX. Some test results depict the evolution of vertical stress on the subgrade surface with cycles, linked to base course deterioration. However, concerns arise about the accuracy of pressure cells installed in the subgrade due to potential rotation, leading to false measurements during loading, rendering subgrade stress more as a qualitative indicator of trends than a source of precise quantitative results.

Furthermore, some authors in the literature highlight the limitations of vertical applied loading in plate load tests and the restricted dimensions of experimental boxes. They stress the importance of replicating authentic traffic loading and unpaved road dimensions, advocating for in situ tests. To address this, researchers explore in situ testing under site conditions to reproduce soil layer dimensions and traffic loading. Alternatively, some authors take a more innovative approach, developing simulators for traffic loads, allowing testing in smaller laboratory platforms, minimizing soil layer consumption over significant lengths. Therefore, in addition to plate load tests, we will perform traffic load tests, and the subsequent sections provide a summary of noteworthy studies on traffic load testing, incorporating rolling loads.

Table 2-1: Summary of laboratory plate load tests

Reference	Type of test	Loading type Loading plate diameter, D, (mm)	Platform size Length x width x height (m)	Subgrade type CBR(%)	Base course Type Thickness, h, (mm)	GSY type	GSY position	GSY number
Akond (2012)	Small scale laboratory plate load tests	Monotonic plate load (ASTM D 1196-93) D=190 mm	1.5 x 0.91 x 0.91	Silty saturated clay soil CBR = 1	Kentucky limestone h = 200, 300, 450	Biaxial GGRs Triaxial GGRs Woven GTXs	Interface Within the base course	Single Double
Demir et al. (2013)	Field plate load test	Monotonic plate load test (ASTM D 1196-93) D =300, 450, 600, 900 mm	2.8 x 2.8 x 2	In situ saturated Clay CBR = 2-2.5	Granular fill h = 200, 300, 400, and 600	Biaxial GGR	Interface Within the base course	Single Double
Abu-Farsakh et al. (2016)	Small scale laboratory plate load tests	Monotonic plate load (ASTM D 1196-93) D=190 mm	1.5 x 0.91 x 0.91	Silty saturated clay soil CBR = 1	Crushed limestone h = 305	Biaxial GGRs Triaxial GGRs Woven GTXs	Interface Within the base course	Single Double
Gallage et al. (2023)	Small scale laboratory plate load tests	Monotonic plate load (ASTM D 1196-93) D=200 mm	1.0 x 1.0 x 1.2	Plastic silt CBR = 1	quarry materials h = 200, 300, and 400	GGR Geocomposite	Interface	Single
Palmeira et Antunes (2010)	Laboratory plate load test	Monotonic & cyclic plate load, D= 300 mm	1.2 x 1.6 x 1.6	Fine tropic soil CBR = 8	Well graded aggregates h = 200	knitted biaxial GGR woven GTX were	Interface	Single
Kiptoo et al. (2017)	Laboratory plate load test	Monotonic & cyclic plate load, D= 305 mm	1.2x1.2x0.8	Kaolin Clay CBR = 2%,	Clayey sand h= 300 mm	Biaxial GGRs Woven GTX	Interface Within the base course	Single Double
Qian et al. (2011) & Qian et al. (2013)	Laboratory plate load test	Cyclic plate load, D=300 mm Max pressure=560 kPa Frequency=0.77 Hz	2 x 2.2 x 2	25% kaolinite and 75% of Kansas river sand CBR= 2	Well-graded aggregates h= 150, 230 and 300 mm	Triaxial GGRs	Interface	Single

Palmeira et al. (2016)	Laboratory plate load test	Cyclic plate load, D=200 mm Max pressure=560 kPa Frequency=1 Hz	1.2x1.2x0.52	Loose sand CBR= 1.6	Gravel h= 300 mm	Uniaxial GGRs Biaxial GGRs Woven GTX	Interface	Single
Bräu and Vogt (2018)	Laboratory plate load test	Cyclic plate load, D=300 mm Max pressure=350, 450, and 550 kPa Frequency=0.3 Hz	3.3x5.0x1.35	low-plasticity clay CBR= 1 and 2	Well-graded gravel with rounded grains h= 150, 300 and 450 mm	Biaxial GGR Woven GTX Geocomposite	Interface	Single
Khoueiry (2020)	Laboratory plate load test	Cyclic plate load, D=300 mm Max pressure=566 kPa Frequency=0.77 Hz	1.8 x 1.9 x 1.1	25% kaolinite and 75% Hostun sand CBR= 2	Well-graded aggregates h= 220 and 350	Knitted GGRs Extruded GGR with hexagonal apeture	Interface Base course middle depth	Single
Jayalath et al. (2021)	Laboratory plate load test	Cyclic plate load, D=200 mm Max pressure=550 kPa Frequency=0.33 Hz	1.0x1.0x1.2	high-plasticity silt CBR= 2.5	granular material h=200 mm, 300 mm, and 400 mm	CGG	Interface	single

2.5.2. Large scale in situ tests under traffic loading

This section presents various research projects that have developed in situ test protocols under real traffic conditions.

Hufenus et al. (2006) conducted field tests to assess the impact of reinforcement GSYs on the bearing capacity of an unpaved road laid over soft subgrade soil. The testing track, divided into 12 sections of 8 m length and 5 m width each, featured a truck with specific characteristics for trafficking tests. The subgrade, composed of clayey silt and exhibited non-uniform properties along the track with CBR values ranging from 1% to 8%. It was difficult to compare the plots with such a wide difference in CBR. The base course, constructed in three layers of 200 mm thickness each, comprised recycled rubble for the first two layers (with particle diameter ranging from 8 to 64 mm) and finer-grained recycled material for the third layer (particle size: 0–32mm), aiming to enhance density and interlocking. Compaction methods varied for each layer, involving static compaction, dynamic compaction, and loading by a truck. Seven different types of GSYs, including nonwoven and woven GTXs, extruded and knitted GGRs, were employed. Quality control measures encompassed CBR measurements, shear vane measurements, specific gravity measurements, static and dynamic plate load tests, a dynamic falling weight deflectometer (FWD), dynamic compaction control. The ruts at the base course surface and the strain along the GTX were measured during the circulation. The findings of the study revealed a noteworthy enhancement in bearing capacity and rut reduction for the reinforced fill layers, particularly for thin layers ($h \leq 500$ mm) on very weak ground ($CBR \leq 2$). Furthermore, in the configuration with two GSYs, the authors recommended placing the GGR 5 cm above the non-woven GTX located at the base course subgrade interface to optimize shear interaction, enhance bearing capacity, and prevent GGR sliding.

Cuelho and Perkins (2009) and Cuelho et al. (2014) conducted in situ tests on unpaved road sections in two pits to explore the correlation between GSY properties and the performance of reinforced granular platforms over weak subgrade soil.

The study of Cuelho and Perkins (2009) constituted of 12 test sections measuring 15 m in length, 4 m in width, and 1.2 m in height (Figure 2-16). Each test section constituted of granular layer of 200 mm of thickness laid over a subgrade layer with a CBR ranging between 1.4% and 2.2%. Various type of GGRs and GTXs were tested and placed at the base course-subgrade interface of the reinforced sections. The testing involved the application of channelized traffic loading from a fully loaded three-axle dump truck (tire pressure: 690 kPa, speed: 15 km/h). Termination of trafficking occurred after 40 truck passes, causing an average elevation rutting of 100 mm in the strongest test sections.

In Cuelho et al. (2014) study constituted of 17 test sections measuring 15.2 m in length, 4.8 m in width, and 1.5 m in height. Various type of GGRs and GTXs were tested and placed at the base course-subgrade interface of the reinforced sections. Three unreinforced control section with three different thickness 300 mm, 414 mm, and 632 mm. 14 reinforced sections had a thickness of the base course of 300 mm. The subgrade layer had a CBR values between 1.4% and 2 %. The testing procedure involved the application of channelized traffic load from a three-axle dump truck (tire pressure: 620 kPa, speed: 8 km/h). Results indicated that 80 truck passes were necessary to cause an elevation rut of 70 mm in the weakest unreinforced test section, while 680 truck passes were needed to induce a 60 mm rut in the strongest reinforced test section among those with a 300 mm base course thickness.

Both studies identified a relationship between GSY properties and the performance of the reinforced granular platform over weak subgrade. In scenarios with minimal structural benefit from the gravel base course with a thin base course of 200 mm (as in Phase I of Cuelho and Perkins (2009)), GSY tensile stiffness and strength became crucial in rut suppression, particularly due to rapid deterioration under traffic load. In addition, the strength and stiffness of GGR the junctions in the cross-machine direction plays a role but diminishes as rut develops. Whereas in situations with a thicker base course (thickness $\geq$ 300 mm) and slower rut development (as in Cuelho et al. (2014)), the significance of GGR junction stiffness and strength increased as reliance on these properties for performance grew with rut progression.

a) Installation of the GSY

b) Final grading of the base course

c) Three-axle dump truck used for trafficking

Figure 2-16: Overview of construction procedure of unpaved test pit and the three-axle loading truck (Cuelho and Perkins, 2009)

Bräu and Vogt (2018) conducted in situ tests on fields measuring 110 m in length and 4 m in width, subjected to the passage of loaded trucks delivering bulk freight for nearby construction activities. The subsoil composition comprises low to medium plastic clay, including a small fraction of sand and gravel particles, with an estimated undrained shear strength ranging from c_u = 140 kN/m² (CBR=4.6%) to 190 kN/m² (CBR=6.3%). Various types of GSYs, such as woven GTXs, GGRs, and geocomposites consisting of a GGR and a non-woven GTX, were placed over the subsoil layer, with a base course thickness of approximately 300 mm. Bearing capacity characterization of the test fields was performed using static plate loading tests (German DIN 18134 and ASTM D1194/1195/1196). A circular plate with a diameter of 300 mm applied a maximum load of 500 kN/m². The modulus Ev1 (first loading) and Ev2 (second loading), defined as the secant stiffness between stresses of 150 kN/m² and 350 kN/m², showed no significant differences among the various test fields, whether reinforced or unreinforced. To assess the influence of GSYs on bearing resistance, additional tests were conducted, increasing the plate stress to 700 kN/m². The deformation modulus values between zero stress and 700 kN/m² did not indicate any influence of the GSYs. Following the completion of the initial static plate tests, the thickness of the bearing layer for the unpaved road was increased to 60 cm. After approximately 2000 loaded truck passes, rut depths ranged from about 20 mm to 40 mm in the test field, with seemingly no significant strains observed within the GSYs. Thus, no clear influence of the GSYs on rut development could be discerned.

Singh et al. (2022) constructed three test sections for unpaved roads within a test pit measuring 9 m in length, 2.7 m in width, and 0.8 m in depth (Figure 2-17). The objective was to assess the effectiveness of GSY-reinforced unpaved roads under dynamic wheel loads. The subgrade soil, identified as silty sand (SM) per the Unified Soil Classification System (USCS), exhibited a CBR of approximately 1.7% and had a thickness of 500 mm. Given the subgrade CBR below 2 %, a capping layer, equivalent to 100 mm of modified soil with a CBR of 12%, was installed and compacted over the subgrade. The base course, comprised of well-graded aggregates, had a thickness of 200 mm. After compaction by a 10-ton three-

wheeled roller, a surface course with a thickness of 50 mm was applied over the granular layer. Two types of GSY were incorporated at the capping layer-base course interface in the reinforced test sections:

- A GGR with aperture dimensions of 30 cm, possessing tensile stiffness at 0.5% strain of 550 kN/m in the machine direction and 350 kN/m in the cross-machine direction.
- A woven GTX with a tensile strength of 45 kN/m in the machine direction and 35 kN/m in the cross-machine direction.

For traffic simulation, a single axle testing vehicle weighing 1530 kg, with tire pressure equivalent to 220.6 kPa, was employed to traverse each unpaved test section. A total of 350 unidirectional passes, at a speed of 15 km/h, were applied to the sections. Transverse rut depths on the base course surface were meticulously measured using a laser meter with an accuracy of ±0.1 mm. In the unreinforced section, the maximum rut depths reached approximately 50 mm after enduring 350 passes. Introducing the GTX resulted in a notable 45 % reduction in the maximum rut depth, while the GGR contributed to a substantial 29 % reduction in the same parameter. Additionally, Dynamic Cone Penetrometer (DCP) tests were conducted on the rutted area to assess the strength of the unpaved road in terms of CBR values after completing the moving wheel load tests. The reinforced test section exhibited greater penetration resistance compared to the unreinforced section, as indicated by the DCPI values. The CBR values for the GTX-reinforced and GGR-reinforced unpaved test sections increased by 27 % and 23 %, respectively.

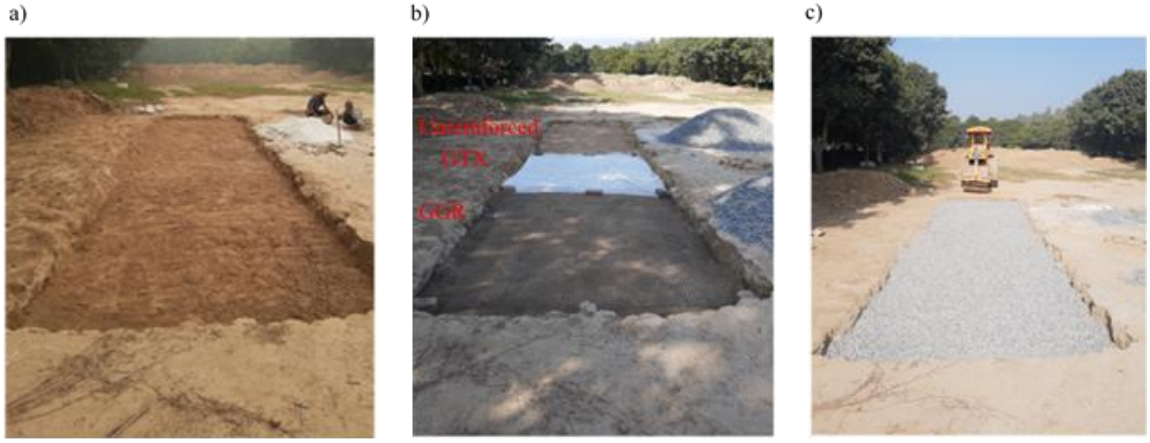

Figure 2-17: Overview of construction procedure of unpaved test pit: a) placing and spreading subgrade soil and compaction of the subgrade in 3 layers; b) placing the GGR and GTX over the capping layer; c) placing and spreading granular layer over GSY reinforcement and compacting (Singh et al., 2022)

In situ tests review

The in-situ tests, as summarized in Table 2-2, offer a close simulation of site conditions by applying loading through trucks and testing sections with authentic dimensions close to the real unpaved road sections. Despite their advantages, these tests had some limitations. In fact, maintaining control over soil conditions and ensuring test repeatability in an outdoor field presented challenges. Hufenus et al. (2006) illustrated the variability of the CBR of the subgrade soil, ranging from 1% to 8%, posing a significant obstacle to effective test comparisons. Furthermore, the installation procedure for the platform is time-consuming and demands a substantial budget. In addition, truck traffic is limited by the restricted passes number allowed, making it difficult to meet the FHWA recommendation of 10,000 cycles (passes). In practice, the tests carried out were limited to a maximum of 40 and 2,000 truck axle passages. This limitation is explained by the fact that the maximum permissible rut development was reached before the 10,000 cycles recommended by the FHWA (2008).

Table 2-2: Summary of the large scale in situ tests under traffic loading

Reference	Type of test	Loading type	Platform size Test number (Length x width x height) (m)	Subgrade type CBR (%)	Base course Type Thickness, h, (mm)	GSY type	GSY position	GSY number
Hufenus et al. (2006)	Full-scale in-situ test	Uncontrolled full and empty truck passes	12 x (8 x 5 x Variable)	In situ silty clay variable CBR ranging from 1% to 8%	Relatively poorly compactable recycled rubble h= 200, 400 and 600 mm	nonwoven and woven GTXs, extruded and knitted GGRs	Interface Within the base course	Single Double
Cuelho & Perkins (2009)	Full-scale in situ test	fully loaded three-axle dump truck (a tire pressure of 690 kPa)	12 x (15 x 4 x 1)	A saturated subgrade CBR between 1.4 and 2.2%	crushed gravel grade 6A h=200 mm	nonwoven and woven GTXs, extruded and knitted GGRs	Interface	Single
Cuelho et al. (2014)	Full-scale in situ test	fully loaded three-axle dump truck (tire pressure: 620 kPa)	17 x (15.2 x 4.8 x 1.5)	A saturated subgrade CBR between 1.4 and 2%	crushed gravel grade 6A h=300, 414 and 632 mm	nonwoven and woven GTXs, extruded and knitted GGRs	Interface	Single
Bräu and Vogt (2018)	Full-scale in situ test	Static plate load (D=300 mm) and loaded truck passes.	the subgrade)	sand and gravel particles CBR between 4.6 and 6.3 %	Gravel h=600 mm	GGR nonwoven GTX, Geocomposites	Interface	Single
Singh et al. (2020)	Full-scale in situ test	Single axle vehicle with tire pressure of 220.6 kPa	3x(3 x 2.7 x 0.8)	Silty sand subgrade with a CBR = 1.7% + Capping layer: Improved subgrade stabilised with lime h = 100 mm and CBR = 12 %.	well-graded aggregates h= 200 mm	GGR Woven GTX	Capping layer – base course interface	Single

2.5.3. Large-scale laboratory tests using traffic loading simulators

The challenges associated with large-scale tests encompass the considerable cost, the substantial material requirements for platform preparation, and the meticulous management of environmental conditions and numerous testing cycles. Over the years, researchers in the field of transportation have leveraged full-scale Accelerated Pavement Testing (f-sAPT) facilities to replicate traffic loads on tested platforms, providing an effective means to overcome the constraints of on-site full-scale testing. This section highlights four f-sAPT facilities specifically utilized for testing unpaved roads.

2.5.3.1. Accelerated Pavement Testing (APT) facility at Kansas State University

The Accelerated Pavement Testing (APT) facility at Kansas State University is an indoor fixed facility that applies a linear bi-directional traffic load using single or dual axles (Figure 2-18). The test pit of the facility, measuring 6.1 m in length, 4.9 m in width, and 1.8 m in depth, was instrumental in studies conducted by Pokharel et al. (2011) and Yang et al. (2012), focusing on the effectiveness of GCE reinforcement in unpaved roads on soft soil.

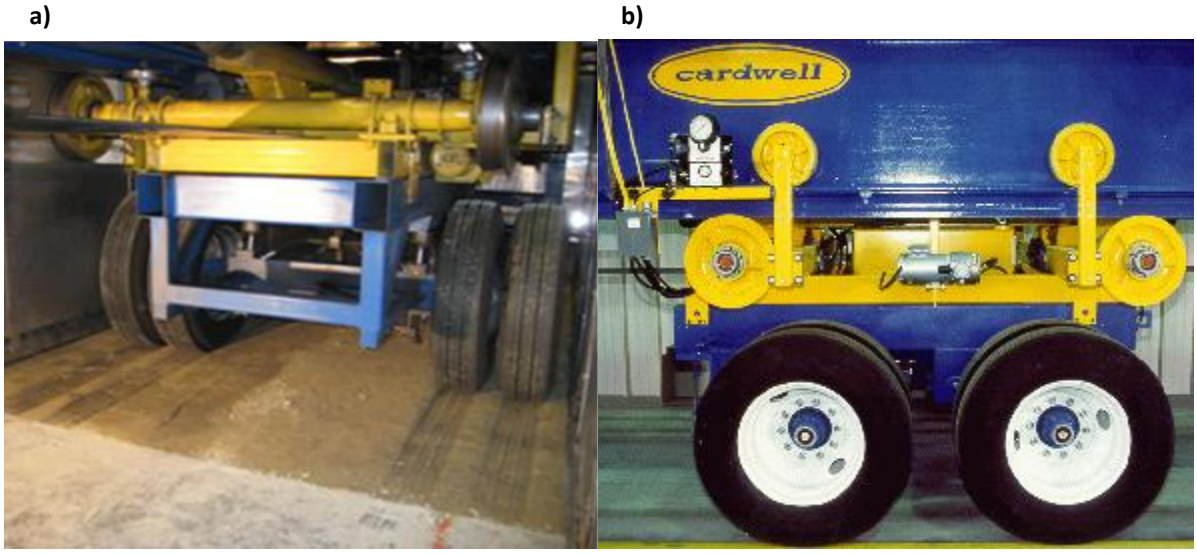

Figure 2-18: Accelerated Pavement Testing (APT) Facility at Kansas State University: a) a rear view; b) a frontal view

In the research conducted by Pokharel et al. (2011), the test pit was divided into four equal sections, each with dimensions of 3.05 m in length and 2.45 m in width (Figure 2-19). The subgrade, classified as A-7-6 Clay according to AASHTO soil classification, exhibited CBR values ranging from 2.5% to 3.4%. Nonwoven GTX served as a separator between the subgrade and base course in reinforced sections. The GCEs utilized in the study were 150 mm high, possessing a tensile strength of 20.3 kN/m and a secant elastic modulus of 355 MPa at 2% strain. Section 1 featured an unreinforced base with well-graded crushed-limestone aggregates (AB-3), measuring 300 mm thick over the subgrade. Sections 2, 3, and 4 utilized GCE -reinforced quarry waste (QW), recycled asphalt pavement (RAP), and AB-3, respectively, with a 20 mm

thick cover of the respective in-fill materials on top of the GCE -reinforced bases measuring 150 mm in thickness. A series of tests, including vane shear, dynamic cone penetrometer (DCP), nuclear gauge, light-falling-weight deflectometer (LFWD), and falling-weight deflectometer (FWD), were conducted to assess the density and stiffness of the soil layers.

Trafficking was applied using a single axle dual wheel, resulting in an 80 kN load and a tire pressure of 552 kPa. The moving-wheel test was executed at a speed of 11.3 km/h and a frequency of 0.167 Hz within the test pit. The testing concluded at 305 passes, halting due to reach a rut depth of about 130 mm. Comparative analysis revealed that the GCE - reinforced crushed-stone section (170 mm thick) and the GCE -reinforced RAP section significantly reduced rut depths at the base course surface by 14% and 35%, respectively, compared to the thicker unreinforced crushed-stone control section (300 mm thick). However, the GCE -reinforced QW section exhibited the maximum rut depth among the tested configurations.

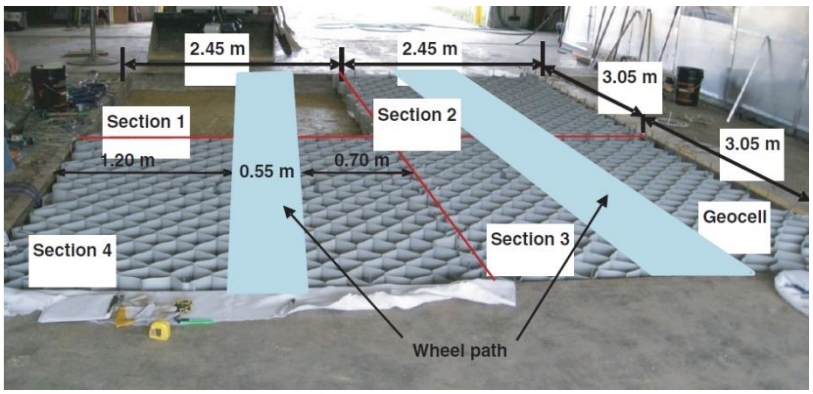

Figure 2-19: Plan layout of test sections

2.5.3.2. Accelerated Load Facility (ALF)

The Accelerated Load Facility (ALF) of the Federal Highway Administration, situated in McLean, Virginia, serves as a testing apparatus designed to subject test sections to unidirectional trafficking at a nominal speed of 16.8 km/h (Figure 2-20). ALF utilizes a dual-tire axle, applying a 43.4-kN load—half of the standard 80-kN single-axle load. Notably, it can simulate live traffic patterns by incorporating a normally distributed wander covering a transverse distance of 76 cm, with the wheel path generated extending approximately 12 m. Tang et al. (2015) leveraged ALF to underscore the advantages of GSY reinforcement–stabilization in mitigating permanent deformation in pavement structures.

Figure 2-20: ALF with insertion of dual-wheel assembly

At an outdoor site, six test lane sections (Figure 2-21), being either reinforced or unreinforced, were constructed over native soft soil. Each section was measuring 24 m in long and 4 m in wide. The heavy clay subgrade soil, classified as A-7-6 according to the (USCS), exhibited CBR values between 0.6 and 0.8%. The aggregate used, a dense-graded crushed limestone, was classified as GW. The study employed a triaxial GGR and a high-strength woven GTX. A needle-punched nonwoven GTX was placed beneath at the base–subgrade interface for separation and filtration. Various instruments, including earth pressure cells, piezometers, LVDTs, and potentiometers, were placed to measure total vertical stresses, excess pore water pressure, total subgrade deformation, and aggregate layer strain, respectively. Additionally, a wireless laser profilometer was used to measure the transverse rut profile at eight locations along the wheel path during load repetitions. Multiple strain gauges were affixed in the transverse direction to measure strains developed along the GSY. In situ layer properties of pavement layers were measured at different stages using devices such as a nuclear density gauge, lightweight deflectometer (LWD), GeoGauge, dynamic cone penetrometer (DCP), and vane shear device.

Results from the full-scale accelerated load testing showcased the substantial benefits of both the woven GTX and the triaxial GGR products in significantly reducing total permanent deformation and surface rutting in unpaved test sections. Additionally, test sections 5 and 6, reinforced with high-strength GTXs, demonstrated a permanent deformation approximately 8 mm less significant than the deformations observed in test sections 2 and 3, which were reinforced by GGRs and showed deformations around 17 mm.

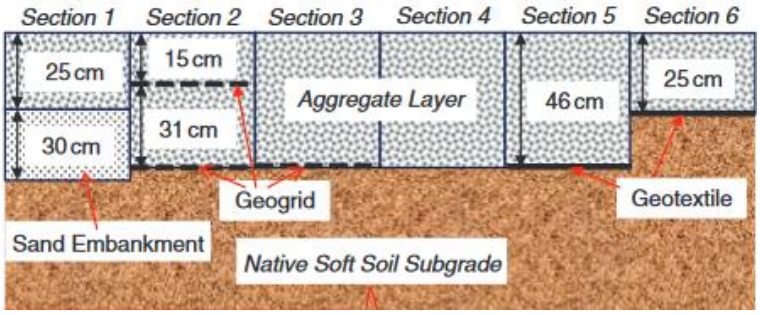

Figure 2-21: Cross section of the tested pavements (Tang et al.,2015)

2.5.3.3. The Pavement Test Facility (PTF)

The Pavement Test Facility (PTF) at the Transport Research Laboratory (TRL Limited) is equipped to handle both single and twin road wheels, with axle loadings ranging from 23 kN to 100 kN (Figure 2-22). The PTF allows for a maximum speed range of 20 km/h. The test setup involved a 10 m wide, 25 m long, and 3 m deep pit.

In the study conducted by Watts et al. (2004), the PTF was employed to assess the performance of the reinforced unpaved roads under trafficking conditions. A dual wheel pair with an axle loading of 40 kN, approximately half of a standard axle load, were used. 21 test sections measuring 2.4 m in width were constructed during two testing campaigns. The subgrade consisted of a grey silty London clay with an average CBR value of around 2%, and it had a thickness of 550 mm. The base course, made of crushed granite aggregate, had two different thicknesses: 320 mm for the first testing campaign and 280 mm for the second. Various types of GSY reinforcements, including woven GTX, welded bonded grid, woven grid, extruded internal grid, punched and stretched integral grid, were incorporated at the base course – subgrade interface or within the base course layer. A static penetrometer controlled the clay installation and compaction protocol, proposing a correlation between the cone index (CI) and the subgrade CBR. The Falling Weight Deflectometer (FWD) was employed to measure the pavement modulus on the compacted surface of the base course.

The bi-directional wheels moved along the centreline of each section with a speed of 15 km/h. The tests ended when the section was found to have failed, resulting in a vertical deformation of over 80 mm in the wheel's trajectory. Vertical deformation was systematically monitored at intervals using an optical level. In particular, the unreinforced section failed after just 500 passes, underlining its limited resistance. The reinforced sections, on the other hand, showed a notable ability to withstand wheel traffic, indicating greater serviceability.

Figure 2-22: Pavement test facility (Watts et al., 2004)

2.5.3.4. The accelerator pavement traffic (APT)

The Simulator Acceleration Traffic (SAT), developed at the Geomas laboratory at INSA Lyon during Khoueiry's (2020) study, is designed to apply traffic loads to road structures (Figure 2-23). This adaptable SAT accommodates either a single or double wheel, enabling the application of a 28 kN load, utilizing the machine's self-weight. The SAT's wheel operates in both unidirectional and bidirectional modes, with adjustable speeds ranging from 2 to 7 km/h. The wheel path spans approximately 3 m, with an effective

length of 2 m beyond the impact zone. Rut deformation on the surface is limited to a maximum of 100 mm. In Khoueiry's (2020) study, the SAT was utilized to apply traffic loading to an unpaved section constructed within a geotechnical box measuring 1.8 m in width, 5 m in length, and 1.1 m in height. This same SAT will be employed in the current thesis for a similar purpose.

In addition to the cyclic loading tests carried out with a circular plate in the study by Khoueiry (2020), a second series of tests was carried out in which two types of loading were applied to three sections of unpaved road: vertical loading using a specially shaped plate and loading due to traffic. The SAT apparatus applied a traffic load of 28 kN on the wheel, resulting in 650 kPa on the platform surface at a velocity of 4 km/h. The plate load was applied with a plate having the same wheel contact area shape, with an applied load of 28 kN resulting in a contact stress of 650 kPa.

Three platforms were tested: an unreinforced platform, a reinforced platform with knitted GGR, and a reinforced platform with triaxial GGR. Throughout these tests, the base course thickness was maintained at 220 mm, and the subgrade CBR exhibited a value of 2%. The platform preparation and compaction protocol from the first series of testing were consistently followed in the second series. To measure stress and settlement, earth pressure cells and hydraulic sensors were employed on the top of the subgrade layer, respectively. Fiber optic sensors were attached to the GGR to measure strain, while laser displacement sensors were used to measure the rutting profile at the base course surface. The knitted GGR and the triaxial GGR showed a 30% reduction in base course settlement after 10,000 cycles under the plate load test. Under the traffic load test, both the knitted GGR and the triaxial GGR reduced the subgrade surface settlement by about 40%. Furthermore, a comparison between the plate and traffic load results revealed that traffic load is more damaging due to the induced lateral movement of gravel and surface repulsion, phenomena not observed under the plate load test. Additionally, the developed strain in the triaxial GGR was more mobilized during installation than the knitted GGR, owing to the node stability of the triaxial GGR and special geometry that limits the lateral movement of the aggregates more effectively.

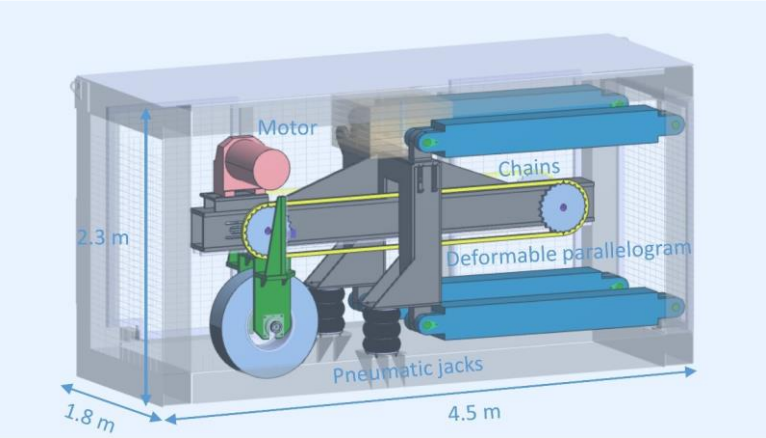

Figure 2-23: SAT plan (Khoueiry, 2020)

Full-scale Accelerated Pavement Testing (f-sAPT) review

The full-scale tests accelerator pavement traffic presented in this section replicate real traffic loading conditions, benefitting from the controlled indoor environment that enables parameter control and minimizes environmental variables. Table 2-3 summarizes the conditions of the large-scale laboratory tests using f-sAPT. Despite the smaller dimensions of the pits compared to in situ tests, this disparity proves advantageous as it saves time, materials, and effort during platform preparation. Additionally, the automatic application of the load allows for the implementation of a higher number of cycles.

The Simulator Accelerated Traffic (SAT) machine, developed in Khoueiry's (2020) thesis and located in the GEOMAS laboratory, demonstrates the ability to apply traffic loading efficiently, with its optimal

dimensions contributing to material and effort savings. Leveraging these advantages of the SAT machine, we plan to use it to assess the performance of reinforced granular platforms over soft soil under traffic loading, aiming to contribute to the advancement of knowledge in this field.

Table 2-3: Summary of the conditions of the large-scale laboratory tests using using f-sAPT

Reference	Type of test	Loading type	Platform size Test number (Length x width x height) (m)	Subgrade type CBR(%)	Base course Type Thickness, h, (mm)	GSY type	GSY position	GSY number
Pokharel et al. (2011)	Large scale circulation laboratory test	Accelerated Pavement Testing (APT) facility at Kansas State University single axle dual wheel, resulting in an 80 kN load and a tire pressure of 552 kPa	4x (3.05x2.45)	A-7-6 Clay CBR= 2.5% to 3.4%.	Section 1: well-graded crushed-limestone aggregates (AB-3), h=300 mm Section 2: Quarry waste h= 170 mm (QW), Section 3: Recycled asphalt pavement (RAP), h= 170 mm, Section 4: (AB-3), h= 170 mm,	GCE	Interface	Single
Tang et al. (2015)	Large scale circulation laboratory test	The Federal Highway Administration Accelerated Load Facility (ALF) with an applied load of 43.4 kN	6x (24 x 4 x existing in situ soil)	Heavy clay clay classified as A-7-6 (USCS)	Dense-graded crushed limestone CBR= 0.6 -0.8%	Triaxial GGR woven GTX	Interface Within the base course	Single Double
Watts et al. (2004)	Large scale circulation laboratory test	The Pavement Test Facility (PTF) at the Transport Research Laboratory (TRL Limited) with axle loadings ranging from 23 kN to 100 kN	21x(12 x (6 x 3 x 3))	Grey silty London clay CBR = 2%	Crushed granite aggregate h= 320, 280 mm	woven GTX, welded bonded grid, woven grid, extruded internal grid, punched and stretched integral grid,	Interface Within the base course	Single Double
Khoueiry et al. (2020)	Large scale circulation and plate load laboratory test	Simulator Acceleration Traffic (SAT) at Geomas laboratory (INSA Lyon) with a 28 kN load +	3x (1.8 x 5 x 1.1)	25% kaolinite and 75 % of Hostun sand CBR = 2%	Well-graded aggregates h= 220 m	Knitted GGR Extruded GGR	Interface	Single

		Plate load with a cyclic load of 28 kN of maximum load on was applied with a plate having the same wheel contact area shape and resulting in a contact stress of 650 kPa						

2.6. The design methods of the granular platforms reinforced by geosynthetics

Since 1970, research has demonstrated that the incorporation of GSY sheet at the top of the weak subgrade layers significantly enhances road performance, enabling greater tolerance for deeper ruts and /or reduction in base course thickness. Over the years, several design methodologies have emerged with the specific goal of estimating the aggregate base thickness for unpaved roads, considering the influence of GSY. The main influencing factors discussed in the design methods are the rutting development, the cycle number, the subgrade and base course stiffness, and the contribution of GSY reinforcement. Various theoretical frameworks and analytical methods have been introduced, each offering distinctive perspectives on the interaction between the soil and the GSY. As previously mentioned, the aggregates lateral restraint is established at a smaller rut (or low GSY strain) to optimize road performance. Conversely, the tensioned membrane effect in GSY - reinforced roads is activated at a deeper rut (high GSY strain). Giroud & Noiray (1981) and Barenberg et al. (1975) emphasizes dominant of the tensioned membrane effect at important ruts. Whereas Giroud & Han (2004) and Leng & Gabr (2006) introduced analytical methods, both calibrated using laboratory plate load tests conducted by Gabr (2001) using specific GGR, base course, and subgrade stiffness conditions and considering the soil – GGR interlocking mechanism.

Hammitt & Iii (1970) introduced an empirical design approach for calculating aggregate thickness based on a rutting criterion of 75 mm for unreinforced unpaved roads. This method relies on a comprehensive testing program proposed by Corps and Engineer. The formula for determining the design thickness of the base course (h_{os}) is expressed as:

$$h_{os} = (0.0236\ logN + 0.0161)\sqrt{\frac{P}{CBR} - 17.8\ A} \qquad \textit{Eq 2-1}$$

h_{os} is the design thickness of the base course (m); N represents the number of passages; P denotes the wheel load (kN); CBR corresponds to the California Bearing Ratio of the subgrade; A signifies the tire contact area (m²); It is important to note that this method is not recommended for N values exceeding 10,000 cycles or falling below 20 cycles.

Barenberg et al. (1975) introduced another design method aimed at determining the base layer thickness, incorporating the tensioned membrane effect of the GTX. Rooted in the limit equilibrium bearing capacity theory, their approach considered key factors such as significant rutting, the circular arc shape of reinforcement deflection, the assurance of reinforcement separation function, and the absence of slip at the interface. The fundamental premise of the limit equilibrium bearing capacity theory involves selecting an aggregate base thickness to ensure that the vertical stress applied to the GTX-subgrade interface purges the wheel load-supported by the GSY, if present, below the theoretical limits for subgrade shear failure. This is expressed by the *Eq 2-2*:

$$\sigma_z - \Delta\sigma_{z,GSY} = \sigma_{all} \qquad \textit{Eq 2-2}$$

Here:
σ_z represents the maximum vertical stress on the reinforcement, calculated per the elastic Boussinesq theory under a uniformly loaded circular area (kN/m²), $\Delta\sigma_{z,GSY}$ signifies the portion of the wheel load carried by the GSY for a given rut geometry and reinforcement tensile strength (kN/m²), and $\sigma_{all}=N_c \cdot c_u$ denotes the maximum allowable stress of the subgrade, expressed as a function of the undrained cohesion c_u (kN/m²) and the bearing capacity factor N_c. However, limitations exist in the Barenberg et al. (1975) method, such as the absence of GTX mechanical property consideration and aggregate mechanical property. Furthermore, despite Bender and Barenberg's (1978) acknowledgment that "a layer of aggregate material is always

needed on top of the GTX to anchor it so that the necessary tensile forces can be developed in the fabric," their study does not specify the minimum depth for anchorage or the mechanical properties of the aggregate layer.

Furthermore, Giroud and Noiray (1981) proposed a theoretical design method for reinforced unpaved roads based on the large displacement mechanism. In this approach (Figure 2-24), reinforcement was integrated into the equations to enhance stress distribution and account for a normal stress difference due to the tension membrane effect. This method has since served as the foundation for numerous design approaches, incorporating a tensioned membrane effect and addressing subgrade bearing capacity failure in the reinforced system, specifically as a general shear failure rather than a local shear failure.
The ultimate bearing capacity of the subgrade (q_u) for the unreinforced case is expressed by *Eq 2-3*

$$q_u = N_c\ c_u\ +\ \gamma h_0 =\ p_0 \qquad \textit{Eq 2-3}$$

Where N_c is the bearing capacity factor which is equal to π (elastic limit for a saturated undrained subgrade), c_u is the subgrade undrained cohesion (kPa), γ is the base course volumetric weight (kN/m^3), h_0 is base course thickness the case (m) and p_0 is subgrade pressure (kPa).
The ultimate bearing capacity of the subgrade (q_u) for the reinforced case is expressed by *Eq 2-4*

$$q_u = N_c\ c_u\ +\ \gamma h = p -\ p_g \qquad \textit{Eq 2-4}$$

Where Nc is equal to π +2 (the plastic limit for a saturated undrained subgrade), h is base course thickness (m); h is base course thickness the case (m), p is subgrade pressure (kPa) and p_g is the reduction of the pressure due to the tension-membrane effect (kPa). The failure of the unpaved road can occur in the subgrade or the GSY.
For a base course thickness (h_0) without a GSY, p_0 is given by *Eq 2-5*:

$$p_0 = \frac{2LBp_{ec}}{2(B + 2h_0 \tan\alpha_0)\ (L + 2h_0 \tan\alpha_0)} +\ \gamma h_0 \qquad \textit{Eq 2-5}$$

For a base course thickness (h) with a reinforcement, p is given by *Eq 2-6*:

$$p = \frac{2LBp_{ec}}{2(B + 2h \tan\alpha)\ (L + 2h \tan\alpha)} +\ \gamma h \qquad \textit{Eq 2-6}$$

The parameters in *Eq. 2-5* and *Eq. 2-6*, showed in Figure 2-34, include L and B as dimensions of the contact area (m), p_{ec} as the applied stress at the base course surface (kPa), α_0 and α as stress distribution angles for the unreinforced unpaved road and the GTX-reinforced roads respectively. It is assumed for simplification that α_0 and α are equivalent.

a) Unreinforced section **b) GTX-reinforced section**

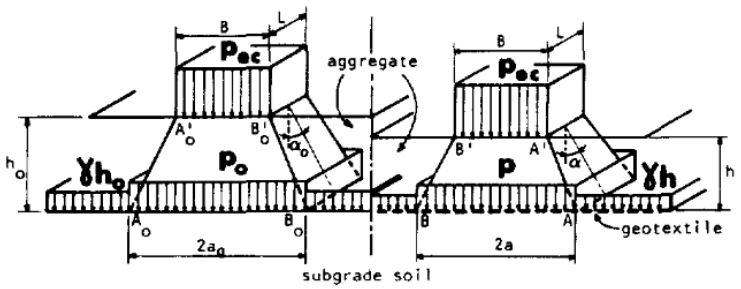

Figure 2-24: Load distribution by base course layer: (a) case without GTX; and (b) case with GTX.

The strain in the GTX (ε) is calculated based on a parabolic deformed shape, given by *Eq 2-7* and by *Eq 2-8* using the Eq 2-9 and Eq 2-10:

$$\varepsilon = \frac{b + b'}{a + a'} - 1 \qquad for\ a' > a \qquad \textit{Eq 2-7}$$

$$\varepsilon = \frac{b}{a} - 1 \qquad for\ a' < a \qquad \textit{Eq 2-8}$$

Here, a and a′ are half the length of the chord subtended by P and P′ (in m) shown in Figure 2-25, and b and b′ are half the length of P and P′ (in m).

$$\frac{b}{a} - 1 = \frac{1}{2}\left[\sqrt{1 + \left(\frac{2s}{a}\right)^2} + \frac{a}{2s}\ln\left(\frac{2s}{a} + \sqrt{1 + \left(\frac{2s}{a}\right)^2}\right) - 2\right] \qquad \textit{Eq 2-9}$$

$$\frac{b'}{a'} - 1 = \frac{1}{2}\left[\sqrt{1 + \left(\frac{2(r-s)}{a'}\right)^2} + \frac{a'}{2(r-s)}\ln\left(\frac{2(r-s)}{a'} + \sqrt{1 + \left(\frac{2(r-s)}{a'}\right)^2}\right) - 2\right] \qquad \textit{Eq 2-10}$$

Here, s is the GTX vertical settlement, and r is the rut depth under the wheel at the base course surface, (both expressed in m). r can be estimated geometrically through a formula containing a, a′, and s.

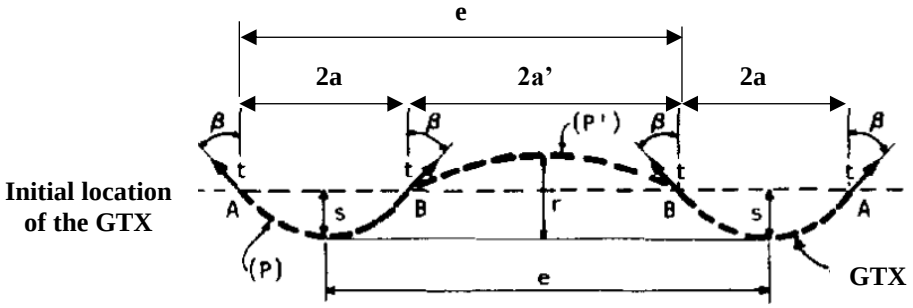

Figure 2-25: Assumed parabolic shape of deformed GTX. (Giroud & Noiray, 1981)

The reduction in pressure due to the tensioned-membrane effect p_g is considered a uniformly distributed pressure on AB (Figure 2-25) and is equal to the vertical component of the tension T in the GSY at points A and B (*Eq 2-11*):

$$p_g = \frac{E_g\,\varepsilon}{a\sqrt{1+\left(\frac{a}{2s}\right)^2}} \qquad \textit{Eq 2-11}$$

E_g is the GTX elastic modulus (kN/m); ε is the GTX strain (%) determined in Eq. 2-7 or Eq. 2-8. Therefore, h_0 and h are determined by *Eq 2-12* and *Eq 2-13* respectively:

$$\pi\, c_u = \frac{P}{2(B+2h_0\tan\alpha_0)\,(L+2h_0\tan\alpha_0)} \qquad \textit{Eq 2-12}$$

$$(\pi+2)\,c_u = \frac{P}{2(B+2h\tan\alpha)\,(L+2h\tan\alpha)} - \frac{E_g\,\varepsilon}{a\sqrt{1+(\frac{a}{2s})^2}} \qquad \textit{Eq 2-13}$$

Following the computations based on the Giroud and Noiray (1981) method, the influence of the GSY tensioned membrane effect on reducing the base course thickness is contingent on the rutting depth. Specifically, no improvement is evident when the rut depth equals 75 mm; a 1% reduction in base course thickness is observed for a rut depth of 85 mm; a 2% reduction is noted for a rut depth of 95 mm, and a substantial 10% reduction occurs for a rut depth of 175 mm. Notably, the Giroud and Noiray (1981) method, initially conceived with the assumption of the tensioned membrane effect's significance, has been employed to illustrate that this effect becomes negligible for rut depths equal to or less than 75 mm. The limitations of the Giroud and Noiray (1981) method include the absence of consideration for base course quality, a fixed stress distribution angle, base thickness reduction based on static loading rather than cyclic loading, a lack of differentiation among various GSY materials, and the influence of rut depth determined by an empirical relationship designed for paved materials.

The enhanced Giroud and Han method (2004a and 2004b) was developed specifically for GGR-reinforced unpaved roads to overcome certain limitations present in the Giroud and Noiray (1981) approach. The Giroud-Han method addresses considerations such as base course quality, variations in stress distribution angle with traffic loading passes (Figure 2-26), base course thickness reduction based on cyclic loading, interlocking between aggregates and GGR apertures, influence of rut depth based on stress-strain

relationships, as well as calibration and verification through field data. The equation proposed by Giroud & Han (2004a) is presented in *Eq 2-14*:

$$h = \frac{1.26\ (1 + k \log N)}{1 + 0.204\ (R_E - 1)} \left[\sqrt{\frac{\frac{P}{\pi r^2}}{\left(\frac{s}{f_s}\right)\left\{1 - 0.9\ exp\left[-\left(\frac{r}{h}\right)^n\right]\right\}\ N_c\ f_C\ CBR_{sg}} - 1} \right] r \qquad \textit{Eq 2-14}$$

$$R_E = \min\left(\frac{E_{bc}}{E_{sg}}, 5\right) = \min\left(\frac{3.48\ CBR_{bc}^{0.3}}{CBR_{sg}}, 5\right) \qquad \textit{Eq 2-15}$$

Where:
h is the required base course thickness (in m),
k is a dimensionless parameter dependent on base thickness and reinforcement, requiring calibration,
N is the number of axle passages,
P is the wheel load (kN),
r is the radius of the equivalent tire contact area (in m),
R_E is the limited modulus ratio of base course to subgrade soil (defined by *Eq. 2-15*),
s is the allowable rut depth (mm),
f_s is a factor equal to 75 mm,
N_c is the bearing capacity factor (equal to 3.14 for unreinforced unpaved roads, 5.14 for GTX-reinforced roads, and 5.71 for GGR-reinforced roads),
f_C is a factor equal to 30 kPa, and
CBR_{sg} is the CBR of the subgrade soil.
It's crucial to note that the undrained cohesion of subgrade soil, c_u, can be determined using:

$$c_u = f_c\ CBR_{sg} \qquad \textit{Eq 2-16}$$

After calibration of the equation using biaxial GGRs and validation through field tests, the Giroud & Han (2004b) equation became:

$$h = \frac{0.868 + (0.661 - 1.006\ J^2)\left(\frac{r}{h}\right)^{1.5} \log N}{1 + 0.204\ (R_E - 1)} \times \left[\sqrt{\frac{\frac{P}{\pi r^2}}{\left(\frac{s}{f_s}\right)\left\{1 - 0.9\ exp\left[-\left(\frac{r}{h}\right)^2\right]\right\}\ N_c\ c_u} - 1} \right] r \qquad \textit{Eq 2-17}$$

Where: J is the GGR aperture stability modulus (in m N/°), with =0 for unreinforced and GTX-reinforced unpaved roads.
The equation proposed by Giroud & Han (2004a and 2004b) has been integrated into the "GSY Design and Construction Guidelines" manual by the FHWA (2008), as outlined in *Eq 2-14*. Nevertheless, the Giroud and Han (2004a and 2004b) method has the following limitations:

1. Validity constraints: The method's validity is confined to rut depths ranging between 50 and 100 mm.

2. Assumed GGR interlock: All GGR are assumed to provide sufficient interlock with the base course material, justifying the use of N_c=5.71. However, this assumption may not hold true when there is a mismatch in size between the GGR aperture and the aggregate size (mean aggregate diameter or maximum aggregate diameter).
3. Sole parameter differentiation: The GGR stability modulus stands as the only parameter distinguishing between various types of GGRs. Other GGR properties, such as thickness, stiffness, shape of ribs, size and shape of apertures, junction strength, and tensile modulus at low strains, are not considered.
4. Traffic load design: The method is designed for a maximum traffic load of 100,000 axle passes.
5. Neglect of tensioned membrane effect: The tensioned membrane effect is not considered in the Giroud and Han (2004a) method.
6. Subgrade soil requirements: It is applicable only to subgrade soils with a CBR less than 5.0. However, this limitation is not overly restrictive since reinforced unpaved roads are typically constructed on soils with a CBR less than 3.

It is important to highlight that the design method proposed by Giroud and Han (2004a) has been calibrated subsequently for a particular GCE and specific GTX (Giroud and Han, 2016). Nevertheless, it is crucial to acknowledge that this approach remains calibrated for a specific type of GSY sheet.

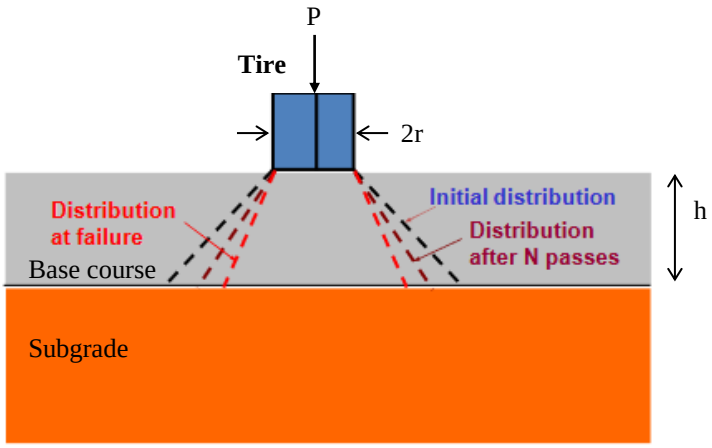

Figure 2-26: Stress distribution at initial loading cycle, N loading cycle and failure (Giroud and Han, 2004)

Leng & Gabr (2006) proposed a further development in GSY reinforced unpaved roads design. Their method considers several key factors, including the base course properties, the mobilization of subgrade bearing capacity with rutting, the contribution of GGR reinforcement through tensile stiffness at 2% strain, and the degradation of the base course under cyclic loading. The degradation of the unpaved road is quantified by considering both the base course–subgrade elastic modulus ratio (E_1/E_2) and the load distribution angle, both of which degrade with an increasing number of wheel repetitions. This method is built upon Odemark's approach, an approximate method that transforms a two-layer system with different moduli into an equivalent one-layer system. The base course thickness h is represented in *Eq 2-18*:

$$h = \frac{\left(1 + \left(\left(\frac{r}{h}\right)^{0.81}\left(0.58 - 0.000046\,{J_t}^{4.5}\right)\right)\log N\right)}{\tan\alpha_1} \times \left(\sqrt{\frac{p_c}{\left(\frac{s}{f_s}\right)\left(1 - e^{\left(-0.78\frac{r}{h}\right)}\right) N_c\, c_u}} - 1\right) r \qquad \textit{Eq 2-18}$$

Where: h is the base course thickness (m), J_t is the average GGR tensile strength at 2% strain (kN/m), r is the radius of the equivalent tire contact area (m), N is the number of passages, p_c is the tire contact pressure (kPa), s is the design rutting criterion (mm), f_s is the critical subgrade deformation (mm), N_c is the bearing capacity factor (N_c=3.8 for unreinforced unpaved roads, N_c=6 for GGR-reinforced unpaved roads), c_u is the subgrade undrained cohesion (kPa) with the same formula as before (*Eq 2-14)* and α_1 is the initial stress distribution angle. It is important to highlight that the proposed model underwent validation through a field study conducted by Fannin and Sigurdsson (1996). The computed base course thickness aligned well with the test results. However, further verification of the method through additional field testing is needed before it is widely accepted as a reliable design tool.

Watts et al. (2004) concluded that the calculated values of the required aggregate layer depth, determined using the Giroud and Noiray (1981) method, provided a safe solution, although occasionally proving overly conservative for reinforced unpaved sections. This outcome aligns with expectations, given that the rut did not exceed 60 mm, which is below the 75 mm threshold displacement triggering the tensioned membrane effect. Moreover, Calvarano et al. (2016a) conducted a comparative study, showing that Giroud and Noiray (1981)'s design procedure exhibits greater reinforcement-induced improvement than the method of Barenberg et al. (1975). This discrepancy is attributed to Barenberg et al. (1975) relying on load distribution as per the Boussinesq theory without considering the mechanical properties of the base, while Giroud and Noiray (1981) incorporate a trapezoidal pressure distribution, accounting for the mechanical characteristics of the base aggregate.

Furthermore, the calibration of Leng & Gabr (2006) and Giroud and Han (2004a and 2004b) was based on a limited selection of GGR. Consequently, a broader experimental investigation encompassing various GGR types and considering the average size of base particles (D_{50}) relative to GGR apertures is essential. This broader approach aims to establish a comprehensive database that enhances the generality and applicability of design methodologies to diverse GGR types. In a comparative analysis, Calvarano et al. (2016b) determined that the method proposed by Leng & Gabr (2006) tends to be more conservative than Giroud & Han (2004) due to its consideration of the degradation of the ratio E_1/E_2, influencing subgrade deformations with wheel load repetitions. Moreover, Cuelho and Perkins (2009) found that Giroud and Han (2004a & b) tended to underestimate the required base course thickness for supporting applied loads during trafficking. They identified potential causes for premature platform failure, attributing it to the quality and/or in-place strength of the base coarse aggregate, along with increased tire pressures in the test vehicle (690 kPa) compared to the tire pressures used in formulating the design methodology (550 kPa).

The design methods mentioned above exhibit limitations and require calibration across various scenarios, encompassing different types of GSYs, their diverse characteristics, and numerous soil parameters.

2.7. State of the art on the numerical modelling

2.7.1. Continuous models

2.7.1.1. Overview of Continuous methods

There are two main types of continuous models employed in the study of soil mechanics: finite element method (FEM) and finite difference method (FDM). These methodologies facilitate the solution of stress-strain differential equations throughout a soil mass, accounting for initial and/or boundary conditions.

The FEM involves the creation of a stiffness matrix that connects forces and displacements within the structure. Solving the resulting system of equations typically entails employing a Newton-Raphson linearization method. This optimization involves calculating the stiffness matrix and the Jacobian matrix of the system at a frequency determined over a specified number of computational iterations.

On the other hand, FDM deviates from storing the stiffness matrix data utilized in FEM. In this approach, equations are stepwise reformulated, with node coordinates being updated at each time step. The mesh deforms using a Lagrangian formulation, in contrast to the Eulerian formulation of finite elements, where the mesh remains fixed. An explicit solution scheme is employed in this process.

In continuous meshes, GSY reinforcements, often represented by structural elements like "membrane," are inserted. The choice between emphasizing the shearing nature of the soil/GSY interface or the flexural behavior of the GSY reinforcement determines the specific representation. Ideally, soil-GSY interface parameters are established through experimental tests. It is crucial to note that simulating the membrane effect in the GSY sheet necessitates reaching sufficient deformation levels. However, achieving a high level of deformation is often difficult in continuous models.

2.7.1.2. Applications of finite element method

Calvarano et al. (2017) conducted a numerical study on the performance of a reinforced aggregate base course over a soft subgrade using FEM analysis via ABAQUS software. In the finite element model (Figure 2-27), shell elements were employed to represent both the base course and the subgrade layers. The reinforcement GGR element at the base-subgrade interface was simulated using a truss element with a thickness of 0.003 m. The two soil layers were modeled using an extended Drucker-Prager model, while a linear elastic constitutive model was adopted for the GGR. To ensure accurate representation of the interfaces, a "tie constraint" connection type was used at either the GGR -aggregate or the GGR -subgrade interfaces in reinforced sections, and the aggregate-subgrade interface in unreinforced sections, ensuring perfect adherence to each interface. For the simulation, 1000 loading cycles were applied with a maximum load of 40 kN (550 kPa) over a circular area with a diameter (D) of 0.34 m and a frequency of 0.5 Hz. The findings of the study indicated that the unreinforced section with a 300 mm base course and the GGR-reinforced section with half the base course thickness produced a comparable range of rut development after 1000 loading cycles (around 6 mm). This suggests the potential effectiveness of the GGR -reinforced section in achieving comparable performance with a reduced base course thickness.

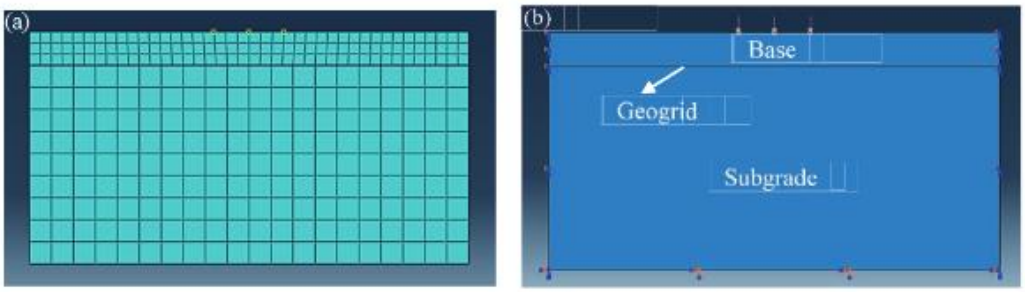

Figure 2-27: Finite element model: a) Mesh view; b) load and bond condition Calvarano et al. (2017)

Leonardi et al. (2020) conducted a numerical study focusing on the enhancement of a reinforced unpaved road subjected to repeated wheel traffic loads (Figure 2-28). Employing FEM analysis with ABAQUS software, the study modeled the base and subgrade layers using a Drucker–Prager model. The GGR was simulated using a 3-D deformable shell planar (membrane elements section type) with a thickness of 0.003 m and open meshes (Figure 2-28 c). Furthermore, a linear elastic constitutive model was employed to describe the behavior of the GGR. The simulation of GGR-soil interaction involved two components: one normal to the surfaces and one tangential to the surfaces. The interface in the normal direction was assumed to be a "hard contact," disallowing any separation. In the tangential direction, full interlocking was assumed between the GGR and the surrounding soil. To replicate the impact of heavy vehicular traffic, a cyclic load of triangular type, with an amplitude of 40 kN (550 kPa) and 2000 cyclic repetitions, was applied over two rectangular areas (Figure 2-28 a). Each cycle featured a load application duration of 0.01 sec, simulating typical vehicle speed. The authors concluded that the presence of the GGR significantly reduced surface displacement from 22 mm (unreinforced) to 16 mm (reinforced).

In a parallel study, Alkaissi et al. (2021) employed ABAQUS to delve into the behavior of unpaved roads. Their simulated model, spanning 5 m in width and 7 m in length, featured an unpaved surface granular layer of 150 mm and a subgrade soil layer of 300 mm. The GGR was conceptualized as a membrane element situated between the base and subgrade layers. The ABAQUS finite element model replicated traffic loading using a standard axle load of 80 kN with dual tires and a contact pressure of 600 kPa. The results indicated a noticeable reduction in surface displacement in the presence of the GGR. Specifically, the displacement at the surface of the granular layer decreased from 7 mm in the unreinforced model to 4 mm in the reinforced section.

It is crucial to acknowledge that the models presented in the study offer valuable insights; however, they come with limitations, notably in the utilization of simplified constitutive models for both the soil layers and the GGR reinforcement. Furthermore, it's noteworthy that the range of soil displacement considered in the analysis is relatively conservative compared to scenarios where GSY typically activate the tensioned membrane effect. The focus solely on displacement and stress stems from the inherent limitations of FEM in providing information regarding the extent of cracking under repeated vehicular loadings.

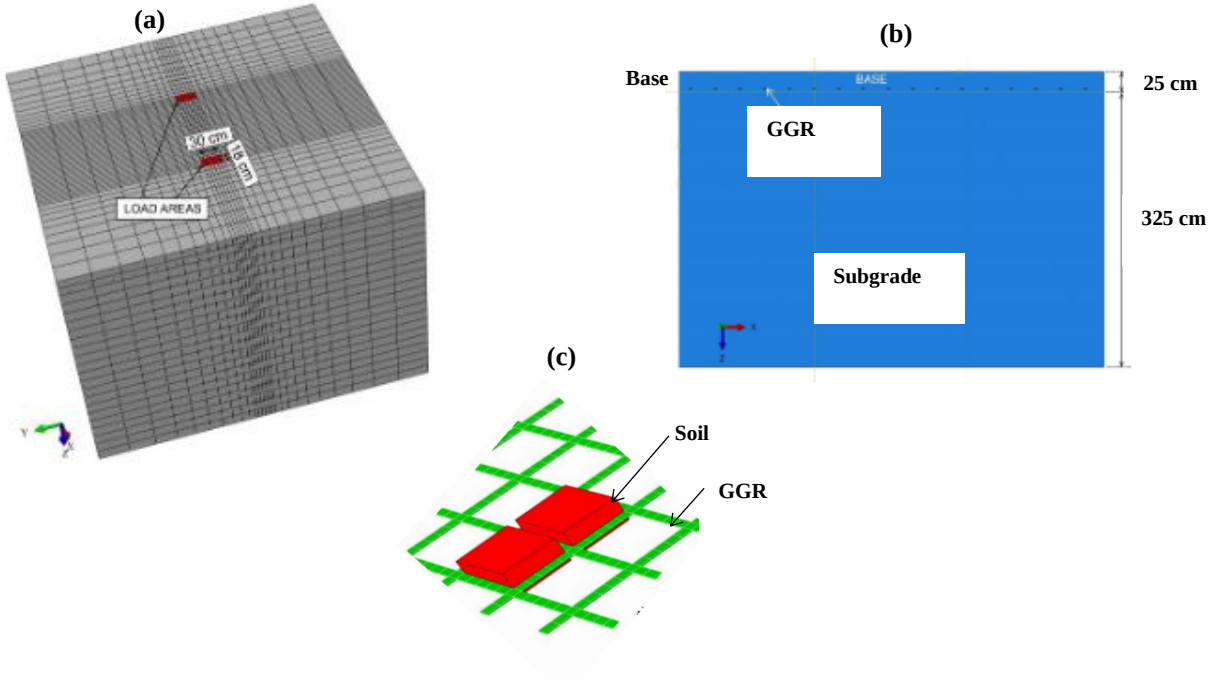

Figure 2-28: The 3D finite element model model (a) 3D view showing the area of applied loads; (b) Sketch of the pavement geometry; (c) Soil–GGR interlocking (Leonardi et al. ,2020)

2.7.1.3. Application of the finite difference method

In the study conducted by Khoueiry (2020), a numerical model was developed using the differential element method and implemented in FLAC 3D software to investigate the behaviour of GSY reinforcement in unpaved roads (Figure 2-29). The explicit numerical method employed by FLAC facilitated nonlinear computations without additional iterations, making it advantageous for the analysis. The Cap-yield model was utilized to simulate the subgrade soil, with calibration based on triaxial tests under both monotonic and cyclic loads. The Mohr-Coulomb constitutive model was used to simulate the base course layer behavior, albeit without considering the nonlinear behavior associated with grain rearrangements. The reinforcement was modelled as a membrane with elastic characteristics within its plane. The base course/subgrade interface was designed to prioritize the influence of soft soil, while the base course/ GSY interface was simplified to a shear elastic perfectly plastic behavior, representing a limitation of the model. Simulations of reinforced and unreinforced platforms, both with a 220 mm base course thickness, were conducted and compared to experimental results after the first loading cycle. A monotonic vertical load of 40 kN was applied to a loading plate of 300 mm of diameter equivalent to 560 kPa. The study aimed to validate the numerical model's capability to replicate experimental outcomes in terms of surface soil layer displacement and GSY strain. The comparative analysis of reinforced and unreinforced numerical results revealed the reinforcement's effectiveness in reducing the maximum vertical stress on the subgrade, consequently mitigating surface settlement. Interestingly, no discernible impact on the stress distribution angle was observed. A subsequent parametric study investigated the factors that influence the reinforcement mechanisms, yielding the following limitations:

- The base course factor that affected the most the subgrade stress distribution is the friction angle. This indicates that failure occurs in the base course layer in the first cycle, and that the analytical methods based on the elastic approaches are not applicable anymore.
- The base course/GSY interface parametric study showed no interface influence on the vertical stress distribution. This indicates that the reduction of the interface to an elastic perfectly plastic behaviour do not simulate adequately the GGRs apertures, aggregates interlocking mechanisms, and reduces the GGR reinforcement mechanism to a tension membrane.

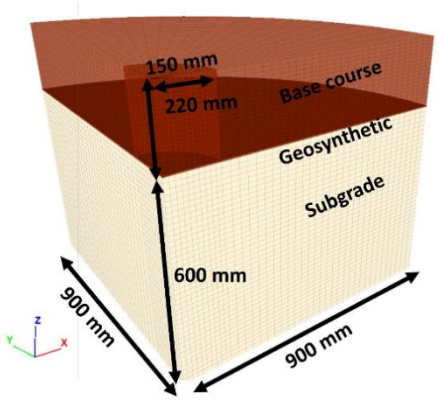

Figure 2-29: The DEF model geometry (Khoueiry, 2020)

2.7.1.4. Limitations on the continuous models

In the various applications of continuous models mentioned above, GSY are commonly characterized by a linear elastic mechanical behavior, which, however, falls short of fully capturing the inherent anisotropic nature of these reinforcement GSY. The representation of interface behavior often relies on interface elements that, generally, limit extensive relative displacements at the interface, restricting their overall applicability and versatility. Furthermore, soil modeling frequently involves the use of simple elastoplastic laws, which, while providing an approximation, do not entirely reflect the complex and dynamic nature of real soil behavior. Parameterizing soils becomes particularly challenging when attempting to accurately incorporate phenomena such as swelling, collapse, cracking, and rupture.

Moreover, the continuum approach employed in these models does not account for the effects of particle angularity, particle rolling, and sliding on the performance of GSY-reinforced structures. In contrast, the discontinue approach tackles the problem at the micro-scale, applying a force-displacement law at individual grains and requiring minimal parameters to replicate the response.

Additionally, it is noteworthy that the finite element models often consider a lower range of soil displacement when compared to scenarios where GSY reinforcement initiates the activation of the tensioned membrane effect. This discrepancy underscores the need for a nuanced understanding of the limitations and assumptions inherent in continuous models, urging the investigation in alternative approaches that better capture the complex interplay of factors influencing the performance of GSY - reinforced structures.

2.7.2. Discrete element modelling

2.7.2.1. Overview of discrete element method

Diverging from FEM constrained by the macroscopic behavioural parameters of soil layers, the discrete element method (DEM) delves into a representation of the behaviour of the soil at the scale of its individual grains. This methodology unveils phenomena such as granular rearrangements, discontinuities, or ruptures, which remain imperceptible through continuous methods. In practical terms, the discrete approach facilitates the incorporation of factors like large displacements, particle rotations, swelling or compaction, shear, and load transfers.

In the discrete element model, the soil is represented as an assembly of particles in contact with one another, each element retaining all its degrees of freedom in terms of displacement and rotation. Generally, discrete elements can take various shapes, such as polyhedral or spheropolyhedra. A contact law is established between discrete elements, incorporating considerations of contact stiffness and criteria for rupture in tension, compression, or shear at the microscopic scale of intergranular contacts. Two approaches with distinct resolution schemes exists:

1. The contact dynamics when particles are undeformable with no interpenetration (Jean and Moreau, 1992; Jean, 1999),
2. The molecular dynamics when particles are undeformable allowing for a slight interpenetration at contact. Cundall (1971) introduced the DEM formulated from molecular dynamics for studying rock mechanics problems. This method has been further developed (Cundall and Strack, 1979), and its application has spread in the field of civil engineering.

The potential for interpenetration between discrete element permits to rely on the interpenetration distance to contact force. This relation forms the basis for creating an explicit resolution scheme, as illustrated in Figure 2-30. The iterative resolution process unfolds over time encompassing successive phases: 1) contact detection, 2) the computation of interaction forces among discrete elements in contact, and 3) the subsequent calculation of particle positions and velocities for the next time step. To ensure accuracy and stability in the solution, a meticulous choice of a small-time step is crucial. In addressing quasi-static applications, damping models, whether viscous or local, can be incorporated. These models play a pivotal role in facilitating convergence by restricting the propagation of elastic waves.

The contribution of the DEM in the presented models can be classified as either entirely through the discrete element models or partially through the coupled finite element - discrete element model. However, limitations in modelling GSY reinforcement will be shown in the DEM. Consequently, the FEM will be used to model the GSY while retaining the DEM to model the soil and the soil - GSY interface. Thus, the model become a coupled model integrating both finite element and discrete element methods.

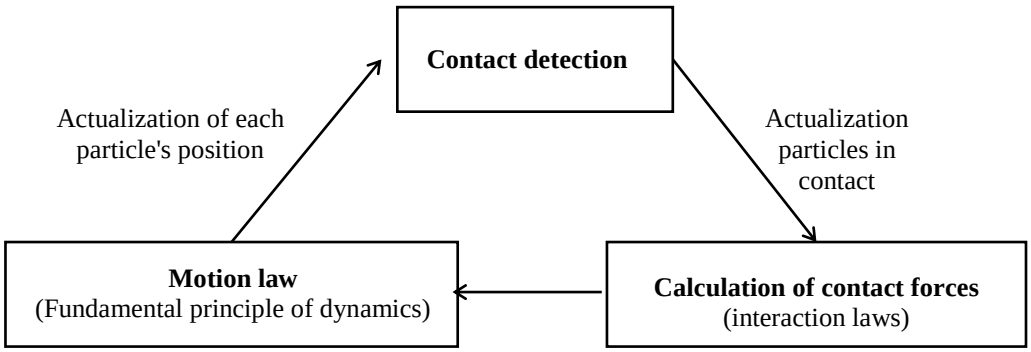

Figure 2-30: Calculation cycle in DEM

2.7.2.2. Bidimensional models

Chareyre et al. (2002) employed the PFC^{2D} software (Itasca, 1997) and the DEM to represent the soil- GSY system in two dimensions. In this model, granular soil particles were modelled as an assembly of disks, while GSY reinforcements were represented as a chain of disks (depicted in Figure 2-31a). The tensile strength and stiffness of the GSY were directly linked to the tensile strength and tensile stiffness of the contacts between the disks. The utilization of a properly parameterized microscopic contact law ensured an accurate representation of the macroscopic tensile behavior of the GSY. Despite yielding relevant results, this model had two notable limitations. Firstly, the roughness of the soil/ GSY interface was influenced by the size of the GSY disks and the elongation of the GSY, resulting in a complex interface behavior that was not ideal for cases involving GSY with a perfectly planar and continuous interface. Secondly, to prevent excessive separation of initially connected disks in the GSY and alterations to the soil/ GSY interface, axial efforts and deformations in the GSY reinforcement had to be limited.

Subsequently, Chareyre and Villard (2005) proposed an optimization of this two-dimensional GSY reinforcement model. They introduced a set of "spar" elements connected by nodes to represent the GSY (Figure 2-31b). The length of these elements was considered variable, with axial deformation accounted for by variations in the distances between nodes. The flexion of the GSY was represented by rotations at the nodes, while the flexion of an individual element was not considered (Figure 2-31c & Figure 2-31d). These "bar" elements were integrated into the discrete element code simulating the behavior of the soil. The interaction between the GDY and the granular matter was addressed using a soft contact approach, allowing the disks and spar elements to overlap at contact points. A notable advantage of this optimized model is the maintenance of a relatively smooth interface roughness, facilitating its characterization.

In addition, Bhandari and Han al. (2010) explored the interaction between GTX and soil under cyclic wheel loads also using PFC^{2D}. The sample box, depicted in Figure 2-32 with dimensions of 0.38 m in length and 0.10 m in height, was partitioned into two components to accommodate the soil. The sand was modelled as unbonded cylindrical particles and were generated simultaneously using the radius expansion technique (Itasca, 2004) to achieve the required 2-D porosity of 0.16. The cylindrical shape resulted in a lower strength of the granular base (Skermer and Hillis, 1970; Lekarp et al., 2000). Biaxial tests were conducted to establish micro-parameters for reasonable mechanical properties. GTX modelling involved bonded particles with a 1.0 mm diameter, utilizing an elastic spring in the contact of two particles (contact-bond model). The contact bond force and normal stiffness between GTX particles corresponded to their tensile strength and stiffness at a strain, respectively. Microscopic parameters for the GTX were calibrated through tensile tests. A wheel (diameter = 40 mm) was positioned at mid-length to apply a cyclic load of 353 N in the discrete element model, with the load applied vertically and no horizontal movement allowed. The study

involved 25 loading-unloading cycles. The results of the wheel circulation showed that the GTX restrained vertical particle movement while facilitating horizontal movement due to lower frictional resistance compared to the soil frictional resistance. Moreover, the effectiveness of the GTX in minimizing vertical deformation depended on its depth. The GTX at a depth of 25mm exhibited small tensile stresses and was less effective in minimizing surface deformation caused by cyclic vertical loads compared to the GTX at a depth of 12.5 mm.

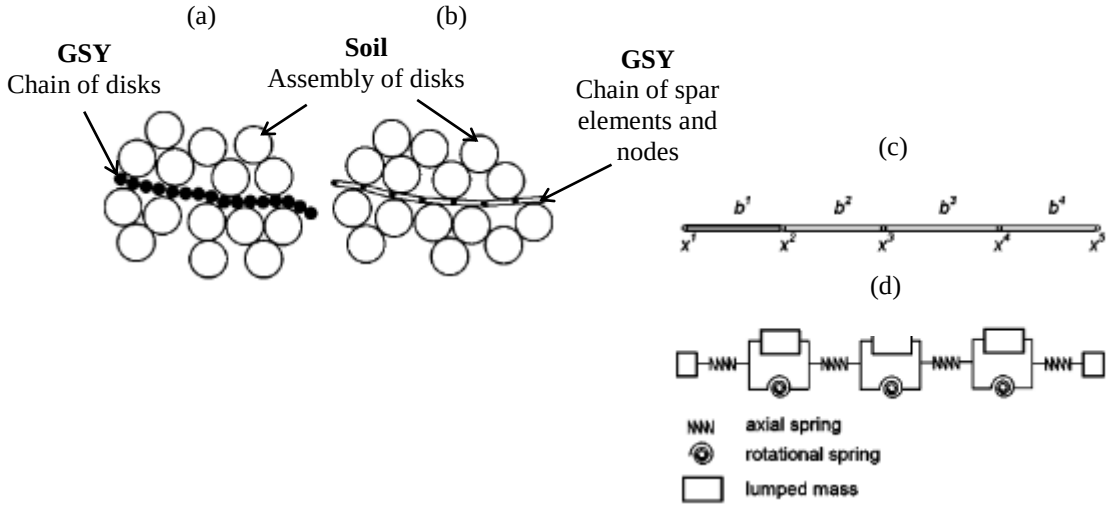

Figure 2-31: Modeling Approaches for Soil-GSY Systems: a) Full-DEM Modeling, b) DEM–Dynamic Spar Element Model, c) Node and Spar Element Details, and d) Rheological Model for a Five-Noded GSY

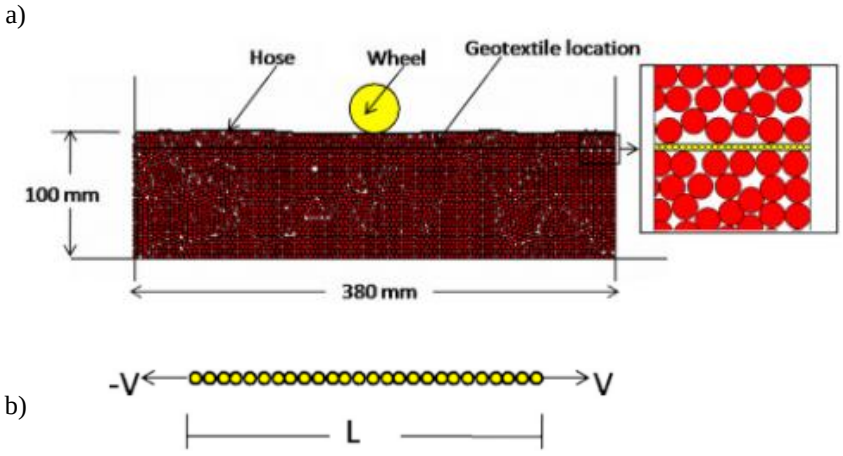

Figure 2-32: DEM model of: a) cyclic wheel load test simulation; b) GTX particle assembly for a tensile test simulation (Bhandari et al.,2010)

2.7.2.3. Three-dimensional models

In three dimensional models, spheres or clusters of spheres are commonly employed due to their efficiency in optimizing contact detection processes, thereby reducing computation time.

Chen et al. (2012) employed the (DEM) to simulate both the soil of the embankment and the GGR. The GGR was represented by a set of spherical particles arranged to replicate its grid-shaped structure (Figure 2-33). The interaction between the soil and GGR was managed through contacts between discrete elements of the soil and the grid. However, accurately reproducing the GGR's behavior during an extraction test posed challenges due to the complexity of its geometry. Despite adjustments of microscopic contact parameters based on loading tests, the rigid connections between GGR particles might not precisely replicate the reinforcement's tension and flexion behaviour. Tran et al. (2013) further analysed this model, emphasizing that the stresses and deformations of the GGR may not accurately represent reality. A potential solution involves coupling discrete elements to represent the embankment and finite elements to represent the GSY reinforcement.

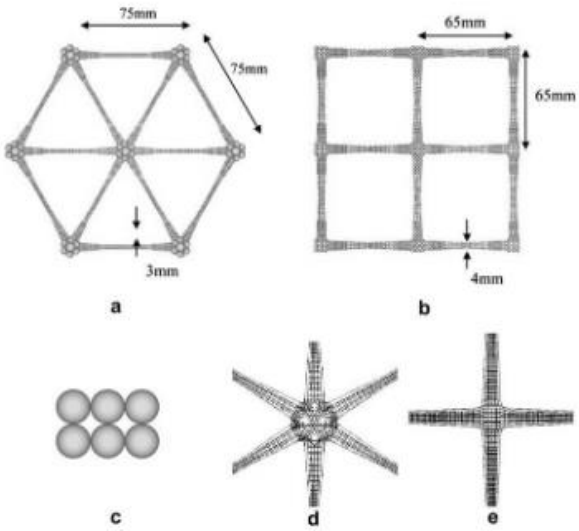

Figure 2-33: Discrete element modelling of a GGR: a) triaxial reinforcement, b) biaxial reinforcement, c) cross-sectional view of cables, d) contacts linked to triaxial e) and biaxial reinforcements (Chen et al., 2012)

To exceed this limitation, Villard et al. (2009) developed a coupled model that considers the discrete nature of the granular material, the fibrous and continuous nature of the GSY, and the frictional interaction at the interface (Figure 2-34a). This GSY sheet was modelled by three-node triangular finite elements, each comprising fibers with various orientations forming a plan (Figure 2-34b). The behaviour of the fibre network was determined by superimposing behaviours obtained in each fibre direction, with no sliding between fibres. The mechanical behaviour of the fibres was non-linear elastic, and the compression elasticity modulus was considerably lower compared to the tensile elasticity modulus. These elements described the membrane and tensile behaviour of the reinforcement under large deformations. Specific interaction laws were defined at the interface between the soil and the GSY, considering normal and tangential contact rigidities and a friction angle (refer to Figure 3). The numerical model underwent validation through analytical membrane calculations on simple cases and comparisons with results from laboratory or full-scale experiments (Briançon and Villard, 2006; Villard et al., 2009; Villard et al., 2016).

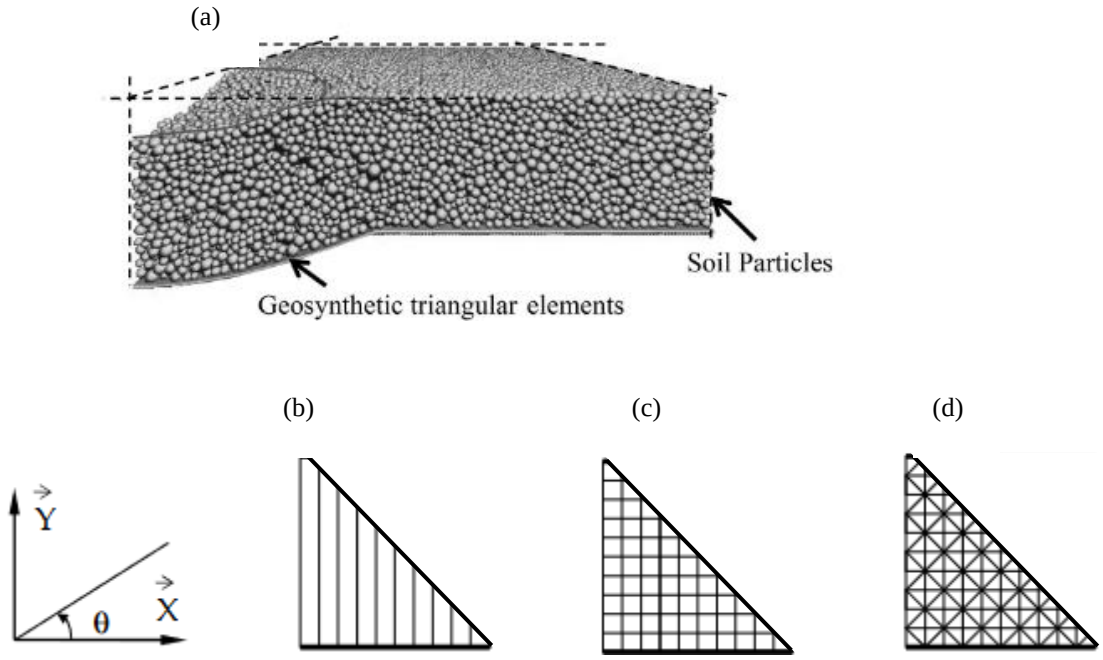

Figure 2-34: a) Geometry of the numerical samples; and thread distribution patterns in triangular elements: b) mono-directional sheet element, c) bi-directional sheet element, d) multi-directional sheet element (Villard et al., 2009)

Tran et al. (2013) implemented coupling model utilizing a discrete element code for the soil of embankment and a finite element code for the GGR reinforcement. The GGR was modelled using 8-noded brick elements with 8 integration points (Figure 2-35a). The finite element modelling employed a dynamic relaxation method with numerical damping until achieving a stable state. Since both the discrete and finite element models used an explicit dynamic approach, they were compatible and could be effectively coupled. Interface elements facilitated the transfer of contact forces between the domains governed by the FEM and the DEM. The contact algorithm between discrete elements and interface elements resembled that governing contact between discrete elements. In the pull-out test simulation, the modelled reinforcement featured a grid with rectangular openings of 25 mm by 33 mm (Figure 2-35b). Consequently, the grid cables in the loading direction experienced tension, while the transverse elements underwent flexural stresses. The simulations revealed that the highest displacements and stresses in the grid were concentrated near the loading point, diminishing rapidly toward very low values at the midpoint of the reinforcement. An increase in soil stresses and deformations was also observed on the loading side and near the grid. Comparisons with experimental results highlighted alignment between the soil movements and the distribution of contact forces in the numerical model with experimental observations.

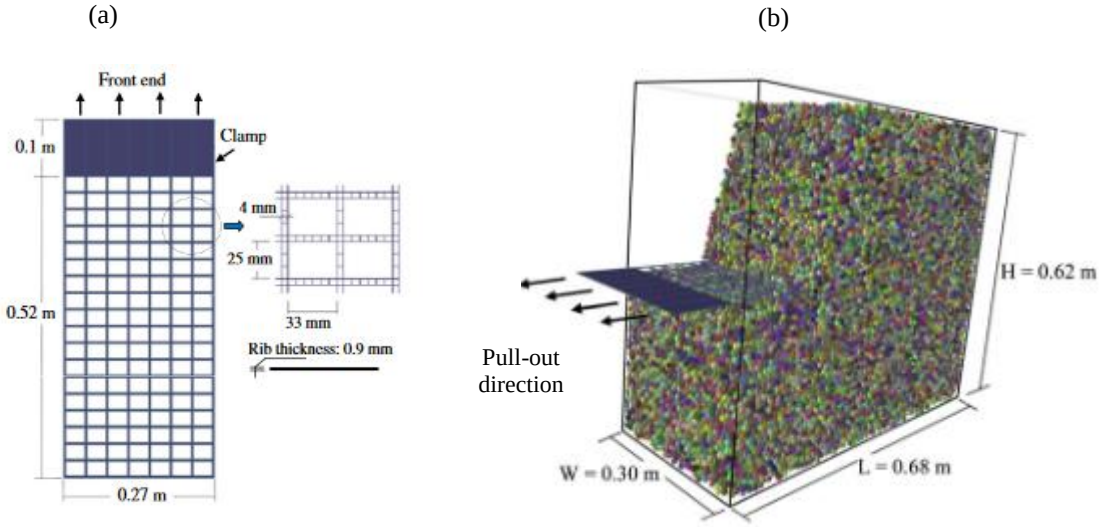

Figure 2-35: a) Geometry of the GGR and b) partial view of the model before reinforcement extraction (Tran et al., 2013)

2.7.3. Selected model

The decision to integrate the DEM) and the FEM in this thesis stems from the necessity to use a model that accounts for the discrete nature of granular material, the fibrous and continuous characteristics of GSY, and the frictional interaction at the interface. This coupling model is crucial for examining the behavior of the platform at the grain level, understanding the mechanisms governing GSY-soil interaction at the interface, and comprehending the GSY behavior under cyclic loading.

Continuous methods face limitations in capturing these intricacies, such as the microscopic interaction parameters of the soil material, excessive mesh deformations in the platform, and realistic interactions between soil grains and the GSY at their interface. Consequently, the DEM-FEM coupling allows for the consideration of soil mechanisms, encompassing aspects like large displacements, rotations, bulking or compaction, shear, and load transfers.

The distinctive advantage of DEM lies in its explicit consideration of micromechanical level mechanisms, including irreversible displacements between particles and granular rearrangements, without the necessity for implementing complex behavior laws as seen in FEM. Adjusting microscopic parameters requires the comparison between the numerical characterization tests and traditional characterization laboratory tests (triaxial tests, direct shear tests, pullout tests, etc.).

For this research, the specific DEM code chosen is the SDEC software (Spherical Discrete Elements Code, developed by Donzé & Magnier (1997). Originally designed for applications involving spheres, it has been adapted and validated for soil reinforcement applications using GSY layers. This adaptation involved the incorporation of clusters (Salot, 2007) and specific elements characterizing GSYs (Le Hello, 2007). The selection of SDEC ensures a robust and validated platform for studying the intricate interactions within granular materials and GSY sheets.

2.8. Conclusion

A properly designed and placed GSY can improve the performance of unpaved sections by reducing rutting under traffic loads and possibly reducing the required thickness of the base course. As we have shown in this chapter, it remains difficult to fully understand and physically quantify this improvement. The three mechanisms involved in unpaved reinforced sections are the lateral restraint mechanism, the tensioned membrane effect and separation. The challenge arises from the fact that the load is applied vertically, and the reinforcement is applied horizontally, leading to some difficulty in explaining and determining the predominance of these mechanisms.

Authors have been proposed empirical and analytical methods to estimate the base course thickness needed to design the structure by taking into consideration the GSY impact. In fact, based on supposed dominant mechanism different theories were suggested. The most used method has been proposed by Giroud and Han (2004) and accounts for the confinement mechanism by interlocking between the GGR and the aggregates of the base course material or friction between the GTX and the aggregate of the base course material with neglection of the tensioned membrane effect. This method is validated when the rut depths range between 50 mm and 100 mm and is calibrated on a limited type of GGRs. The lack of knowledge and the various factors and parameters that affect the behaviour of the unpaved road structure results in the fact that there are no clear and general design method for this structure. This clearly highlights the need of further investigations in this field.

Experimental studies were carried out to help understand structural behavior under cyclic loading. Various types of tests have been carried out: laboratory plate load test, in situ tests and large-scale laboratory traffic load test. The plate load test is one of the most used tests to characterize the behavior of an unpaved road section, since it is a laboratory test with controllable parameters. The applied load can be either vertical or cyclic. The static load showed an underestimate of the enhancement provided by the GSY within the road structure, when compared to the cyclic load. Nevertheless, it is clearly established that in situ tests better simulate the actual applied load, but it is difficult to control the consistency of soil parameters across test sections due to their large dimensions. Furthermore, the number of axles passes poses problems for in situ testing, whereas such a structure is normally designed to withstand more than 10,000 cycles. Furthermore, Accelerated Pavement Test Facilities were employed in large-scale laboratory experiments to replicate traffic loads on constructed road structures. These expansive facilities, often resembling large containers with extended circulation lengths, are commonly found in Transportation Research Departments. They serve the purpose of characterizing the impact of reinforcement in unpaved roads on soft subgrade. The preparation and installation work for the soil layer are comparatively less critical than in in-situ tests since the dimensions of the pit are typically smaller.

The aim of our work is to provide more knowledge regarding the mechanisms that takes place within the reinforced structure, the influencing parameters, the overall structure behaviour and response. Therefore, the experimental protocol aimed to test the unpaved roads under two loading types: the cyclic plate load and the circulation traffic load. The Accelerator Simulator of Traffic developed Khoueiry (2020) study specially for the unpaved road under soft subgrade structure testing are used to apply the traffic load. This facility was designed to simulate circulation traffic load by taking into consideration the large settlement development (around 100 mm) at the surface of this unpaved road structure. In addition, the dimensions of the facility have been optimised in a way to reduce the installation and preparation soil works. In this experimental protocol, a special attention to the soil layers preparation and installation has been considered to insure the repeatability of the tests.

Numerous studies have sought to develop numerical models for simulating the behavior of structures under monotone or cyclic loads. The continuum – based finite or differential method showed several limitations. GSYs are often characterized by a linear elastic mechanical behavior, which does not fully capture their inherent anisotropic nature. Moreover, soil modeling often relies on simple elastoplastic laws

that do not entirely reflect the complex and dynamic nature of real soil behavior. When complex soil phenomena such as swelling, collapse, cracking, and rupture need to be presented, sophisticated behavioral laws with a wide range of parameters must be employed. The representation of GSY -soil interface behavior relies on elements that limit extensive relative displacements, restricting their overall applicability and versatility.

The discrete-based method provides a more realistic simulation of the granular layer's discrete nature and phenomena like swelling, collapse, cracking, and rupture without resorting to complex laws. Adjusting soil microscopic parameters requires comparing numerical characterization tests with traditional laboratory tests such as triaxial tests, direct shear tests. However, the discrete method faced challenges in replicating GGR behavior due to the complexity of its geometry. The rigid connections between GGR particles fail to replicate the tension and flexion behavior of the reinforcement.

To overcome this limitation, a coupled model was developed by Villard et al. (2009), considering the discrete nature of the granular material, the fibrous and continuous nature of GSYs, and the frictional interaction at the the soil- GSY interface. In this model, the specific DEM code is the SDEC software (Spherical Discrete Elements Code), initially designed for applications involving spheres and adapted and validated for soil reinforcement applications using GSY layers. The selection of SDEC ensures a robust and validated platform for studying the intricate interactions within granular materials and GSY sheets, making it the chosen model to simulate the behavior of reinforced granular platforms over soft subgrade soil.

3. Chapter 3. Full scale laboratory test

3.1. Introduction

This chapter provides a comprehensive description of the experimental protocol employed for constructing and controlling the granular platforms over soft subgrade soil. The study focuses on two key factors: the influence of different GTX s with varying stiffness and the effect of base course thickness. To this end, two GTX s with two different stiffness were tested and two base course thicknesses: 300 mm and 500 mm were used.

One or two types of tests were conducted on the unpaved road platform to achieve the project objectives:

- A cyclic plate load test using a circular plate.
- A traffic load test utilizing a Simulator Accelerator of Traffic (SAT), developed during Khoueiry's research (2020).

To ensure reliable and comparable results, careful attention was given to the preparation and installation of the unpaved structure layers and the weak soil layer, as well as quality control tests and instrumentation of the solicited areas. A comprehensive preparation protocol was established and strictly followed for each tested platform. Additionally, multiple tests were conducted to verify the installation protocol's repeatability. Furthermore, sensors were strategically positioned to measure soil displacement, rut development, and load distribution.

This chapter provides an overview of the experimental devices and configurations utilized in the study. It also details the composition of the tested platform and the materials employed. Moreover, the installation protocol, aimed at achieving uniform platform properties for each test, and the quality control tests are presented. Lastly, the instrumentation techniques employed for both types of tests are thoroughly explained. It is noteworthy that the experimental protocol developed by Khoueiry (2020) in their thesis served as the foundation for this work, with certain adaptations made to suit the specific requirements of the study.

3.2. Experimental configurations and devices

3.2.1. Experimental box

An experimental box measuring 5 m in length, 1.8 m in width, and 1.1 m in height (Figure 3-1a & Figure 3-1b) was utilized for the construction and testing of seven unpaved road sections. These sections were subjected to either plate load, or both plate load and traffic load.

Khoueiry (2020) conducted a comprehensive study to investigate the boundary effect of an experimental box. The boundary effect analysis involved strategically placing earth pressure cells vertically along the borders of the box during plate load tests. Remarkably, the results revealed that the application of cyclic load at the box centre did not induce any stress on the borders, indicating the effectiveness of the box dimensions in mitigating boundary effects.

The initial four sections were constructed within a designated area of the experimental box, measuring 2 m in length and 1.8 m in width, and were subjected to cyclic plate load testing. These sections consisted of a 300 mm thick granular compacted layer placed over a 600 mm thick, soft subgrade layer.

The remaining three unpaved road sections were constructed across the entire experimental box. Within these sections, a granular compacted platform of either 300 mm or 500 mm thickness was installed over the soft subgrade layer. Initially, a hydraulic jack was positioned at the centre of the zone designated for the plate load test, which measured 2 m in length and 1.8 m in width, located at the front side of the box. After completion of the plate load test, the hydraulic jack was removed, and the Simulator Accelerator of Traffic

(SAT) was placed on the box to apply traffic loads on the central zone, measuring 3 m in length and 1.8 m in width.

Reinforcement GSY can be used to improve the low-strength subgrade of CBR lower than 3% regarding the FHWA (2008). On top of that, granular platform with a minimum CBR of 20% is required. A CBR of 20% indicates that the granular platform has a relatively high bearing capacity and can withstand heavy loads without significant deformation.

In the reinforced sections, the tested GTX was placed at the interface between the soft subgrade layer and the base course layer, serving the purpose of both separation and reinforcement. In the unreinforced sections, a lightweight non-woven GTX was placed at the interface between the soft subgrade layer and the base course layer to prevent contamination between these two distinct layers, which were repeatedly used in all tests. The selected GTX was non-intrusive and did not add any mechanical resistance to the unpaved road sections.

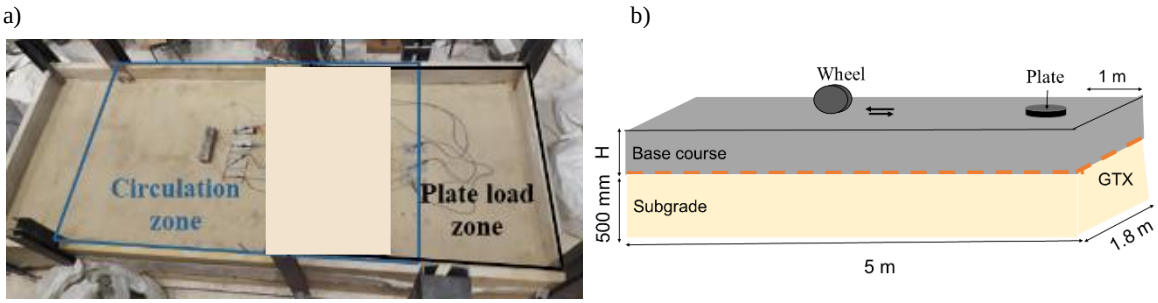

Figure 3-1: Experimental box Top view; b) Experimental box 3D schema

3.2.2 Cyclic plate load test

Seven unpaved road sections were tested under vertical cyclic load. The vertical load is applied by a hydraulic jack on a circular plate of 320 mm of diameter placed at the granular platform surface (Figure 3-2a). The maximum applied load of 45 kN has been chosen to obtain a pressure equal to 566 kPa which is equivalent to the contact pressure of a half single-axle regarding AASHTO (2000).

The loading and unloading pulse duration for each cycle is 0.8 s (Figure 3-2b) and is in accordance with the recommendation of the AASHTO standard (Berg et al., 2000) for which a range was set between 0.1 s and 1s. The frequency equals to 0.76 Hz less than 1 Hz according to Berg (2000) to prevent dynamic effects that can affect the results of the test. According to FHWA (2008), the unpaved road is expected to carry 10 000 ESAL (equivalent single axle load) passes, with a maximum rutting of 75 mm. Each load cycle will be considered as one ESAL. Hence, 10, 000 cycles are applied to each tested platform except the test 2 because of the excessive rutting.

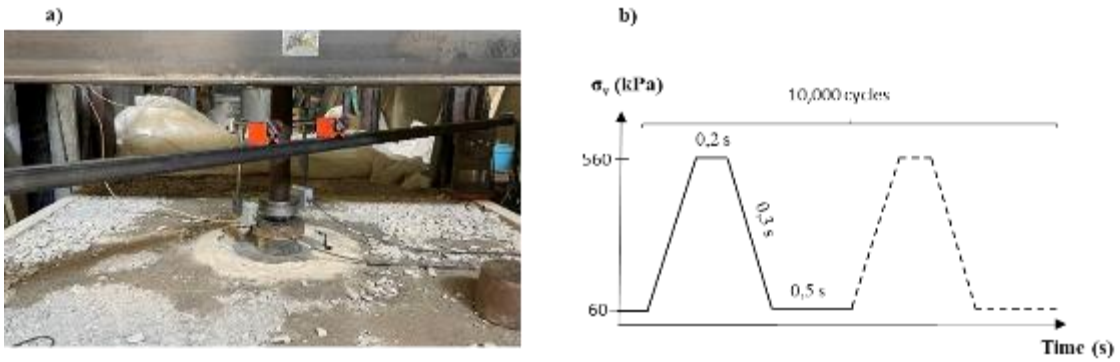

Figure 3-2: (a) Cyclic plate load test setup, (b) Cycles applied.

3.2.3 Traffic load test

Three unpaved road sections were subjected to traffic load testing using the SAT, which was developed in the thesis of Khoueiry (2020).

The SAT is installed within a frame measuring 4.5 m in length, 1.8 m in width, and 2.3 m in height (Figure 3-3 a & Figure 3-3 b). It is supported by four adjustable feet that allow the load to be applied at various heights, ranging from 0.9 m to 1.3 m, or at ground level without the feet. The device consists of a central metal beam measuring 3.3 m in length, equipped with two chains that facilitate the movement of the tire axis, along with an electric motor that controls the motion of the two chains. A deformable parallelogram, attached to the main beam, and two pneumatic cylinders ensure that the force is evenly distributed at each tire position and that a consistent load is applied to the road surface, even in the presence of excessive ruts. During load application, the two pneumatic cylinders compress and allow for vertical settlement of the surface, ranging from 0 to 100 mm.

Table 3-1 provides an overview of the main specifications of the SAT facility. The total weight of the SAT is 8400 kg, with a minimum load applied by the tire of 28 kN, corresponding to the weight of the machine itself. The tire has a diameter of 820 mm, a width of 210 mm, and weighs 86 kg. The wheel path has a total length of approximately 3 m, with an effective length of 2 m outside the impact zone. The wheel speed can be adjusted between 2 km/h and 7 km/h, and the load application can be unidirectional or bidirectional. In the conducted tests, a bidirectional load was applied, and a velocity of 4 km/h was selected to minimize excessive deformation of the base course surface, which helps maintain load distribution throughout the depth.

Table 3-1: Main specifications of the SAT facility

Parameter	Specification
Number of axles	1
Tire movement	• Linear, Uni-directional • Linear, bi-directional
Experiment location	• Laboratory • In situ
Application area	Roads
Load range	• 28 kN equal to the self-weight of the device • Can be higher depending on the application
Tire details	• Single filled Diameter = 821 mm Weight = 86 kg width =210 mm • Can be modified to dual tires configuration
Speed range	2-7 km/h / Variable depending on the application
Suspension	Yes, can be stopped in a specific position, with load application
Maximum vertical displacement	100 mm
Load application altitude range	• 0 • 0.9 m -1.3 m

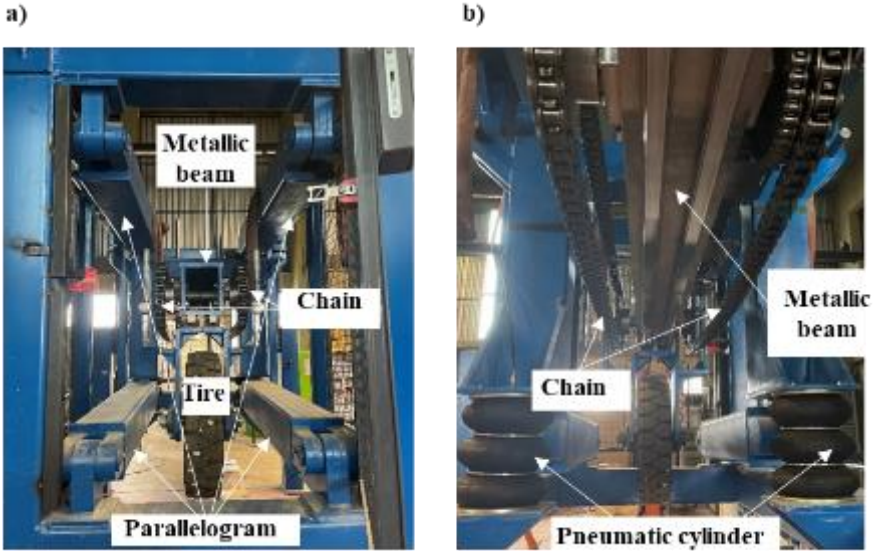

Figure 3-3: (a) Front view of the SAT; (b) low-angle view of the SAT

3.3. Materials

The laboratory-scale unpaved road platform was constructed at a 1:1 scale. Experimental tests conducted by Khoueiry (2020) in the designated experimental box demonstrated that these dimensions effectively mitigate border effects. Moreover, the chosen dimensions significantly reduce the labor involved in soil installation.

3.3.1. Subgrade

3.3.1.1. Subgrade composition

To replicate the properties of the soft subgrade soil requiring a reinforcing GSY, an artificial mixture comprised of sand and clay was developed. Due to the water table being generally located below the top meter on site, it is necessary to utilize unsaturated soil to more effectively simulate the site's conditions. As per the FHWA (2008) guidelines, the presence of GSY reinforcement is required when the CBR of the subgrade is less than 3%. Although Khoueiry (2020) has indicated in literature that a GSY layer located at the interface between a subgrade with a CBR value of 2 and a granular layer of 35 cm thickness did not provide additional effectiveness under vertical cyclic loading. Feedback has established that the use of a GSY becomes increasingly crucial as the subgrade becomes weaker. As a result, it was decided to target a subgrade soil with lower mechanical characteristics than that produced by Khoueiry (2020) to highlight the impact of using a reinforcement GSY at the interface of the subgrade and granular layers. Consequently, to more appropriately imitate the critical conditions of the site, the test shall be performed utilizing a soft, unsaturated subgrade with a CBR value of 1%.

The selected artificial subgrade soil is composed of a mixture of 20% kaolinite clay and 80% Hostun sand (HN 34) by weight. The used Hostun sand was classified as a poorly graded sand (Cu =1.6 et CC=0.85) regarding the USCS standard with particles diameters ranging between 0.08 and 1 mm. This mixture is adopted in Khoueiry's (2020) thesis from among seven tested mixtures of clay (kaolin or bentonite) and Hostun sand (HN 34) because of the degree of saturation is 75% with a CBR value of 2 % is far enough from the 100% of saturation.

Three samples taken from the used mixture with the same percentage of kaolinite and Hostun sand showed similar particle distribution curves, strongly indicating that the two soil types were mixed properly (Figure 3-4). In addition, the comparison between the Hostun sand curve and the mixture curves showed that the percentage of the fine particles reflecting closely the inclusion of the clay. Nevertheless, due to the interaction between the sand and the kaolin particles, not all of the fine clay particles were able to pass through the 0.1 mm sieve due to a chemical reaction. Therefore, wet particle size distribution is the optimal method to demonstrate this type of particle diameter dispersion.

In this work, several water contents were tested to get the water content that will attend a CBR ratio of 1% at the right side of the proctor optimum ($w > w_{optimal}$), within the unsaturated condition (Figure 3-5). The selected mixture of 20% of kaolinite clay and 80% of Hostun sand was compacted at 13.5% of water content in order to give a CBR ratio of 1% and a dry density of 17.8 kN/m^3. The degree of saturation is 75% with a CBR value of 1 % is far enough from the 100% of saturation.

In order to obtain a uniform soil layer with a consistent CBR value of 1% throughout the area and depth, the challenge was to properly prepare and compact in particular way the soil in the laboratory box. The subsequent sections will detail the exact process adopted to accomplish this objective.

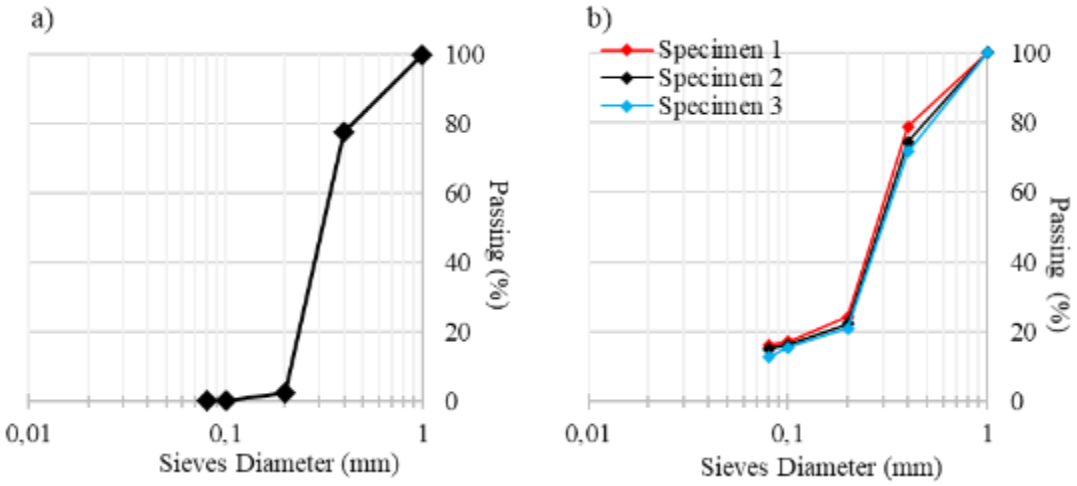

Figure 3-4: Particles size distribution of the used Hostun sand, (b) Particles size distribution of the mixture 20% kaolinite Clay and 80% Hostun sand

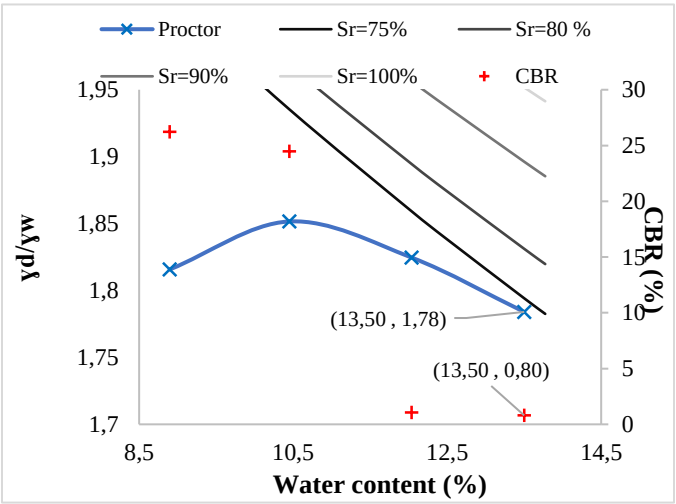

Figure 3-5 : Kaolin and Hostun sand mixtures proctor and CBR curves

3.3.1.2. Subgrade characterization

3.3.1.2.1. Cyclic plate load test

The performed vertical cyclic plate test aimed to determine the rigidity of the soft subgrade and its evolution with loading cycles. The deduced behaviour law of the soft soil under cyclic load was subsequently employed in the numerical simulation of the unpaved road structure under vertical cyclic load (chapter 5). The challenge was to replicate the mechanical properties of the subgrade layer beneath the granular platform in the laboratory tests of unpaved road. In these tests, the soft subgrade was installed in three sublayers,

each 20 cm thick, with light compaction. However, when the granular layer was placed and compacted on top of the soft subgrade, settlement sensors indicated a settlement ranging from 50 to 60 mm at the top of the subgrade layer (Section 4.5.2). Thus, the installation and compaction of the granular platform marginally improved some mechanical characteristics of the subgrade, particularly the top surface layer. To achieve a more proportional effect of the granular layer installation and compaction on the subgrade, each sub-layer of the subgrade soil was compacted by passing a vibrating plate over it once after installation.

The subgrade layer mixture was installed in three sub-layers, each 20 cm thick in the experimental setup (2m x 1.8m and 0.6m). This layer showed a water content of 13.5% and a CBR of approximately 0.5 %. After compacting each sub-layer, the average CBR value increased to 1.5 %. It is important to note that the cyclic plate test described was conducted directly on the soft soil without introducing a granular layer. Figure 3-6a illustrates the plate test configuration.

Since the stress measured under the centre of the plate load at the top of the subgrade layer was around 100 kPa layer (section 4.4.3.4), the applied stress path to the subgrade surface layer during this test ranged between 0 and 100 kPa. A total of seven load-unload cycles (Figure 3-6b) were applied directly to the circular plate (D = 60 cm) located on the subgrade surface layer using a hydraulic jack equipped with a 10 T load cell. Two laser sensors were placed on the plate to measure its displacement during the test. It is crucial to emphasize that the test conducted followed the principles outlined in standard NF P 94 117 1. However, certain adjustments were made to align it with the conditions of the unpaved load test, particularly regarding the load transmitted to the subgrade surface layer. Furthermore, a suitable time period was selected to ensure proper adherence to the load transmission. The determined modulus and its evolution are then employed in the numerical simulation to characterize the subgrade soil.

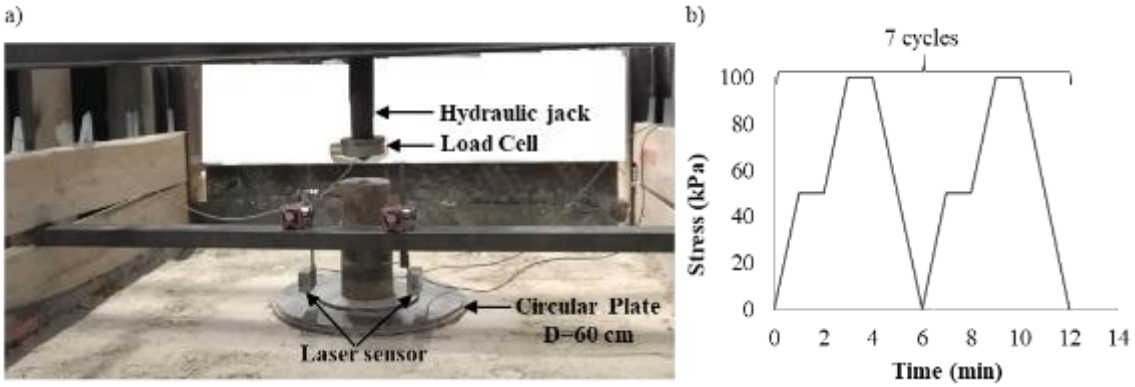

Figure 3-6: Cyclic plate test configuration (b) Cycles applied

During the loading phase of each cycle, the reaction moduli (k_{c1}, k_{c2},…, k_{c7}) were determined using linear regression models, as shown in Figure 3-7a and Figure 3-7b. The soil behavior during the unloading phase of the first two cycles was also determined using a linear regression model (Figure 3-7b). Moreover, third-degree polynomial regression models were suitable to simulate the behavior of the remaining unloading phases. However, to simplify the numerical model, a fixed reaction modulus value was employed for the unloading phase of the cycles.

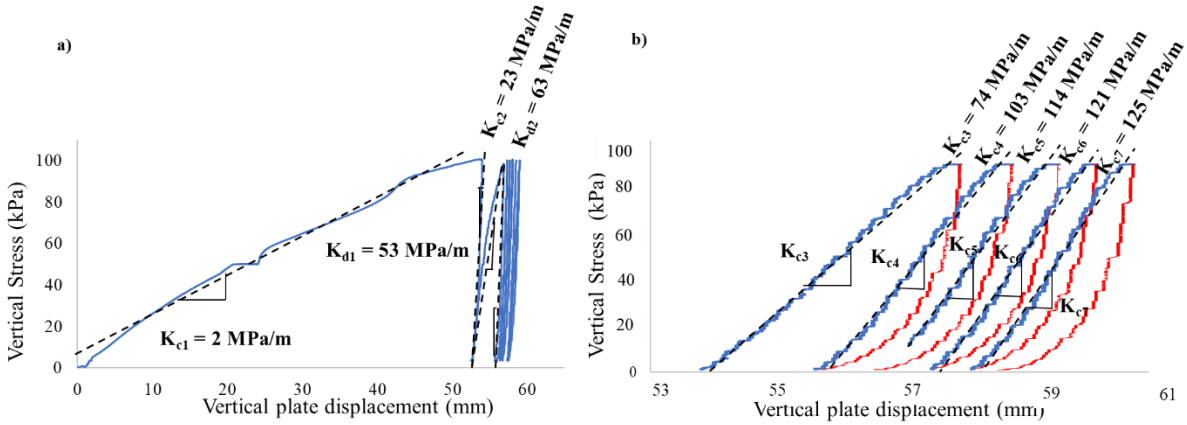

Figure 3-7: Stress-displacement curve for the applied cycles, b) Zoom on the stress-displacement curves of the cycles 3,4,5,6 & 7

Figure 3-7a depicts a reaction modulus of approximately k_{c1}=1.9 MPa and k_{u1}=53 MPa/m during the loading and unloading of the first cycle, respectively. It can be observed that the plastic displacement was 52 mm, while the elastic displacement was 2 mm in the first cycle. In the second cycle, the reaction moduli (K_{c2} and K_{u2}) increased compared to the first cycle, reaching 23 MPa and 63 MPa for the loading and unloading phases, respectively. The plastic displacement was 4.5 mm, and the elastic displacement was 1.2 mm in the second cycle. From Figure 3-7b showed the subsequent cycles, it can be deduced that the plastic displacement decreased with each cycle, eventually reaching 0.5 mm by the seventh cycle, indicating that the soil behaviour became nearly elastic (quasi-elastic).

The numerical simulation of the unpaved road structure under vertical cyclic loading incorporates a behaviour law that accounts for the initial rigidity of the soft subgrade during the loading of the first cycle. This behaviour law takes into consideration the reduction in plastic deformation and the transition towards an elastic soil behaviour with cycles. The simulation aligns with the findings of the test, which highlighted the decreasing plastic deformation and the shift towards elastic behaviour in subsequent cycles.

3.3.2. Base Course

3.3.2.1. Base course composition

Non-treated aggregates with particles diameters ranging between 0 and 31.5 mm (GNT 0/31.5) were used over the subgrade layer in the tested unpaved road sections. It worth to mention that this type of aggregates was used in Khoueiry (2020) performed tests and it is the most commonly used material in France for platform constructions.

Since the aggregates size distribution curves presented in Figure 3-8 shows that the Cu and Cc factors are respectively equal 25 and 4, this soil is classified as a GP (poorly graded gravel) soil regarding the USCS standard.

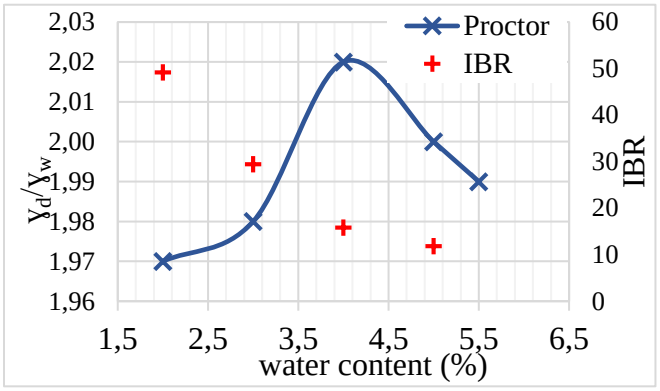

Figure 3-8: Aggregates size distribution curves

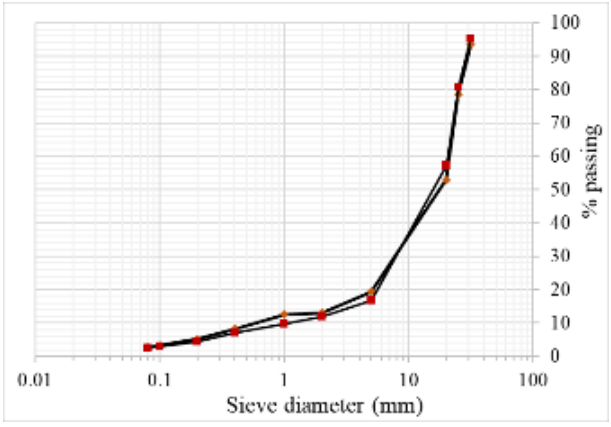

Figure 3-9: Aggregates proctor and IBR curves

The immediate bearing ratio (IBR) intended for the base course layer is 20% regarding the recommendations of FHWA (2008). The proctor curve of the aggregates presented in Figure 3-9 shows that the optimum water content at which the aggregate achieves the maximum dry density is 4%. The IBR curve is presented as well in the Figure 3-11. It is worth noting that the plate vibrator employed for compacting the aggregate layer has proven to be insufficient in effectively compacting this material. However, using a heavy compactor poses the risk of depleting the compressibility of the soft subgrade before the load application. Consequently, the decision has been made to conduct the compaction of the aggregates at a water content of 4% using the plate vibrator, aiming to come as close as possible to a CBR value of approximately 20%. This value aligns with the requirement stipulated by the FHWA (2008).

3.3.2.2. Base course characterization

3.3.2.2.1. Direct shear test

Large-scale shear box tests were conducted, according to NF EN ISO 17892-10, in order to determine the friction angle and the cohesion of the aggregates. The shear box setup consisted of a large lower box measuring 450 mm in length, 200 mm in width, and 200 mm in depth, along with a small upper box

measuring 200 mm in length, 200 mm in width, and 200 mm in depth (Figure 3-10). The height of the shear box used in accordance with NF EN ISO 17892-10 exceeds the requirement of being at least 6 times the maximum particle size diameter (Dmax = 31.5 mm). By meeting this standard, it ensures that there is ample space within the shear box to accommodate the specimen and allow for appropriate shear displacement during testing. Due to the box geometry, the shear plane remained constant throughout the displacement.

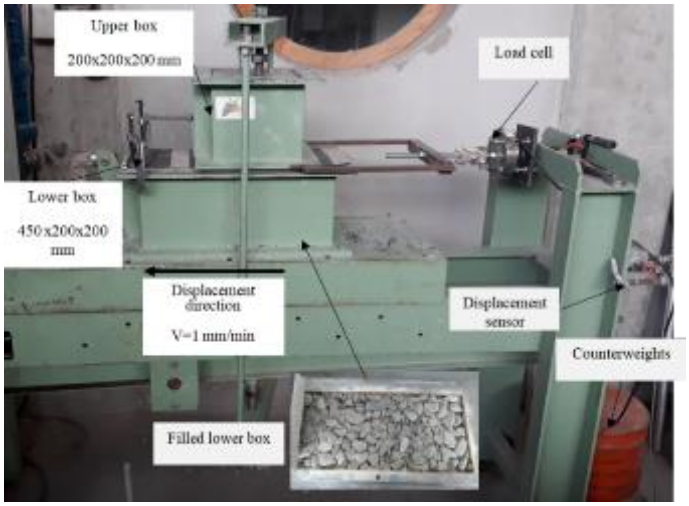

Figure 3-10: Shear test configuration

Three different normal stresses were applied during the shearing process: 66 kPa, 120 kPa, and 200 kPa. The upper box remained fixed while the lower box moved at a velocity of 1 mm/min. The aggregates were placed in six layers within the box and compacted using the Proctor hammer with a water content of 4% (equivalent to 2 drops per position). This compaction protocol, established by Khoueiry (2020), aimed to achieve a consistent soil density of approximately 17 kN/m^3 for each test. Figure 3-11 shows the shear stress versus the horizontal deformation. Analysis of the results led to two possible options: a purely frictional soil with a friction angle of 41°, or a soil with a friction angle of 37° and a cohesion of 20 kPa (Figure 3-12b). Considering the presence of fine particles and water, the second option appears to be more representative of the soil characteristics. However, both sets of parameters were utilized in characterizing the base course layer in the numerical simulations to determine which option best simulates its behavior.

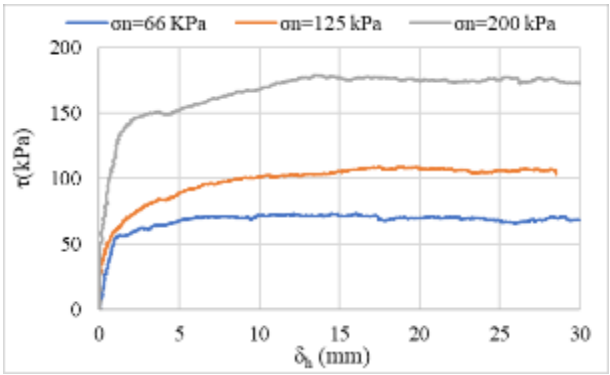

Figure 3-11: Shear stress versus horizontal deformation at different normal stresses

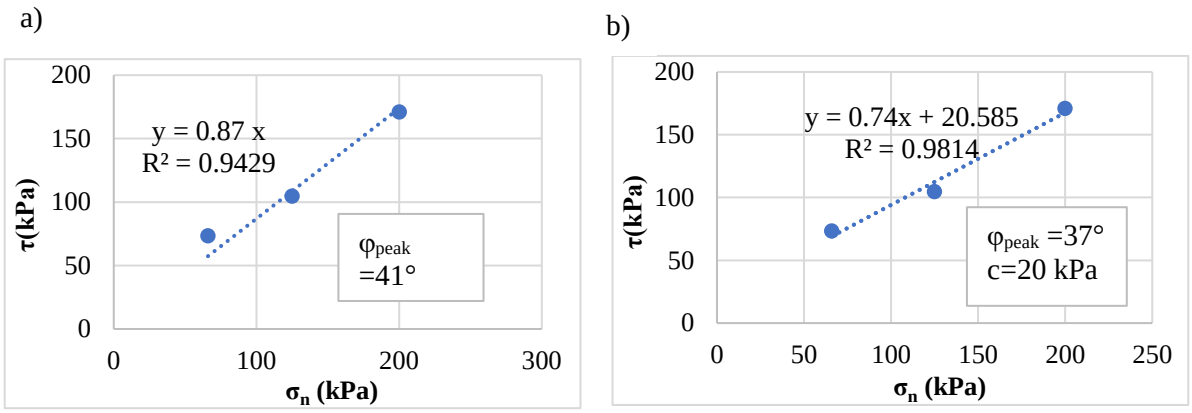

Figure 3-12: Maximum shear versus the normal stress of the aggregate-aggregate interface

3.3.3. Geotextile

The two tested GTX s (GTX1 and GTX2) are woven made of an assembling of polypropylene filaments with high modulus.

The mechanical properties of the two GTX s obtained during tensile tests performed according to NF EN ISO 10319 are shown in Table 3-2. At small axial strain (2% and 3%), the GTX1 and the GTX2 have approximatively the same stiffnesses in the transverse direction, but the GTX1 has almost the triple stiffness of the GTX2 in the longitudinal direction. The vertical loading on the plate mobilizes equally the GSY in both directions, so an average stiffness equals the mean of the stiffnesses in the two directions is assumed is characterize each GTX. In this case, the GTX1 is stiffer than the GTX2 at small axial strain (2% and 3%) if the applied load is vertical. On the contrary, the circulation load mobilizes the GSY in the transverse direction more than the longitudinal one.

In addition to the reinforcement, the two GTX s provide separation and filtration. The water permeability and the filtration aperture of each GTX were tested according to the NF EN ISO 11058 and NF EN ISO 12956 respectively. These values are presented in Table 3-2.

Table 3-2: Relevant properties of the two tested GTXs

			GTX1		GTX2
Tensile test NF EN ISO 10319	longitudinal direction				
	$T_{2\%}$	kN/m	23.9		8.9
	$T_{3\%}$	kN/m	37.3		13.0
	$T_{5\%}$	kN/m	61.2		23.7
	transverse direction				
	$T_{2\%}$	kN/m	26.3		27.8
	$T_{3\%}$	kN/m	37.7		43.8
	$T_{5\%}$	kN/m	56.3		72.5
Water permeability NF EN ISO 11058		mm/s	11.7		33.1
Filtration aperture NF EN ISO 12956		µm	284		241

3.3.4. GTX-Soil interface

The reinforcement GSY serves various functions, such as separation, stabilization, and reinforcement, in unpaved road sections. To fulfil its intended role, the GSY relies on load transfer between the soil and the GSY, primarily through shear stress.

The interaction between soil and GSYs can be complex and influenced by factors such as the structural, geometrical, and mechanical characteristics of the GSY, as well as soil properties, boundary conditions, and loading conditions. When a GTX is used as the GSY, friction is typically the primary mechanism that develops at the soil- GSY interface. An overall resistance for the entire reinforcement surface can be assessed by approximating the interaction using an equivalent frictional shear stress.

A series of direct shear tests (NF EN ISO 12957-1) and pull-out tests (NF EN ISO 13738) were conducted to assess the interface properties between the GTX (GTX1 / GTX2) and the underlying soft subgrade layer, as well as the overlying base course layer in the unpaved road structure. Specifically, the same subgrade soil as the one where the GTX was placed in the tested section of the unpaved road was utilized in these tests. Similarly, the base course layer used in the tests corresponded to the layer beneath which the GTX was positioned in the unpaved road section. The four interfaces tested were: a) GTX1-Base course interface, b) GTX2-Base course interface, c) GTX1-subgrade soil interface, and d) GTX2-subgrade soil interface.

The direct shear test and the pull-out test each has their distinct mechanisms. In the direct shear test, the soil sample placed on the GTX was sheared along the interface within a direct shear box. Conversely, in the pull-out test, the GTX (GTX1 / GTX2) confined between the subgrade layer and the base course layer was extracted into an extraction box.

The resulting friction and cohesion coefficients obtained from these tests were employed in numerical simulations to describe the interaction between GTX1/GTX2 and both the overlying base course layer and the underlying soft subgrade soil.

3.3.4.1. Direct shear tests

The same large shear box depicted in Figure 3-13, which was utilized for characterizing the base course, was also employed to evaluate both the GTX-Base course interface and the GTX-Soft soil interface. The direct shear test involved moving a lower soil-filled box with a GTX anchored on top while the upper soil-filled box, where the interface with the GTX was to be tested, remained fixed. This setup allowed for determining the interaction coefficients between the soil in the upper box and the GTX. When testing the GTX-Base course interface, the base course was placed in the upper box while the GTX was anchored on top of the lower box containing the subgrade. Conversely, for testing the GTX-Soft soil interface, the soft soil was placed in the upper box while the GTX was anchored on top of the lower box containing the base course. According to NF EN ISO 12957-1, three tests were conducted to determine the interaction coefficients (friction and cohesion) at each interface. The lower box was moved at a speed of approximately 1 mm/min.

The shear test configuration specific to studying the GTX-Base course interface is depicted in Figure 3-13 (a). The lower box contained a soft soil with a water content of 13.5%. The soil was placed in three layers and compacted seven times using the Proctor hammer to achieve a consistent soil density of around 17.85 kN/m³, similar to the density determined with the Proctor test (3.3.1.1). The GTX was anchored on top of the lower box, while the aggregate, with a water content of 4% and a density of around 17 kN/m³, was placed in the upper box. The gravel was compacted in three layers, with each layer being compacted twice in each position. A gap of 0.5 mm was maintained between the upper and lower boxes to prevent soil loss during the test while avoiding excessive friction between the two boxes, as per EN ISO 12957-1. To

examine the GTX-subgrade soil interface, as shown in Figure 3-13 (b), the aggregate was placed in the lower box with the GTX anchored on top, while the soft soil was placed in the upper box. The same water content and compaction protocols used for the GTX-Base interfaces were applied to both layers. Three normal stresses of 59 kPa, 108 kPa, and 158 kPa were applied for the shearing tests.

Figure 3-14 illustrates the shear stress versus horizontal deformation for the two interfaces, GTX1-Base course and GTX2-Base course. These graphs indicate that the maximum shear stresses were reached relatively quickly, indicating a low mobilization coefficient for friction. Furthermore, the shear stress evolution at the two interfaces is nearly identical under normal stresses of 59 kPa and 108 kPa, but the GTX1-Base course interface exhibited higher shear stress values than the GTX2-Base course interface under a normal stress of 158 kPa. Figure 3-15 presents the intrinsic curves of the GTX1-Base course and the GTX2-Base course interfaces, showing a friction angle of 38.1° for the GTX1-Base course interface, which is greater than the angle of 36.3° for the base course-GTX2 interface. Both interfaces exhibited no cohesion.

Figure 3-16 displays the shear stress versus horizontal displacement for the GTX1-Soft soil and GTX2-Soft soil interfaces. The shear stress evolution at the two interfaces was almost similar across all three normal stresses. Figure 3-17 presents the intrinsic curves of the GTX1-Soft soil and GTX2-Soft soil interfaces, revealing a friction angle of 32° for both interfaces, lower than the friction angle observed between GTX1 or GTX2 and the base course layer. Both interfaces exhibited no cohesion.

In summary, the friction angle at the interface between GTX1 or GTX2 and the soft soil was lower than that observed between GTX1 or GTX2 and the base course interface. While GTX1 and GTX2 exhibited the same friction angles with the soft soil, GTX1 demonstrated a friction angle approximately 1.8° higher than GTX2 at the base course interface.

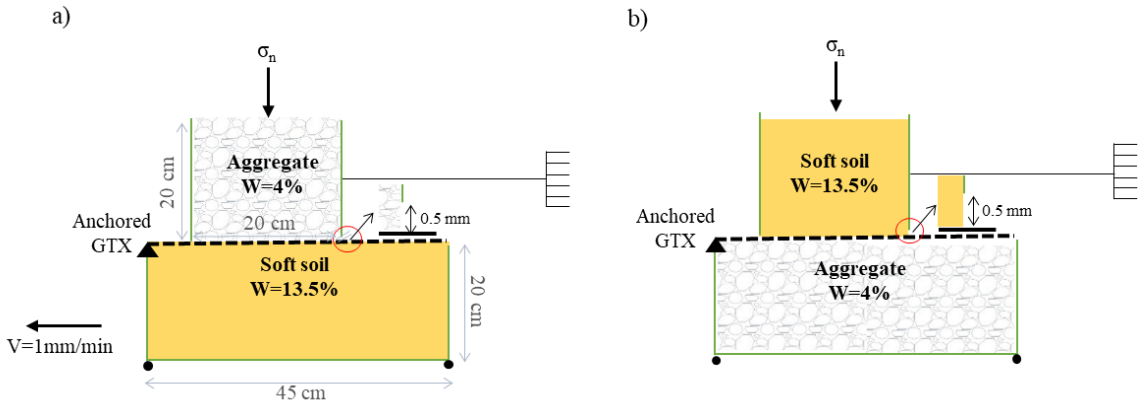

Figure 3-13: Shear test configurations for the tested: a) Base course-GTX interface; b) Subgrade-GTX interface.

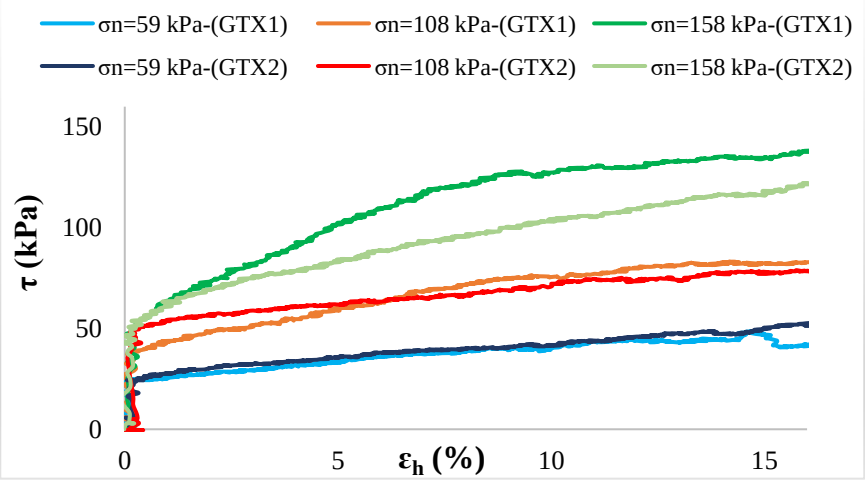

Figure 3-14: Shear stress versus horizontal deformation for the base course- GTXs interfaces at different normal stresses

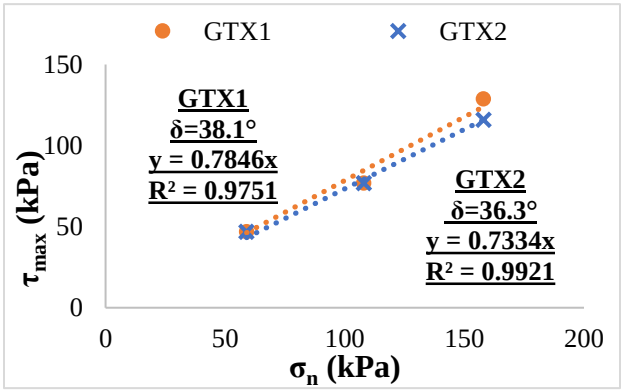

Figure 3-15: Maximum shear versus the normal stress of the base course- GTXs interfaces

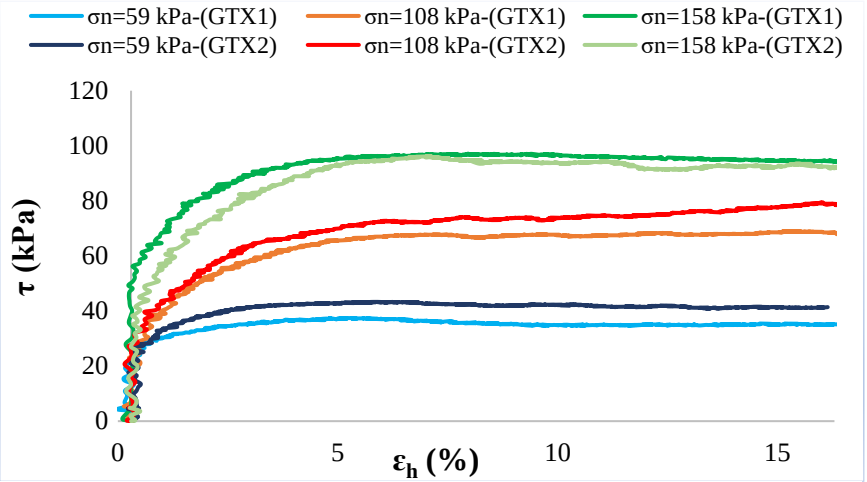

Figure 3-16: Shear stress versus horizontal deformation for the subgrade- GTXs interfaces at different normal stresses

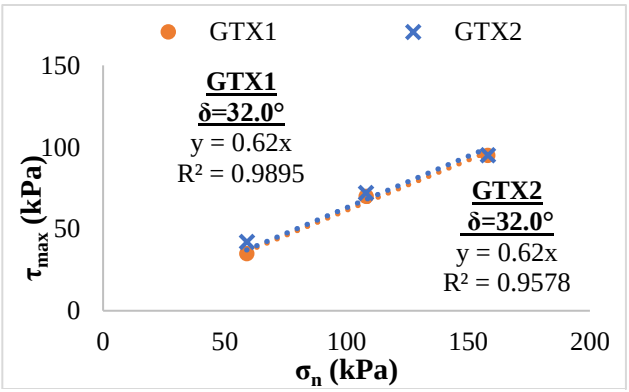

Figure 3-17: Maximum shear versus the normal stress of the subgrade- GTXs interfaces

3.3.4.2. Pullout tests

In the experimental tank measuring 2.0 m x 1.1 m x 1.1 m, a 38 cm layer of sand was installed (Figure 3-18). To ensure a flat surface and prevent mixing between the sand and the upper layer, a geomembrane was placed on top of the sand. Above the geomembrane, the soft soil with a water content of 13.5% was added. The soft soil layer, with a thickness of 10 cm, was lightly compacted using a manual compactor. The GTX measuring 1.50 m x 0.50 m was placed on top of the soft soil layer, with one edge firmly inserted into anchor clamps for the purpose of pulling it during the test. The upper box, measuring 50 cm x 50 cm x 30 cm, was placed above the GTX and attached to the back wall of the tank, enabling the study of the double interface: GTX-upper aggregate layer and GTX-lower soft soil. This box was filled with aggregate having a water content of 4% and a density of approximately 17 kN/m³. The compaction process involved

placing the aggregate in two layers and compacting each layer twice. Three tests were conducted following the NF EN ISO 13738 standard. For the first test, the aggregate layer had a thickness of 15 cm (equivalent to a vertical stress of 2.78 kPa), while for the second and third tests, the thickness was increased to 30 cm (equivalent to a stress of 5.18 kPa). To increase the vertical stress to 9.18 kPa in the third test, four sandbags weighing 25 kg each were placed on top of the upper box. During the test, the GTX was pulled out by the anchor clamp to which it was anchored at a rate of 1 mm/min. The displacement and pullout force at the head of the GTX were measured.

The pullout curves of GTX1 and GTX2 from both the underlying soft soil layer and the overlying base course layer are illustrated in Figure 3-18. The shear stress τ was calculated by dividing the pullout force by the interface surface area (0.5 m x 0.5 m). It is important to note that the only displacement measured during the extraction test is the horizontal displacement of the anchor clamps. Consequently, the initial portion of the extraction curves (Figure 3-18) represents the tensioning of GTX1/GTX2 outside its confinement zone. The relative displacement between GTX1/GTX2 and the soil was not measured in the performed tests. Comparison of the evolution of shear stress with displacement showed nearly identical behavior under each vertical stress for GTX1 and GTX2 (Figure 3-19). Noting that there were slight differences in the maximum shear stresses and GTX tensioning.

$\tau_{s\text{-}max}$ and $\tau_{b\text{-}max}$ represent the maximum shear stresses at the GTX-Soft soil interface and at the GTX-Base course interface, respectively, and are calculated using equation (*Eq 3-1*) derived from the results of the direct shear tests conducted in section (3.3.2.2.1). $\tau_{s\text{-}max}$ and $\tau_{b\text{-}max}$ calculated values are shown in Table 3-3.

$$\tau_{s\text{-}max}\ (\tau_{b\text{-}max}) = \sigma_n \tan(\delta) \qquad \textit{Eq 3-1}$$

Here, δ represents the friction angles: 38.1° at the GTX1-Base course interface, 36.3° at the GTX2-Base course interface, and 36.3° at the GTX1/GTX2-Subgrade interface. The sum of $\tau_{s\text{-}max}$ and $\tau_{b\text{-}max}$ represents the maximum shear stresses at both the GTX-Base course interface and the GTX-Subgrade interface. These values are then compared to the maximum shear stress τ_{max} obtained in the pullout test under the three normal stresses, as shown in Table 3-3. The calculated percentage difference in maximum shear stresses $\%\,\Delta\,\tau_{max}$ (presented in *Eq 3-2*) ranges from 3% to 16%.

$$\%\,\Delta\,\tau_{max} = 100\,\frac{\left(\tau_{s\_max} + \tau_{b-max}\right) - \tau_{max}}{\tau_{max}} \qquad \textit{Eq 3-2}$$

Therefore, the pullout test results were validated the friction angle values obtained from the direct shear tests.

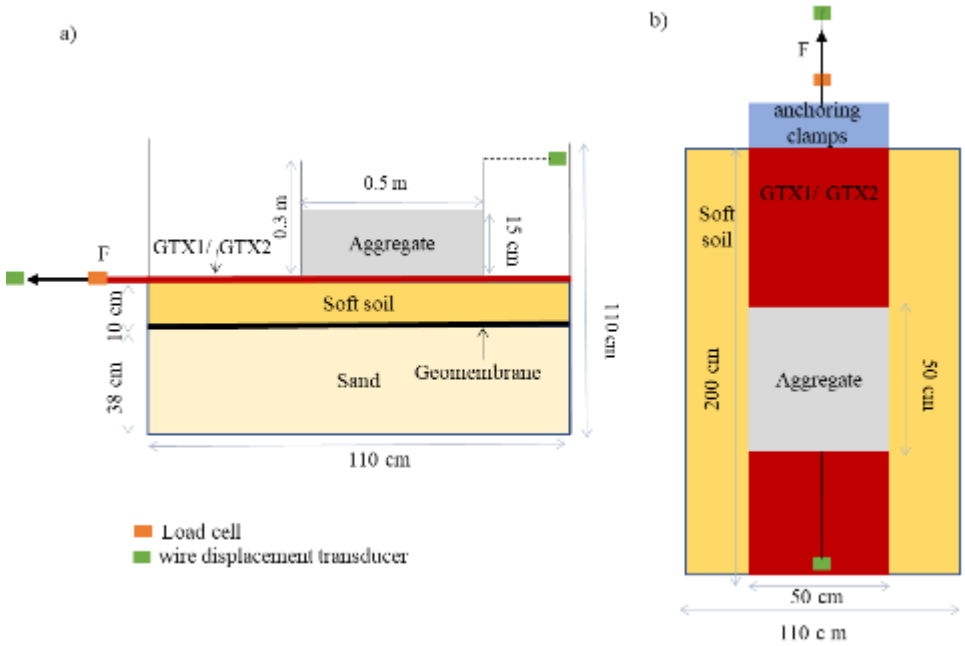

Figure 3-18: Pull-out test set up a) front view; b) Top view of the pull-out test

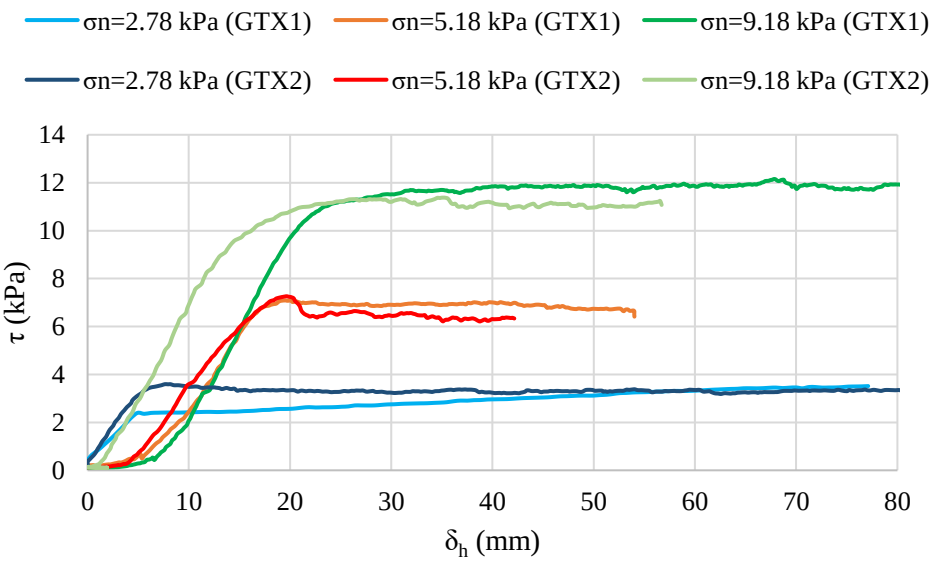

Figure 3-19: The shear stress versus the head horizontal displacement at the GTX1/ GTX2-subgrade interface and the GTX1/ GTX2-aggregate interface

Table 3-3: Summary of results

		Direct shear					Pull-out	Direct shear Vs Pull-out
Interface		GTX-Subgrade		GTX-Base course		GTX-Subgrade & GTX-Base course	GTX-Subgrade & GTX-Base course	GTX-Subgrade & GTX-Base course
	σ_n (kPa)	δ(°)	$T_{s\text{-}max}$ (kPa)	δ (°)	$\tau_{b\text{-}max}$ (kPa)	$\tau_{smax} + \tau_{bmax}$ (kPa)	τ_{max} (kPa)	Percentage difference in maximum shear stresses $\Delta\,\tau_{max}$ (%)
GTX1	2.78	32	1.74	38.1	2.18	3.92	3.39	16
	5.18		3.24		4.06	7.30	7.00	4
	9.18		5.74		7.20	12.94	12.0	8
GTX2	2.78	32	1.74	36	2.04	3.78	3.59	5
	5.18		3.24		3.81	7.05	7.26	3
	9.18		5.74		6.74	12.48	11.27	11

3.4 Implementation of unpaved road sections

3.4.1 Implementation steps

A grout mixer (EIRICH R08), showed in Figure 3-20(a), was used for mixing the subgrade soil. To install a 600 mm of subgrade layer thickness in the part of the experimental box dedicated for the plate cyclic load test (2 m x 1.8 m x 0.6 m), 3.85 Tonnes of soil were mixed in 65 kg per batches, which is the maximum capacity of the mixer. While 9.61 Tonnes were prepared to fill 600 mm of the whole experimental box dedicated to both the plate cyclic load test and the traffic load test successively. The big bag containing the subgrade was transported by an overhead crane, positioned at the minimum possible height above the experimental box, then opened from below to empty it to keep emptying the bag with less gravity force. Thereafter, the soil was evenly spread over the surface of the box area using a manual shovel. The installation was carried out in 3 sub-layers (Figure 3-21), each one was manually compacted using a light manual compaction in order to obtain a homogeneous subgrade layer with a CBR of approximately 1% in both surface and depth (Figure 2-22(a)).

At the subgrade surface, a reinforcement GTX was installed for the reinforced test, while a simple separation GTX with negligible stiffness was installed for the unreinforced test (Figure 3-21).

To install a 300 mm (500 mm) of base course layer thickness over the GTX in the part of the experimental box dedicated for the plate cyclic load test (2 m x 1.8 m x 0.6 m), 1.84 Tonnes (3.06 Tonnes) of aggregate with 4 % of water content was used. While the filling of 300 mm (500 mm) base course layer thickness over the GTX in the whole experimental box surface required 4.60 Tonnes (7.65 Tonnes). The process of emptying and spreading the gravel over the GTX was like the subgrade emptying and spreading process. The installation was carried out in 3 sub-layers (Figure 3-21), each one was compacted using a plate compactor (DQ-0139), illustrated in Figure 3-20(b) by passing it 4 times per sublayer. The compaction process was aimed to obtain a homogeneous layer in depth and over the whole area with an CBR ratio of 20% for the fill material (Figure 2-22 (c)).

Table 3-4 presumes the details of the implementation steps.

Therefore, various quality control tests were performed to control the installed soil properties and homogeneity in depth and over all area of the two layers. The quality control tests performed will be presented in the next section.

a) b)

Figure 3-20:a) The mixer and b) The plate compactor

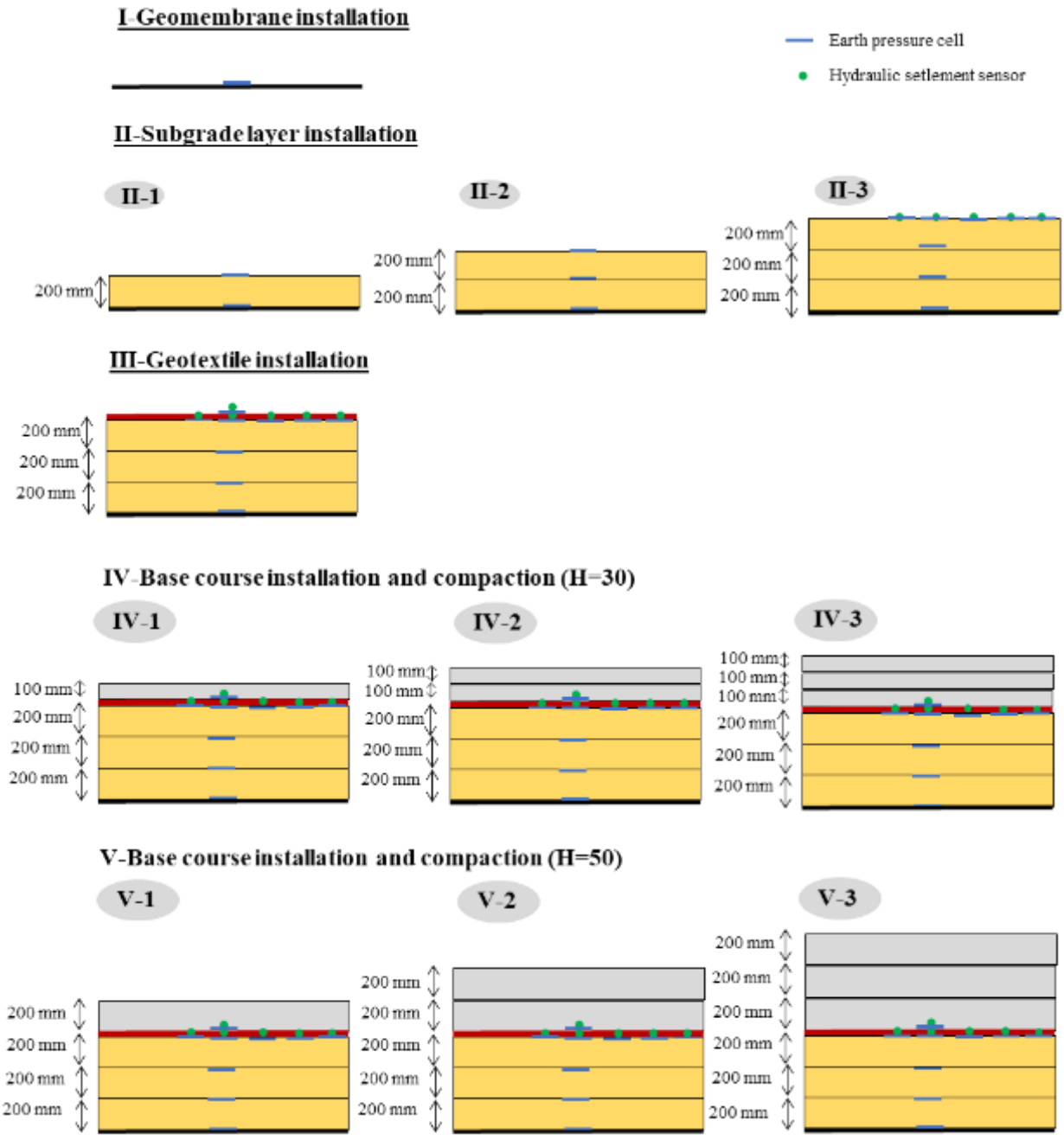

Figure 3-21: Illustrations of the implementation steps

a)

b)

c)

Figure 3-22: a) Subgrade layer implementation; b) Base course layer installation, and c) a section of the platform during the dismantling

Table 3-4: Descriptions of the implementation steps

	Stage number	Implementation description	Compaction description
Geomembrane	I	A geomembrane was installed at the bottom of the experimental box, instrumented with earth pressure to measure the stress at the base of the centre of the foundation layer which is the point below the centre of the plate load.	-
Subgrade layer	II-1	1280 kg of subgrade soil was installed on the geomembrane to fill the first 200 mm thick sub-layer in the case of the plate load platform preparation. While 3200 kg of soil was used to install the first sub-layer of 200 mm thick in the case of the preparations of traffic load and plate load platform.	Lightly compaction (4 drops per position)
	II-2	A soil pressure sensor was placed in the centre of the surface. The second sub-layer was installed by adding the same amount of soil added in the first sub-layer.	Lightly compaction (4 drops per position)
	II-3	A soil pressure sensor was placed in the centre of the surface. The third sub-layer was installed by adding the same amount of soil added in the first or second sub-layer. In addition, 4-5 soil pressure sensors and 4-5 settlement sensors were placed on the surface.	Lightly compaction (4 drops per position)
GTX	III	A reinforcement or separation GTX was placed over the subgrade layer. 1 earth pressure sensor and 1 settlement sensor were placed at the GTX centre.	-
Base course (H=300 mm)	IV-1	620 kg of gravel was installed on the GTX to fill the first 100 mm thick subgrade in the case of the plate load platform preparation. While 1530 kg of gravel was used to install the first 100 mm thick subgrade in the case of the traffic load and plate load platform preparations. An amount of water equivalent to 4% of the weight of the gravel was sprinkled on the base course sub-layer.	Four compactor passes for each sub-layer using the plate compactor (DQ-0139)
	IV-2	The second sub-layer was installed by adding the same amount of soil added in the first sub-layer.	
	IV-3	The second sub-layer was installed by adding the same amount of soil added in the first sub-layer.	
Base course (H=500 mm)	V-1	1230 kg of gravel was installed on the GTX to fill the first 200 mm thick subgrade in the case of the plate load platform preparation. While 3060 kg of gravel was used to install the first 200 mm thick subgrade in the case of the traffic load and plate load platform preparations. An amount of water equivalent to 4% of the weight of the gravel was sprinkled on the base course sub-layer.	Four compactor passes for each sub-layer using the plate compactor (DQ-0139)
	V-2	The second sub-layer was installed by adding the same amount of soil added in the first sub-layer.	
	V-3	620 kg of gravel was installed on the GTX to fill the third 100 mm thick subgrade in the case of the plate load platform preparation. While 1530 kg of gravel was used to install the first 100 mm thick subgrade in the case of the traffic load and plate load platform preparations. An amount of water equivalent to 4% of the weight of the gravel was sprinkled on the base course sub-layer.	

3.5 Quality control tests

This section presents a comprehensive set of tests aimed at ensuring the repeatability of constructing compacted granular platforms over soft subgrade soil. The primary objective is to compare the results of plate load tests and traffic load tests conducted on various unpaved structures, requiring consistent soil properties across all tests. Therefore, a series of quality control tests were conducted to meticulously monitor and verify the properties of each constructed soil layer (Figure 3-23). These quality control tests, outlined by Khoueiry (2020), encompassed a water content profile analysis, vane shear test, static penetrometer test, dynamic penetrometer test, and Clegg impact soil test.

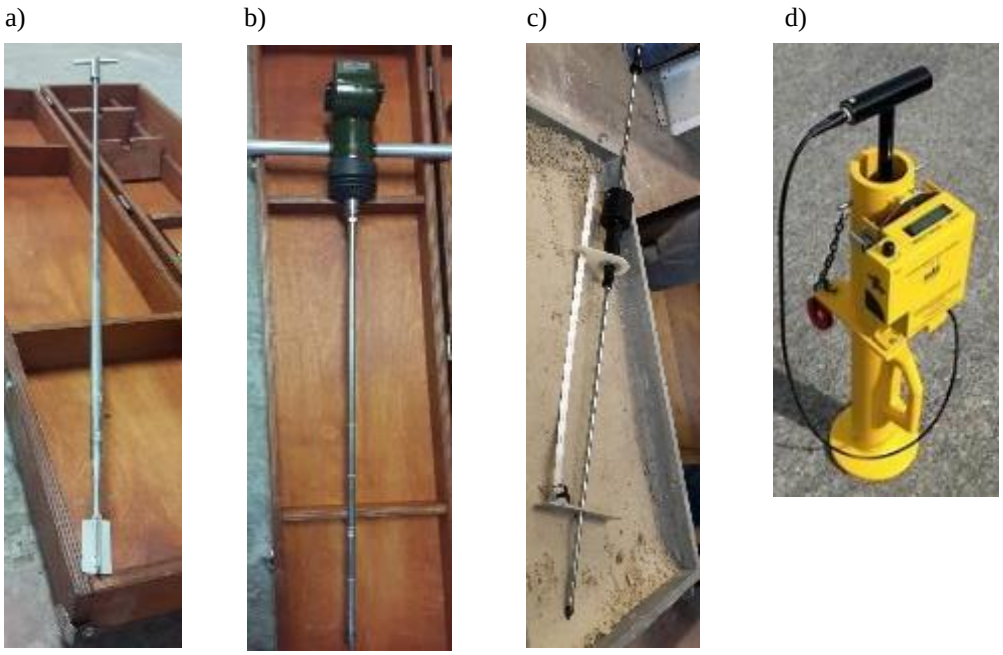

Figure 3-23:Quality control test instruments: a) Vane shear instrument, b) Cone penetration instrument, c) Dynamic penetration instrument and d) Clegg impact soil tester

3.5.1 Water content profile

Several samples were taken along the depth of the subgrade before and after each test to measure their water content. Comparison of the pre- and post-test water content profiles can show whether the water content is uniform across the depth and surface of the subgrade. If it is, so there is no migration of water from the upper to the lower layers of the subgrade layer. In addition, the comparison between the water content profiles of the different subgrade layers can show whether the water content remains consistent throughout the tested subgrade layers, thus ensuring credibility in comparing between the results of different tests.

3.5.2 Shear vane tests

The test involves driving the rod-mounted vanes several depths into the subgrade layer and then rotating them. The gauge at the top of the rod measures the torque required to cause the subgrade to rupture and provides a conversion to shear strength. In fact, the shear strength obtained is the undrained cohesion (S_u) in the case of a fully saturated clay. Since the tested soil is an unsaturated mixture of sand and clay, the obtained shear strength does not correspond to a characteristic value of the soil, so it is used for comparison purposes.
Two values are obtained for the same vanes position:

- ✓ The maximum shear strength, which is the value determined at the first applied turning moment: τ_u
- ✓ The residual shear strength, which is the value determined after 25 rotations: τ_r

The soil sensitivity is the ratio of the τ_u and τ_r values. The obtained values at different subgrade layer depths are compared to check the soil homogeneity throughout the depth. The profiles along the depth of the tested subgrade layers are compared to verify that all soil sensibility profiles have comparable orders of magnitude.

3.5.3 Static cone penetration test

The static penetrometer test (CPT) is used to evaluate the penetration resistance of the soil. A lightweight instrument was used to quickly measure the penetration resistance throughout the layer depth. Penetration resistance is appeared in a dial in terms of the in-situ CBR (California Bearing Ratio) value and the Cone Index (CI) value. In the dial, the CBR range value is between 0 and 15% and the CI value is between 0 and 300 with 60 divisions on a linear scale.

At first, the instrument is put vertically on the subgrade surface. A vertical force is applied to the handles of the device until a steady, downward movement occurs in the subgrade. During the penetration process that occurred at a constant speed (1.5 -2.5 cm/s), the cone is driven along the depth of the tested zone and the dial indicates the corresponding CI and CBR values throughout the depth. Measurements are taken over the entire depth with an interval of 75 mm.

The CBR of the subgrade layer is measured before the granular layer installation and after its removal, since compaction of the granular layer increases the CBR of the subgrade layer.

3.5.4 Dynamic cone penetration test

Dynamic Cone Penetrometer (DCP) tests were carried-out in both the base course and the subgrade layers to determine their strength.

The used DCP (A 2465) is a lightweight instrument customized for the rapid measurement of the material's in-situ resistance to penetration. The test is performed by driving the metal cone into the base course and the subgrade layers by repeated striking them with an 8 kg (17.6 lb) weight dropped from a height of 575 mm (2.26 feet). The instrument must be held vertically during the test. The penetration of the cone is recorded after each blow and can be correlated to California Bearing Ratios (CBR) using Kleyn and Van Heerden formula (*Eq 3-3*) given by the manufacturer technical file.

$$\text{Log CBR}=2.632-1.28\ log_{10}(DCPI) \qquad \textit{(Eq 3-3)}$$

Where DCPI = dynamic cone penetration index (mm/blow), which is calculated based on the penetration per each blow.

3.5.5 Clegg impact soil test

The 4.5 kg CIST/883 Clegg Impact Soil Tester was used to measure and control the base course strength and its consolidation level.

The tester consists of a 4.5 kg compaction hammer operating within a vertical guide tube. The test consists of setting the guide tube vertically and steadily on the base course surface layer. The hammer is raised until a determine height indicated by a white ring. Then, the Hammer falls through the tube when it is released and strikes the surface under test, decelerating at a rate determined by the stiffness of the material within the region of impact. The readout registers the deceleration in units of Impact Value (IV). The IV is an indication of soil strength. This procedure is repeated for a further 4 drops to give a total of 5 readings at the test position. The first two or three drops effectively take up the surface irregularities and loose material immediately beneath the hammer. The readings thereafter should get progressively higher. The 3rd, 4th and 5th readings should level out and register the stiffness of the compacted layer under test. The 4th reading is the critical reading; it represents the degree of compaction being measured and can correlated to California Bearing Ratios by an empirical equation (*Eq. 3-4*).

$$\text{CBR} = [(0.24 \times IV4) + 1]^2 \qquad \textit{(Eq 3-4)}$$

Where IV4 is the 4th impact value.

3.6 Instrumentation

This section aims to provide an overview of the instrumentation system and its role in monitoring changes occurring in the unpaved road layers under vertical or traffic load, or both. Specifically, certain areas within the base course layer, subgrade layer, and GTX were equipped with instrumentation. The instrumentation system primarily comprised hydraulic settlement sensors (S) to track vertical soil displacement, earth pressure cells (EPC) to measure vertical stress, and laser displacement sensors (L) to monitor vertical displacement of the base course surface. Additionally, a load cell (F) with an 8-ton capacity and a displacement transducer (LVDT) were attached to the hydraulic jack to measure the applied load and its displacement during the plate load test.

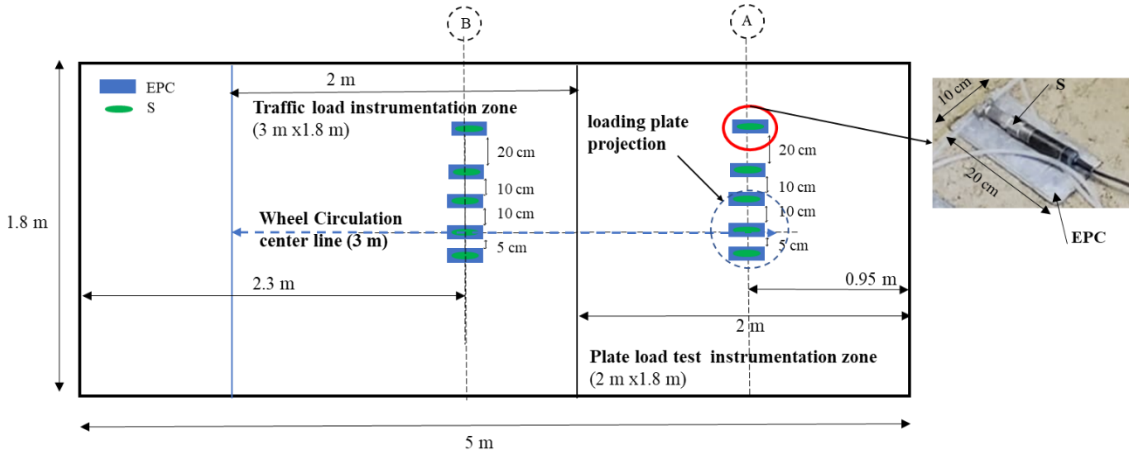

Figure 3-24: The instrumentation system at the subgrade surface used for both the plate load test zone and the traffic load test zone, view from above with the details of the EPC

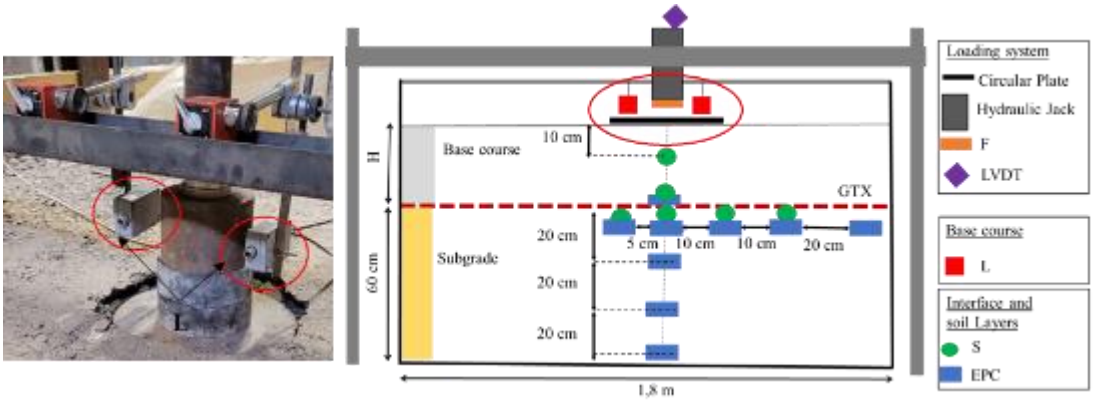

Figure 3-25: The instrumentation system used for the plate load test zone, section A with the configuration the displacement of laser sensor (L).

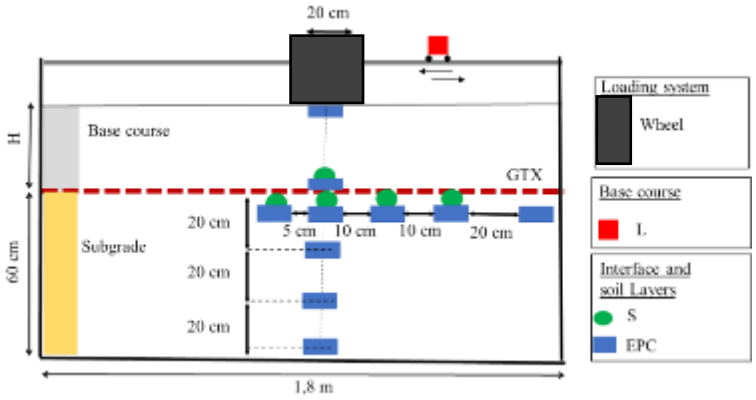

Figure 3-26: The instrumentation system used for the traffic load test zone, section B

3.6.1 Hydraulic settlement sensor (S)

The hydraulic sensor technology is based on measuring displacement through variations in hydraulic pressure. In this system, a water tank must maintain the sensors in a saturated state under constant water pressure. The transmitter calculates the pressure difference between its position and the tank's position, resulting in pressure changes when the sensor's position shifts. Each transmitter is connected to the data logger via an electrical cable. It is important to note that using these sensors for settlement measurements during cycles is not feasible due to perturbations caused by vibrations. More details about the hydraulic sensor characteristics are presented in Table 3-5.

The distribution of the hydraulic sensors in the plate load instrumentation zone was shown in Figure 3-25 and Figure 3-24. To gauge the GTX 's vertical displacement, one hydraulic settlement sensor (S) was strategically positioned directly on the GTX beneath the loading plate center. Additional sensors were placed on the top layer of the subgrade, both beneath the center of the loading plate and at various distances from it, to assess the settlement of the subgrade profile during the testing cycles. Furthermore, one sensor was positioned at a specific depth below the base course, one-third from the top, directly beneath the loading plate, in order to measure the base course displacement at this position.

The distribution of the hydraulic sensors in the traffic load instrumentation zone was shown in Figure 3-26 and Figure 3-24. One hydraulic settlement sensor (S) was strategically positioned directly on the GTX beneath the wheel centerline to gauge the GTX's vertical displacement. Additional sensors were placed on the top layer of the subgrade, both beneath the wheel center line and at various distances from it, to assess the settlement of the subgrade profile after the wheel passes.

3.6.2 Earth pressure cell (EPC)

In this section, the usage and placement of Earth Pressure Cells (EPC) for measuring vertical stress distribution are discussed. Each EPC was connected to a continuous acquisition instrument through an electrical cable, necessitating a continuous power supply for pressure measurements during testing cycles. Table 3-5 provides further details regarding the characteristics of the EPCs.

For the plate load instrumentation zone (section 3.2.2), the distribution of EPC sensors is illustrated in Figure 3-24 and Figure 3-25. A strategically positioned EPC beneath the center of the loading plate, directly on the GTX, measured the vertical stress. Additional EPCs were placed on the top of the subgrade layer, both beneath the center of the loading plate and at various distances from it, to evaluate stress transfer to the subgrade surface. Furthermore, three EPCs were strategically positioned at different depths within the subgrade, directly beneath the loading plate, to measure stress levels within the subgrade.

Regarding the traffic load instrumentation zone (section 3.2.3), Figure 3-24 Figure 3-7 demonstrate the distribution of EPC sensors. One EPC was strategically positioned directly on the base course surface beneath the wheel centerline to measure applied vertical stress. Another EPC was placed directly on the GTX beneath the wheel centerline to assess vertical stress on the GTX. Additional sensors were positioned on the top layer of the subgrade, both beneath the wheel centerline and at various distances from it, to examine stress transfer to the subgrade layer. Additionally, three EPCs were strategically placed at different depths within the subgrade, directly beneath the wheel centerline, to measure stress levels within the subgrade.

3.6.3 Displacement laser sensor (L)

Within the plate load instrumentation zone, two laser displacement sensors (L) were affixed to a rectangular steel bar positioned above the circular plate. These sensors accurately measured the displacement of the plate throughout the test. Additionally, one of the laser displacement sensors (L) was mounted on a rail,

allowing it to move and measure the rut profile in the transverse direction after a specified number of wheel passages.

Each laser displacement sensor (L) was connected to a 24V external generator via an electrical cable to provide power. The tension output signal from the sensors was then connected to the acquisition center for data collection. Further information regarding the characteristics of the displacement laser sensors used can be found in Table 3-5.

Table 3-5: Summary of sensor properties used in the experimental test

Sensor	Measurement Range	Sensitivity
Hydraulic Settlement	0-1000 mm 0-2000 mm	± 0.014% of the full scale
Earth pressure cell	0-500 kPa	±0.5% of the full scale
Displacement laser	200-700 mm	± 0.07% of the full scale

3.7 Data recording system

The ST80 logger, shown in Figure 3-27, is a versatile tool utilized in this application for measuring and recording various quantities and values. However, it has a limitation when it comes to continuous measurements at high frequencies. Each input channel of the logger is independently powered and measured for output values.

During the initial three plate load tests, the ST80 logger was used to measure the static settlement values obtained from hydraulic settlement sensors (S) and the static vertical pressures from earth pressure cells (EPC). To accommodate the acquisition frequency, these measurements were initially recorded with programmed interruptions during the unloading and loading phases. However, these interruptions, especially during the first loading phase, led to additional settlement that did not accurately represent cyclic loading. To overcome this issue, starting from the 4th test, stress sensors were installed on a separate data acquisition unit called Scaime (Figure 3-27), with a maximum acquisition frequency of 960 Hz. This enabled continuous measurement of stress increase during the loading phase without interrupting the cycle. The advantage of this data logger is its ability to power all channels simultaneously and record continuous output values. It can be used with various types of sensors, with the entry modulus adjusted accordingly.

Only the measurements during unloading phases were performed statically to ensure the stability of settlement measurements. During the first three cycles, static measurements were taken during both loading and unloading phases at cycle numbers: 1, 200, 300, 400, 500, 1,000, 2,000, 3,000, 4,000, 5,000, 6,000, 7,000, 8,000, 9,000, and 10,000. From the 4th test onwards, static measurements were exclusively taken during the unloading phases for the following cycle numbers: 1, 5, 10, 50, 100, 200, 300, 500, 1,000, 2,000, 3,000, 4,000, 5,000, 6,000, 7,000, 8,000, 9,000, and 10,000. The EPCs and the displacement laser sensors were connected to the Scaime during the whole time for continuous measurement.

Figure 3-27:Data Taker setup, and Scaime setup with the external generator of the laser sensors.

3.8 Conclusion

This chapter provides a detailed overview of the materials used in the platform and their characterization. Furthermore, the experimental setup, including the devices used, platform construction, materials preparation, and quality control tests is thoroughly discussed. To ensure the achievement of reliable and comparable results, special attention was dedicated to the preparation and installation of the unpaved structure layers and the weak soil layer, as well as the execution of quality control tests. However, replicating the precise preparation and installation of substantial quantities of soil layers, particularly when dealing with soft soil, posed challenges. Furthermore, attaining identical compaction of the granular platform as observed on-site presented difficulties. In fact, the use of a heavy compactor similar to the one employed on-site was limited, as it would deplete the entire compressibility of the soft soil. Consequently, the decision was made to utilize a less effective compaction machine for compacting the granular platform. Despite these challenges, meticulous care was taken to recreate the identical initial state prior to each test and to closely monitor and control this initial state through a series of rigorous quality control tests. The presentation and analysis of the quality control tests results are provided in Chapter 4.

Moreover, the instrumentation and data acquisition systems employed to collect a comprehensive set of measurements and data are also described in this chapter.

4. Chapter 4. Experimental test results

4.1 Introduction

In this chapter, we present and analyze the results of the seven plate load tests and the three traffic load tests. The plate load tests were conducted on an unpaved platform placed in a box measuring 2.0 m in length, 1.8 m in width, and 1.1 m in height (Test 1, Test 2, Test 3, and Test 4). In addition, a portion of the unpaved platform placed in a larger box measuring 5 m in length, 1.8 m in width, and 1.1 m in height was tested also under plate load (Test 5, Test 6, and Test 7). Following the plate load tests, the remaining part of the platforms for Test 5, Test 6, and Test 7 were subjected to traffic load simulations using the Simulator Accelerator of Traffic (SAT), as developed in the Khoueiry (2020) project.

Seven plate load tests were performed according to the condition detailed in the section 3.2.2. The performed tests involved various parameters, including two GTXs with two different stiffnesses, two base course thicknesses (300 mm and 500 mm). The reinforcement was placed at the interface between the base course and the subgrade in the case of reinforced unpaved roads sections.

Three traffic load tests were performed in a larger box measuring 1.8 m in width, 5 m in length, and 1.1 m in height for the traffic load tests. The load was applied by the SAT detailed in the section 3.2.3. Various platform configurations were tested under these loading conditions, including a reinforced platform with a GTX1 of 300 mm thickness, two platforms with a thickness of 500 mm (one unreinforced and the other reinforced with GTX1).

Furthermore, the results of the quality control tests presented in Chapter 3 are presented and analyzed. These results demonstrate that the constructed unpaved sections are reproducible and exhibit similar soil properties within certain limits. Additionally, this chapter presents the results of the plate load tests and traffic load tests in terms of subgrade surface settlements, base course surface settlements, and the development of vertical stresses at the subgrade surface. A comparison was conducted between platforms subjected to vertical cyclic plate loading to examine the influence of reinforcement. Likewise, a comparison was made between platforms subjected to traffic loading to assess the impact of reinforcement.

4.2 Performed tests

The objective of these tests was to investigate the influence of GTX rigidity and platform thickness. Indeed, the effect of base course thickness was investigated by conducting tests on reinforced and unreinforced platforms with two different base course thicknesses: 300 mm and 500 mm. Additionally, two GTXs, GTX1 and GTX2, with different stiffness were tested. To ensure accurate comparison, it was crucial to verify the reproducibility of the constructed sections and the repeatability of the tests. A series of quality control tests were conducted to confirm the reproducibility of the constructed sections. Additionally, two identical tests were performed on platforms reinforced with GTX1 and GTX2 under cyclic vertical loading.

The measurement of thickness was carried out after the end of the tests by dismantling the extremity of the experimental box. These thickness measurements were also verified during dynamic cone penetrometer tests, where the immediate bearing ratio (CBR) values decreased suddenly during the transition between the base course layer and the subgrade layer. Table 4-1 provides details of the conducted tests, including the measured thickness values. These values indicate that it was not possible to achieve exact control over the base course thickness for each test, as the thickness varied within H ± 6%.

Table 4-1: Performed test details.

Test number	Base course thickness (mm)	Measured base course thickness (mm)	Reinforcement type	Loading type	Status test
Test 1	300	319	GTX1	Vertical	GTX1-reinforced platform
Test 2	300	300	Unreinforced	Vertical	Reference test for medium thickness platform
Test 3	300	320	GTX2	Vertical	GTX2-reinforced platform
Test 4	300	300	GTX2	Vertical	Replicate test 3
Test 5	300	320	GTX1	Vertical + Traffic	Replicate test 1
Test 6	500	501	GTX1	Vertical + Traffic	GTX1-reinforced platform
Test 7	500	520	Unreinforced	Vertical + Traffic	Reference test for thick platform

4.3 Quality control test results

Comprehensive quality control tests were conducted on each prepared platform to assess the properties and conditions of the subgrade and base course layers. These tests aimed to ensure consistency between constructed unpaved roads and to evaluate the overall quality of the layers. Chapter 3 provides a thorough explanation of these tests. In the subsequent sections, a detailed overview of the results obtained from the performed quality control tests are presented.

4.3.1 Water content results

Water content measurements were conducted at various depths for each prepared subgrade. Figure 4-1(a) illustrates the water content profiles both after the subgrade installation in Test 1 (before Test 1) and after the disassembly of Test 1 (after Test 1). The profiles reveal that the water content within the depths ranges from 12.3% to 13.3%. Moreover, they demonstrate that there is no significant variation of water content before and after the test indicating consistent subgrade moisture conditions during the test. Figure 4-1(b) represents the water content points across the depth of the subgrade for each prepared subgrade layer. The plot exhibits a distribution of points ranging from 11.9% to 13.3%, indicating that the soil's water content fluctuates within an acceptable range.

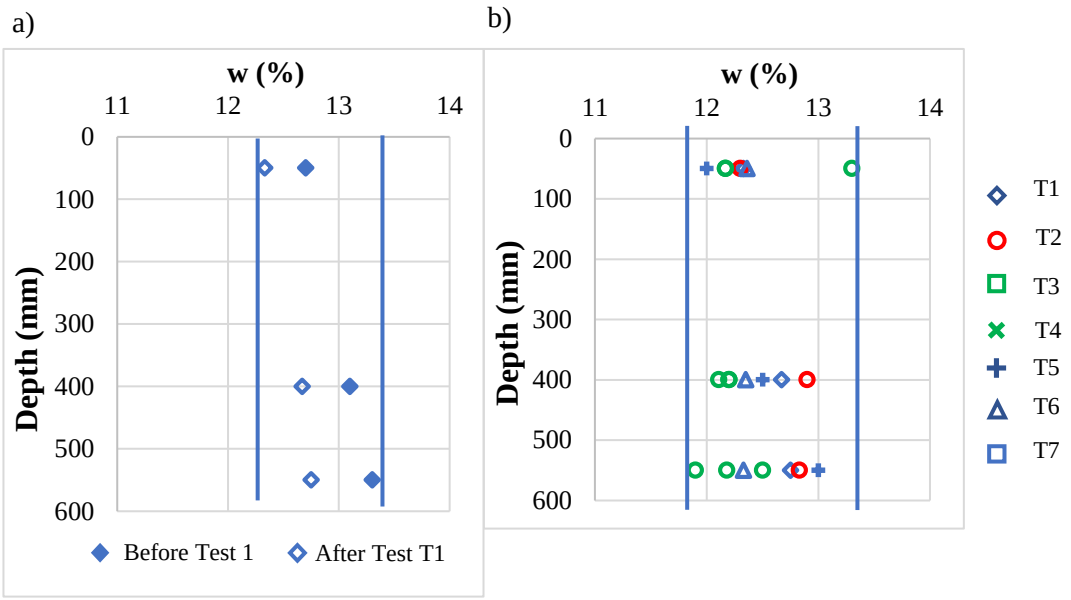

Figure 4-1: a) Water content profile before and after the test T1; b) Water content profiles of all the test.

4.3.2 Vane shear test results

The vane shear test is typically utilized to determine the undrained cohesion (C_u) in saturated soil. However, despite the prepared subgrade being composed of unsaturated soil, the shear vane test was still conducted to establish a basis for comparison. The soil sensitivity index (S_t), obtained by calculating the ratio between τ_u and τ_r, was employed to evaluate the uniformity of the soil across the prepared platforms and within the depth.

In Figure 4-2(a), displays the S_t profile, depicting two different positions for subgrade of the Test 1. The graph demonstrates a good uniformity in soil sensitivity values (S_t) across the subgrade depth and between the positions. Notably, there is a concentration of S_t values ranging from 2.5 to 6.5. This consistency in values between the two positions indicates an acceptable level of homogeneity within the same subgrade layer, extending throughout the entire layer area and depth.

Figure 4-2(b) displays a scatter plot representing the distribution of S_t values throughout the depth for each prepared platform, forming a cloud of points. The graph clearly illustrates a concentration of soil sensitivity values ranging from 2.5 to 6.5. By analysing the results obtained from the shear vane test and comparing the soil sensitivity values, we were able to assess the homogeneity of the soil within the depth. This characteristic proved partially the appropriate installation and compaction protocols.

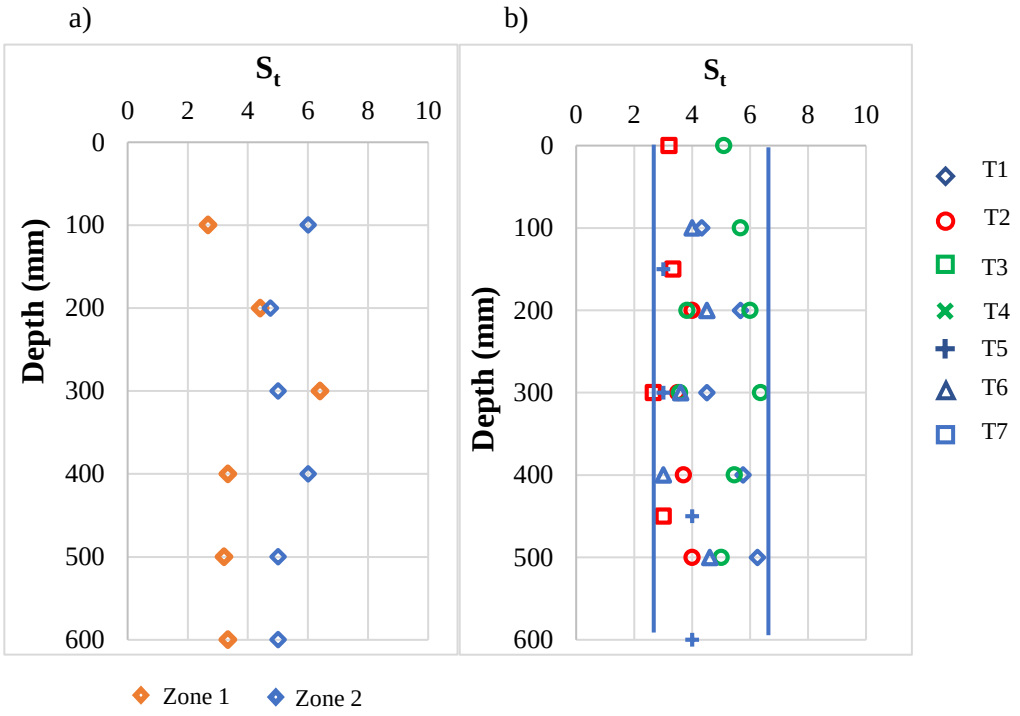

Figure 4-2: a) The St profiles in two specific zones within the subgrade layer; b) The St profiles of all the performed test across the depth.

4.3.3 Static penetrometer test results

The static penetrometer was utilized on the subgrade soil to determine the cone index, which is correlated to the CBR (%) using the manufacturer's apparatus. Figure 4-3 illustrates the in-depth profiles of CBR for three different zones within the subgrade layer of Test 1 following the compaction of the base course. The profile demonstrates a relatively uniform soil homogeneity across the subgrade depth and among the positions. This characteristic validates the suitability of the installation of the subgrade and the compaction protocols of the top base course layer.

Figure 4-4 illustrates the depth profiles of CBR for the subgrade layers in all the conducted tests before and after the base course installation and compaction. The profile displays a range of CBR values, as summarized in Table 4-2, ranging from 0.2% to 0.5% prior to base course installation and compaction. However, after the compaction of the base course, this range of values increased to 1.0% to 1.5%, indicating a significant impact of the base course compaction on the underlying soft soil. Although there is a 0.5% difference between the lowest and highest CBR average values, it is important to note that obtaining the exact same CBR profile for each subgrade layer is challenging. Nevertheless, the CBR range remains acceptable for a credible comparison with plate load test results and the traffic load test results.

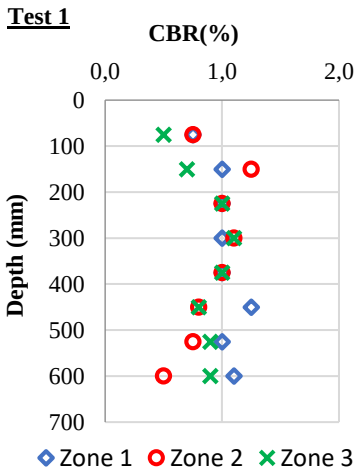

Figure 4-3: CBR profiles of three different zones within the subgrade layer of Test 1

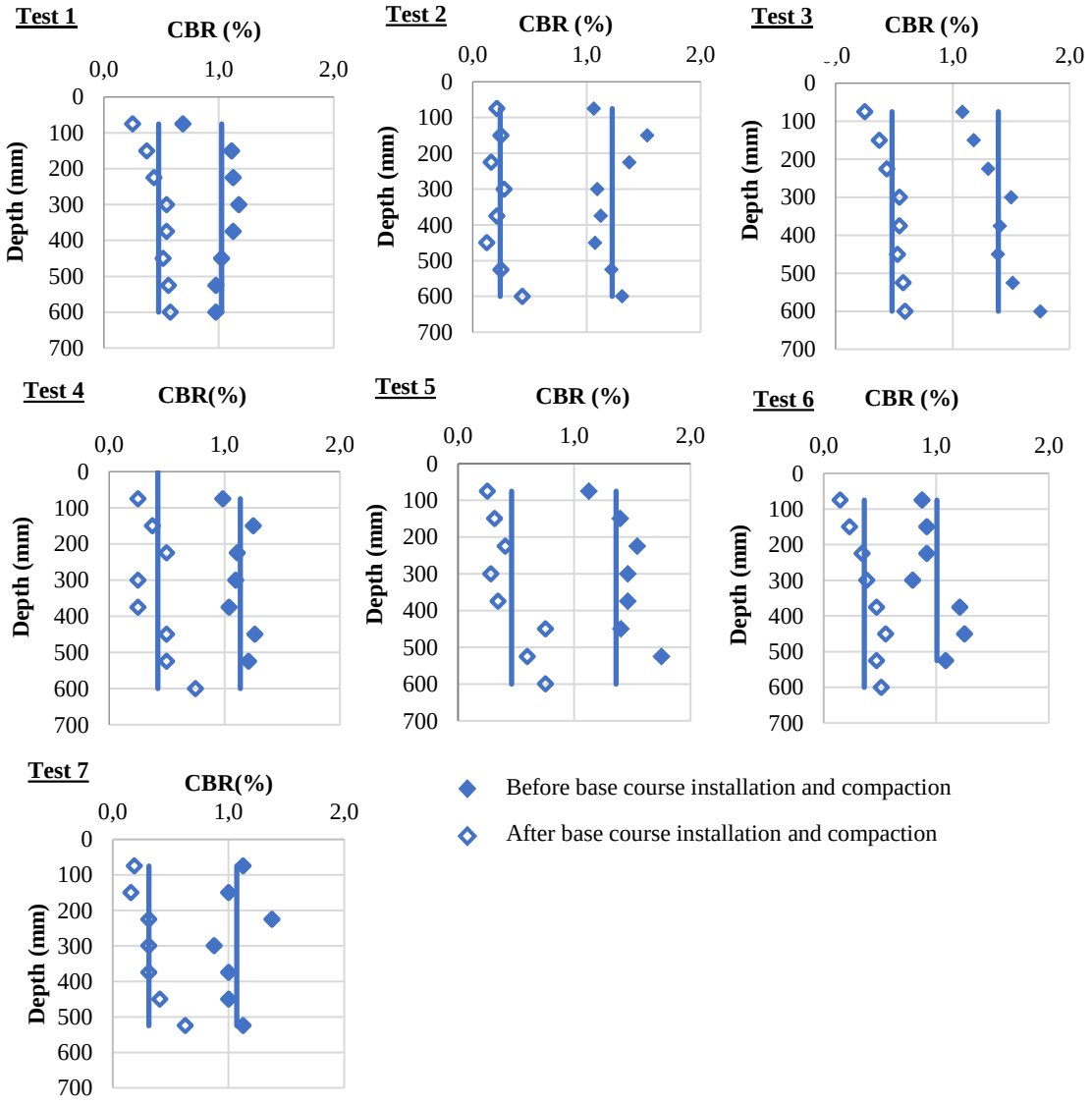

Figure 4-4: CBR (%) Profiles of subgrade layers in depth for all the performed tests before and after the compaction of the base course layer

Table 4-2: Average CBR Values of All Performed Tests

	T1	T2	T3	T4	T5	T6	T7
CBR_b (%) Before base course compaction	0.4	0.2	0.5	0.4	0.4	0.3	0.3
CBR_a (%) After base course compaction	1.0	1.2	1.4	1.1	1.4	1.0	1.1

4.3.4 Dynamic penetrometer test

The dynamic penetrometer was utilized on both the base course and the subgrade soil to determine the dynamic cone penetration index, which is correlated to the CBR (%) using the Eq 3-3.

Figure 4-5 illustrates the in-depth CBR profiles values for the base course and the corresponding CBR profiles of the subgrade layer in two distinct positions for each test, where the base course had a uniform thickness of 300 mm (Test 1, Test 2, Test 3, Test 4 & Test 5). The profiles from the two zones exhibit superposition, indicating relatively consistent soil compaction across the positions within the base course layer. Furthermore, at the surface of the base course, the CBR values were consistently around 5% for all tests due to soil repulsion. However, as we move deeper, the CBR values exhibit variability. In Test 2 (unreinforced), the CBR ranges between 5% and 10%, while in Test 1, Test 3, and Test 4 (all reinforced tests), it ranges between 5% and 15%. Test 5 (reinforced) shows a wider range, with CBR varying between 5% and 20% and reaching 25% at certain points. These findings indicate that the platform for Test 5 (reinforced) underwent effective compaction, followed by the platforms of Test 1, Test 3, and Test 4 (reinforced) at a similar level. The platform for Test 2 (unreinforced) exhibited comparatively lower levels of compaction. These results highlight the positive impact of reinforcement on improving the compaction of the base course layer of 300 mm of thickness.

Figure 4-6 presents the depth profiles of CBR values for the base course and the corresponding CBR profiles of the subgrade layer in Test 6 and Test 7, both featuring a base course thickness of approximately 500 mm. Each pair of profiles obtained from two different zones within the same platform exhibit superposition, indicating a consistent level of soil compaction across positions within the base course layer. Moreover, at the surface of the base course, the CBR values consistently remain around 5% across both tests due to soil repulsion. However, as we go deeper into the base course layers, the CBR values show variations. In both Test 6 and Test 7, the CBR ranges from 5% to 20%, with Test 7 peaking at 23% at a specific point. The similarity in compaction between the two platforms suggests that there is no significant difference in the level of compaction between the reinforced and unreinforced platforms with a thickness of 500 mm.

Figure 4-5 and Figure 4-6 reveal that the CBR values are consistently close to 1%, which aligns with the findings from the graph obtained using the static penetrometer (Figure 4-4). This close correspondence confirms the reliability of the CBR correlation obtained through both static and dynamic penetrometers.

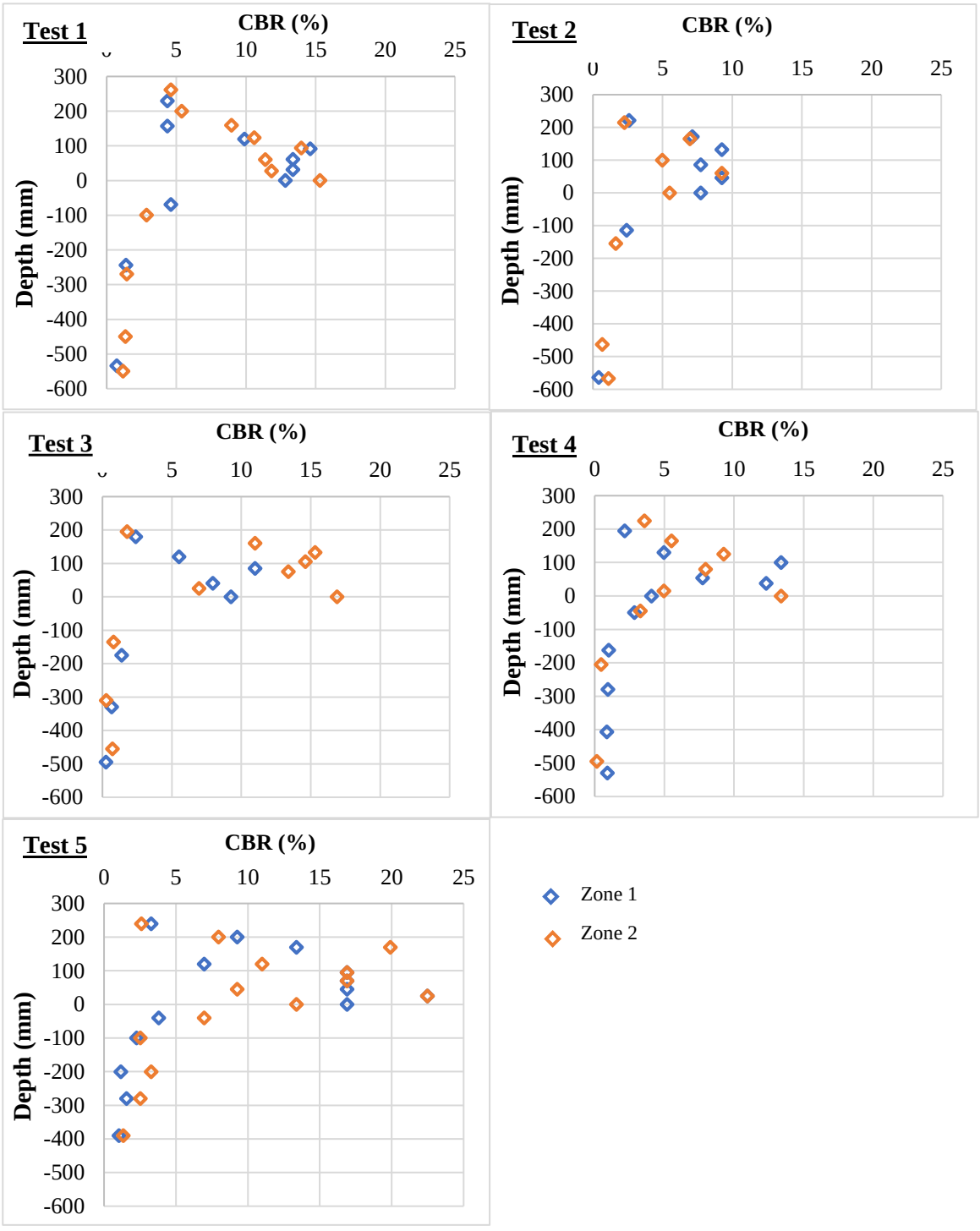

Figure 4-5: CBR (%) profiles of the base course layers and the CBR (%) profiles of the subgrade layers in the conducted tests with 300 mm platforms of thickness

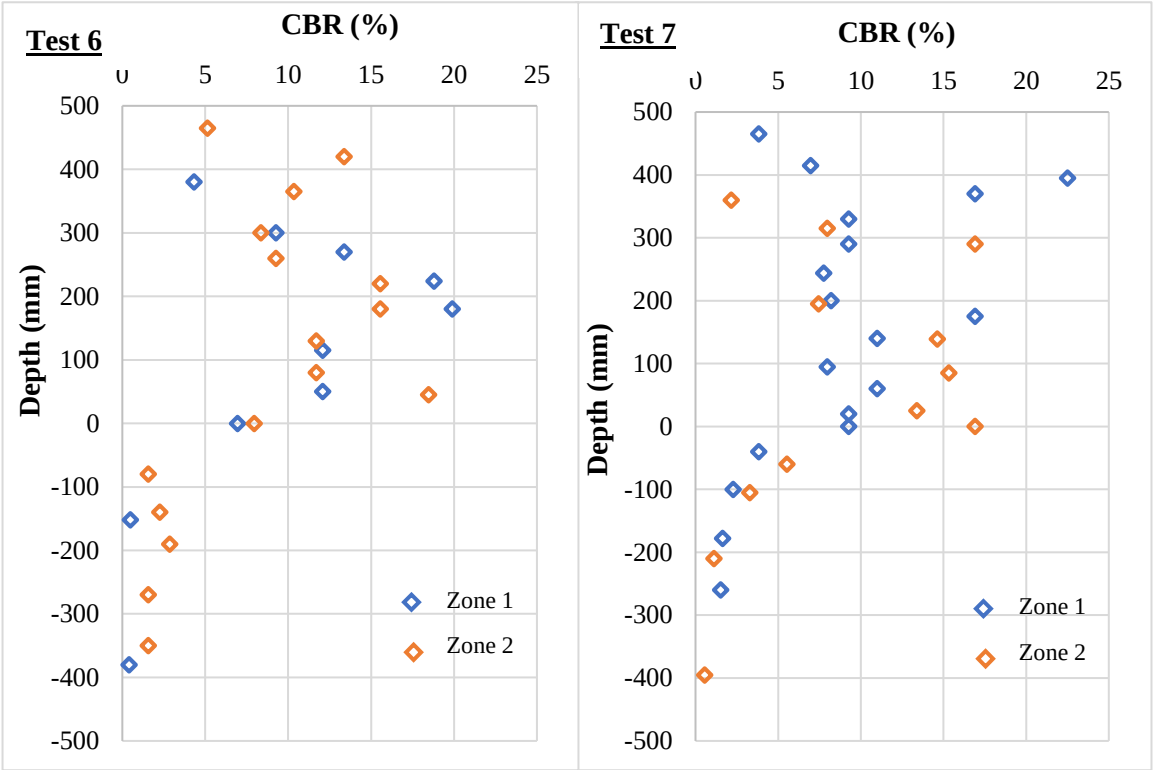

Figure 4-6: CBR (%) profiles of the base course layers and the CBR (%) profiles of the subgrade layers in the conducted tests with 500 mm platforms of thickness

4.3.5 Clegg impact soil test

The Clegg Impact Soil Test was utilized to determine the Impact Values (IV) of the base course layer. The 4th IV, representing the critical IV value, was correlated with the CBR using *Eq 3-4* to assess the degree of compaction. Multiple tests were conducted at various positions for each platform. Figure 4.7(a) displays a histogram showing the CBR values for seven different zones at the surface of Test 5's platform. The obtained CBR values range from 15% to 21%, indicating a consistent soil compaction across the base course surface layer with a mean CBR value of 17%. This range of CBR values aligns approximately with those obtained from the dynamic cone penetrometer results of Test 5's platform. In Figure 4.7(b), a histogram represents the mean CBR values (CBR_{mean}) derived from multiple tests conducted on each platform as well as the CBR calculated standard deviation (σ). The obtained CBR_{mean} values highlight significant variations in soil compaction among the constructed platforms. The platforms of Test 5, Test 6, and Test 7 underwent effective compaction with an CBR value of 17%, followed by the platforms of Test 3 and Test 4 (reinforced) at a similar level with an CBR of 12%. Test 2's platform (unreinforced) displayed comparatively lower levels of compaction with an CBR of 10%. Importantly, this classification of compaction levels based on the Clegg Soil Test aligns with the classification derived from the dynamic penetrometer test. This correspondence confirms the reliability of the CBR correlation obtained through both the dynamic penetrometers and the Clegg Impact Soil Test.

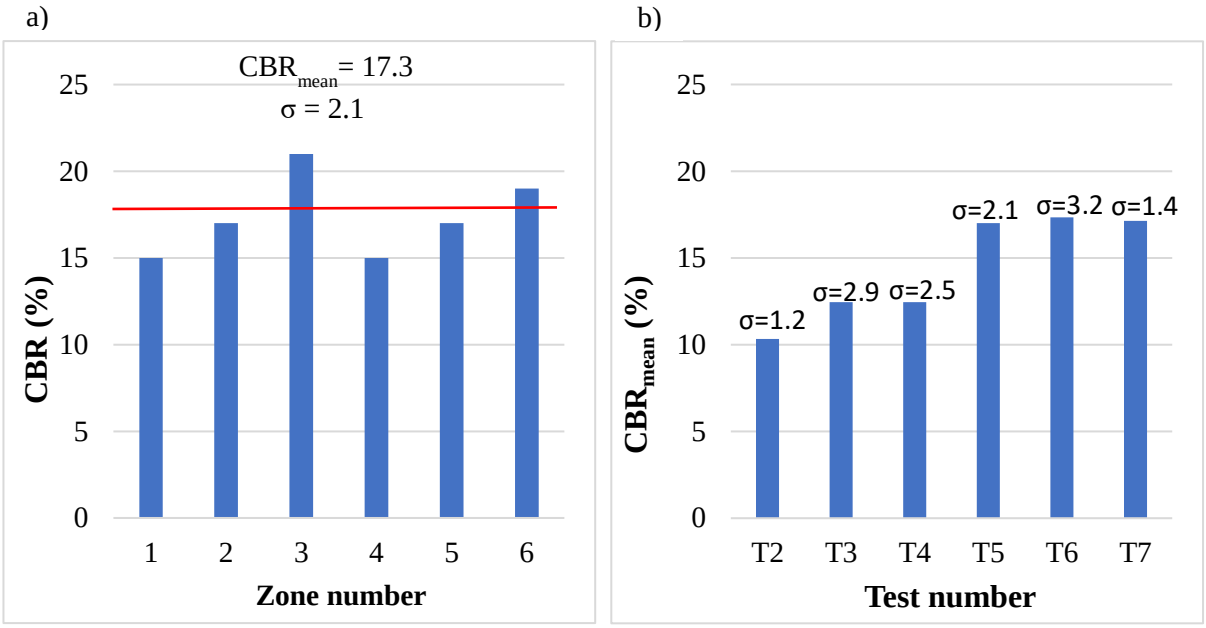

Figure 4-7: a) CBR (%) average values of the base course surface in test 5; b) CBR (%) average values of the base course surface in the conducted tests

4.4 Vertical cyclic plate load tests

4.4.1 Assessment of sensors performance

Khoueiry (2020)'s study provides valuable insights into the uncertainties involved in stress measurements in soft soils. The research confirms that the distribution of sensors does not disrupt subgrade behavior while also identifying challenges related to sensor inclination.

The study involved comparing settlement profiles in both monitored and non-monitored areas after subjecting them to 10,000 loading cycles. Encouragingly, the results indicated that the distribution of sensors did not cause any disturbance in subgrade behavior, confirming their non-disruptive nature. Overall, the placement of sensors on the subgrade surface layer and within the subgrade layer had no adverse effects on subgrade behavior under cyclic load.

Additionally, Khoueiry (2020) addressed uncertainties in stress measurements within an inclined zone by utilizing inclinometers on the earth pressure cells. The central sensor, positioned beneath the centre of the plate load and at the subgrade surface, consistently showed inclinations ranging from approximately 0° to 2° in both the x and y directions. This suggests reliable measurement of vertical stress within that specific zone. However, the sensor located 200 mm away from the plate sensor, specifically in a curved zone along the x-axis at the surface, displayed significant inclinations during the initial cycles. These inclinations progressively increased and reached the inclinometer's upper limit of 15° after 2,000 cycles, highlighting the uncertainties associated with the sensor's inclination and the measured values obtained. In summary, the central earth pressure cell positioned at the subgrade surface beneath the centre of the plate accurately reflects the vertical stress transferred to the zone where it is placed. On the other hand, the sensor located in a potentially inclined zone due to load distribution does not accurately reflect the true vertical load in its respective zone.

4.4.2 Base course compaction

The compaction of the base course sub-layers directly influences the compressibility of the subgrade layer.

The compaction was made by the plate compactor with working surface equal to 520 mm x 460 mm. Hydraulic settlement sensors, positioned at the subgrade surface layer, were utilized to measure the displacement resulting from the installation and compaction of the base course layers. These sensors operate by circulating water from a reservoir positioned at a higher elevation. Any leakage in the system would end the measurement of displacement in subsequent cycles of the test. To ensure reliable readings, the sensor positions were adjusted twice during the experimental work of the seven tests, specifically after Test 3 and Test 4, with a focus on the critical position beneath the centre of the plate load to be monitored by two sensors. The hydraulic sensors arrangement is showed in Figure 4-8(a).

In Figure 4-8(b), the graph illustrates the displacement at specific positions across the width of the box at the surface of the subgrade layer due to the compaction of a 300 mm thick base course layer. The settlement profiles for Test 1, Test 3, Test 4, and Test 5 (which included reinforcement) ranged from approximately 40 to 80 mm. However, Test 2 (without reinforcement) displayed a noticeably larger settlement profile, ranging from 100 to 150 mm.

Since Test 1, Test 2, and Test 3 shared the same sensor arrangement, a comparison was made to assess the homogeneity of the displacement profiles and evaluate the impact of compaction. Test 1, reinforced with GTX1, exhibited a homogeneous displacement profile, with a difference of approximately 20 mm between the highest and lowest displacement values. Test 3, reinforced with GTX2, demonstrated a slightly less homogeneous profile, with a difference of around 30 mm. In contrast, Test 2, which lacked reinforcement, showed the highest settlement difference of approximately 60 mm between points, indicating the least homogeneous profile among the tests. This emphasizes the role of reinforcement GTX in enhancing base course compaction. For Tests 4 and 5, there were not enough monitored zones in the larger to compare profiles.

In Figure 4-8(c), the graph illustrates the displacement at specific positions across the width of the box at the surface of the subgrade layer due to the compaction of a 500 mm thick base course layer. The settlement profiles for Test 6 exhibited a range of settlement values. However, Test 7 (without reinforcement) displayed a slightly larger settlement profile, ranging from 70 to 90 mm. For these two tests, there were not enough monitored zones in the larger to compare profiles.

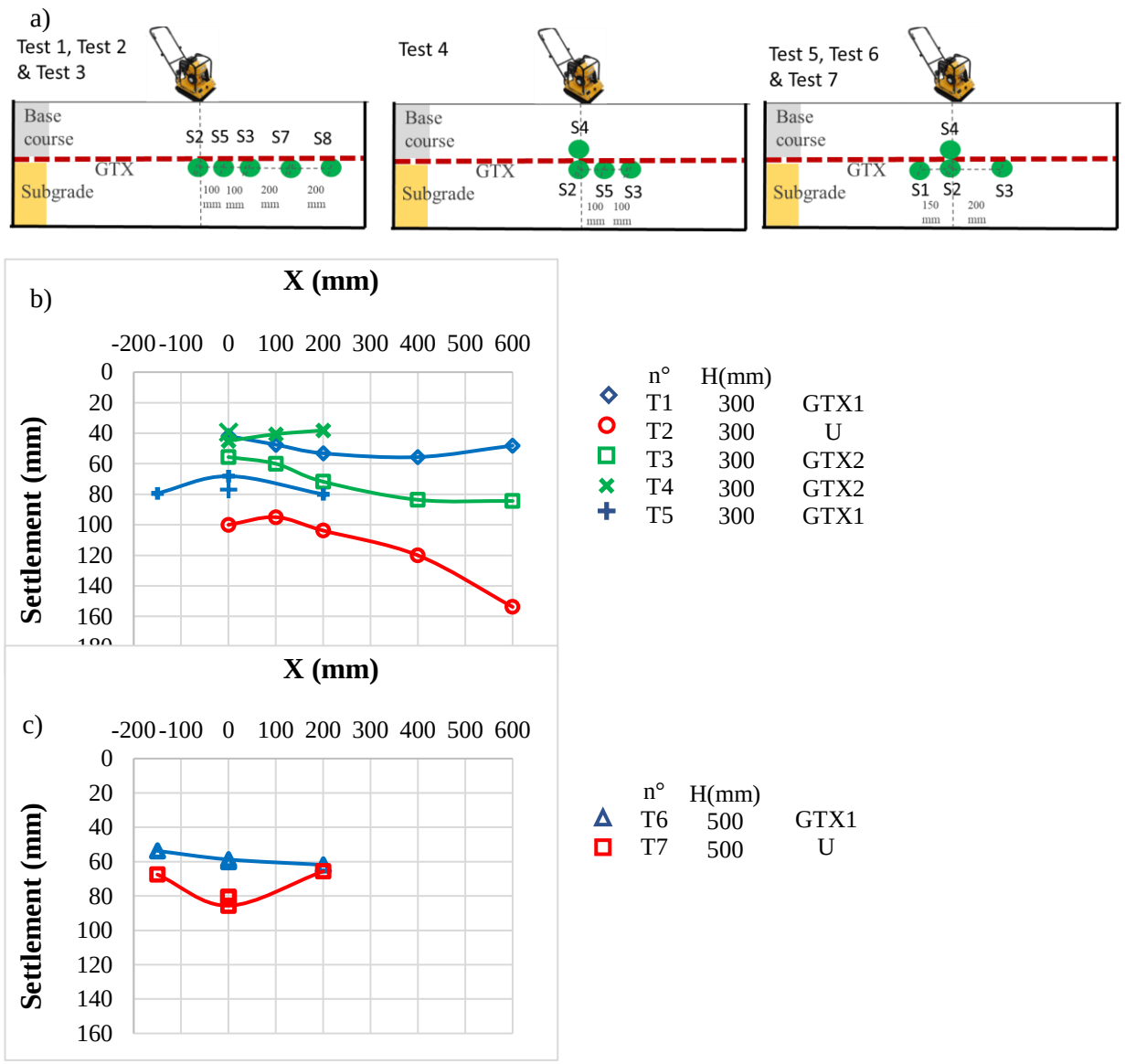

Figure 4-8: Hydraulic settlement sensors a) arrangement b) displacement due to the base course layer installation and compaction in Test 1, Test 2, Test 3, Test 4 & Test 5; b) displacement due to the base course layer installation and compaction in Tests 6 & Test 7.

4.4.3 Vertical cyclic plate load tests results

4.4.3.1 Repeatability tests

To ensure reliable and comparable results, identical tests were conducted to assess the repeatability of the experiments. This is particularly crucial in large-scale tests where consistency is importance. Four reinforced platforms were subjected to two repeatability tests, utilizing GTX1 and GTX2 reinforcement. Tests 1 and 5 shared the same configuration with GTX1 reinforcement, while Tests 3 and 4 shared the same

configuration with GSY2 reinforcement. All repeatability tests were performed with a base course thickness of 300 mm.

The evolution of central subgrade settlement beneath the centre of the loading plate during the cycles of the identical tests is shown in Figure 4-9. In the first cycle, the subgrade surface experienced the same displacement for both the two identical tests (Test 1 and Test 5) of about 17 mm. In Test 3 and Test 4 the subgrade surface displacement was 38 mm and 32 mm respectively. As the cycles progressed, the subgrade settlement evolution followed a similar trend with close values for each of the identical tests.

Similarly, Figure 4-10 shows the evolution of plate load displacement during the cycles of the identical tests. The plate showed the same displacement of 19 mm for both Test 1 and Test 5 mirroring the subgrade surface displacement. In Test 3 and Test 4 the plate load showed a displacement of about 39 mm and 43 mm respectively. The evolution of plate load displacement followed a consistent pattern with closely aligned values throughout the cycles for each pair of identical tests. These consistent displacements demonstrate the reliability of the identical tests at the two critical positions: the loading plate located at the base course surface layer and the surface of the subgrade layer beneath the centre of the plate loading.

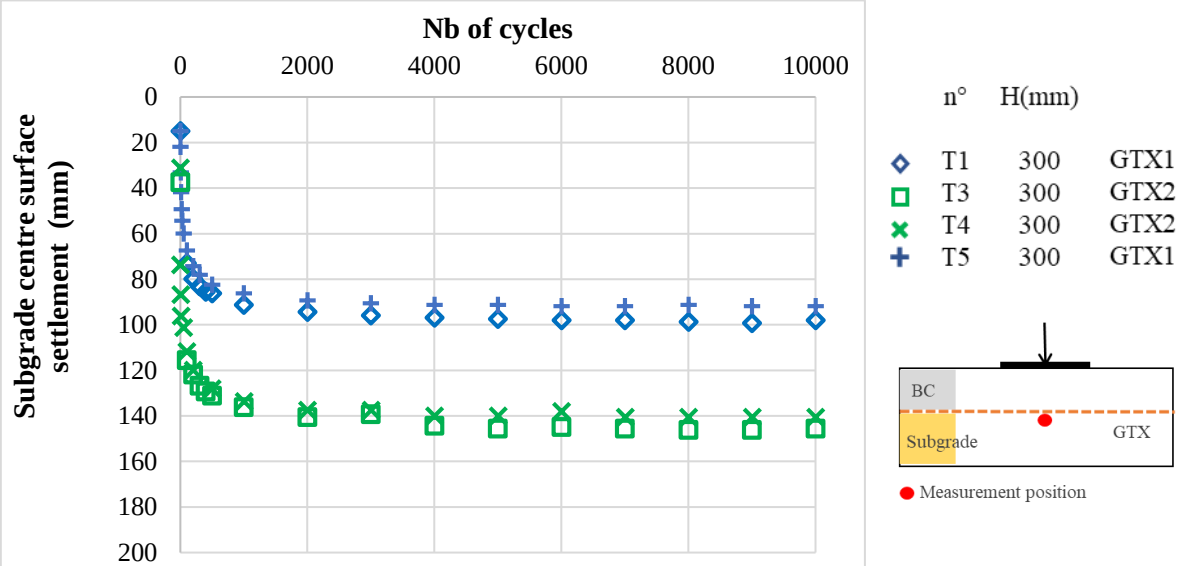

Figure 4-9: Subgrade centre surface settlement evolution with cycles

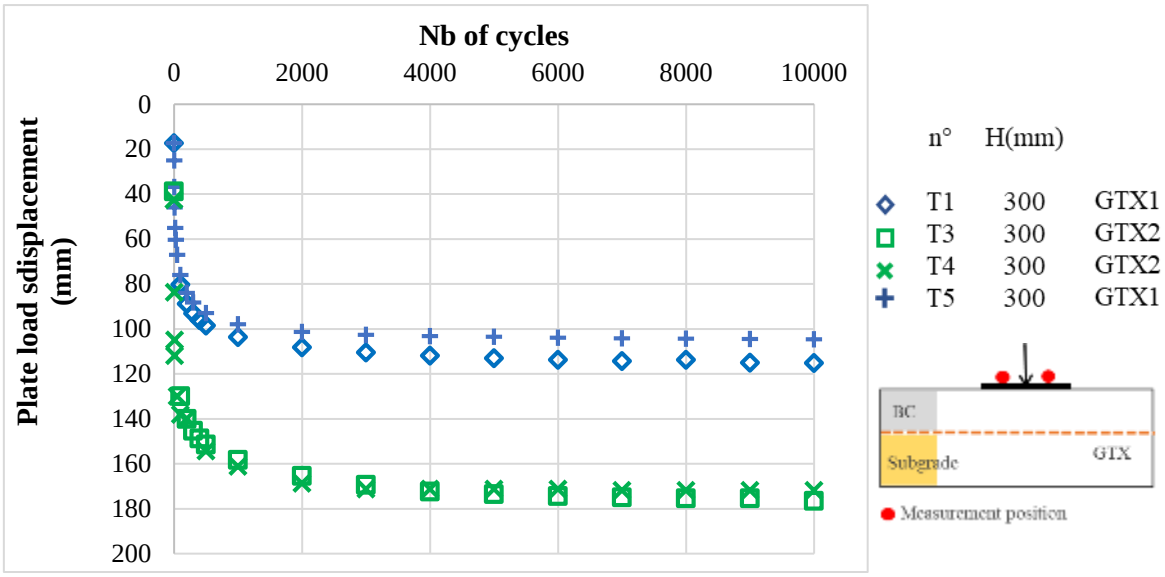

Figure 4-10: Plate load displacement evolution with cycles

Figure 4-11 shows the subgrade surface displacement profile across the width of the experimental box after 10,000 cycles. Multiple settlement sensors were strategically placed to capture the settlement values. The profiles obtained from the two identical tests, Test 1 and Test 5, exhibited similarity under the loading plate centre and at 200 mm from it. While the profiles showed a high degree of similarity beneath the loading centre and at 100 mm from the loading plate center for Test 3 and Test 4, it is worth noting that slight deviations in settlement values were observed at the 200 mm of the loading plate centre. Overall, the results indicate a considerable level of repeatability in the subgrade surface settlement and the loading plate displacement.

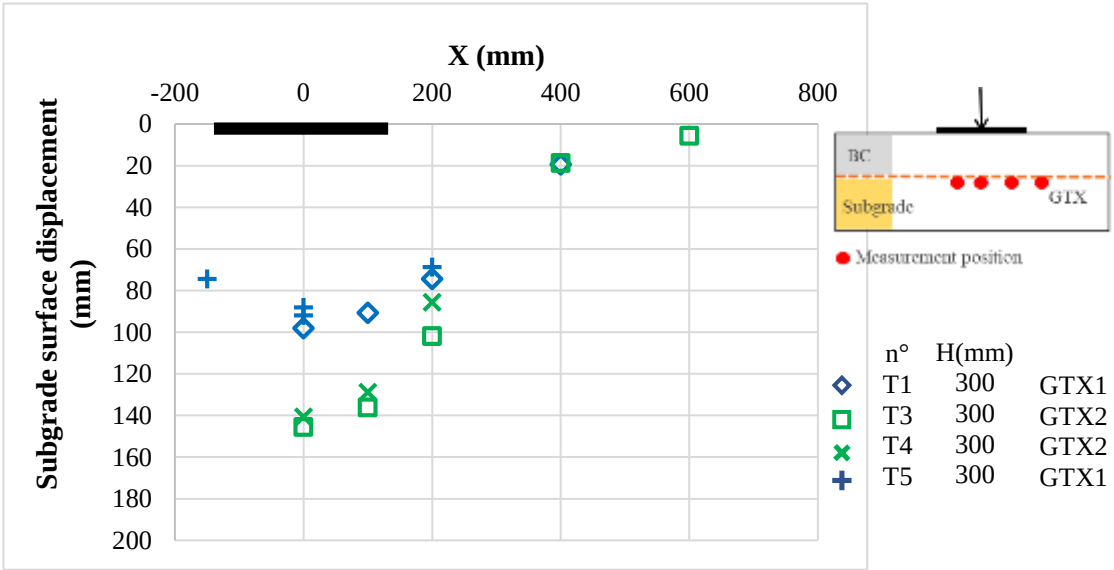

Figure 4-11: Subgrade settlement profile after 10, 000 cycles

Figure 4-12 depicts the progressive evolution of vertical stress at the subgrade surface center with cycles. The subgrade vertical stress evolution follows a similar trend with close values for each of the identical tests.

In summary, when comparing each pair of identical tests, a notable level of consistency was observed in terms of settlement throughout the depth and the width. Additionally, the vertical stress also showed a remarkable degree of similarity.

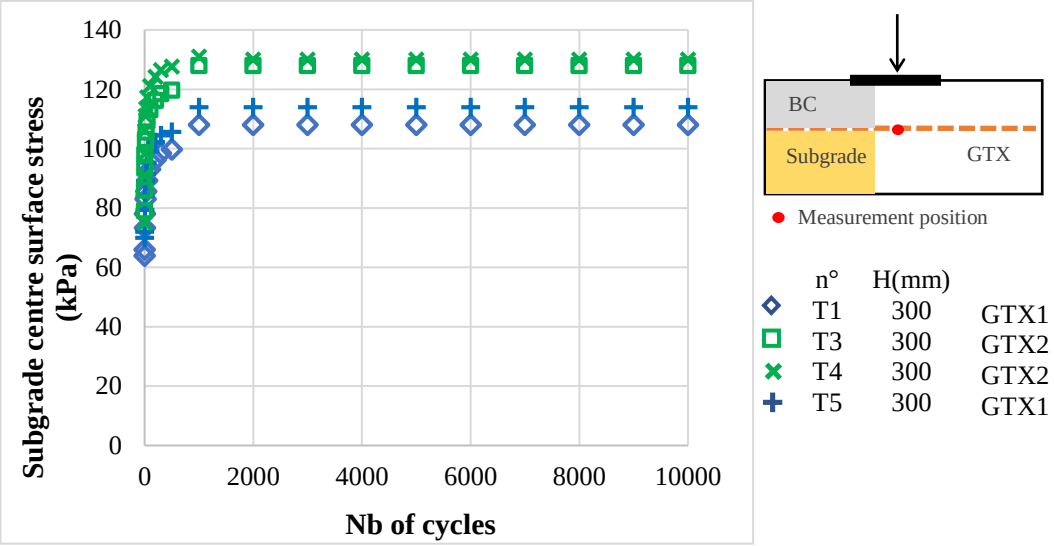

Figure 4-12: Evolution of the vertical stress at the subgrade surface beneath the loading plate with cycles

4.4.3.2 Base course settlement

This section aims to discuss the impact of GTX reinforcement on the performance of constructed unpaved road sections. These road sections were constructed with a compacted granular platform, which had a thickness of either 300 mm or 500 mm. The granular platform was placed over a soft subgrade soil with a CBR of approximately 1%. The key component in these road sections was the placement of GTX reinforcement between the subgrade and the base course layer. The two GTXs (GTX1 and GTX2) utilized in this study are woven GTXs with two different rigidities. Our primary focus is to analyse the settlement behavior of the subgrade surface layers as well as the settlement of the surface of the base course layer. By evaluating these aspects, we can assess the effectiveness of GTX reinforcement in the overall performance of the road sections.

1. Test 2: This test is unreinforced and has a granular platform with a thickness of approximately 300 mm. Unfortunately, subgrade settlement data collected from sensors placed at the subgrade surface layer, directly beneath the plate load center and at a distance of 100 mm from it, is missing after 100 cycles due to sensor failure. Additionally, the base course surface settlement profile after 1,000 cycles is unavailable due to excessive rutting, causing the jack to reach its maximum displacement.
2. Test 4: This is one of the identical reinforced tests using GTX2 with a granular platform of approximately 300 mm.
3. Test 5: This is one of the identical reinforced tests using GTX1 with a granular platform of approximately 300 mm.

4. Test 6: This test involves a reinforced platform with GTX1 and a thickness of about 500 mm.
5. Test 7: This test features a thick unreinforced platform with a thickness of about 500 mm.

It is important to highlight that the thickness of the granular layer in each test was measured at various locations within the unsolicited area after the end of each test. Additionally, to validate the accuracy of the measurements, a dynamic penetrometer was employed to assess the drop in CBR (California Bearing Ratio) during the transition from the granular soil to the soft soil condition. This verification process ensured the reliability of the obtained thickness values.

The cyclic plate load test involved the monitoring of the loading plate using two displacement laser sensors. Figure 4-13 presents the measured plate displacement above the 300 mm platforms (Test 2, Test 4, Test 5) and the 500 mm platforms (Test 6 and Test 7) after the 1st cycle, the 2nd cycle, the 1000th cycle. The loading plate exhibited inclination due to the difference between the monitored points on the plate. The differential settlements between the two displacement sensors after the first cycle were observed as follows: 2 mm for Test 2, 0 mm for Test 3, 0.4 mm for Test 5, 2 mm for Test 6, and 3 mm for Test 7 (Figure 4-13(a)). The differential settlements between the two displacement sensors after 1,000 cycles increased to reach 13 mm in Test 2, 8 mm for Test 3, 8 mm in Test 6, and 12 mm in Test 7 (Figure 4-13(c)). Only the Test 5 maintained in initial negligible differential settlement. While these differential settlements of the other tests were not negligible, they were uncontrollable, especially after the beginning of the test. However, for later comparisons, the displacement used is the average between the two measured displacements.

In Figure 4-13 (a), initial displacements after the 1st cycle vary among tests. Tests 7 and 5 had the smallest plate displacement (19 mm), while Test 6 showed the highest (59 mm). After the 2nd cycle, Tests 7 and 5 maintained the same rank (27 mm), while Test 6 still had the highest displacement alongside Test 4 (83 mm). The significant difference between the initial displacement is primarily influenced by the compaction method rather than the reinforcement or base course thickness. Therefore, this initial displacement can be mitigated by using heavy compaction machinery. For this reason, the effect of reinforcement will be further investigated after the second cycle (Figure 4-13).

The base course displacement evolution for each test is illustrated in Figure 4-14. Initially, the base course settlement increased with each cycle, which can be attributed to the decreasing rate of soil settlement with cycles. As the cycles progressed, the settlement of the base course eventually reached a state of stability and remained relatively constant. This indicates that the base course reached equilibrium, and further cycles had minimal impact on the settlement of the base course. Notably, the 300 mm reinforced platform with GTX1, which had a higher stiffness GTX, reached stabilization after 1000 cycles at a settlement value of approximately 100 mm. In contrast, the 300 mm reinforced platform with GTX2 reached stabilization after 2000 cycles with a settlement value of 170 mm in Test 2. The 500 mm platform exhibited the latest stabilization, continuing to settle until the 5000th cycle, with settlement values of 193 mm in Test 6 and 140 mm in Test 7. It is worth mentioning that Test 1 was stopped after 1000 cycles due to excessive settlement, causing the jack to reach its maximum displacement. The exact stabilization point for this test is uncertain, as it is unclear whether it would occur at 1000 cycles or later (Figure 4-14).

When considering the dispersion of initial settlements and their differences among the tests, it becomes imprecise to assess the specific impact of reinforcement without accounting for the effect of initial settlement. However, it is worth noting that the 300 mm platform reinforced with GTX1 (Test 5), the stiffest GTX, demonstrated the best performance in reducing base course settlement. After 1000 cycles, it achieved a 55% reduction in settlement compared to the 300 mm unreinforced platform (Test 2), and a 25% reduction compared to the 500 mm unreinforced platform after 10,000 cycles (Test 7).

The 300 mm platform reinforced with GTX2 (Test 4) also exhibited a reduction in settlement compared to the 300 mm unreinforced platform after 1000 cycles, although to a lesser extent (46%). However, it experienced more settlement than the 500 mm unreinforced test (Test 7) after 10 000 cycles due to the high initial settlement in the first two cycles which was 83 mm. Notably, Test 6, which involved the 500 mm reinforced platform with GTX1, experienced significant initial settlement approximatively 83 mm. As a result, after 10,000 cycles, the settlement reached 195 mm, compared to 140 mm in Test 7 with the same platform thickness but without reinforcement. To eliminate the influence of initial settlements, an additional

settlement evolution analysis is presented (Figure 4-15), starting from the third cycle. This analysis aims to provide a clearer understanding of settlement values, considering that initial settlements can be mitigated on-site using heavy compaction machinery (Figure 4-15).

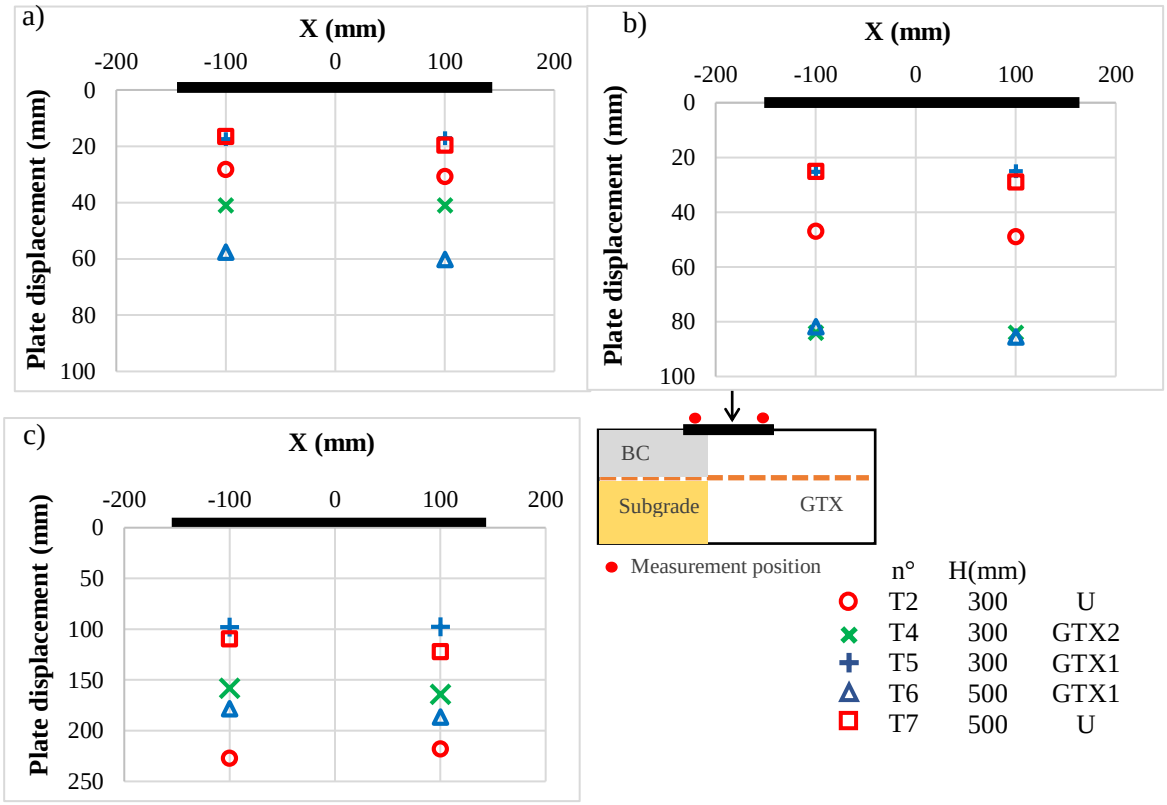

Figure 4-13: Loading plate displacement: a) after the first cycle b) after the 2nd cycle, and c) after the 1000th cycle.

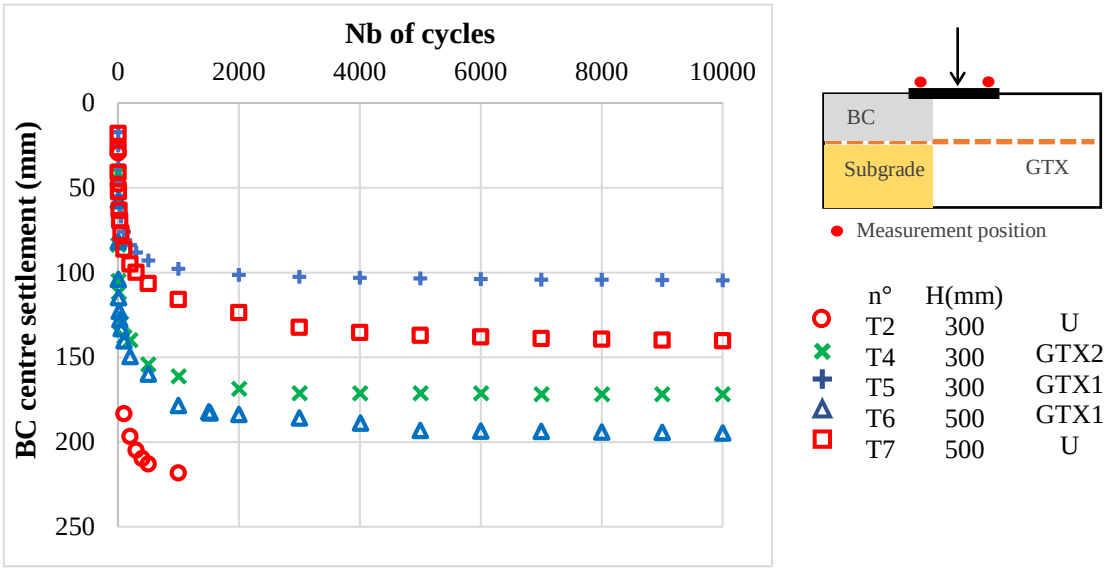

Figure 4-14: Base course surface centre settlement evolution with cycles

In Figure 4-15, a close evolution curve can be observed between Test 5 and Test 3 until 1,000 cycles. However, a small difference emerges after 10,000 cycles, resulting in an 8 mm settlement difference. This indicates that the stiffer GTX, GTX1, provides greater efficiency in reducing settlement. Similarly, Test 5 and Test 7 exhibit a similar evolution curve until the 10th cycle. However, a difference starts to emerge and gradually increases with each cycle, resulting in a 33 mm settlement difference after 10,000 cycles. The reinforcement of the 300 mm platform with GTX1 (Test 5) reduces settlement by 30% compared to the unreinforced 500 mm platform. Likewise, Test 4 and Test 7 show a similar evolution curve until the 100th cycle. However, a difference starts to appear and progressively increases with cycles, resulting in a 25 mm settlement difference after 10,000 cycles. The reinforcement of the 300 mm platform with GTX2 (Test 4) also reduces surface base course settlement by 22% compared to the unreinforced 500 mm platform. These results highlight the effectiveness of reinforcement in reducing settlement, with GTX1 performing better than GTX2 in terms of settlement reduction.

Furthermore, when examining the GTX1 reinforcement in the 500 mm platform (Test 6) shown in Figure 4-15, no improvement in terms of settlement reduction was observed compared to the unreinforced platform of the same thickness (Test 7), even after excluding the initial settlement values (Figure 4-15). Several reasons could account for the absence of reinforcement improvement in this case. Firstly, although the GTX was installed in accordance with the longitudinal direction and without any folds, it was not anchored from the extremities. This decision was made based on site conditions and feedback received, particularly in France, where GTX s are typically not anchored in such applications. However, conducting the test with an anchored GTX could provide insight into the effect of anchorage on the GTX's performance and its early engagement in the test. Secondly, while reinforcement showed improvement in the 300 mm platform without anchorage, as evident from the comparison between Test 2 and Tests 4 and 5, it is possible that a platform with a greater thickness may require anchorage. Since the dimensions of the constructed and tested platform are smaller than those of actual roads in site conditions, additional measures are needed to bridge the gap between site conditions and laboratory conditions. Another possibility to explore is the placement of a GGR at the upper third depth of the subgrade to investigate its potential contribution in settlement reduction when used in conjunction with or without the GTX at the interface. Lastly, it is also plausible that the range of applied load was insufficient to fully engage and tension the GTX.

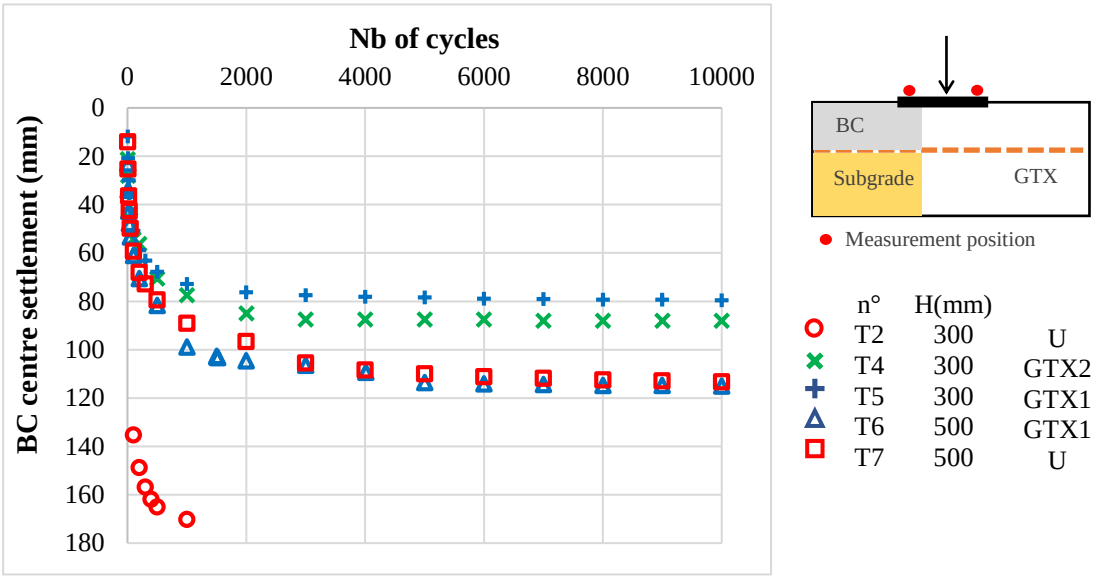

Figure 4-15: Evolution of base course surface settlement at the centre with cycles, starting from the 3rd cycle

4.4.3.3 Subgrade settlement

Figure 4-16 illustrates the settlement profiles at the subgrade surface after the 1st cycle, the 2nd cycle, and the 10,000th cycle. It can be observed that for the unreinforced test (Test 2), the settlement is negligible starting from 400 mm away from the plate center, confirming the respect of boundary conditions. Consequently, sensors were not placed in these positions for the other tests, as the focus was primarily on the critical solicited zones. Concerning the settlement profiles (Figure 4-16), a comparable curvature was evident between the reinforced and unreinforced tests.

The initial displacements at the subgrade surface beneath the plate center align in ranking with the initial displacements of the loading plate (Figure 4-16a). This alignment signifies a correspondence between the displacement of the base course and the subgrade, with minor discrepancies attributed to variations in base course compaction. Notably, the same rank of settlement is observed beneath the plate centre, as well as at 100 mm and 200 mm distances from the plate centre.

Upon comparing and analysing the settlement profiles after 10,000 cycles (Figure 4-16c), the impact of reinforcement becomes evident sometimes. In fact, the 300 mm platform reinforced by GTX1 (Test 5) demonstrated settlement profiles with lower values compared to all the tests, especially the unreinforced profiles of the 500 mm platform (Test 7). This suggests that the reinforcement had a positive effect in reducing settlement, particularly when compared to the 200 mm thicker platform without reinforcement. However, it should be noted that the reinforcement GTX2 showed high settlement values during the first two cycles, which had a significant influence on the settlement values after 10,000 cycles. Similarly, the 500 mm reinforced platform with GTX1 experienced high initial settlement values that continued to affect the settlement values after 10,000 cycles.

Figure 4-17 presents the evolution of subgrade centre settlement with cycles, which generally exhibits a similar trend to the settlement at the base course surface and Figure 4-18 illustrates the evolution of subgrade center settlement with cycles, starting from the third cycle. Test 5 reinforced with GTX1 (the stiffest GTX) maintains its position as having the most reduced settlement at the subgrade surface after 10,000 cycles. Moreover, Test 4 reinforced with GTX2 demonstrates significant progress after eliminating the impact of the initial two cycles, positioning itself as the second lowest subgrade settlement after 10,000 cycles. Regarding the tests with 500 mm of platform thickness, the Test 6 reinforced with GTX1 and the

Test 7 unreinforced display similar behavior after removing the initial two cycles, up until the 2000th cycle. After the 2000th cycle, the settlement rate of the Test 7 unreinforced exceeds that of the Test 6 reinforced with GTX1. However, the difference in subgrade settlement between these two tests is only 9 mm, which may not be significant given the inherent uncertainties associated with these types of tests. Nevertheless, it is evident that the 300 mm reinforced platform, whether reinforced with GTX1 or GTX2, outperforms the 500 mm unreinforced platform in terms of settlement reduction.

Across all conducted tests, difference in surface settlement between the base course and subgrade is noticed due to vertical platform deformation. Figure 4-19 graphically depicts vertical platform deformation, calculated as the difference between subgrade and base course settlements divided by the platform thickness, over cycles. Notably, the 300 mm platform reinforced by GTX1 exhibited the highest stiffness, registering around 4% vertical deformation after 10,000 cycles (Test 5). In an intermediate range, the 300 mm reinforced platform with GTX2 and the 500 mm unreinforced platform displayed similar stiffness levels, both showing approximately 6.3% and 7% of vertical deformation, respectively, after 10,000 cycles. The 500 mm reinforced platform followed with a 10% vertical deformation after 10,000 cycles, placing it third in stiffness. The platform with the least stiffness was the 300 mm unreinforced platform, showing a 10% of vertical deformation after just 100 cycles.

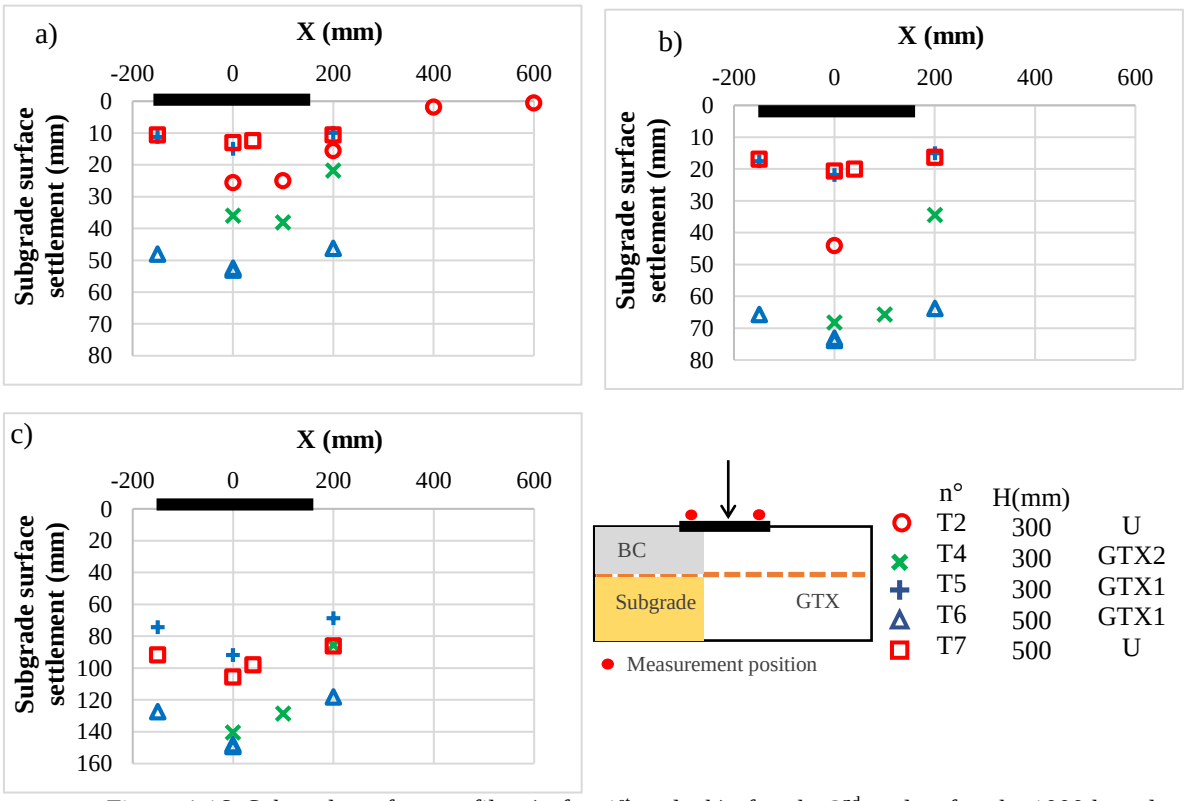

Figure 4-16: Subgrade surface profile: a) after 1st cycle, b) after the 2nd cycle, after the 1000th cycle

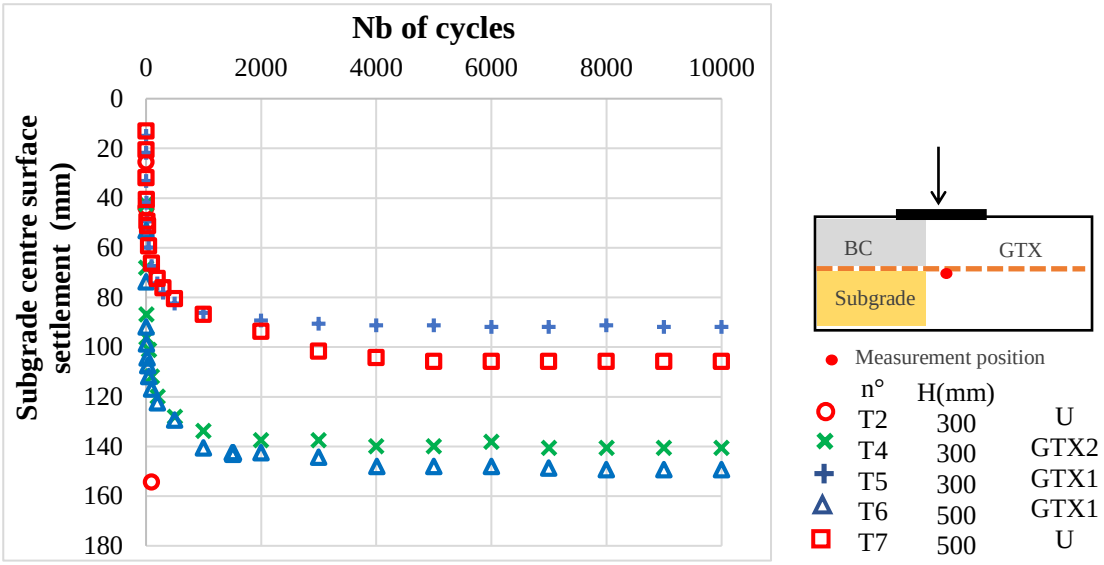

Figure 4-17: Subgrade settlement evolution with cycles

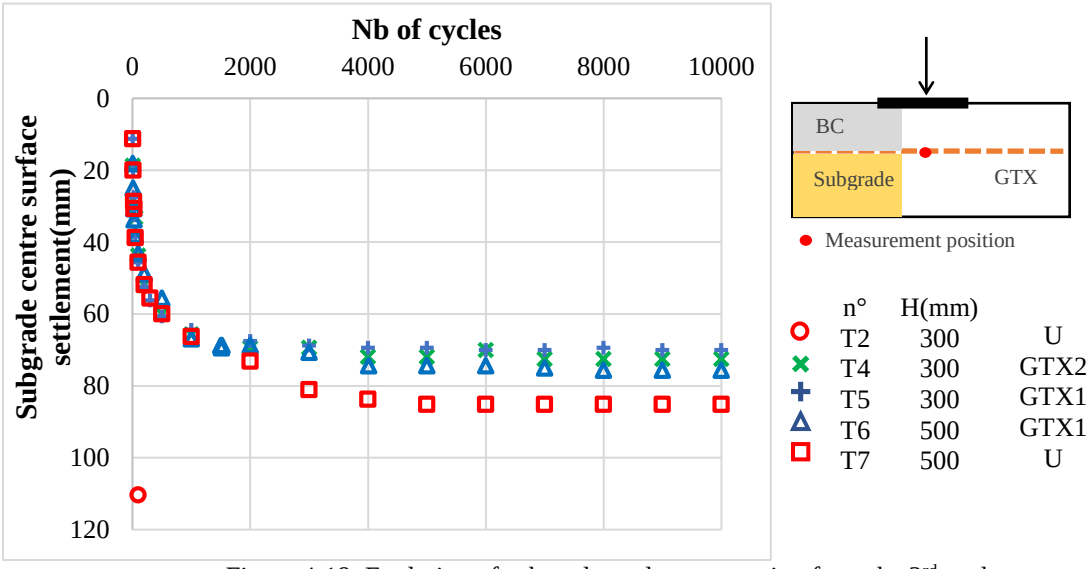

Figure 4-18: Evolution of subgrade settlement starting from the 3rd cycle

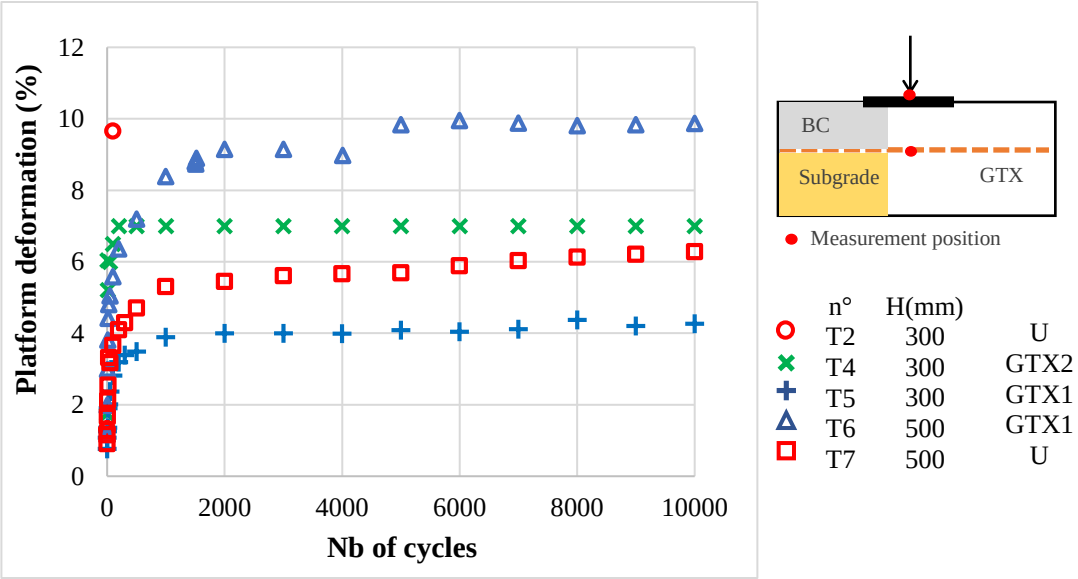

Figure 4-19: Evolution of vertical base course deformation with cycles

4.4.3.4 Subgrade stress

Figure 4-20 provides an insight into the vertical stress at the subgrade surface beneath the plate load center over cycles. The behavior of vertical stress remains largely consistent across the tests, with a notable exception in Test 2.

In Test 2, The subgrade center experienced the highest initial stress with 201 kPa, but this stress decreases gradually to reach 100 kPa at 1000 cycles. This reduction can be attributed to the hydraulic jack reaching its operational limit, leading to a loss of contact pressure at the plate level.

For the 300 mm reinforced platforms, the influence of the two types of GTX reinforcement, GTX1 and GTX2, becomes apparent. In Test 4, reinforced with GTX2, the initial vertical stress of 70 kPa undergoes a progressive increase, reaching 131 kPa before stabilizing with subsequent cycles. Conversely, in Test 5, reinforced with GTX1, an initial subgrade stress of 64 kPa increases to 100 kPa after 1000 cycles before finding stability. This trend parallels the settlement conclusion, highlighting how GTX1's application reduced both stress and settlement compared to GTX2.

Regarding the 500 mm platforms, Tests 6 and 7 exhibit closely aligned stress behavior over cycles, with similar values after 1000 cycles. Test 7 begins with an initial stress of 44 kPa, ascending to 68 kPa after 1000 cycles and remaining consistent afterward. For Test 6, the 500 mm platform reinforced with GTX1 starts at an initial subgrade stress of approximately 33 kPa. This stress increases gradually to 70 kPa by the 1000^{th} cycle, maintaining this level until the end of the 10,000 cycles. The parallel stress ranges suggest that GTX1's inclusion does not significantly affect stress or settlement in these cases.

Figure 4-21 establish a correlation between stress and displacement and show the stress evolution in relation to the settlement at the central point of the subgrade surface (beneath the loading plate). Tests 5 and 4, featuring GTX1 and GTX2 reinforcement respectively, demonstrated similar stress-settlement slopes. However, Test 2 showcased higher stress values accompanied by elevated settlement levels. Regarding Test 6 with GTX1 reinforcement and Test 7 unreinforced, their stress-settlement slopes deviate. Settlements in Test 6 exceeded those observed in Test 7, even though both shared a comparable stress range and settlement level.

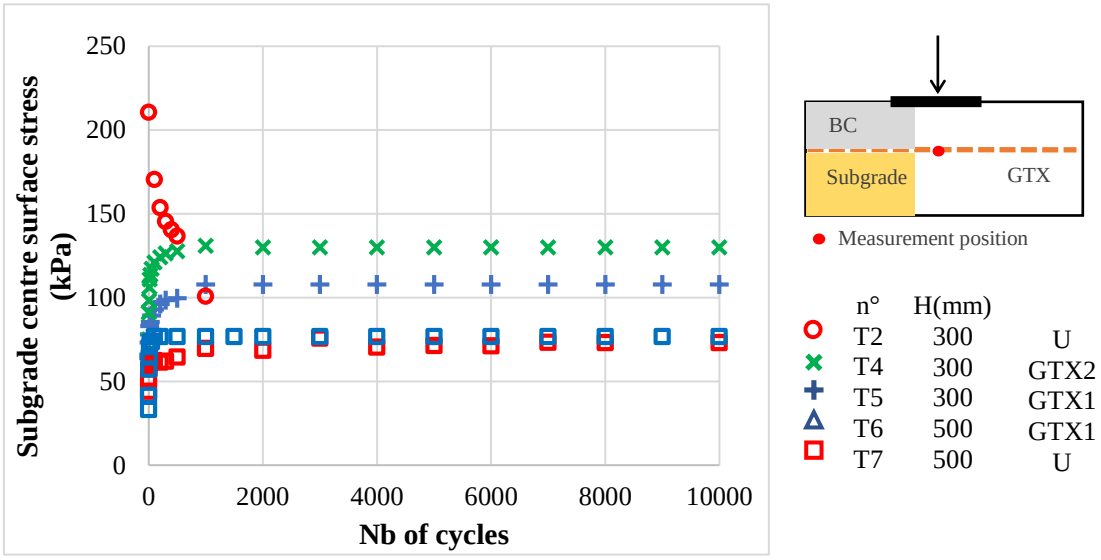

Figure 4-20: Subgrade surface central vertical stress evolution with cycles

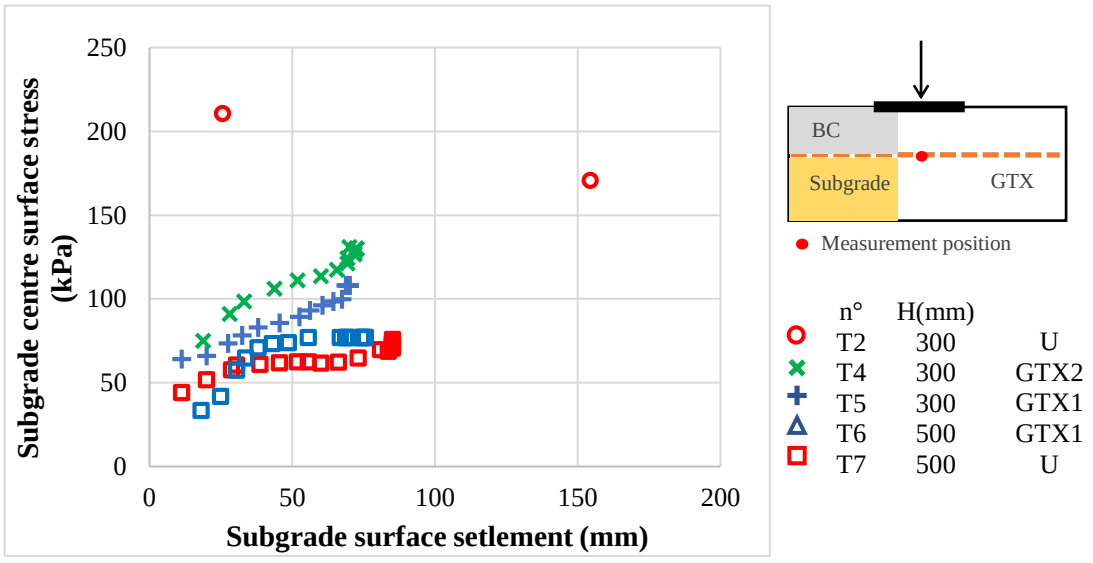

Figure 4-21: Subgrade surface central vertical stress evolution with settlement starting from the 3rd cycle

4.5 Traffic load tests

4.5.1 Performed tests

This section studies the impact of reinforcement on the behavior of unpaved roads. The SAT machine was used to subject both reinforced and unreinforced platforms to traffic loading. Three platforms were tested and compared in terms of settlement and stress:

1) Test 5': A 500 mm unreinforced platform,
2) Test 6': A 500 mm platform reinforced with GTX1.
3) Test 7': A 300 mm platform reinforced with GTX1.

4.5.2 Base course compaction

The base course compaction affects the compressibility of the subgrade layer. Figure 4-22 shows displacement at different points across the subgrade layer's surface. This displacement is due to compacting a 300 mm thick base course in Test 5'- and 500-mm thick ones in Tests 6' and 7'. Tests 6' and 7', which used GTX1 reinforcement, had consistent displacement, indicating uniform base course compaction. In contrast, Test 7' without reinforcement showed significant settlement differences of around 40 mm between points. This highlights the impact of reinforcement on achieving homogenous compaction.

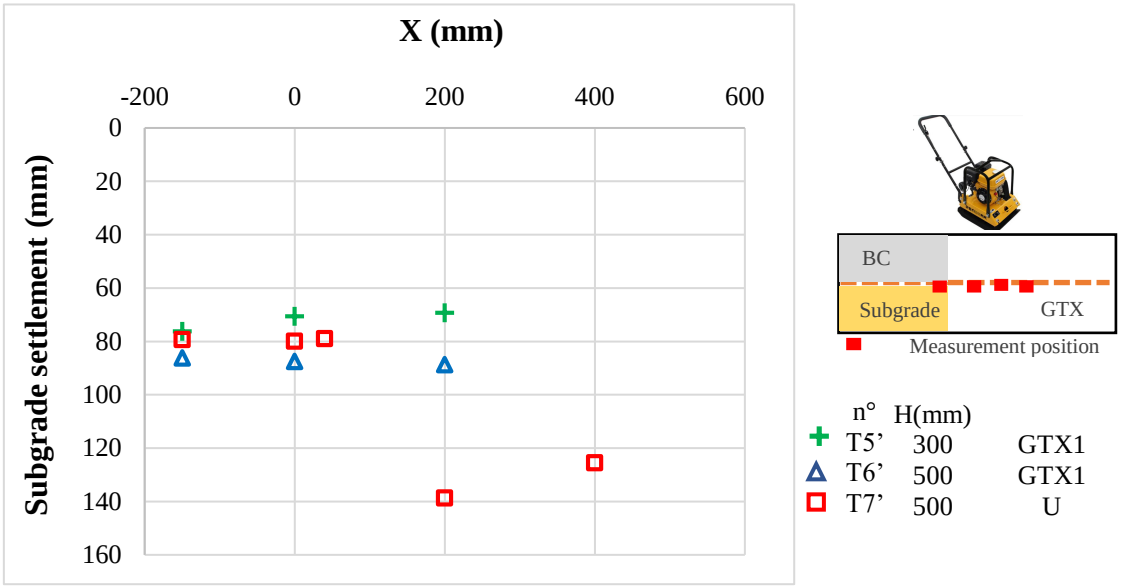

Figure 4-22: Subgrade top displacement due to the base course layer compaction

4.5.3 Assessment of installed sensors

Upon disassembling the test and removing the base course layer, it was observed that the earth pressure cell placed directly under the wheel exhibited a vertical orientation without significant inclination. This finding

aligns with the study conducted by Khoueiry (2020), where an inclinometer was placed at the same position as the earth pressure cell and demonstrated a negligible of inclination with cycles.

In contrast, the earth pressure sensors positioned at 150 mm from the left side of the wheel center and at 200 mm from the right side of the wheel center exhibited noticeable inclinations. These inclinations were attributed to the curvature generated under the traffic load. This observation supports the findings of Khoueiry (2020), which demonstrated an increasing inclination of the sensors with cycles.

In summary, the central earth pressure cell positioned directly beneath the wheel center accurately reflects the vertical stress transferred to the specific zone where it is placed. It remains vertical and does not exhibit significant inclination due to load distribution. However, the sensors located in areas potentially subjected to load-induced curvature do not accurately reflect the true vertical load in their respective zones. Therefore, it is important to consider the potential inclinations induced by load distribution when interpreting the measurements from sensors placed in such areas.

4.5.4 Traffic load tests results

The instrumentation used to measure the traffic load influence on the tested unpaved road sections specially in the solicited area is presented in chapter 3. The monitoring included measuring subgrade stress and displacement, as well as base course settlement during the passage of the simulator accelerator traffic (SAT). During the first passes of the wheel over the base course surface, the vertical stress applied to the top of the base course was measured. Additionally, vertical stress measurements were taken on the top of the subgrade along the wheel centerline, 150 mm from the left side of the centerline, and at 200 mm and 400 mm from the right side of the centerline, using the scaime (3.7). The settlement of the subgrade surface was also measured after a specific number of cycles using the data taker (3.7). After a predetermined number of SAT passes, a laser sensor was attached to a rail to measure the rutting profile across the width of the experimental box.

4.5.4.1 Base course settlement

Figure 4-23 depicts rutting profiles after 2 cycles and 500 cycles of traffic load. These profiles clearly reveal substantial base course surface elevation at wheel borders, indicating notable settlements due to lateral aggregate movement under these load conditions.

Comparing base course rut profiles across the three tests, close profiles emerge after the second cycle, with minor disparities. Noteworthy is Test 7' (500 mm unreinforced platform), consistently displaying the lowest profile values post 2 cycles and maintaining this position even after 500 cycles. As previously mentioned, the rutting limit set for the SAT apparatus is 150 mm. This limit was reached after 500 cycles for Test 5', 1000 cycles for Test 6', and 2000 cycles for Test 7'. Hence, the impact of reinforcement cannot be deduced here since Tests 6' and 7' continued settling after 500 cycles. To probe the reinforcement effect, we delve into the evolution of maximum ruts under traffic loads as shown in Figure 4-24.

In Figure 4-24, the measured maximum rut at the base course surface is established from the initial measuring point at the box's edge. Post second cycle, the 500 mm unreinforced platform (Test 7') exhibits the smallest rut depth at 12 mm, followed by the 500 mm reinforced platform (Test 6') at 20 mm. The 300 mm reinforced platform (Test 5') records the largest rut depth of 35 mm. During the initial 20 cycles, Tests 6' and 7' with thick base courses share comparable rut evolution. Subsequently, they diverge: the unreinforced Test 7' showing slower evolution, reaching 99 mm at cycle 1000, compared to the reinforced Test 6' that reaching 124 mm. Test 5', with medium base course thickness, undergoes the fastest evolution, hitting 135 mm after 500 cycles.

In summary, GTX1 reinforcement has no influence on rut development or its evolution between Tests 6' and 7'. Interestingly, the thick unreinforced platform (Test 7') surpasses the medium-thick reinforced platform in terms of retarding rut evolution and reducing maximum rut depth over cycles. This is the

opposite of the what happened with the same platforms under vertical load where the medium-thick reinforced platform (Test) reduced the maximum rut depth over cycles compared to the thick unreinforced platform (Test 7).

To induce further subgrade displacement, rutted areas are backfilled with aggregate and compacted after the cessation of wheel-base course contact. Given differing rut evolution rates among the three tests, maximum ruts are attained at varying cycle counts: 500 cycles for Test 5' (135 mm rut depth), 1000 cycles for Test 6' (124 mm), and 2000 cycles for Test 7' (105 mm). Notably, analyzing post-backfilling base course rutting evolution relies on added aggregate compaction quality, prompting focus on post-backfilling subgrade settlement evolution.

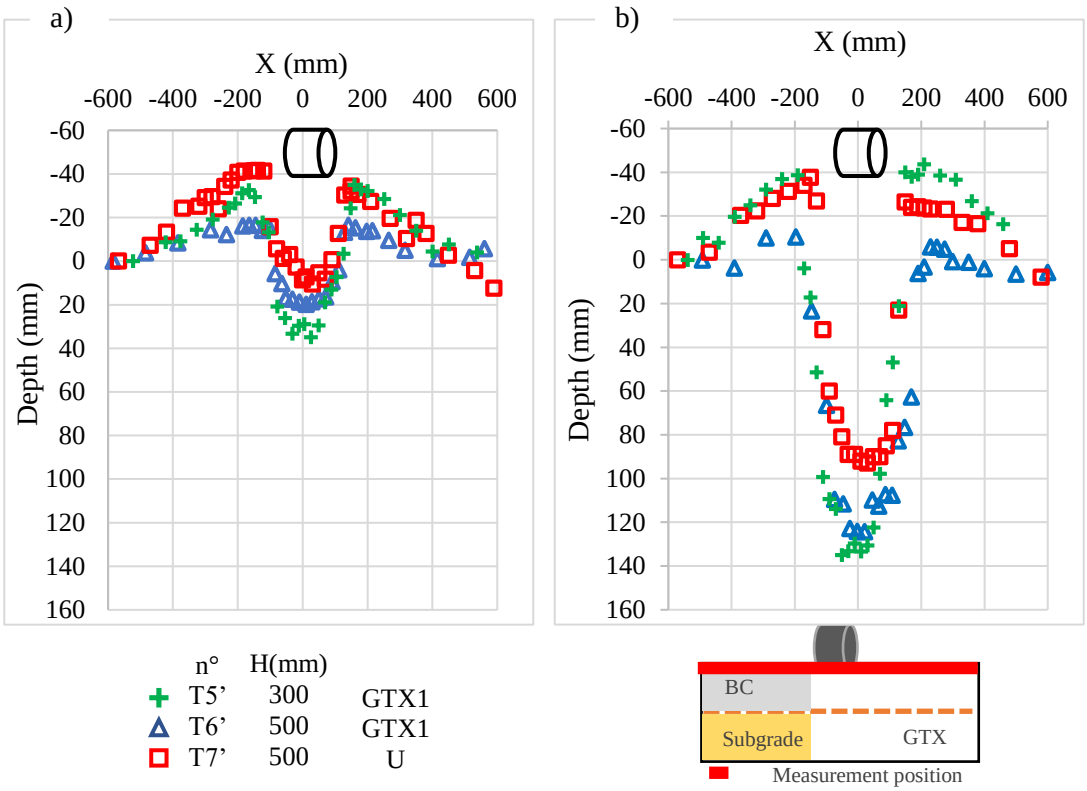

Figure 4-23: Developed rutting at the base course surface: a) after 2 passes of the SAT, b) after 500 passes of the SAT.

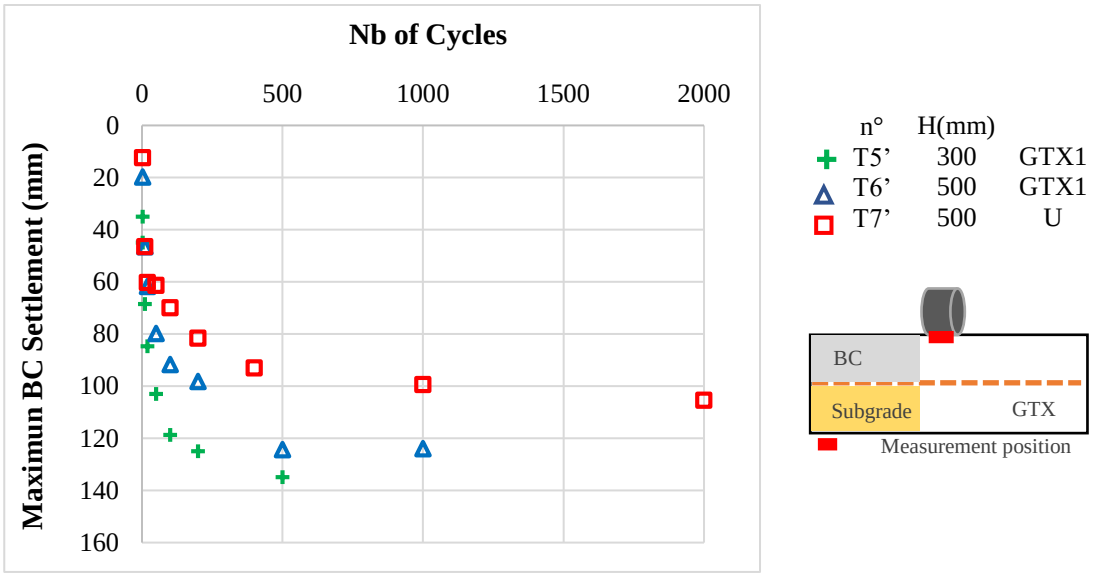

Figure 4-24: Maximum developed ruts with cycles under traffic loading

4.5.4.2 Subgrade settlement

Figure 4-25 (a) illustrates settlement profiles at the subgrade surface after the second cycle. The ranking of initial ruts at the base course surface aligns with the subgrade surface, albeit with variations due to base course particle reorganization. Notably, Test 5' (medium thick with GTX1) displays the highest settlement at around 20 mm after the 2nd cycle, while Test 6' (thick with GTX1) settles at approximately 11 mm. Test 7' (thick without reinforcement) settles around 7 mm after the second cycle. Intriguingly, these settlement rankings persist at both 100 mm and 200 mm distances from the tire center, with Test 5' exhibiting pronounced curvature.

Figure 4-25 (b) presents settlement profiles after the 3000th cycle of traffic load. The profiles showcase similar settlement value ranges, with a difference of about 15 mm between the highest maximum settlement in Test 5' and the lowest in Test 7'. To comprehensively explore the impact of reinforcement, it's crucial to investigate the maximum subgrade surface settlement evolution with cycles before drawing conclusions.

Figure 4-26 illustrates the evolution of maximum subgrade surface settlement beneath the wheel center. The trend in maximum rut evolution at the base course surface is mirrored in the subgrade surface. Test 7 settles the slowest, reaching 54 mm at 1,000 cycles and 63 mm at 2,000 cycles. Test 6' settles faster, reaching 71 mm after 1,000 cycles, while Test 5' settles the quickest, reaching 75 mm at 500 cycles. Once allowable settlement limits are reached and ruts are backfilled, subsequent traffic elevates the base course surface. However, subgrade surface settlement remains nearly constant across tests.

To summarize, these findings align with the base course rutting results. In Tests 6' and 7', GTX1 reinforcement does not significantly reduce maximum subgrade settlement under the 500 mm platform. Likewise, GTX1 installed under the 300 mm platform (Test 5') does not effectively diminish maximum subgrade settlement or slow its evolution compared to the 500 mm unreinforced platform (Test 7') as in case Test 5 and Test 7 subjected to vertical plate load tests.

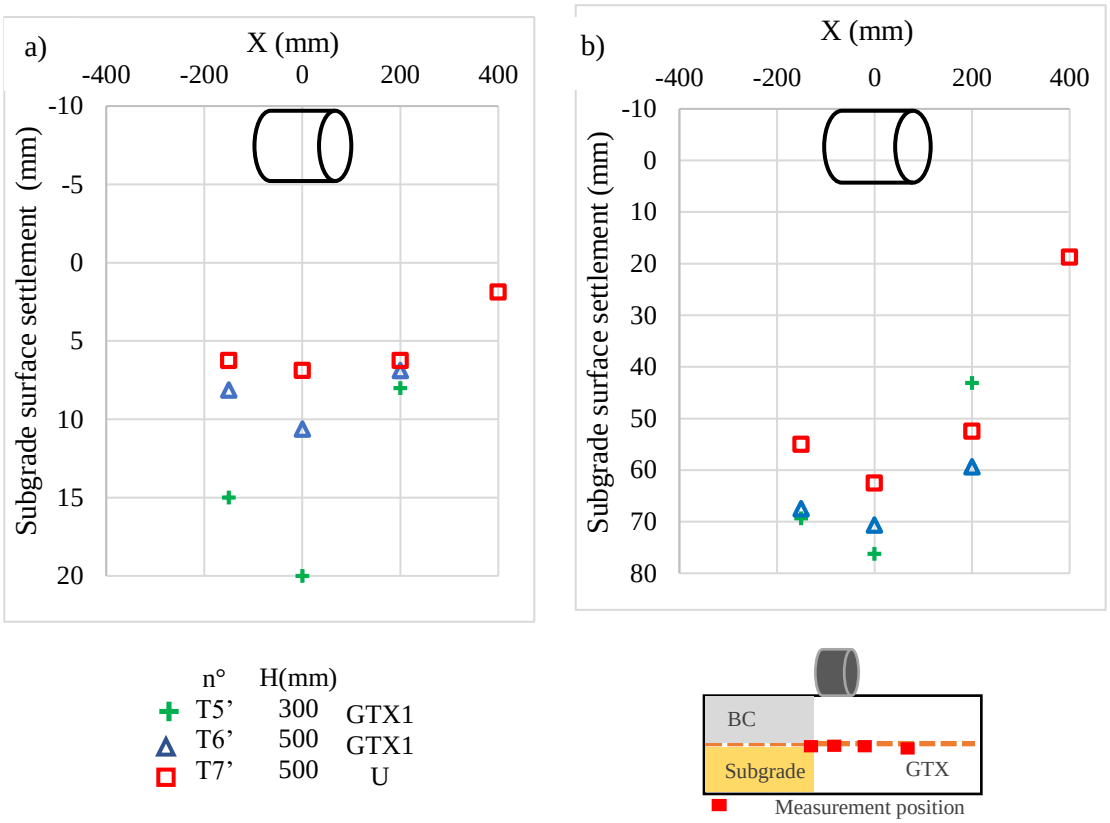

Figure 4-25:Settlement profile at the top of the subgrade layer: a) after 2 passes of the SAT, b) after 3000 passes of the SAT

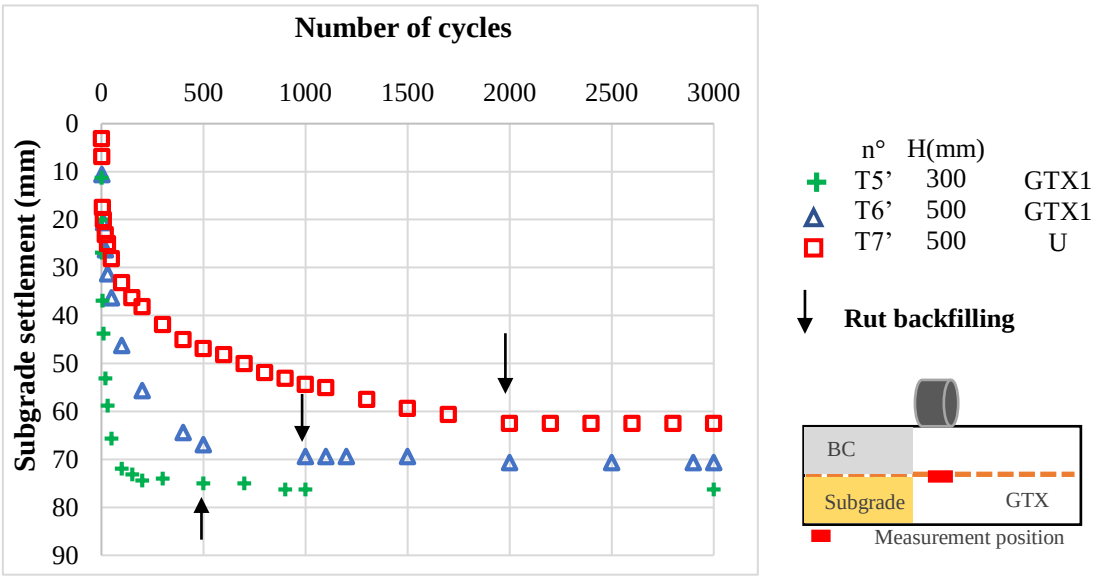

Figure 4-26: Evolution of the base course deformation with cycles

4.5.4.3 Base course deformation

A noticeable difference has been noticed between the maximum settlement at the base course surface and the subgrade surface directly beneath the wheel center. This differentiation arises from the deformation within the base course. As illustrated in Figure 4-27, the deformation of the base course beneath the wheel center is visualized.

Among the platforms tested, the unreinforced thick platform (Test 7') exhibited the least deformation, measured at 9%. Comparatively, the thick reinforced platform (Test 6') showed 12% deformation, which is greater than that of Test 7', but less than the medium thick reinforced platform (Test 5'), which measured 20% deformation. This disparity underscores Test 7' has the most rigid platform, contributing to its reduced settlement at both the base course surface and subgrade level, in contrast to the other platforms (Test 5' and Test 6').

In these specific experimental conditions, considering the loading, installation, and dimensions of the experimental box, the introduction of a 200 mm base course has proven effective in reducing base course deformation. This reduction in deformation leads to a slower progression of base course rutting and subgrade settlement, surpassing the effect of the GTX1 addition (Test 5).

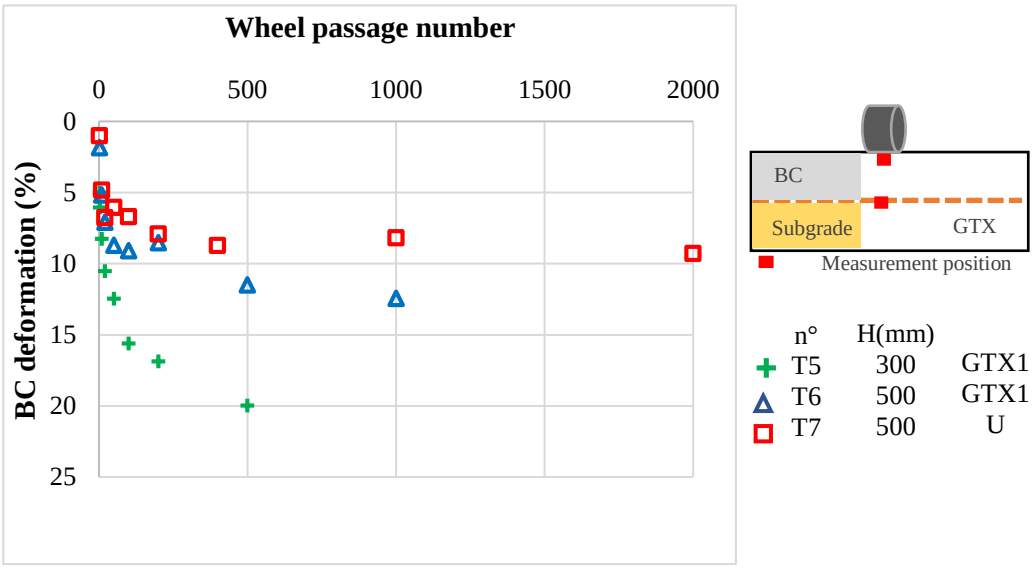

Figure 4-27: Maximum subgrade settlement with cycles under traffic loading

4.5.4.4 Vertical stress at the base course surface

In Khoueiry's study (2020), the wheel contact pressure was determined by dividing the machine's self-weight (28 kN) by the contact area between the colored wheel and a white paper (colorimetric method). This yielded a contact pressure estimation of 650 kPa.

However, in Test 7, an earth pressure cell was placed strategically on the base course surface at the wheel centerline to measure the vertical stress applied by the SAT machine. The earth pressure cell effectively recorded stress for the first five cycles. The stress values recorded by the earth pressure cell, as shown in Figure 4-28, offer valuable insights. During the first, second, third, and fifth cycles, stress values ranged between 260 to 300 kPa, indicating consistent and stable stress distribution within that range. However, the fourth cycle showed a notable increase in stress range, reaching approximately 460 kPa. Due to the significant rut development during testing, the earth pressure cell was removed after the fifth to prevent damage. The removal of the earth pressure cell after the fifth cycle halted further observation of stress changes in subsequent cycles.

The divergence between the calculated contact pressure under static conditions (Khoueiry 2020) and the measured vertical stress during wheel circulation at about 4 km/h is attributed to horizontal stress induced by traffic loads. Generally, traffic loads encompass both vertical and horizontal stress components, unlike pure vertical loads. The lack of specialized pressure cells to measure horizontal stress limits our understanding of its contribution to the overall stress distribution. Further investigation and analysis are important to comprehensively assess the impact and magnitude of horizontal stress on the road structure.

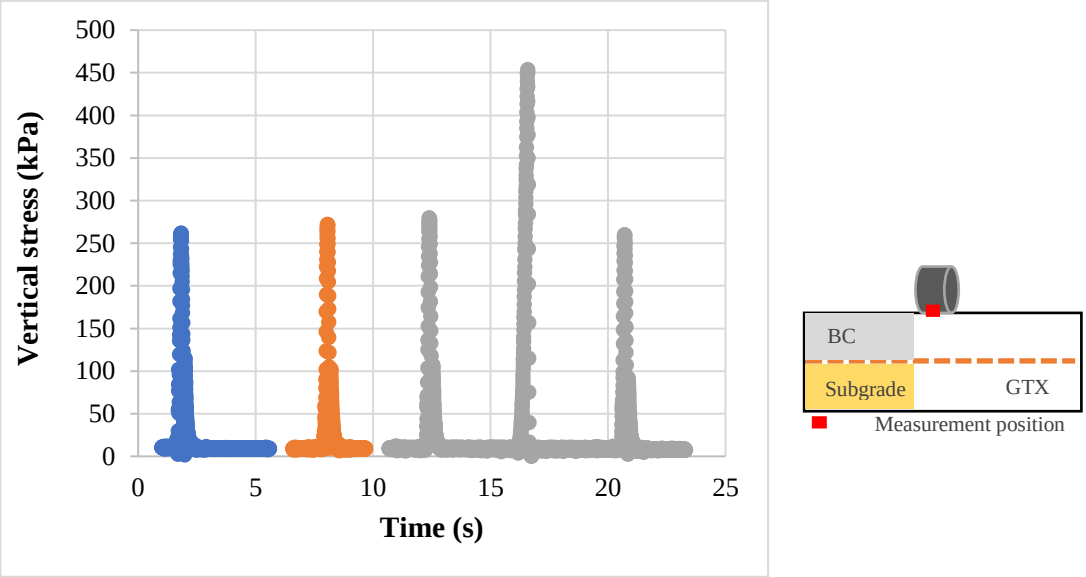

Figure 4-28:The vertical stress applied by the SAT under the wheel in the Test 7'

4.5.4.5 Vertical stress at the subgrade surface

Figure 4-29 provides general insights into the vertical stress applied on the subgrade surface beneath the wheel and its evolution with cycles. The measurements of vertical stress under traffic load reveal specific patterns.

After the second cycle, the vertical stress measured at the top of the subgrade beneath the wheel was 70 kPa for Test 6', while both Test 5' and Test 7' exhibited a vertical stress measurement of 86 kPa.
For the reinforced tests: Test 5' and Test 6', the stress increases with cycles reaching a maximum value of 140 kPa after 500 cycles for Test 5' and 114 kPa after 1000 cycles for Test 6'. Then the stresses decreased after the backfilling of the ruts with stabilization of the stress at around 100 kPa for the remaining cycles of both tests. That indicates that the compaction process did not fully restore the initial state of stress distribution and explains why no further subgrade settlement was generated after the rut was backfilled and compacted.

In the case of Test 7', the stress increased with cycles, reaching 106 kPa after 5 cycles. Subsequently, it decreased to 80 kPa at 100 cycles. This reduction reveals uncertainties which mainly related to the gravel blocked around the sensors because it is unreinforced tests. The stress remained stable at this value until the allowable SAT settlement was reached before the rut was backfilled. After backfilling, the stress further decreased to around 60 kPa and remained stable for the remainder of the test. Test 7' generated the least subgrade settlement values and exhibited the slowest stress evolution with cycles compared to the other tests. This can be attributed to its ability to maintain lower stress values after the 5^{th} cycle compared to Test 6' and Test 5'.

To establish a coherent relationship between stress analysis and displacement, we utilized Figure 4-30, depicting the evolution of stress in correlation with settlement at the central point of the subgrade surface. Notably, reinforced Test 5' and Test 6' exhibited a consistent slope (stress-displacement) prior to backfilling. Subsequent to the interruption of full contact between the wheel and the base course surface, both tests experienced a reduction in stress following rut backfilling, accompanied by a cessation of further settlement.

Contrastingly, unreinforced Test 7' showcased a stress-displacement slope akin to that of Test 5' and Test 6', yet it displayed the lowest stress and displacement values, albeit only over a limited cycle range. However, these trends were subject to changes due to stress fluctuations, mainly influenced by sensor positioning uncertainties and the presence of surrounding gravel. Following backfilling, a comparable loss of full contact manifested, paralleling the scenarios observed in Test 5' and Test 6'.

Overall, our analysis underscores the absence of significant reinforcement-induced stress reduction effects. This observation holds true when comparing the stress levels of reinforced Test 6' to those of unreinforced Test 7', as well as when comparing reinforced Test 5' to unreinforced Test 7'. In essence, the presence of reinforcement did not yield noteworthy stress reduction benefits.

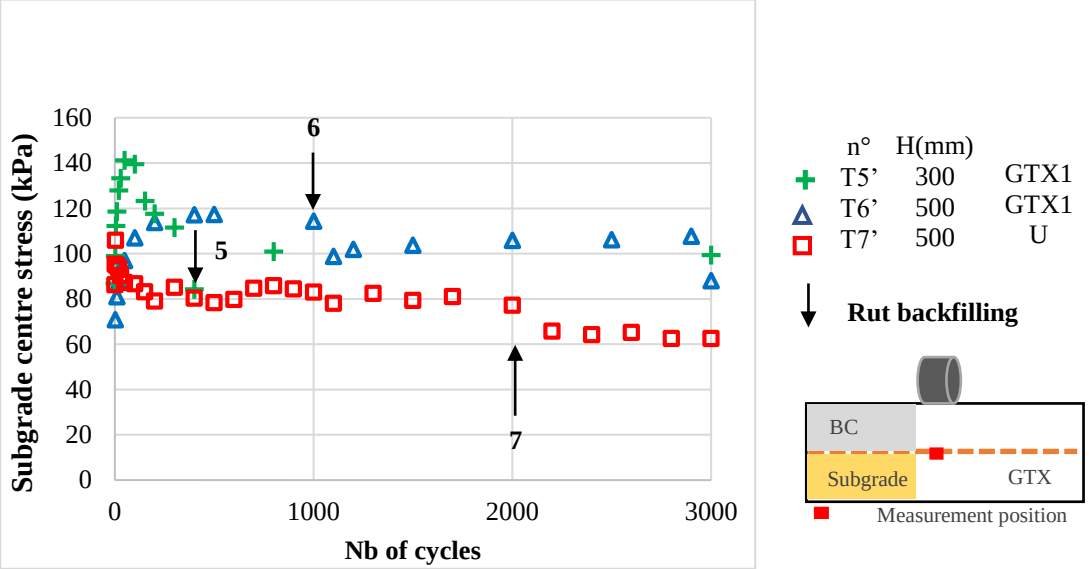

Figure 4-29: Subgrade surface central vertical stress evolution with cycles

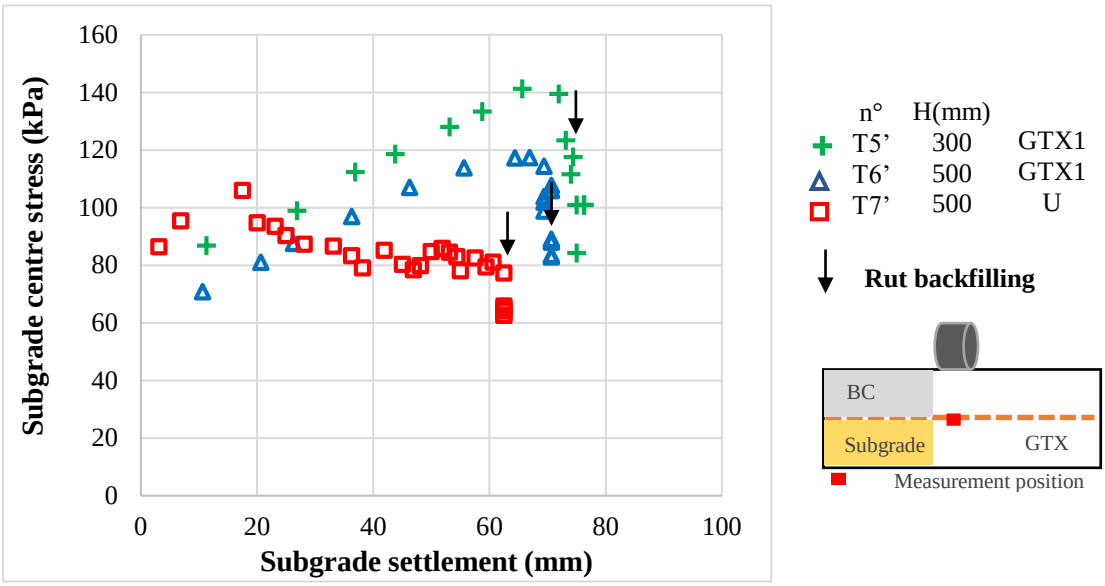

Figure 4-30: Stress evolution with settlement at the base course beneath the wheel centerline

4.6 Comparison between plate load and traffic load

In tests 5' and 5 involving a reinforced base course of medium thickness (300 mm), settlement evolution with cycles is presented in Figure 4-31a and revealed distinct impacts of traffic load compared to plate load. The base course experienced accelerated settlement under traffic load compared to plate load, while subgrade settlement under traffic load is slightly reduced compared to base course settlement under plate load (Figure 4-31a). This indicates that traffic load disproportionately damages the base course, potentially due to base course surface lifting at wheel borders, which disperses load and minimizes subgrade settlement. In contrast, the vertical and concentrated nature of plate load induces more localized settlement at the base course surface. Furthermore, the deformation of the base course thickness exhibited accelerated rate under traffic load compared to plate load (Figure 4-32a). After enduring 500 cycles of traffic load, the base course thickness experiences a substantial 20% deformation, which contrasts sharply with the only 4% deformation under vertical load conditions. This observation aligns seamlessly with the base course settlement evolution, providing further validation to the notion that traffic load induces a more adverse effect on the base course, resulting in amplified deformation of the thickness and settlement at its surface. The intricate interplay between these findings serves to underscore the elevated impact of damage caused by traffic load, highlighting the critical importance of understanding load types when designing the unpaved road section.

In tests involving thick base courses (tests 6 and 6' as well as tests 7 and 7'), the settlement evolution is different than that observed in Test 5 and 5' (Figure 4-31 b & c). Comparing base course settlements, it becomes evident that the rate of settlement evolution under traffic load is comparatively slower than that under plate load. Similarly, the subgrade settlements under traffic load exhibit a reduced rate of change compared to plate load conditions. A noteworthy consideration is the possibility of base course surface lifting at wheel borders. Interestingly, despite this factor, the plate load leads to greater settlement on the base course. This could partly stem from limitations inherent in simulating traffic load using the Static Plate Load Test (SAT), with its constrained allowable displacement rate (100-150 mm) potentially limiting the base course settlement. An alternative perspective is that the plate load inflicts more significant damage to the base course than traffic load. To validate the influence of SAT limitations on reduced base course settlement and differentiate it from the plate load's potential for greater damage, attention is drawn to the accelerated deformation rate of the base course thickness under traffic load ((Figure 4-31b & c). Following

1000 cycles of traffic load, the base course thickness experienced 12% deformation higher than 8% deformation under vertical load conditions for test 6' (Figure 4-32b), and a 9.5% deformation higher than 5.5% deformation under vertical load conditions for test 7' (Figure 4-32c). This disparity in deformation rates reinforces the argument that the observed differences in base course settlement can be attributed to the limitations of the SAT rather than an inherently heightened damage capacity of the plate load.

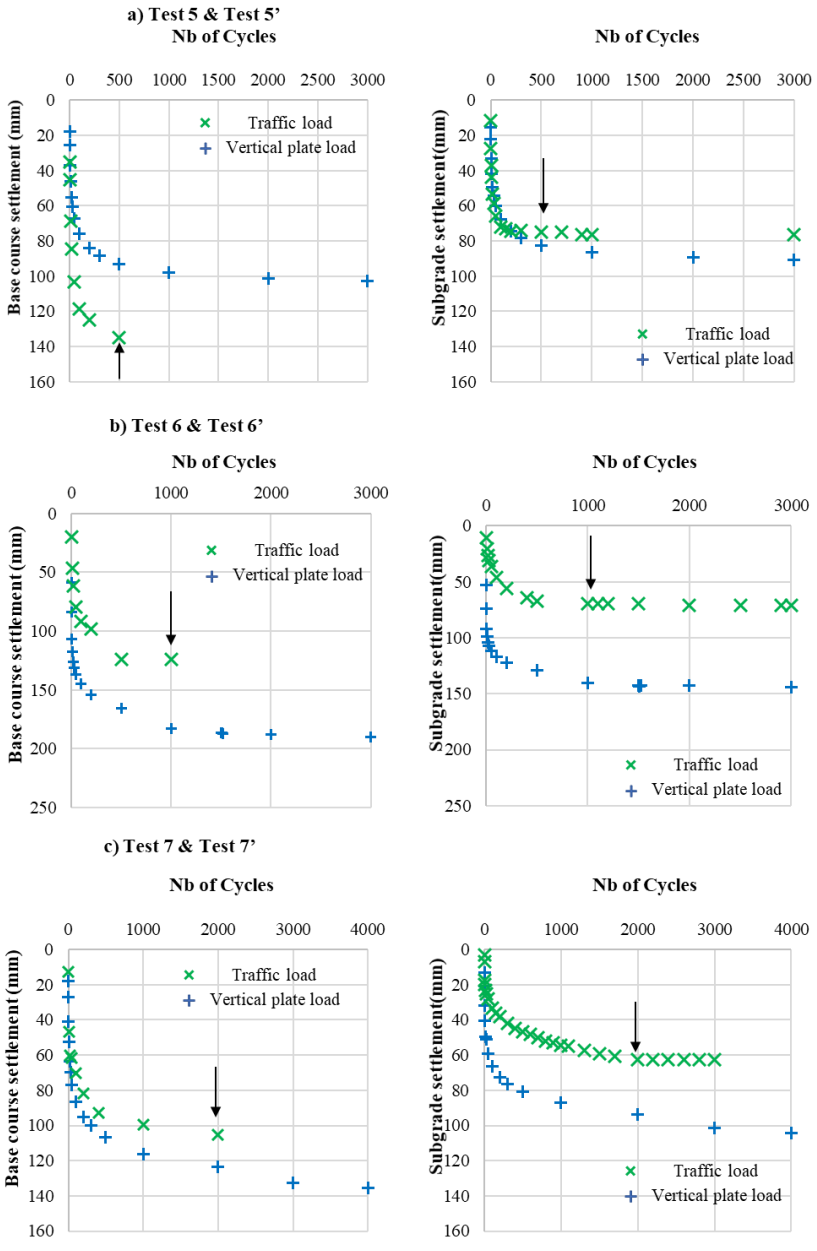

Figure 4-31: evolution of settlement under traffic and vertical loads

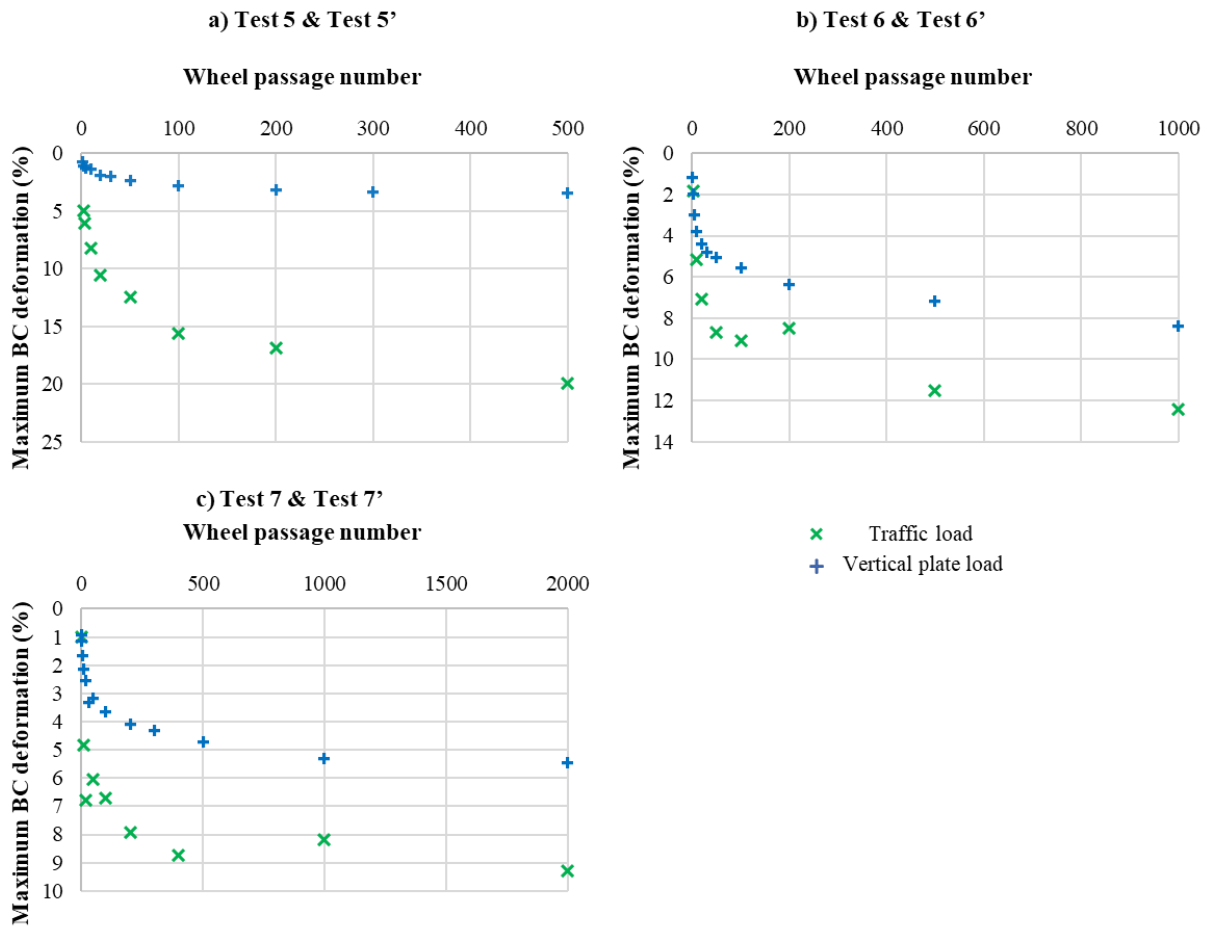

Figure 4-32: Base course thickness deformation of the plate load tests and the traffic load tests

4.7 Base course thickness deformation under traffic and vertical loads

The Simulator Accelerated Load (SAT) has proven more effective in evaluating reinforced road sections with medium to low base course thickness compared to those featuring a thicker base course. In tests 7' and 6', where a 500 mm thick base course was used, the non-reinforced test 7' showed a subgrade settlement of 60 mm after 2000 cycles of traffic load, while the reinforced test 6' (GTX1) registered 70 mm after 1000 cycles of traffic load. This indicates that the reinforcement GTX had no impact on subgrade settlement reduction in the reinforced test compared to the unreinforced test.

Conversely, Khoueiry's 2020 experiments, using the same SAT loading methodology but with a smaller 220 mm base course thickness, underscored the significant impact of reinforcement. The disparity in subgrade settlements was evident, ranging from 65-70 mm for reinforced tests to 115 mm for unreinforced tests following 1200 cycles of traffic loads (Figure 4-33a). Subgrade stresses beneath the wheel center ranged from 150 kPa to 250 kPa (Figure 4-33b).

The subgrade vertical stress beneath the wheel center varied between 100 and 105 kPa in the thick platforms of the actual experiments (Tests 6' and 7') Figure 4-29, lower than the 150-250 kPa range observed in Khoueiry's experiments with a smaller base course thickness. Higher vertical subgrade stress levels in Khoueiry's experiments likely engaged the reinforcement to evoke a membrane effect, a

phenomenon absent in test 6'. This highlights the intricate relationship between reinforcement, stress levels, and the behavior of road sections.

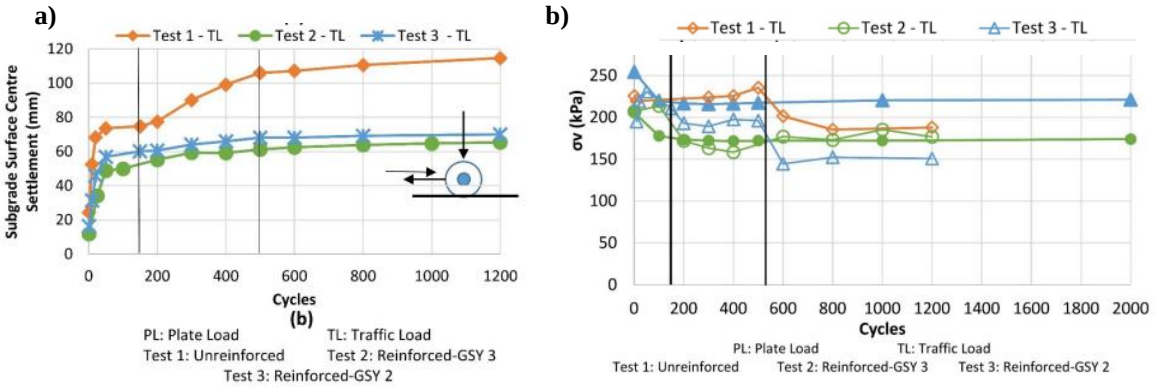

Figure 4-33: a) Subgrade surface centre settlement evolution; b) Subgrade surface centre stress evolution with cycles under the Traffic load test (Khoueiry, 2020).

4.8 Empirical and analytical design methods

The design methods outlined in section 2.6 for determining aggregate thickness primarily rely on factors such as rutting development, cycle number, subgrade and base course stiffness, and the contribution of GSY reinforcement. This section compares the aggregate layer thickness calculated using these design methods to experimental tests conducted as part of this thesis. Key soil and GTX parameters, along with load characteristics, are referenced. The California Bearing Ratio range of the subgrade (CBR_{sg}) in the tested platforms is 1%, and the average CBR of the base course (CBR_{bc}) was approximately 12%. Vertical plate load tests were carried out with a maximum of 10,000 loading cycles. However, the settlement of the subgrade ceased after around 1,000 cycles in the experimental tests. Consequently, the aggregate thickness is specifically compared with the experimental results after 1,000 cycles. The maximum applied load, equivalent to 40 kN, was imposed using a rigid circular plate with a diameter (D) of 300 mm, resulting in a vertical contact pressure of 560 kPa in an area (A). The used GTX1 exhibited a strength value of approximately 1,200 kN/m.

The empirical formula for an unreinforced unpaved road, proposed by Hammitt and III (1970) with a rutting criterion of 75mm previously introduced and referenced in *Eq 2-1* (section 2.6), is reiterated in *Eq 4-1*.

$$h_0 = (0.0236\ logN + 0.0161)\sqrt{\frac{P}{CBR_{sg}} - 17.8\ A} \qquad \textit{Eq 4-1}$$

The calculated unreinforced base course thicknesses for N = 1,000 cycles and N = 10,000, with P set to 40 kN and A representing the circular contact area with a diameter of 300 mm, are presented in Table 4-3. Notably, the unreinforced base course thicknesses exhibit a 33% increase when the applied cycle number increases from 1,000 cycles to 10,000 cycles.

Table 4-3: Calculated unreinforced base course thicknesses using Hammitt and Iii (1970) design method

N (cycles)	h (mm)
1 000	570
10 000	760

Giroud & Noiray (1981) introduced a practical method for designing the aggregate layer thickness, both without reinforcement and with GTX reinforcement (see Figure 4-34). For unpaved roads without reinforcement, two approaches have been presented: (1) a quasi-static analysis leading to a thickness h_0 in *Eq 2-12*, recalled in *Eq 4-2*, of the aggregate layer; and (2) an empirical method considering traffic, providing a thickness h_0' of the aggregate layer empirically derived from test results presented by Webster and Watkins (1977) and presented in *Eq 4-3*. In the case of unpaved roads with GTX, only a quasi-static analysis has been presented, leading to a thickness h of the aggregate layer in *Eq 2-13*, reiterated in *Eq 4-4*. The thickness h′ of the aggregate layer when traffic is considered is yet to be determined in the case of unpaved roads with GTX. The authors propose the following procedure:

$$\pi\, c_u = \frac{P}{2(B + 2h_0 \tan\alpha_0)\,(L + 2h_0 \tan\alpha_0)} \qquad \textit{Eq 4-2}$$

$$h_0{}' = \frac{0.19\,[\log(N) - 2.34(s - 0.075)]}{CBR^{0.63}} \qquad \textit{Eq 4-3}$$

$$(\pi + 2)\, c_u = \frac{P}{2(B + 2h\tan\alpha)\,(L + 2h\tan\alpha)} - \frac{E_g\,\varepsilon}{a\sqrt{1 + (\frac{a}{2s})^2}} \qquad \textit{Eq 4-4}$$

The reduction of aggregate thickness, Δh, resulting from the use of a GTX, is deduced from the quasi-static analyses by *Eq 4-5*:

$$\Delta h = h - h_0 \qquad \textit{Eq 4-5}$$

The thickness h′ of the aggregate layer in the case of a GTX-reinforced, unpaved road when traffic is considered is determined by *Eq 4-6*:

$$h' = h_0{}' - \Delta h \qquad \textit{Eq 4-6}$$

It is crucial to acknowledge a limitation of this procedure: it assumes that the value of Δh does not vary with traffic conditions. However, feedback from this application suggests that the impact of reinforcement becomes more pronounced with increasing loading cycles. To determine the aggregate thickness at a settlement (s) of 75 mm at 1,000 cycles and 10,000 cycles, and at a settlement of 100 mm at 1,000 and 10,000 cycles, the above procedure is employed. P is taken as equal to 80 kN, equivalent to the axle loads, as P in the formula represents the load applied on the two contact areas of the two wheels; hence, the load applied in one contact area is 40 kN. The loading parameters are presented in Figure 4-34. Additionnaly, tanα is taken as equal to 0.6 (as recommended by the authors), E_g is taken as equal to 1200 kN/m, equivalent to the tensile modulus of the GTX_1, and ε is calculated based on *Eq 2-8* and *Eq 2-9* (section 2.6). is also presented Table 4-4 presents the calculated unreinforced and reinforced base course thicknesses (h_0' and h′). Notably, after 1,000 cycles, the GTX demonstrates its effectiveness by reducing base course thickness

by 21% for a settlement of s = 75 mm and 26% for s = 100 mm. As the loading cycles increase to 10,000, the GTX continues to play a significant role, resulting in a 14% reduction for s = 75 mm and 19% for s = 100 mm. These results emphasize the impact of GTX reinforcement in reducing base course thickness.

Table 4-4: Calculated unreinforced and reinforced base course thicknesses using Giroud & Noiray (1981) design method

N (cycles)	s (mm)	h_0 (mm)	h (mm)	Δh (mm)	h_0' (mm)	h' (mm)
1,000	75	275	160	115	570	450
	100	275	130	145	560	415
10,000	75	275	160	115	760	650
	100	275	130	145	750	605

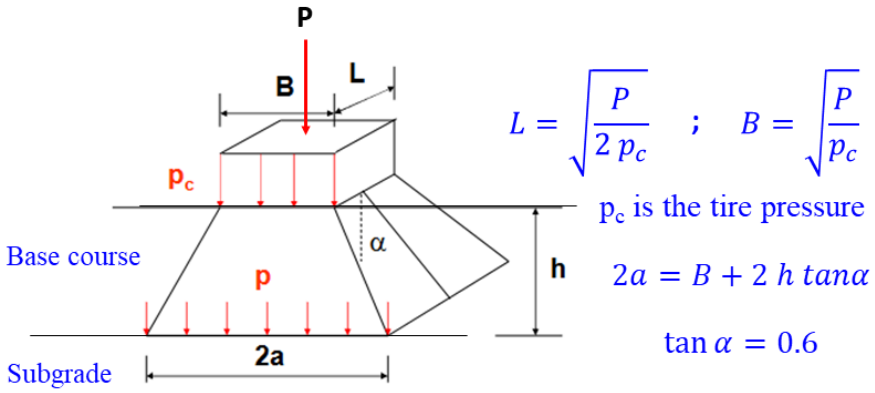

Figure 4-34: Illustration of an unpaved road section applied loading parameters and loading distribution parameter

Giroud and Han (2004 a & b) proposed the *Eq. 2-17* and reiterated in *Eq 4-6:*

$$h = \frac{0.868 + (0.661 - 1.006\,J^2)\left(\frac{r}{h}\right)^{1.5} \log N}{1 + 0.204\,(R_E - 1)} \times \left[\sqrt{\frac{\frac{P}{\pi r^2}}{\left(\frac{s}{f_s}\right)\left\{1 - 0.9\,exp\left[-\left(\frac{r}{h}\right)^2\right]\right\} N_c\,c_u} - 1}\right] r \qquad \textit{Eq 4-6}$$

For more details regarding this analytical method refers to section 2.6. In the case of no reinforcement, the Giroud and Han (2004) analytical method was applied with the following parameters: N_c=3.14; CBR_{sg}=1; CBRbc=12; P=40kN; r=0.15m (resulting in a contact pressure of 560 kPa); J=0m.N/°; s=75mm and 100 mm. In this method, the subgrade soil is assumed to be saturated and possess low permeability, hence its bearing capacity is considered equal to $m \cdot N_C \cdot c_u$, where c_u is taken as equal to 30 CBR_{sg}, equivalent to 30 kPa in this instance.

Similar conditions were applied in the reinforced case using reinforcement (GTX1), with N_c=5.14 because it is a reinforced case with GTX, and J=0m.N/° as it is a parameter specific to a GGR. However, it

is crucial to highlight that this analytical method is calibrated for specific GGRs characterized by the node stability factor (J). Calibration is essential for its application in the case of GTXs or other GGRs that do not possess node stability. Table 4-5 provides the calculated unreinforced and reinforced base course thicknesses using the Giroud & Han (2004 a & b) method. After 1,000 cycles, the GTX demonstrates its effectiveness by reducing base course thickness by 16 % for a settlement of s = 75 mm and 18% for s = 100 mm. As the loading cycles increase to 10,000, the GTX continues to play a significant role, resulting in a 17% reduction for s = 75 mm and s = 100 mm. These findings underscore the significant impact of GTX reinforcement in minimizing the base course thickness.

Table 4-5: Calculated unreinforced and reinforced base course thicknesses using Giroud & Han (2004 a & b) design method

N (cycles)	s (mm)	Unreinforced h_0 (mm)	Reinforced h (mm)
1,000	75	335	280
	100	280	230
10,000	75	445	370
	100	375	310

Leng and Gabr (2006) formulated the analytical equation (*Eq 2-18*), reiterated in *Eq 4-7*, to determine aggregate thickness for both unreinforced and GGR-reinforced cases. However, their publication does not address GTX reinforcement cases.

$$h = \frac{\left(1 + \left(\left(\frac{r}{h}\right)^{0.81}\left(0.58 - 0.000046\,{J_t}^{4.5}\right)\right)\log N\right)}{\tan\alpha_1} \times \left(\sqrt{\frac{p_c}{\left(\frac{s}{f_s}\right)\left(1 - e^{\left(-0.78\frac{r}{h}\right)}\right) N_c\, c_u}} - 1\right) r \qquad \textit{Eq 4-7}$$

Additionally, the analytical approach of Leng and Gabr (2006) was applied with parameters consistent with those used in the Giroud and Han (2004) method. In fact, N_c is set to 3.8 in the unreinforced case, and J_t, representing the average GGR tensile strength at 2% strain, is assigned a value of 0 kN/m. Similar to the previous method, the bearing capacity is determined as $m \cdot N_C \cdot c_u$, where c_u equals $30 \times CBR_{sg}$ (30 kPa in this case). According to the authors' recommendation, the change in the base course stress distribution angle α, shifting from α_1 at 45.37° to an α_n of 27.55° after 10,000 cycles. In the analytical method of Leng and Gabr (2006), when introducing a GTX instead of a GGR, Nc was set to 5.14, equivalent to the value proposed by Giroud and Han (2004) for GTX. However, the expression involving GTX characteristics yields a negative result for J_t >11kN/m. Consequently, the comparison with empirical and analytical methods was exclusively conducted for unreinforced conditions. Table 4-6 outlines the calculated unreinforced base course thicknesses using the of Leng and Gabr (2006).

Table 4-6: Calculated unreinforced base course thicknesses using Leng and Gabr (2006) design method

N (cycles)	s (mm)	Unreinforced h_0 (mm)	Reinforced h (mm)
1,000	75	890	-
	100	730	-
10,000	75	980	-
	100	810	-

In summary, Table 4-7 provides an overview of the outcomes of the design methods in terms of base course thicknesses compared to two experimental tests (T_5 and T_7): one reinforced with GTX1 with base course thickness of 300 mm and the other unreinforced with 500 mm of base course thickness. Both experimental tests exhibited approximately 100 mm of subgrade settlement at 1000 cycles.
For the unreinforced base course with s=75mm after 1000 cycles, the Giroud & Han (2004 a & b) method estimated a base course thickness of 335 mm, significantly less than Hammitt and Iii (1970) (570 mm) and Giroud and Noiray (1981) (890 mm) methods. The same trend is observed for s=100mm, although Hammitt and Iii (1970) method becomes invalid as it is designed for settlement less than 75mm. Leng and Gabr (2006) overestimates the aggregate thickness (730 mm) compared to the experimental thickness (500 mm), while Giroud & Han (2004 a & b) underestimates it (280 mm). Notably, Giroud and Noiray (1981) shows a closer estimate (580 mm) to the experimental thickness of the unreinforced test (500 mm).
For the reinforced base course thickness, Giroud and Noeiry (1981) overestimates the aggregate thickness (415 mm) compared to the experimental value (300 mm). This discrepancy could be attributed to the fact that the effect of reinforcement was only considered under static loading conditions and not dynamic loading conditions. Conversely, the Giroud and Han (2004) method (230 mm) underestimates the aggregate thickness compared to the experimental value (300 mm). This difference in the base course thickness between the performed tests and the design methods explain the need to more research to develop a new method or imporove these methods.

Table 4-7: The comparaison between calculated unreinforced base course thicknesses using the design methods and the experimentation

	s = 75 mm		s = 100 mm	
	Unreinforced h_0 (mm)	Reinforced h (mm)	Unreinforced h_0 (mm)	Reinforced h (mm)
Hammitt and Iii (1970)	570	-	-	-
Giroud & Noiray (1981)	570	440	560	415
Giroud & Han (2004 a & b)	335	280	280	230
Leng and Gabr (2006)	890	-	730	-
Experimental (vertical loading)	-	-	500	300

4.9 Conclusions

The employed installation and compaction protocols demonstrated successful utilization in the construction of all test sections, ensuring repeatability and homogeneity in the unpaved road sections. Quality control

tests were implemented to monitor the installed soil properties, resulting in consistent subgrade soil water content and a homogeneous subgrade layer across all tests, as indicated by shear vane and static penetrometer tests. However, dynamic cone penetrometer tests revealed variations in the compaction of the granular platform, with average CBR values consistently 10% to 15% lower than the required CBR for this application. Despite this difference, excluding the initial settlement tests from the settlement comparison analysis could mitigate the impact.

Furthermore, the plate load tests, and traffic load tests provided detailed results. By performing identical tests on configurations with GTX1 and GTX2 reinforcement, the repeatability of the tests was verified in terms of settlement of the base course surface and the subgrade surface.

The comparison between reinforced and unreinforced tests under cyclic vertical loading yielded the following findings:

1) The 300 mm platform reinforced with GTX1 demonstrated the best performance, achieving a 55% reduction in base course settlement compared to the unreinforced platform of the same thickness after 1000 cycles. It also reduced the settlement 25% compared to the 500 mm unreinforced platform after 10,000 cycles.
2) The 300 mm platform reinforced with GTX2 exhibited a 46% reduction in settlement compared to the unreinforced platform after 1000 cycles, but it experienced more settlement than the 500 mm unreinforced platform after 10,000 cycles when considering initial settlement. However, after removing the settlement due to the first two cycles, the 300 mm reinforced with GTX2 outperformed the 500 mm unreinforced platform after 100 cycles and reduced the settlement by 22% compared to the 500 mm unreinforced platform after 10,000 cycles.
3) GTX1, the stiffer GTX, proved to be more efficient in reducing settlement compared to GTX2.
4) The 500 mm platform reinforced with GTX1 did not show any improvement in settlement reduction compared to the unreinforced platform of the same thickness, even after excluding initial settlement values.

The validation of findings from the vertical plate load test with traffic loads has yielded valuable insights regarding the performance of different configurations under varying loading conditions. Notably, the reinforced 500 mm thick GTX1 platform showed no improvement in settlement reduction compared to the unreinforced platform of the same thickness under traffic load, which is consistent with the results observed in the plate load test. Conversely, the 300 mm thick GTX1-reinforced platform exhibited a faster rate of settlement evolution and higher settlements value after 3000 cycles of traffic load compared to the 500 mm thick unreinforced platform. While, under vertical cyclic load, the 300 mm reinforced platform with GTX1 demonstrated less settlement at the base course surface and subgrade surface compared to the 500 mm unreinforced platform. These findings underscore the importance of considering specific factors when assessing settlement reduction in both vertical and traffic load scenarios.

In the plate load tests, the initial cycles played important role in enhancing the compaction of the base course beneath the plate load. This compaction helps contributing to effective load-distribution within the base course. However, when transitioning to the simulation of traffic load using the Simulator Accelerated Load (SAT), a distinct phenomenon emerges. The localized nature of the vertical load under the plate is replaced by dynamic forces that lead to uplifting effects around the wheel's centerline. This difference in loads type led to an accelerated rate of the base course thickness deformation for the base course subjected to the traffic load compared to base course subjected to the plate load. This heightened deformation underscores a potential weakness in the base course, resulting in compromised load distribution. Consequently, the compromised load distribution undermines the capacity of the GTX to effectively initiate the tension membrane effect. This explanation can potentially validate by the effectiveness of the GTX1 reinforcement in Test 5, where a reduced settlement was observed compared to the unreinforced Test 7 featuring a thicker base course under plate load conditions. While, in Test 5', also reinforced with GTX1 and sharing the same base course thickness as Test 5, no settlement reduction was apparent when compared to Test 7', which similarly shared the same base course thickness, but under traffic load conditions.

Finally, the lack of impact of the GTX1 in the thick platform under traffic load can be related to relatively low value of GTX deflexion that was around 60 mm (Test 7') and this range may not sufficiently solicit the GTX to initiate the membrane tension effect. An additional factor to consider is that the GTXs were not anchored, which theoretically limits their contribution from the initial settlement stage.

5. Chapter 5. Numerical modelling

5.1 Introduction

The reinforcement using GSYs has been a subject of various research. The coupling method of discrete elements and finite elements, as introduced by Villard et al. in 2009, has been used and has shown an important role in advancing the understanding of these structures. In this numerical study, this coupling model is used to investigate the behavior of the granular mattress reinforced by GSY over soft subgrade soil subjected to cyclic loading.

The chapter is initiated by providing a comprehensive explanation of the FEM-DEM coupling method, as initially introduced by Villard et al. in 2009. The numerical model is thoroughly described and characterized based on insights derived from laboratory experiments, observations of material behaviors, and prior applications by authors of this coupling method. A sensitivity analysis is undertaken to select the two interdependent parameters: the load increment and the damping factor. These two parameters wield a profound influence on simulation stability and accuracy, elevating the pursuit of the right balance between them to paramount importance.

Furthermore, two calibration processes are performed to confront the numerical model with the experimental setup. The first calibration is dedicated to refining the subgrade soil behavior law within the numerical model. Its objective is to streamline the simulation process, minimizing the number of loading-unloading cycles while faithfully reproducing subgrade settlement patterns akin to those observed in extensive experimental tests. The second calibration focuses on enhancing the granular mattress within the simulation by introducing adhesion between its grains to increase their resistance to external forces. This calibration encompasses a thorough comparative analysis, assessing numerical and experimental findings at different loading stages. It involves a detailed examination of settlement and vertical stress profiles after the 1st and last cycles, as well as the tracking of their evolution across multiple cycles.

This chapter provides a detailed analysis of a numerical model able to simulate the behavior of a GTX -reinforced granular platform on soft subgrade soil under cyclic loading. It evaluates the model's performance in providing valuable insights into the system's complex interactions. The study covers the examination of vertical and horizontal particle movements in the granular mattress, as well as patterns of particle rearrangement. It explores principal stress orientations and contact forces within the mattress. Moreover, the analysis includes GTX displacement, deflection, and strain, revealing its contribution to reinforcement mechanisms and changes in load transfer. An evaluation of the frictional interaction between the GTX and the mattress grains, as well as the mechanisms related to the tensioned membrane effect, are investigated throughout the loading cycles.

5.2 Description of the coupled DEM-FEM method and overview the numerical model incorporating this method

To simulate a reinforced granular platform with GTX laying over soft subgrade soil, the study utilizes the FEM-DEM coupled numerical model introduced by Villard et al. (2009) which is based on the definition of the discrete properties of the granular material and the continuous characteristics of the GSY, considering its fibrous nature. Additionally, the model accounts for various types of interaction, such as rolling, sliding, and friction, between the soil particles and the finite elements that represent the behavior of the GSY.

5.2.1 Description of the coupled DEM-FEM method

5.2.1.1 Modelling of soil using the discrete element

Modelling soils through a set of discrete particles that interact with each other at their contact points allows for representing their heterogeneity and real mechanisms, such as particle rearrangement (expansion or compaction) or failure mechanisms (shear or block sliding).

The molecular dynamic method developed by Cundall and Strack (1979) is used to manage the interaction between discrete elements of the granular mattress. According to this method, the grain particles are considered non-deformable but can slightly interpenetrate at the contact level. When two grains interact, the contact forces are determined by normal stiffness (k_n) and tangential stiffness (k_t) along with an intergranular friction angle (ϕ_{int}) and an adhesion (a) as showed the Figure 5-1. It's worth mentioning that the normal contact stiffness k_n (or tangential contact stiffness k_t), illustrated in Figure 5-1, between two spheres of radii r_i and r_j, expressed in N/m, is defined as a function of the normal rigidity, K_n, (or tangential rigidity, K_t,) of the two constitutive materials of the spheres in contact in N/m^2 as showed the *Eq 5-1*.

$$k_n = \frac{K_n}{(r_i + r_j)} (r_i * r_j) \qquad \textit{Eq 5-1}$$

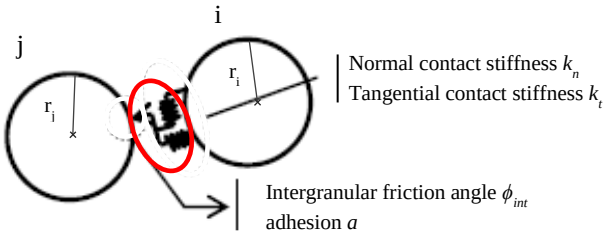

Figure 5-1: Contacts between two spherical particles

The relation between the contact forces (divided into normal and tangential components) and the relative displacements follows a linear elastic-plastic behaviour. In fact, for normal interaction, a classical linear elastic contact law is used, where the normal contact force component (F_n) is related to the normal overlap (u) between the grains by the normal contact stiffness (k_n), detailed in the *Eq 5-2*. Regarding tangential interaction, a perfect elastic-plastic law is employed.

$$F_n = k_n\, u \qquad \textit{Eq 5-2}$$

The incremental tangential force component (ΔF_t) is related to the incremental relative tangential displacement (Δv) through the contact tangential stiffness (k_t), given by *Eq 5-3*. The shear force at a given time step (Δt) is updated by adding the shear force of the previous time step with the incremental vector ΔF_t.

$$\Delta F_t = k_t\, \Delta v \qquad \textit{Eq 5-3}$$

The contact shear stiffness (k_t) can be related to the normal contact stiffness (k_n) by a coefficient α, presented in the *Eq 5-4*.

$$k_n = \alpha\, k_t \qquad \textit{Eq 5-4}$$

After establishing the forces at the contact level, it becomes necessary to consider the concept of failure. In tension, failure is characterized as the disconnection between the two spheres. The tensile failure (detachment or loss of contact) is not reached until the normal contact force F_n exceeds a limiting value defined as the product of allowable stress threshold T_n and the average contact area A_{int}. A_{int} is either physically known or arbitrarily defined by the *Eq 5-5*:

$$A_{int} = \pi\, min((r_i)^2, (r_j)^2) \qquad \textit{Eq 5-5}$$

where r_i and r_j are the respective radii of spheres *i* and *j* that interact with each other.
After the tensile failure of the contact, the normal and shear components of the interaction forces are automatically reset to zero. For shear failure, the Mohr-Coulomb criterion defined in *Eq 5-6* is implemented to restrict the magnitudes of the shear forces.

$$F_{tmax} = a * A_{int} + F_n * tg(\phi_{int}) \qquad \textit{Eq 5-6}$$

Indeed, micromechanical parameters used to define the Mohr-Coulomb criterion in the computational code are as follows: the adhesion (a) and the micromechanical friction angle (ϕ_{int}). In the case of a non-cohesive contact where a is equal to zero, *Eq 5-6* become $F_{tmax} = F_n * \mathrm{tg}(\phi_{int})$ with $\left|\overrightarrow{F_t}\right| \leq \left|\overrightarrow{F_n}\right| tg(\phi_{int})$.

An iterative procedure alternating between resolving Newton's second law of motion and updating the interaction forces at each contact point as illustrated in Figure 5-2 is applied. The motion equations are integrated using an explicit centered finite difference algorithm with a small-time increment (Δt) to ensure convergence. The problem is solved iteratively over time through phases of contact detection, calculation of interaction forces of the discrete elements in contact, and then computing particle positions and velocities for the next time step. Two parameters are introduced in the equations of motion to facilitate and optimize convergence of the calculations: the damping factor K_a, used in *Eq 5-7*, to limit vibrations and dampen the propagation of elastic waves, and the critical integration factor K_{ic}, used in *Eq 5-8* to define the value of Δt based on the critical time step.

$$K_a F_i = m\ddot{x}_i \qquad \textit{Eq 5-7}$$

Where F_i is the force applied to the particle, *m* is the masse of the particle, and $\ddot{x}_i$ is the acceleration of the particle.

$$\Delta \mathrm{t} = K_{ic} \sqrt{\frac{m}{2K}} \qquad \textit{Eq 5-8}$$

Where *K* is the stiffness of the particle. The default value employed subsequently K_{ic} is 0,5.

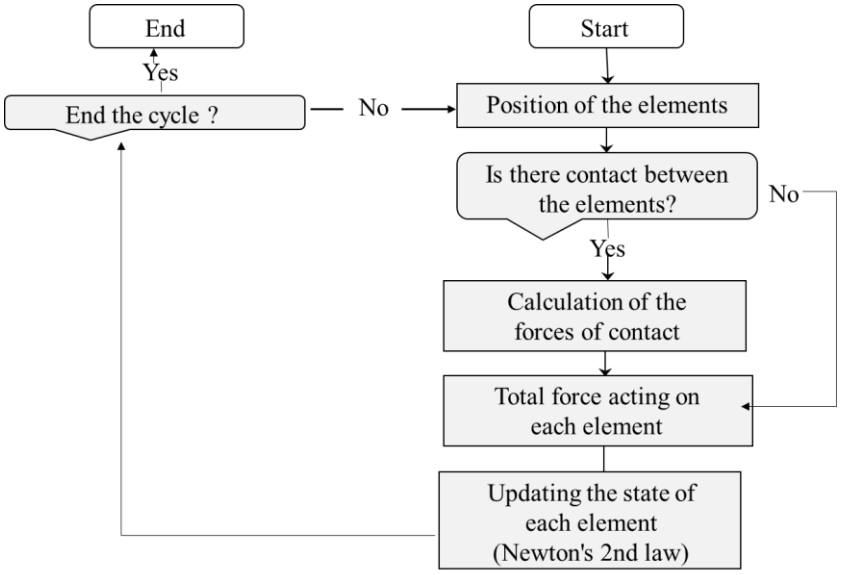

Figure 5-2: Calculation cycle in DEM method

5.2.1.2 Modelling of the geosynthetic sheet

The GSY sheet is modelled using thin triangular elements joined together, forming a continuous contact surface before and during the stretching of the sheet (Figure 5-3). To ensure this regularity and continuity, cylinders and spheres with a diameter equal to the thickness of the sheet element are placed at the edges and nodes of each element. This arrangement allows frictional forces to be maintained when a soil element moves from one sheet element to another. Each triangular element of the GSY comprises fibres with varying orientations forming a plane. The mechanical behaviour of this fibre network is obtained by superposition of behaviours from each fibre direction, with no sliding between the fibres. The fibres' mechanical behaviour is characterized by non-linear elasticity, where the compression elasticity modulus is significantly lower than the tensile elasticity modulus (Villard et Giraud, 1998). Moreover, there is no bending stresses.

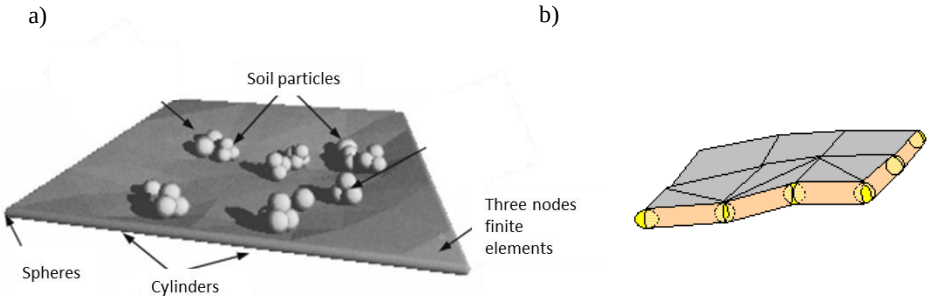

Figure 5-3: a) Numerical model of the GSY elements; b) Close-up on the triangular elements of the GSY sheet (Huckert, 2014)

Within the iterative calculation process embedded in the coupling code, a nonlinear force-displacement relationship, as depicted in *Eq 5-9*, is employed for every triangular finite element. This fundamental relation governing the mechanical behaviour of triangular elements (Villard et Giraud, 1998) helps define the contact forces between jointed finite elements, based on stretching and displacement of each node.

$$\{F_e\} = \{K_e\} * \{u_e\} + \{R_e\} \qquad \textit{Eq 5-9}$$

Where $\{F_e\}$ represents the forces acting on the nodes of an element, $\{u_e\}$ denotes the nodal displacements of the element, $\{K_e\}$ is the elementary matrix of rigidity dependent on the final position of the three nodes, and $\{R_e\}$ represents a corrective vector force resulting from the large displacement formulation. Moreover, each group of fibres with the same direction is assigned a specific behaviour law, where the stiffness J of the fibres relates the tensile force T to the deformation ε. As can be seen in Figure 5-4, numerous behaviour laws have been implemented: linear law with one (a) or two slopes (b) or more sophisticated behaviour law (c).

The behaviour of the sheet elements is governed by a resolution algorithm using a time increment Δt, similar to the one used for discrete elements. The displacement for each finite element is managed using Newton's second law of motion.

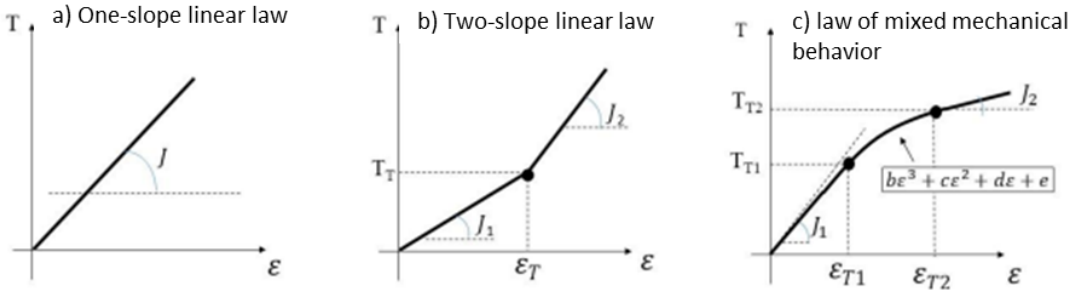

Figure 5-4: Tensile behaviour laws along a fibre direction: a) linear with single stiffness, b) linear with Dual stiffnesses, c) non-linear sophisticated (Delli Carpini, 2021)

5.2.1.3 Interaction between the soil particles and the geosynthetic sheet

The interaction between the soil and the GSY follows a contact law similar to the DEM method used for grain interactions. The contact forces consist of normal F_{ni} and tangential F_{ti} components with respect to the contact plane, influenced by the contact stiffness and relative displacements between the contacting elements. The normal contact stiffness k_{ni} (in N/m) between a particle of radius r_i and a sheet element depends on the modulus of compressibility E of the GSY sheet (in N/m²), its thickness e (in m), and the contact influence area s_{int} between the soil particle and the sheet element (πr_i^2 in m²). It is defined in *Eq 5-10* as:

$$k_{ni} = \frac{E}{e} s_{int} \qquad \textit{Eq 5-10}$$

The normal contact force is expressed by Eq *5-11*:

$$\{F_{ni}\} = k_{ni} * \{U_{ni}\} \qquad \textit{Eq 5-11}$$

where $\{U_{ni}\}$ represents the overlap between the sheet element and the soil particle.

The tangential incremental contact force $d\ (\overrightarrow{F_{tl}})$ between a soil particle and the GSY sheet is determined in a similar way as the tangential contact forces between soil particles. The tangential forces are updated incrementally at each time increment (Δt), considering the increment of force calculated using *Eq 5-12*.

$$\frac{d\ (\overrightarrow{F_{tl}})}{d\ (\overrightarrow{U_{tl}})} = k_{ti} \text{ with} \left|\overrightarrow{F_{tl}}\right| \leq \left|\overrightarrow{F_{nl}}\right| tg(\delta) \qquad \textit{Eq 5-12}$$

where $d\ (\overrightarrow{U_{tl}})$ represents the tangential incremental displacement overlap between the soil particle and the sheet element, k_{ti} (in N/m) the tangential contact stiffness and δ is the friction angle between the soil particle and the GSY.

Macroscopic behavior characterization of soil-GSY contacts relies on experimental laboratory tests, leading to a simple friction law relating tangential stress τ and relative displacement (U) as showed in Figure 5-5 . τ_{max} is the maximum tangential stress, U_0 represents the relative displacement needed to fully mobilize friction and δ is the macroscopic friction angle between soil and GSY as defined in the numerical model.

Similar to the algorithm used for the soil particles, the interacting contact forces are determined from updated overlaps between sheet elements and soil particles at each time increment. Newton's second law of motion provides acceleration, speed, and displacements of each element between successive time increment (Δt). This process iterates until convergence.

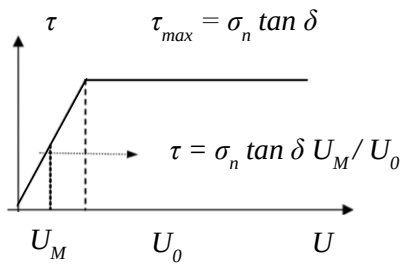

Figure 5-5: Friction interface criterion

5.2.2 Calculation process and general post-processing routines

The SDEC code is designed to operate efficiently on Windows platforms. It comprises a series of modules that systematically generate the initial state and conduct the precise calculations pertinent to the selected application. The primary module undertakes the creation of the fundamental numerical sample through the REFD method (as elaborated in bibliography, Chapter 2). Within the data files, the user provides essential inputs including problem geometry, desired porosity, particle size, number and type of clump elements, behavior laws, and corresponding failure criteria. Upon the generation of elements, the second module facilitates the execution of the chosen application. Pertinent information to be provided includes:

- Identification of data files and their backup files.
- The micromechanical parameters on which the behavior laws and fracture mechanisms are based.
- Option to load contacts from a prior calculation step.
- Maximum permissible iterations and the recording frequency.

The results of computations are stored in either ASCII or binary format files at each time increment. These files contain essentially data for subsequent computations and data analysis: contact forces, positions, velocities, and accelerations for soil particles, and tensions, deformations, and node positions for GSY elements.

5.2.2.1 General post-processing routines

To analyse the extensive and voluminous numerical results, MATLAB procedures were developed during this thesis for processing SDEC results and providing a general post-processing approach. These procedures generate graphical plots for various characteristic quantities during different recording stages:

- Displacements of the mattress clusters.
- Chains of contact forces within the granular material.
- Displacements of the supporting soil.
- Tension and strains in the GSY reinforcement.
- Contact force at the interface between by the soil of the mattress and the GSY
- Stress on the upper and the lower face of the GSY, and the stress transferred by tension membrane effect.
- Stresses within the mattress (explained below).
- Densification or Bulking of the mattress (explained below).
- These post-processing routines collectively assess the kinematic behavior and load transfers within the studied structures.

5.2.2.2 Calculation of stresses within a discrete granular assembly

Stresses within the granular mattress are determined using the Weber formula (1966), providing the stress tensor within a representative volume V that encompasses a given number of particles:

$$\sigma_{ij} = \sum_{\beta=1}^{N_c} \frac{1}{V} f_\beta^i \; l_\beta^j \qquad \textit{Eq 5-13}$$

where N_C represents the number of contacts within the volume V, f_β^i is the projection onto axis i of the contact force at contact β, and l_β^j is the projection onto axis j of the contact branch vector for contact β. This branch vector can have various interpretations. Regardless of the contact type, the branch vector is defined relative to a particle and a contact, representing the characteristic length connecting the particle's centre of gravity to the contact point (Figure 5-6).

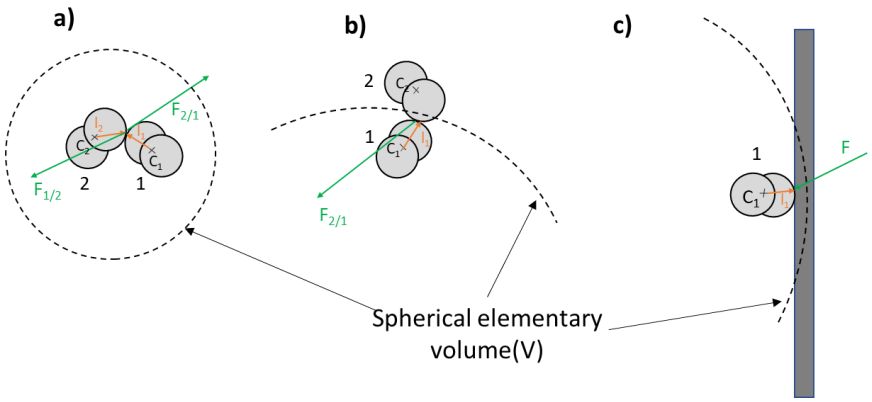

Figure 5-6: Stress calculation within granular mattress: branch vector and corresponding contact force for contacts between: (a) two spheres within the computational volume, (b) two spheres with only one within the computational volume, (c) or a contact between a sphere in the computational volume and a wall of the model

5.2.2.3 Densification and bulking of the granular material during simulation

A random point cloud (around hundreds) is generated within the elementary volume (Figure 5-7). Each randomly generated point is tested to determine whether it lies within a discrete soil particle or an empty space in the granular material. Ultimately, the ratio of the number of randomly placed points within a discrete element of the measurement sphere to the total number of randomly generated points in the measurement sphere yields a numerical value of porosity.

The state of relative density within a calculation volume is subsequently calculated based on the local porosity of the point at the current cycle ($n_{local,N}$) and the initial local porosity ($n_{local,init}$) of the calculation point. These porosities provide the effective material densities within the calculation volume ($D_{local,N}$) at the current cycle and ($D_{local,init}$) at the initial state. The local relative density state $D_{R,local}$ is then given by:

$$D_{R\_local} = \frac{D_{locale,N}}{D_{locale,init}} \qquad \textit{Eq 5-14}$$

For a relative density value greater than 1, the material densifies within the spherical calculation volume. When the relative density is less than 1, the material undergoes bulking or shearing.

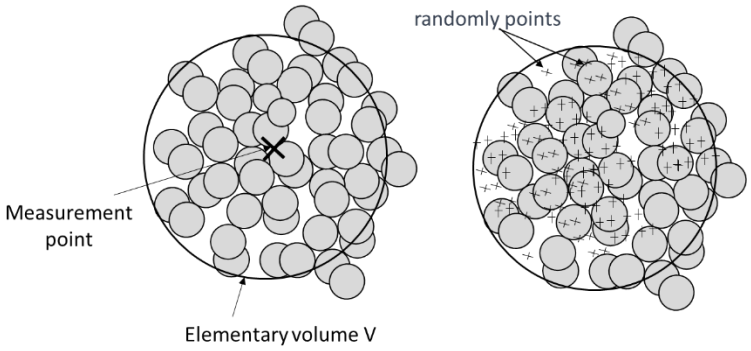

Figure 5-7: Principle of calculating local porosity within a granular material

5.2.3 Description of the employed numerical model

The used basic numerical model, illustrated in Figure 5-8, is 1.8 m long, 1.8 m wide and includes, from top to bottom:

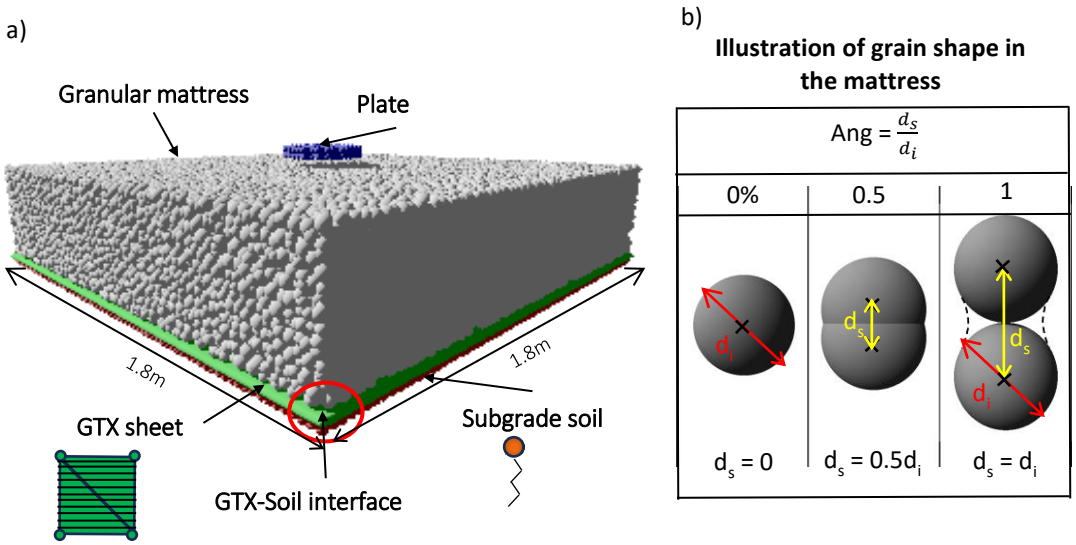

Figure 5-8: a) Geometry of simulated sample (the GTX finite elements shown have fibers in only one direction) and b) illustration potential grain shapes for simulation

1. an assembly of clumps describing the behavior of the granular mattress and interacting through contact points,
2. thin, finite, triangular elements describing the membrane and tension behavior of the GTX,
3. a layer of spheres regularly distributed in a square mesh at the base of the model and associated to springs to represent the supporting soil which displace vertically (no rolling admitted).

Horizontal and vertical frictionless walls are used on the lateral sides to define the boundary conditions. A circular rigid plate (Diameter=0.3 m) is placed at the center of the granular mattress to apply static load (cyclic).

5.2.3.1 Granular mattress

The granular mattress exhibits numerous intergranular parameters, including the number of particles composing a grain of soil (i.e. cluster), angularity (*Ang*), porosity (*n*), and microscopic contact parameters (ϕ_{int}, a, k_n, k_t), among others. The primary objective of employing this mattress is to emulate the mechanical macroscopic behavior of experimental soil, a process adjusted through a calibration procedure.
Within the mattress, individual grains are represented as clusters, each consisting of two overlapping and unbreakable spheres with identical diameters (d_i), where d_s represent the distance between the centers of these two overlapping spheres (Figure 5-8). To introduce variability in sphere diameters within the clusters, a uniform distribution is applied within a specified range, ranging from a minimum diameter (d_{n_min}) to a maximum diameter (d_{n_max}), resulting in an average diameter denoted as $d_{n\_average}$. This distribution is implemented to mitigate any tendencies toward organized particle arrangements.

Angularity (*Ang*) is defined as the ratio between d_i and d_s. It quantifies the concave aspect of the cluster element. Figure 5-8b illustrates the shapes of elements composed of two spheres for various angularity values. When the angularity is 0%, the element closely resembles a sphere, and the spheres become tangent to each other when the angularity reaches 100%.
Regarding the porosity of the cluster arrangement, a numerical porosity value is selected from a range of porosities, extending from a maximum value (n_{max}) to a minimum value (n_{min}), which are determined through the REDF method.

It is worth noting that a selection of values for all the aforementioned parameters will be necessary to accurately simulate the macroscopic behavior of the granular soil when subjected to loading. Numerical triaxial tests can serve to study the macroscopic behaviour of the granular mattress. For simulating the triaxial compression tests, the numerical samples encompass a number of clusters arranged to achieve the desired porosity using the REDF procedure. The execution of the numerical triaxial compression test occurs in two successive phases: firstly, the application of an isotropic confinement stress σ_3 on the sample walls, and subsequently, the application of compressive stress in a single direction and horizontal stresses on vertical walls to replicate the deviatoric phase. This is achieved by simultaneously displacing the horizontal walls at a specified velocity and to adapt the position of the vertical walls to maintain the confining pressure value.

5.2.3.2 GTX sheet (GTX)

At the base of the granular mattress, a GTX is positioned, simulated by deformable triangular plane elements, following the principles described in section 5.2.1.2. In the simulations, the GTX sheet will include two orthogonal reinforcement directions (longitudinal direction and transverse direction).

Moreover, A linear model will be employed to describe the behavior of the GTX, incorporating a single stiffness value for each direction (J_x for the longitudinal direction parallel to x-axis and J_y for the transverse direction parallel to y-axis). J_x and J_y are assumed to be equivalent to stiffness values at a 2% strain level in the machine direction and the transverse direction. The rationale for opting for the 2% strain level is rooted in the feedback indicating that a suitable reinforced GTX in the unpaved road sections experiences strain levels around 2%.

5.2.3.3 Subgrade soil

A layer of spheres, with each sphere associated with a spring, is situated beneath the GSY sheet. This arrangement is employed to represent the supporting soil within the model. The spheres move only vertically and allow integrating frictional mechanisms between the sheet and the supporting soil. The mechanical behaviour of the subgrade soil is a function of the stiffness of the spring that can change during cycles.

An experimental cyclic plate load test has been conducted, as elaborated upon in section 3.3.1.2 and presented in Figure 3-7 to study soil's stiffness evolution under cyclic loading. The observed soil response patterns during loading cycles can be summarized as follows: Initially, the soil exhibits an initial stiffness during the first loading cycle, then the stiffness progressively increases over subsequent cycles. After a certain number of cycles, this stiffness stabilizes and remains constant, indicating a transition from plastic to elastic soil behavior. Notably, the trends of soil response during unloading suggest that changes in unloading stiffness occur within a relatively narrow range throughout the cycles, demonstrating a relatively consistent behavior over cycle. As the soil approaches an elastic state after multiple cycles, the unloading stiffness aligns with the loading stiffness within the same cycle.

All the aforementioned observed trends have been utilized to develop a simplified behavioral model presented in *Eq 5-15*.

$$k_N = k_1 + \frac{N-1}{N_0}(k_u - k_1) \qquad \textit{Eq 5-15}$$

where k_N corresponds to the rigidity of the N^{th} loading cycle, k_1 represents the rigidity of the 1st loading cycle, k_u is the rigidity of all the unloading cycle, N denotes the number of the applied cycle and N_0 is threshold cycle number i.e., the number of cycles at which the subgrade soil became elastic (stops to settle). In the experimentation (T_1, T_2, T_3, T_4, and T_5), the settlement of the subgrade soil evolves with the cycles up to 500 cycles with a decreasing deformation rate (Figure 4-18). After 1000 cycles, the increment of settlement becomes almost negligible. Nevertheless, all the tests were concluded after 10,000 cycles, except for T_2.

Given the challenge of precisely replicating the complete count of experimental cycles within the numerical simulation, a calibrated behavior law for the subgrade soil will be employed in the numerical simulations. This law mirrored a similar range of maximum subgrade settlement achieved in the experimental but with fewer cycles than the experimental cycles. This approach facilitated a comprehensive examination of the responses exhibited by the granular mattress and the GTX, providing insights into the reinforcement mechanism.

5.2.3.4 GTX - Soil interfaces

The parameters that govern the interface between GTX and the surrounding soil play a crucial role in determining how GTX interacts with both the underlying subgrade and the upper granular mattress. Specifically, $\delta_{GTX\text{-}Subgrade}$ represents the friction angle between GTX and the lower subgrade soil, while $\delta_{GTX\text{-}Clusters}$ represents the friction angle between GTX and the upper mattress. The determination of these parameters in the thesis work is accomplished through direct shear tests and pull-out tests, outlined in section 3.3.4.

5.2.3.5 Applied loads and cycle number

The maximum applied load is 40 kN and is selected to give a plate-mattress contact pressure equal to 560 kPa equivalent to contact pressure in the experimentation (Figure 5-9). Numerous cycles will be applying on the circular loading plate.

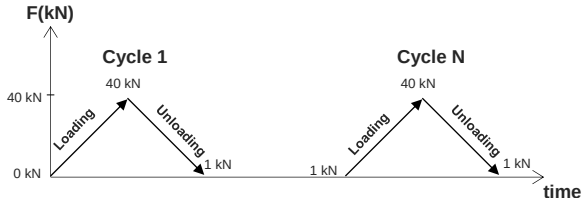

Figure 5-9: Applied loading cycles on the granular mattress surface

5.3 Confrontation between the numerical model and the experimental setup

5.3.1 Introduction

In this section the confrontation between the numerical model and the experimental setup will be discussed. The numerical model will be characterized, drawing upon laboratory tests, material behavior observations, and insights from the literature where the numerical model has been employed by authors in various applications (Villard et al. ,2009). Two primary calibrations will be performed.

The first calibration will focus on the subgrade soil behavior law within the numerical model. The goal is to reduce the number of loading-unloading cycles while achieving subgrade settlement patterns that closely align with those observed in extensive experimental testing. This step will entail the refinement of essential parameters to harmonize the model's performance with the experiments.

The second calibration will be dedicated to the granular mattress within the simulation. The initially purely frictional nature of the granular mattress will be shown insufficient to withstand applied loading. Therefore, adhesion will be introduced between the grains of the mattress to enhance their resistance to external forces.

Following calibration, a sensitivity analysis will be conducted. Here, the focus will be on selecting two inseparable parameters: the load increment and the damping factor. These parameters exert a significant influence on the stability and accuracy of the simulations, and striking the right balance between them is considered of paramount importance.

Next, a comprehensive comparison of numerical and experimental results at various stages will be undertaken. Settlement and vertical stress profiles following the 1st and 30th cycles, as well as their evolution over multiple cycles, will be compared. This comparative analysis will serve to validate the numerical model and shed light on some inherent limitations. These limitations will be closely related to factors such as particle size, shape, and the interface behavior between soil and GSY sheets.

5.3.2 Characterisation and calibration of the numerical model for comparison with the experimental tests

This section aims to select micromechanical parameters of soil grains in the granular mattress to emulate the macroscopic behavior of the soil grains used in the base course layer of the experimental set-up. Moreover, the calibration of the subgrade soil will be detailed.

5.3.2.1 Characteristic parameters for particles in the mattress

5.3.2.1.1 Selection of physical parameters

The selected spheres diameter distribution had a minimum diameter, d_{n_min}, equal to 0.20 m and a maximum diameter maximum diameter, d_{n_max}, equal to 0.40 resulting in an average diameter denoted as "$d_{n\_average}$" equal to 0.26 m. Regarding the angular nature of the gravels comprising the base course layer in the experimental tests, a numerical angularity value (*Ang*) of 1 was employed. As consequence, the clusters of configurations exhibited distinct diameter specifications. Specifically, for each cluster, the diameters were defined as follows: maximum cluster length $l_{n\text{-}max}$ = 0.080 m and minimum cluster length $l_{n\ min}$ = 0.040 m, with an average length of $l_{n\text{-}average}$ = 0.052 m. It worth to note that in the experiment, the gravel's largest diameter (D_{max}) was 0.031 m, smaller than the smallest length ($l_{n\ min}$) of the clusters. However, it is important to develop a mattress presentation that reflects the responses of the base layer in the experiments. The representation chosen for the mattress must ensure that complex cluster-level features, such as particle shape and diameter observed during the experiment, cannot be reproduced in order to reduce computation time. This approach ensures the simulation aligns with the base course's macroscopic behavior. Another diameter distribution will be tested in this thesis with less important diameters than that selected in the basic model and obviously more grain particle number to respect the same mattress dimensions.

The clusters arrangement yielded numerical porosity values of n_{max} = 0.44 and n_{min} = 0.365 through the REDF method. The relative density of the assembly depends to n_{max}, n_{min} and n as detailed in *Eq 5-16*. To select a suitable porosity in accordance with the real state of the density of the soil grains in the base course layer of the experimental setup, an estimation of the experimental relative density was determined. In fact, two Proctor molds were utilized to measure the dry densities of the gravel material that constituted the base course. The first mold was filled without compaction, representing the state of maximum porosity. The second mold was filled and then compacted according to Proctor specifications, representing the state of minimum porosity. The dry density of the base course material in the experimental box was computed by measuring the weight of the filled gravel in relation to the occupied volume after the compaction of the base course. Utilizing the values of maximum dry density, minimum dry density, and the estimated dry density, the experimental D_r was estimated equivalent to 80%.
A numerical porosity (n) value of 0.38 was chosen, corresponding to a relative density of 80% as determined by the formula in Eq 5-16. Therefore, this porosity value selection is related in the compaction state of the base course in the experimental model.

$$D_r = \frac{n_{max} - n}{n_{max} - n_{min}} \qquad \textit{Eq 5-16}$$

5.3.2.1.2 Selection of potential intergranular parameters

This section is focused on introducing the intergranular parameters (Φ_{int}, a) for three potential mattress assemblies and deriving their macroscopic parameters (φ_{peak} and c). The most appropriate assembly to

represent the base course layer in the experimental setup will be selected based on a comprehensive comparison between the results of the three numerical models and the experimental findings. Three distinct assemblies with the micromechanical parameters are presented in Table 5-1.

The initial assembly (A_1) represents a purely frictional soil composition as obtained by the first case of the analysis of direct shear tests results performed on the gravel used in the base course layer of the experimental setup (section 3.3.2.2). Conversely, the second assembly (A_2) involves soil particles exhibiting adhesion characteristics as obtained by the second case of the analysis of direct shear tests results performed on the gravel used in the base course layer of the experimental setup (section 3.3.2.2). The third assembly (A_3) introduces adhesion between soil particles but with a lesser magnitude than that used in A_2 and with the friction angle (Φ_{int}) corresponds to the average value between A_1 and A_2. The motivation behind exploring the A_3 assembly with reduced adhesion is to closely approximate the qualities of purely frictional soil, distinctly veering away from the attributes of highly cohesive soil behavior. This pursuit is a dedicated effort to faithfully represent the intrinsic characteristics of granular soil.

Regarding the triaxial compression tests carried out to determine the macroscopic parameters for each assembly, the numerical samples encompass 8,000 clusters. Three triaxial tests were conducted for each assembly under varying confinement values (σ_3 = 10, 20, 50 kPa). Figure 5-10 (a) represents the results obtained from a series of triaxial compression tests conducted on the sample A_3. The macroscopic behavior of the numerical sample closely resembles to a soil sample exhibiting a peak in deviatoric stress followed by a decline in deviator stress after failure until a residual value is reached. The Mohr-Coulomb failure criterion was applied to define material behavior. Figure 5-10 (b) illustrates the evolution of t versus s to calculate the macro-mechanical parameters (φ_{peak} and c) of A_3 assembly. The macro-mechanical parameters of the three modelled numerical soils, deduced from triaxial test results, are concisely presented in Table 5-1.

Table 5-1: Micro-mechanical and macro-mechanical parameters of the three tested assemblies

Soil's type		A_1	A_2	A_3
Micro-mechanical parameters				
Normal contact stiffness (MN/m^3)	k_n	100		
Tangential contact stiffness to normal contact stiffness	k_s/k_n	1		
Intergranular friction angle (°)	Φ_{int}	22	17	20
Adhesion (kPa)	a	0	35	25
Angularity	Ang	1		
Macro-mechanical parameters				
Porosity	n	0.38		
Peak friction macroscopic angle (°)	φ_{peak}	41	37	39
Cohesion (kPa)	c	0	17	13.5

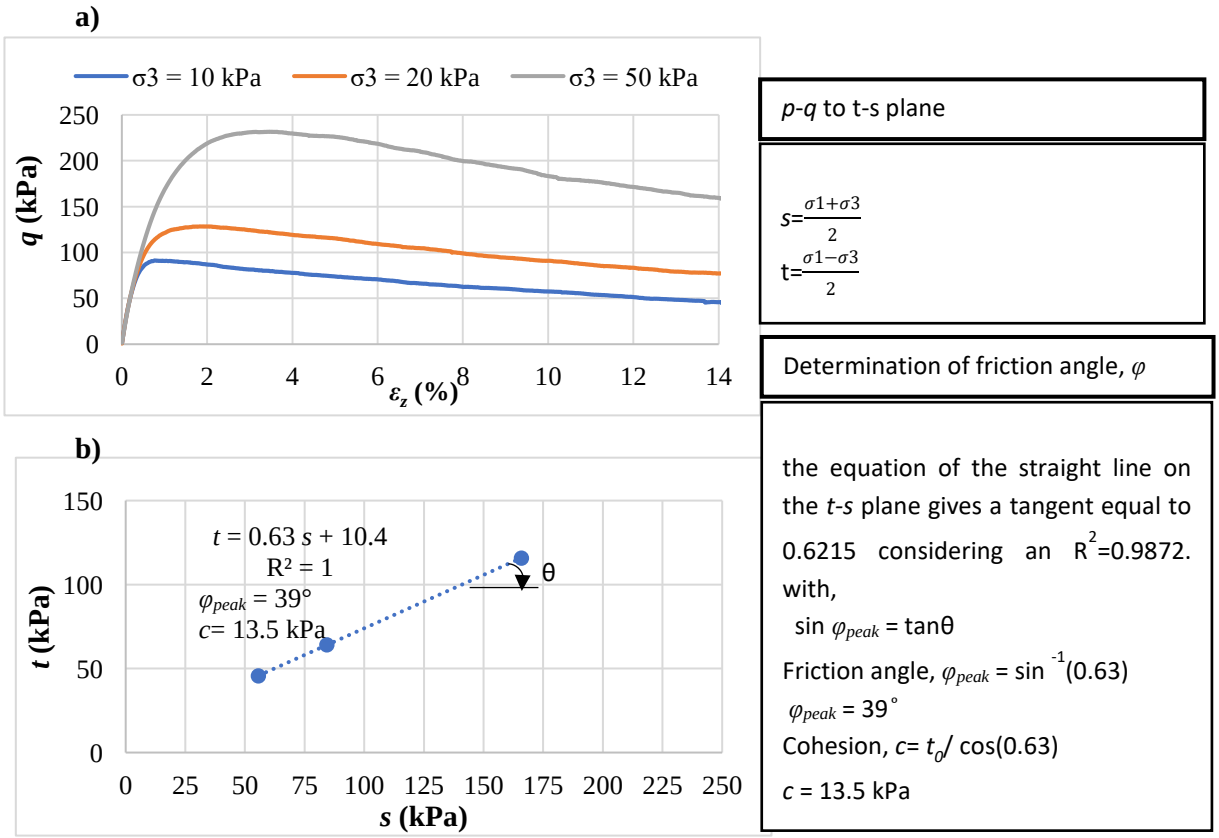

Figure 5-10: a) Evolution of the deviatoric stress q with axial strain ε_z for triaxial tests carried out on A_3; b) q versus p of the soil particles interface

5.3.2.2 Calibrated subgrade soil behaviour law

In the numerical model, the number of cycles applied is intentionally reduced when compared to the extensive 10,000 cycles used in the experimental testing of unpaved road sections. This reduction is carried out while ensuring that the range of subgrade settlement, achieved over a specific number of cycles (N), closely matches the results obtained in the experimental tests after the completion of 10,000 cycles. To achieve this alignment, the model's subgrade rigidity evolution law has been meticulously calibrated. This calibration process aims to replicate a similar range of maximum subgrade settlement, typically around 100 mm, as observed in the experimental tests. All of this is accomplished with fewer cycles in the numerical model compared to the extensive testing conducted in the experimental phase. In the calibrated model, the parameter k_1 was set at 2 MPa/m, which approximates the rigidity obtained in the 1st cycle (1.9 MPa/m). Notably, k_1, N_0, and k_u all play crucial roles in determining an acceptable range for supporting soil displacement across cycles. N_0 was established as 30, indicating the number of cycles required for the supporting soil to become elastic, while k_u was set at 100 MPa/m to represent consistent rigidity during unloading cycles. The selected value of k_u respects the range of the unloading subgrade reaction obtained in the loading plate tests (paragraph 3.3.1.2.1). When N reaches 30 cycles, k_N equates to k_u, at 100 kPa, signifying negligible vertical settlement increment in the supporting soil throughout the entire cyclic loading process.

For the numerical loading/unloading process, an additional 30 cycles will be applied after the initial 30 cycles to study the behavior of the mattress under cyclic loading, especially when the subgrade soil does not exhibit residual settlement across the entire cycle and subsequent cycles. Table 5-2 provides a summary of subgrade soil stiffness values for specific cycles, calculated using Equation 5-15, and includes the selected value that represents the subgrade soil in the numerical model used for the comparison with the experimental tests.

Table 5-2: Subgrade soil rigidities with cycles

N (Cycles)	k_1 (MPa/m)	k_u (MPa/m)	N_0	k_N (MPa/m)
1	2	100	30	2
2				5.3
29				93.4
30				96.7
31				100
60				100

5.3.3 Sensitivity Analysis to the main parameters influencing the dynamic response of the numerical model

This section aims to select a couple of values for the load increment ΔF and the damping factor K_α(detailed in section 5.2.1.1 and expressed in *Eq 5-7*) by studying their potential impact on the results of the numerical model. In fact, the load increment and the damping factor are inseparable because adjusting one typically necessitates adjusting the other to ensure the simulation's stability, accuracy, and convergence. Finding the right balance between these parameters is a critical aspect of numerical modeling and simulation to achieve meaningful and reliable results.

For this study, a granular mattress composed of A3-type material is employed (Table 5-1 in section 5.3.2.1.2). This mattress is reinforced with a bidirectional GSY sheet with a stiffness of 600 kN/m in each direction. The friction angle at the GSY /upper granular interface is 38°. The subgrade behavior law calibrated in section 5.3.2.2 is adopted for the supporting soil with k_1=2 MPa/mm, k_u=100 MPa/mm, and N_0=30. The friction angle at the GSY /lower subgrade interface is 32°. A total of 60 loading cycles (N) are applied on the granular mattress (Figure 5-9) using a circular loading plate with a diameter of 0.3 m. The maximum applied load is 40 kN and is selected to give a plate-mattress contact pressure equivalent to contact pressure in the experimentation.

A particular focus was put on the influence of the damping and the force increment on the results, especially the displacement and the stress beneath the center of the loading plate across the granular mattress.

5.3.3.1 Numerical damping impact

The validation process for the selected numerical damping coefficient D involves a series of three similar simulations. These simulations are distinguished by the varying values assigned to D, specifically D = 0.1 ($D_{0.1}$), D = 0.2 ($D_{0.2}$), and D = 0.4 ($D_{0.4}$). A simulation was launched with a D = 0.05, but the results did not converge to a stable outcome. A load increment in each time increment equal to 2 N was employed. This load increment is rather equivalent to the one employed in the experiment. Its impact will be studied in the next section.

The results of these numerical simulations are presented in both Figure 5-11 and Figure 5-12. Figure 5-11 represents the settlement evolution of the soil beneath the central point of the plate, at both the mattress

surface and the of the compressible soil. The damping coefficient has a discernible impact on the evolution of soil settlement beneath the central zone of the plate across cycles: a lower damping coefficient (involving dynamic effect) corresponds to more pronounced settlement beneath the plate's center. Noting that this influence of damping is more pronounced at the mattress surface (Strip A) compared to the subgrade soil (Strip B). The range of mattress settlement evolution are closer with $D_{0.2}$ is closer to the one of $D_{0.4}$, than the one of $D_{0.1}$.

Figure 5-12 presents the profiles of the vertical stress underneath the plate within the depth of the mattress for the three simulations. The vertical stress is calculated based on application of Weber law in calculation spheres of diameter of 0,1 m for the first cycle and 10th cycle 0. The damping coefficient's influence on the vertical stress profile across the depth of the mattress is generally marginal, except in the first calculation sphere situated directly under the loading plate during the 10th cycle with $D_{0.1}$.

In summary, while the initial experiment was conducted under static conditions, it can hint at potential dynamic effects. Through these simulations, we established the impact of damping on settlement and stress at the plate-mattress interface. Opting for a damping coefficient of D = 0.2 for subsequent simulations, we strike a balance between accuracy and stability for the thesis work.

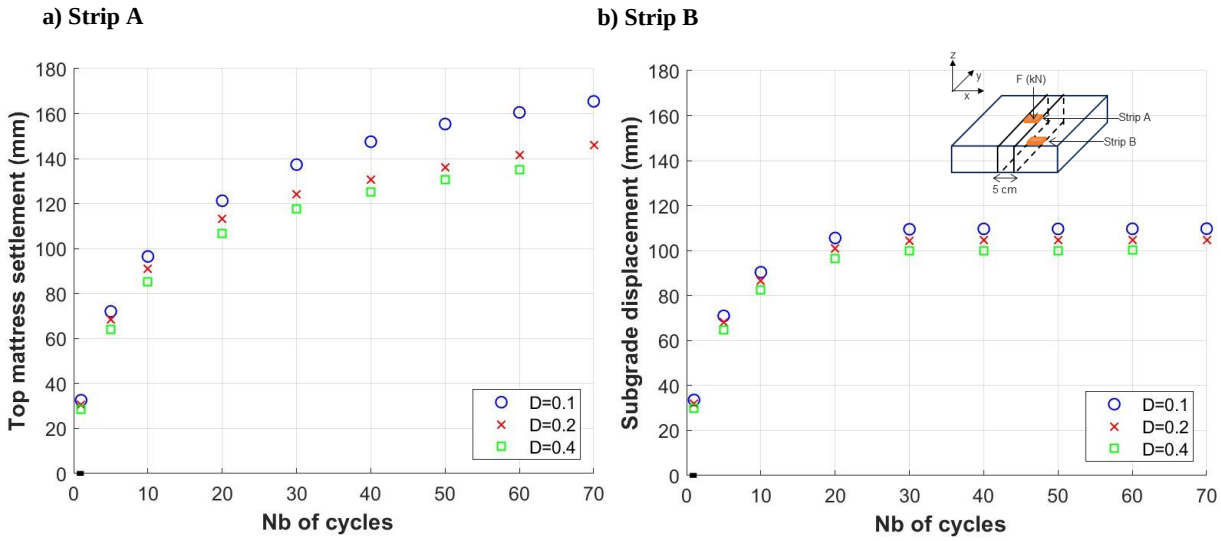

Figure 5-11: Evolution of the settlement beneath the loading plate with cycle: a) at the mattress surface; b) at the subgrade layer

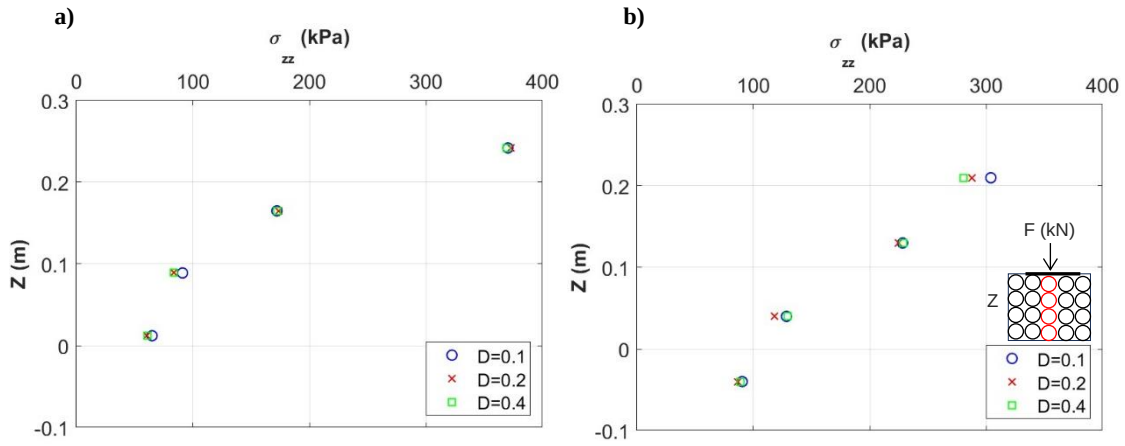

Figure 5-12: Stress profile beneath the loading plate center; a) at the 1st cycle; at the 10th cycle.

5.3.3.2 Load increment impact

Indeed, a very low force increment would not produce results within an acceptable time, while an excessively high force increment could introduce undesirable dynamic effects. In all next simulations, a local damping coefficient of 0.2 is retained, effectively mitigating undesired dynamic influences, aiding in computational convergence, and preventing the propagation of elastic waves within the model. Table 5-3 demonstrates the influence of force increment with Δt equal to 1.365 x10^{-5} s on various results, including the maximum soil settlement beneath the plate, both at the mattress surface and at the subgrade level after the first loading cycle. Additionally, the vertical stress at the mattress surface at the first loading cycle is presented. Within the range of force increments ΔF from 0.5 N to 2 N in each time increment, no substantial influence of ΔF on the results has been observed. The variations in soil settlement are minimal, measuring just a few millimetres. Moreover, the variation in vertical stress is insignificant.

However, notable effects become evident when employing exceptionally high force increments during the time step (e.g., = 5 kN in case B_4). Under these circumstances, potential influences of the force increment on soil settlement beneath the center of the plate (maximum settlement) and the stress at the mattress surface beneath the plate are observed. Interestingly, a higher force increment corresponds to reduced displacement and lower stress. This aligns with the observation that rapid loading might hinder the gradual application of the full load demand and induces undesirable dynamic effect. It's important to note that a load increment equal to 2 N in each time increment was consistently maintained for all simulations in the thesis.

Table 5-3: Results of the simulation after the 1st cycle

	Case B_1	Case B_2	Case B_3	Case B_4
ΔF (N)	0.5	1	2	10
Loading speed (kN/s)	37	73	147	733
Maximum top mattress settlement (mm)	31,1	30,5	30	25
Maximum subgrade settlement (mm)	30	29,4	29	23
Maximum mattress vertical stress (kPa)	380	380	380	295

5.3.3.3 Conclusion

The sensitivity analysis of the calculation procedure confirmed the validity of both the damping and force increment. For the chosen damping value, using a force increment of 2 N per time increment a favourable balance between precision and computational efficiency was achieved. Moreover, a damping value of 0.2 was added to aid convergence in quasi-static scenarios. This damping helps restrict the spread of elastic waves during each loading and unloading phase. However, when applying cycles of loading followed by unloading in the experimental, we can't be certain that a stabilized equilibrium state was reached before transitioning from one cycle to the next. This difference in how the force is applied, controlled and slow in the simulation or uncontrolled in the experiment, could contribute to disparities between numerical and experimental results.

5.3.4 Confrontation of numerical and experimental results

This section aims to confront the experimental results and the numerical results of the first cycle, the last cycle of the experimental and the last cycle of the numerical and the evolution of the results with the cycles starting from the first cycle to the last cycles of each one.

Among the various experimental tests conducted on reinforced platforms approximately 300 mm thick (T_1, T_3, T_4, and T_5), the latter, T_5, emerged as the most suitable test for comparison with the numerical model. This test features a base course thickness around 300 mm and is reinforced with GTX_1. This choice was based on its minimal susceptibility to the initial soil conditions, making it a robust test for validation. In the comparative analysis with T_5, three distinct numerical models, denoted as M_1, M_2, and M_3, were employed. In fact, M_1 incorporates a purely frictional mattress with identical mechanical properties to those of A_1, while M_2 features a cohesive mattress sharing the same mechanical characteristics as A_2 (as outlined in Table 5-1). Meanwhile, M_3 is equipped with a mattress that matches the mechanical attributes of assembly A_3 (as detailed in Table 5-1). Each of the mattresses in M_1, M_2, and M_3 consists of a total of 36,000 clusters.

For a comprehensive understanding of these models, the key characteristic parameters, extensively discussed in the characterization and calibration section (5.3.2), are presented in Table 5-4. Moreover, the tensile stiffnesses characteristic of the GTX behavior laws, J_x and J_y, were set to 1,200 kN/m, equal the stiffness at a 2% strain level in both the machine and transverse directions of the GTX_1 employed in T_5. This choice is driven by the aim to enable a straightforward comparison between the results of the simulations and the results of the test T_5. The friction value utilised for GTX-upper granular mattress $\delta_{clumps\text{-}GTX}$ is 38°, equivalent to the friction angle of the GTX_1-upper base course layer. While the friction value utilised for GTX_1-lower subgrade in $\delta_{sphere\text{-}GTX}$ is 32°, equivalent to the friction angle value utilised for GTX_1-lower subgrade Table 3-3 (Section 3.3.4.1). It is worth noting that the choice of the impact of the mattress particle number will be studied in chapter 6.

The surface settlement profiles of the granular soil, settlement profiles of the soft soil, and the vertical stresses acting on the compressible layer beneath the loading plate were primarily focused on in the experiments. In one of the experimental tests, Test T_5 (selected for comparison purposes), optical fibers were installed on the GTX to measure its deformation, but the signal from the optical fibers was lost after the base course compaction, preventing any results of the GTX deformation from being obtained.

Turning to the multitude of numerical results derived from cycles of simulations, the focus in this section will be on outcomes that can be directly compared with the experimental data. For a comprehensive insight, all numerical findings will be meticulously detailed in section 5.4.

Table 5-4: Numerical model parameters and loading conditions

		M_1	M_2	M_3
Mattress nature		Purely frictional mattress	Cohesive mattress	
Mattress particles				
Type		Cluster	Cluster	Cluster
Number		36 000	36 000	36 000
Density (kN/m^3)	ρ	25.18		
Angularity	Ang	1		
Mattress micro-mechanical parameters				
Normal contact stiffness (MN/m^3)	k_n	100		
Tangential contact stiffness to normal contact stiffness	k_s/k_n	1		
Intergranular friction angle (°)	Φ_{int}	22	17	20
Adhesion (kPa)	a	0	35	25
Mattress macro-mechanical parameters				
Porosity	n	0.38		
Peak friction macroscopic angle (°)	φ_{peak}	41	37	39
Cohesion (kPa)	c	0	17	13.5
Bulk density (kN/m^3)	ρ	25		
GTX				
Tensile stiffness in the x direction (kN/m) [0 - 5% strain]	J_x	1200		
Tensile stiffness in the y direction (kN/m) [0 - 5% strain]	J_y	1200		
Soil-GTX interface friction parameters				
Angle between the clumps and the upper interface of the GTX (°)	$\delta_{clumps\text{-}GTX}$	38		
Angle between the subgrade and the lower interface of the GTX (°)	$\delta_{sphere\text{-}GTX}$	32		
Lower supporting soil				
Rigidity during the loading cycle (MPa/m)	k_l	3		
Rigidity during the unloading cycle (MPa/m)	k_u	100		
Threshold cycle	N_0	30		
Loading				
Number of applied cycles	N	60		
Maximum load (kN)	F_l	40		
Minimum load (kN)	F_u	1		
Force increment in the time increment (N)	ΔF	2		
Damping	K_a	0.2		

5.3.4.1 Confrontation after the 1st cycle

Comparing the subgrade and base course surface settlements in test T_5 following the initial loading-unloading cycle with those obtained from the three models (M_1, M_2, and M_3) after the same cycle (depicted in Figure 5-13), a notable level of correspondence between the settlement profile of T_5 and those of models M_2 and M_3 , where adhesion between the grains of the mattress was introduced, was observed. However, the outcomes of model with the purely frictional mattress M_1 exhibit a greater magnitude of settlement both at the mattress surface and the subgrade, causing it to deviate from the agreement with T_5 results.

To assess the validity of the numerical models, Figure 5-14 presents a comparison of the vertical stress beneath the center of the loading plate in T_5 with the vertical stress distribution of the numerical models M_1, M_2, and M_3. These stress values are measured on the upper surface of the subgrade soil at the end of the loading phase of the first cycle. The vertical stress beneath the loading plate in T_5 closely matches with M_2 and M_3. Conversely, model M_1 generates significantly higher stress levels compared to T_5, which subsequently elucidates the observed elevated range of settlement. When comparing the vertical stresses on the subgrade soil surface in M_1 with those in M_2 and M_3, it becomes evident that the model with purely frictional mattress M_1 is not strong enough to spread and sustain the applied load, the central region

experiences higher vertical stresses, while the surrounding areas exhibit comparatively lower stress levels in contrast to M_2 and M_3.

Additionally, an analytical case study that mirrors numerical simulation M_1 was conducted, involving a plate with a diameter (B) of 0.3 m placed on the surface of a purely frictional mattress with a thickness of 0.35 m. Beneath the mattress lies a subgrade layer (Figure 5-15). The application of Terzaghi's equation in this scenario yielded a calculated bearing capacity at the top of the mattress of approximately 253 kPa (as indicated in Table 5-5. Consequently, Terzaghi's equation confirmed the inability of Model M_1, featuring a purely frictional mattress, to withstand the applied pressure on the plate placed at the top of the mattress, equivalent to 560 kN/m², as evidenced by excessive mattress settlement after the first cycle compared to the settlement profile of the experimental test (T_5).

To address this issue, the introduction of adhesion between the grains composing the granular mattress was suggested for Models M_2 and M_3 to enhance their resistance capabilities. Upon comparing the settlement of the soil between the experimental tests T_5 and the numerical models M_2 and M_3, where adhesion was incorporated between the mattress grain particles, a notable alignment was observed between the experimental and numerical settlement profiles. This underscores the significance of introducing adhesion among the grain particles of the granular mattress as an essential step in the modelling process.

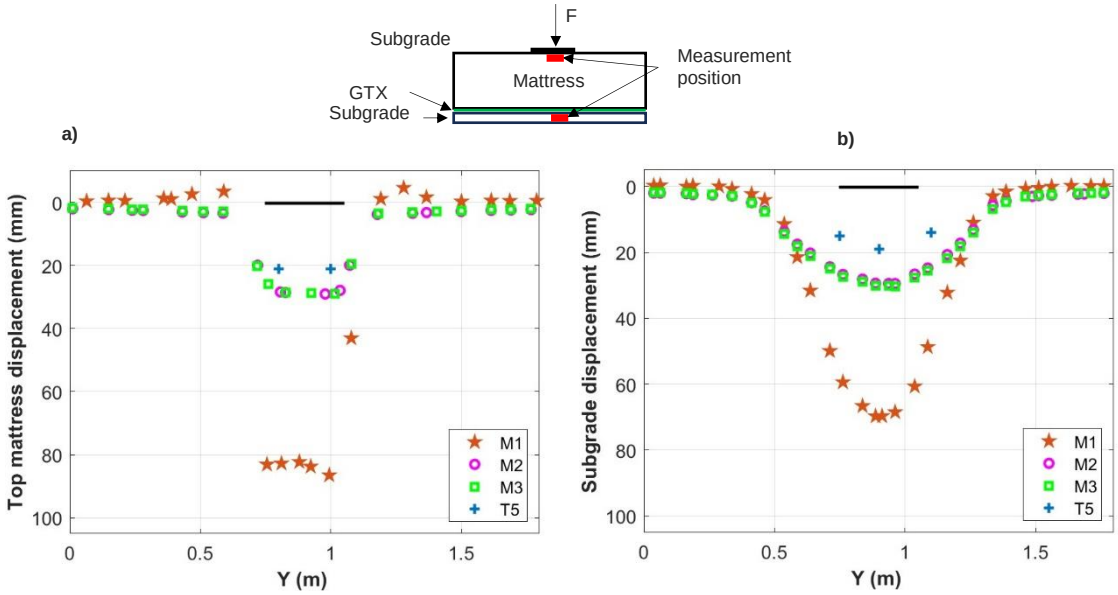

Figure 5-13: Comparison between experimental and numerical at the end of the 1st cycle: a) base course surface settlement, b) subgrade surface settlement

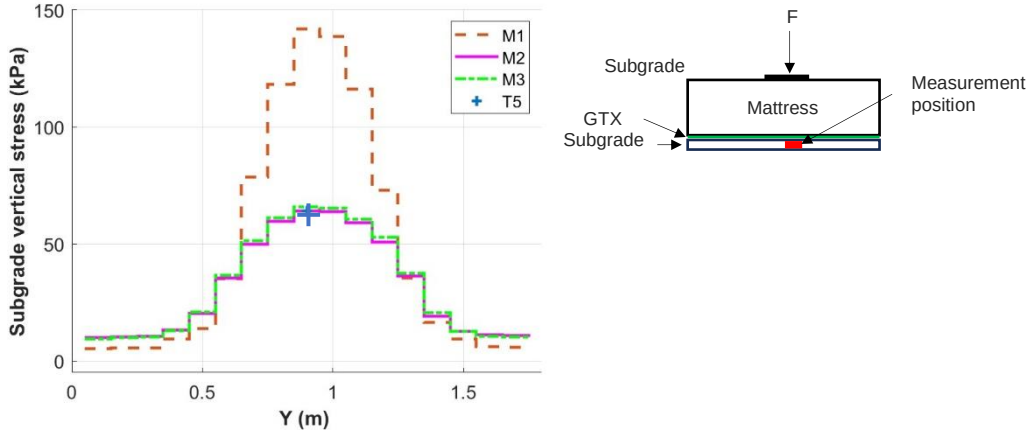

Figure 5-14: Subgrade vertical stress at the end of the loading phase of the 1st cycle

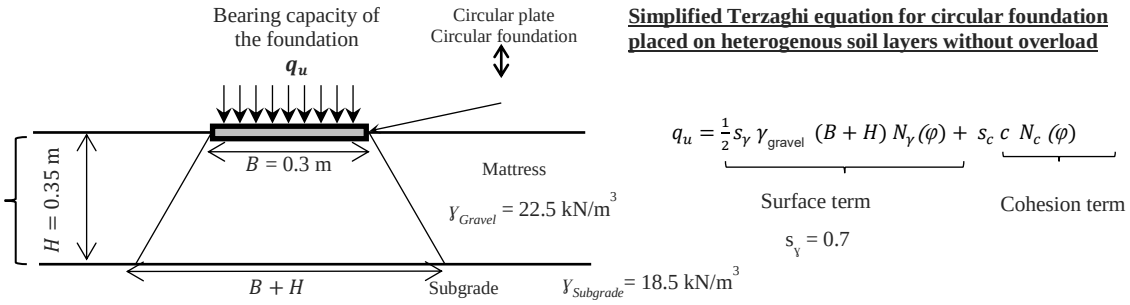

Figure 5-15: Analytical calculation of the bearing capacity of a plate placed on a superficial granular layer above a subgrade soil using the simplified Terzaghi Equation

Table 5-5: Terzaghi equation parameters of the model M_1

	φ_{peak}	c	N_γ (φ_{peak})	q_u (kPa)
M_1	41	0	130.21	253

5.3.4.2 Confrontation at the end of the (30th cycle)

When examining the settlement profiles of the subgrade and base course in test T_5 following the completion of the 1000th cycle and comparing them with the results obtained from the two models, M_2 and M_3, after only 30 cycles (as depicted in Figure 5-16), a notable alignment emerges between the settlement profiles of T_5 and those observed in models M_2 and M_3. This alignment serves as a validation of the calibration of

numerical models M_2 and M_3 in terms of introducing adhesive properties between the mattress grains and expediting the attainment of the required subgrade settlement with a reduced number of cycles in the numerical model when compared to the experimental test. Consequently, the targeted settlement values for both the subgrade and base course can be effectively achieved.

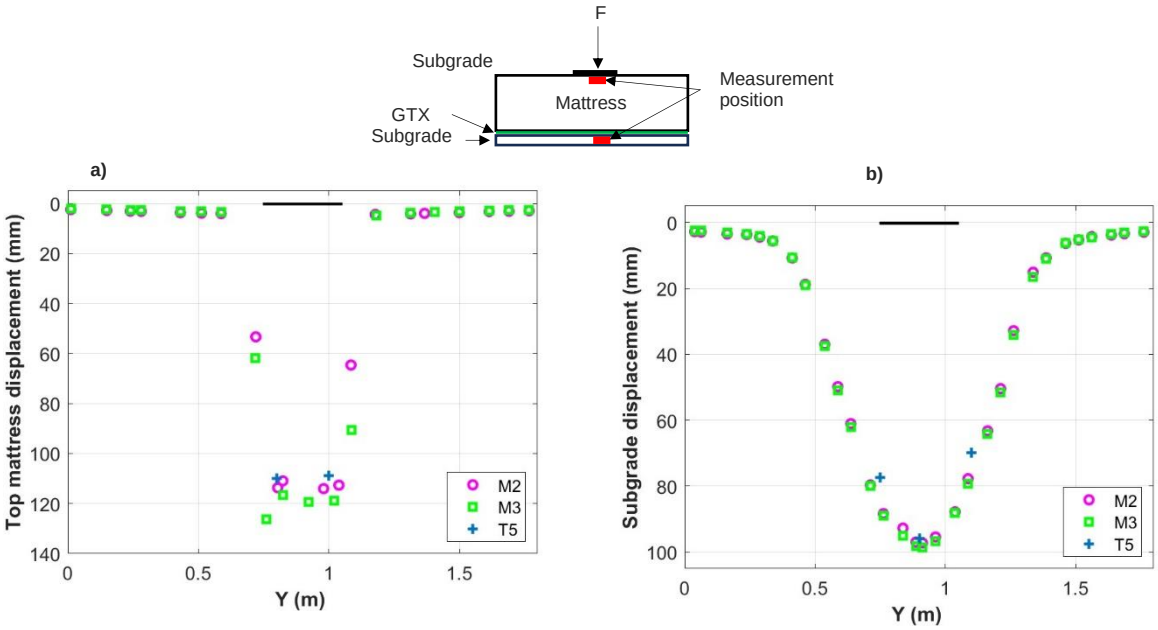

Figure 5-16: Comparison between the results of the experimental at the end 1,000 cycles and numerical at the end of the 30th cycle: a) base course surface settlement, b) subgrade surface settlement

5.3.4.3 Evolution with cycles

Figure 5-17 illustrates the evolution of maximum subgrade and base course settlements over cycles, providing a comparative analysis of data from the experimental test (T_5) and results derived from the numerical models (M_2 and M_3).

A consistent pattern emerges in which subgrade settlement gradually occurs during cycles, accompanied by a decreasing rate of deformation leading to the stabilization of settlements. Notably, in test T_5, the stabilization of subgrade settlement occurs after the 1000th cycle (Figure 5-17b). In contrast, due the numerical model calibration, subgrade settlement closely approximates that of T_5 at 1000 cycles in the 30th cycles, as (Figure 5-17a). After the 30th cycle, residual settlement becomes virtually negligible (Figure 5.15a).

Furthermore, it's noteworthy that, in models M_2 (c = 17 kPa) and M_2 (c= 13.5 kPa), the maximum settlement at the mattress surface beneath the loading plate's center continues to increase with a reduced rate after the stabilization of subgrade settlement at the 30th cycle. This divergence results in a growing difference in settlement between the subgrade and the mattress surface, ultimately reaching values between 25-35 mm by the 60th cycle, as portrayed in Figure 5-17a. Conversely, in test T_5, both the base course and subgrade soil stabilize in close alignment, with a settlement difference of approximately 10 mm (Figure 5-17b).

In addition, Figure 5-18 presents the evolution of vertical subgrade stress in function of the settlement beneath the loading plate centre. Initially, there's an alignment in the evolution of stress between the numerical models (M_2 and M_3) and the experimental T_5, and this alignment holds true up to a displacement

of 90 mm, which corresponds to approximately 20 cycles in the numerical models. However, beyond this critical point, a significant divergence becomes apparent. In the numerical models (M_2 and M_3), the vertical subgrade stress surpasses that observed in the experimental test (T_5). This deviation can be attributed to the decreasing of the subgrade settlement rate with cycles.

The numerical simulation shows ongoing settlement of the mattress even after the underlying subgrade stabilizes, while the experimental setup exhibits base course settlement only during subgrade settling. The loss of contact between clusters leads to a permanent loss of cohesion among them. Consequently, the mattress, having lost local cohesion, continues to deform, resulting in an increase in stress on the soft ground beneath the loading plate. In contrast, in the experimental tests, the presence of soil moisture likely prevents the loss of cohesion between grain particles during each loading cycle. Consequently, this accounts for the improved behavior of the mattress in the experiment, eventually leading to stabilized settlement.

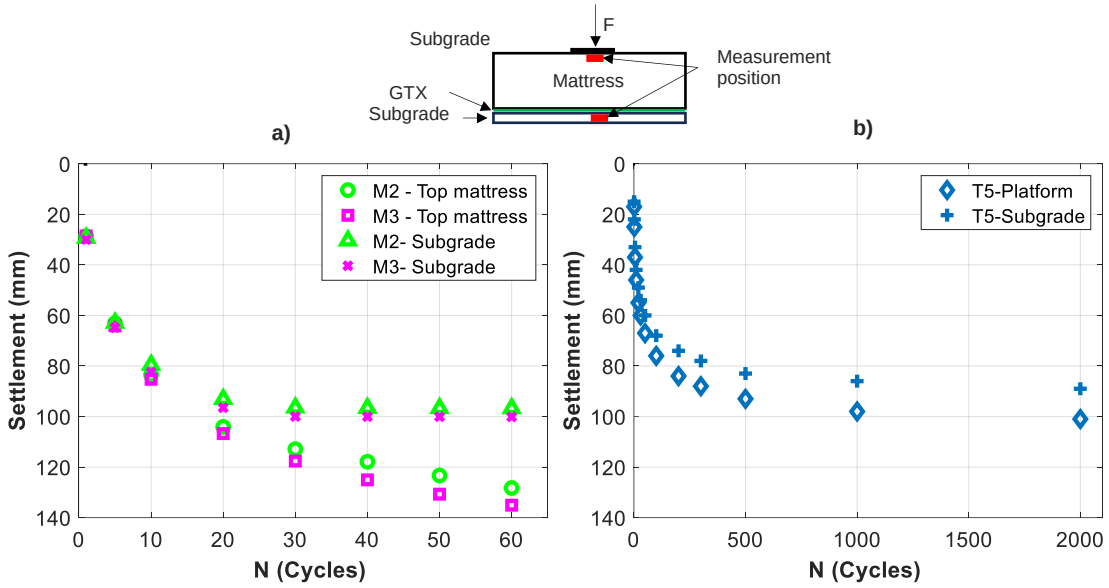

Figure 5-17: Evolution of the maximum settlement beneath the loading plate center with cycles: a) in M_2 & M_3; b) in Test T_5

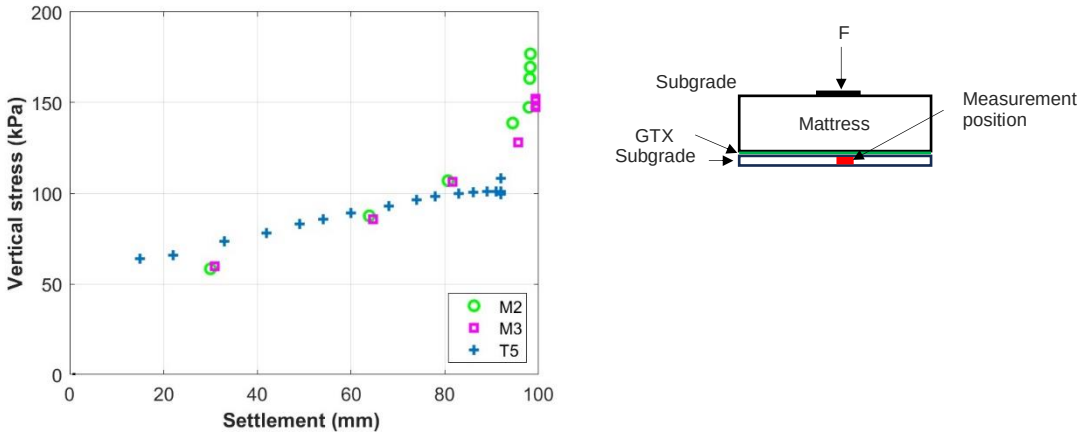

Figure 5-18: The vertical stress versus the settlement at the subgrade beneath the loading center

5.3.5 Limitations of the numerical model

Based on the comparison between the experimental and the numerical, we could reach two calibrated models (M_2 & M_3) that give the same range of displacement and stress as the experimental T_5. There are no results available for GSY deformation in the experiment due to signal loss after base course installation. Despite this resemblance between experimental and numerical, there are shortcomings in numerical simulations when compared to the experimental reality.

When comparing experimental and numerical results, it's important to note the size difference between aggregates in the experiment and the discrete elements in the simulation. While this size disparity can influence shear behavior to some extent, the microscopic parameters controlling contacts between discrete elements (friction, cohesion) have been tuned to replicate the experimental material's macroscopic behavior. However, when validating the numerical material's macro behavior, a concern arises regarding the microscopic parameters governing discrete element contacts. These friction and adhesion parameters are used without a direct real-world link, aiming solely to approximate the desired macro behavior. Nonetheless, at a smaller scale, the simulated micro-level inter-granular behavior may not faithfully mirror reality. Furthermore, the relatively large size of discrete elements can influence locally particle rearrangements (especialy in shearing zones), potentially leading to variations in compaction state (loose or dense).

Replicating the precise shape and size of particles in the experimental fill is difficult due to practical limitations in memory and computational time. As a result, accurately mimicking the bulking and densification behavior of the experimental material becomes challenging.

Another parameterization issue involves characterizing the behavior at the interface between the soil and the GSY in the numerical model. This interface notably relies on a tangential stiffness at the soil/ GSY contact, influencing the potential relative displacement between the soil and its reinforcement. Calibrating the tangential stiffness of the soil/ GSY contact, much like assessing the minimum displacement U_0 required for maximum friction mobilization, proves challenging due to the lack of experimental data especially the deformation of the GSY. Therefore, these two values were taken from previous simulations (Villard et al. ,2009).

5.4 Understanding of the influence of the reinforcement onto the behaviour of the reinforced granular layer

5.4.1 Introduction

To investigate the response of the GTX reinforced platform on a soft subgrade under vertical cyclic loading and assess the reinforcement's impact, a numerical simulation (M4) is conducted in this section. In M4 features a mattress composed of 72,000 clusters, which is double the cluster number compared to M_3, resulting in a refined mattress. It's important to note that cluster number impact will be studied in chapter 6. Additionally, the slopes of the GTX linear behavior law, J_x and J_y, are assumed to be 600 kN/m instead of 1,200 kN/m as in M_3, in the aim to obtain significant vertical settlements. The characteristic parameters of M4 are presented in Table 5-6. This simulation is aimed at examining the response of the mattress under cyclic loading. It is worth pointing out that matlab routines have been developed for this visualization as part of this thesis. Various aspects, including particle displacement, force distribution, and the orientation of principal stresses, will be analysed. Furthermore, displacement and strain within the GTX will be evaluated, along with a detailed study of the reinforcement mechanism. The analysis will focus on key loading cycles, specifically the 1st, 5th, and 30th cycles, involving both loading and unloading stages.

Table 5-6: Main parameters of M4

		M4
Mattress particles		
Type		Cluster
Cluster Number		72 000
Minimum sphere diameter (m)	d_{n_min}	0.016
Maximum sphere diameter (m)	d_{n_max}	0.032
Average sphere diameter (m)	$d_{n\_average}$	0.020
Angularity	Ang	1
Mattress micro-mechanical parameters		
Micromechanical friction angle (°)	Φ_{int}	20
Adhesion (kPa)	a	25
Mattress macro-mechanical parameters		
Peak friction macroscopic angle (°)	φ_{peak}	39
Cohesion (kPa)	c	13.5
GTX		
Tensile stiffness in the x direction (kN/m) [0 - 2% strain]	J_x	600
Tensile stiffness in the y direction (kN/m) [0 - 5% strain]	J_y	600
Soil-GTX interface friction parameters		
Angle between the clumps and the upper interface of the GTX (°)	$\delta_{clumps\text{-}GTX}$	38
Angle between the subgrade and the lower interface of the GTX (°)	$\delta_{sphere\text{-}GTX}$	32
Lower supporting soil		
Rigidity during the loading cycle (MPa/m)	k_1	2
Rigidity during the unloading cycle (MPa/m)	k_u	100
Threshold cycle	N_0	30

5.4.2 Particle displacement

The vertical and horizontal displacements ΔHz and ΔHy of a vertical section (e=72 mm) of the model situated beneath a rigid loading plate (Figure 5-19) are presented in the 1st cycle (Figure 5-20), the 5th cycle (Figure 5-21), the 30th cycle (Figure 5-22) and the 60th cycle (Figure 5-23) respectively. The central part of

the numerical sample, encompassing ordinate values ranging from 0.4 m to 1.4 m, is the focus. Regarding the model's condition, the horizontal subgrade movement is constrained.

The maximum vertical displacements (ΔHz_{max}) under the loading plate for both the upper mattress and the subgrade and the maximum horizontal displacement at the GTX-mattress interface (ΔHy_{max}) are summarized in Table 5-7.

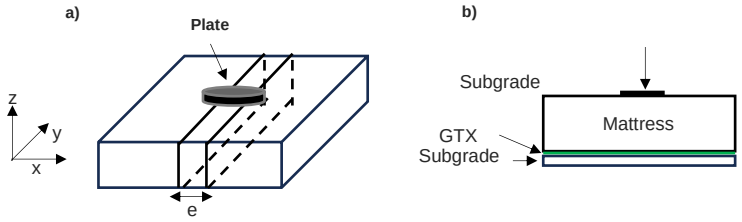

Figure 5-19: Illustration of the model and the studied section

During the initial loading cycle, a semi-cone-shaped block beneath the plate descends vertically, as depicted in Figure 5-20a. This downward movement is characterized by the sliding angle φ_s, which aligns with the friction angle φ_{peak} of the mattress. As a result, particles at the interface between the mattress and the GTX on either side of the central vertical axis exhibit horizontal outward displacement as shown in Figure 5-20d. ΔH_{zmax} and ΔH_{ymax} are showed in the Figure 5-20 and Table 5-7. During the unloading phase, the mattress ascends, causing the block to move upwards, albeit to a lesser extent than its downward motion during loading (Figure 5-20b). Similarly, interface particles with the GTX reverse their movement with reduced magnitude compared to the loading phase (as seen in in Figure 5-20e). Consequently, the initial loading cycle induces permanent horizontal and vertical displacement, as depicted in Figure 5-20c and in Figure 5-20f, respectively. The magnitude of the vertical displacement beneath the loading plate is approximately 32 mm, with the horizontal displacement at the GTX-mattress measuring around 4.5 mm.

A similar mechanism unfolds during the 5th cycle (Figure 5-21), albeit with reduced magnitudes compared to the 1st cycle. This reduction is attributed to the increasing rigidity of the subgrade soil with successive cycles. Consequently, the horizontal residual displacement measures 2.5 mm (Figure 5-21f), and the vertical residual displacement is 7 mm (Figure 5-21c), both less pronounced than those observed during the 1st cycle.

By cycle 30 (as shown in Figure 5-22), there's a further reduction in magnitudes primarily due to the continued increase in subgrade rigidity. Notably, the descending block during loading (Figure 5-22a) slightly ascends during unloading in Figure 5-22b, and the two triangular zones at the GTX-mattress interface exhibit outward movement during loading (Figure 5-22d) and inward movement during unloading (Figure 5-22e). These mechanisms result in minor vertical and horizontal resultant displacements (as seen in Figure 5-22c and Figure 5-22f), with smaller magnitudes than those in cycle 5. Consequently, the horizontal residual displacement is 0.4 mm, and the vertical residual displacement is 1 mm, both less pronounced than those observed during the 5th cycle.

It's worth noting that starting from the 30th cycle, the resultant vertical displacement of the subgrade becomes zero. However, the upper part of the mattress continues to generate vertical resultant displacement, as depicted in Figure 5-23. Indeed, Figure 5-23d demonstrates the generation of resultant vertical displacement with smaller magnitudes than those in cycle 30. The horizontal residual displacement is around 0.1 mm. Both displacements are less pronounced than those observed during the 30th cycle.

Comparing the vertical displacements from the 1st, 5th, 30th and 60th loading cycles reveals a decreasing ΔHz, which can be attributed to the increasing rigidity of the subgrade. Simultaneously, ΔHy also decreases. Conversely, when comparing the 1st, 5th, 30th and 60th unloading cycles, a relatively constant ΔHz is observed due to consistent unloading subgrade rigidity, accompanied by constant ΔHy.

Table 5-7: Maximum displacement values for loading cycle (L), unloading cycle (U), and loading-unloading resultant (L+U) at the upper mattress, the subgrade central surface, and GTX-mattress interface.

	1st cycle			5th cycle			30th cycle			60th cycle		
	L	U	L+U	L	U	L+U	L	U	L+U	L	U	L+U
Upper mattress ΔHz_{max} (mm)	-40	+8	-32	-18	+11	-7	-12	11	-1	-11.4	11	-0.4
Subgrade ΔHz_{max} (mm)	-38	+3	-35	-8	+1	-7	-3	3	0	-1	1	0
GTX-mattress ΔHy_{max} (mm)	6	1	5	3	1.6	2.5	2	1.8	0.2	1.8	1.7	0.1

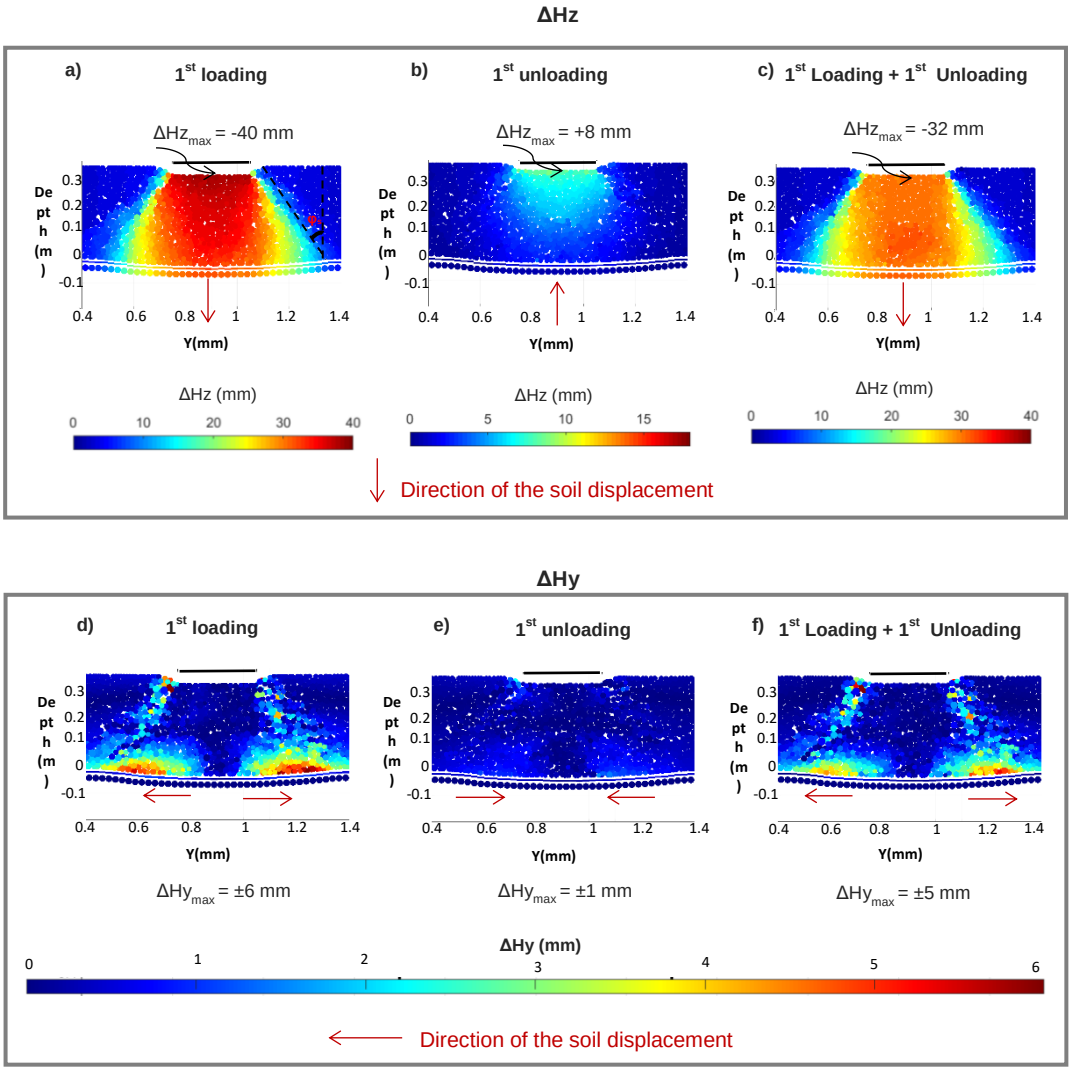

Figure 5-20: Soil displacement: a)ΔHz due to the 1st loading cycle; b) ΔHz due to the 1st unloading cycle; c) ΔHz resultant of the 1st loading-unloading; e) ΔHy due to the 1st loading cycle; f) ΔHy due to the 1st unloading cycle; g) ΔHy resultant of the 1st loading-unloading

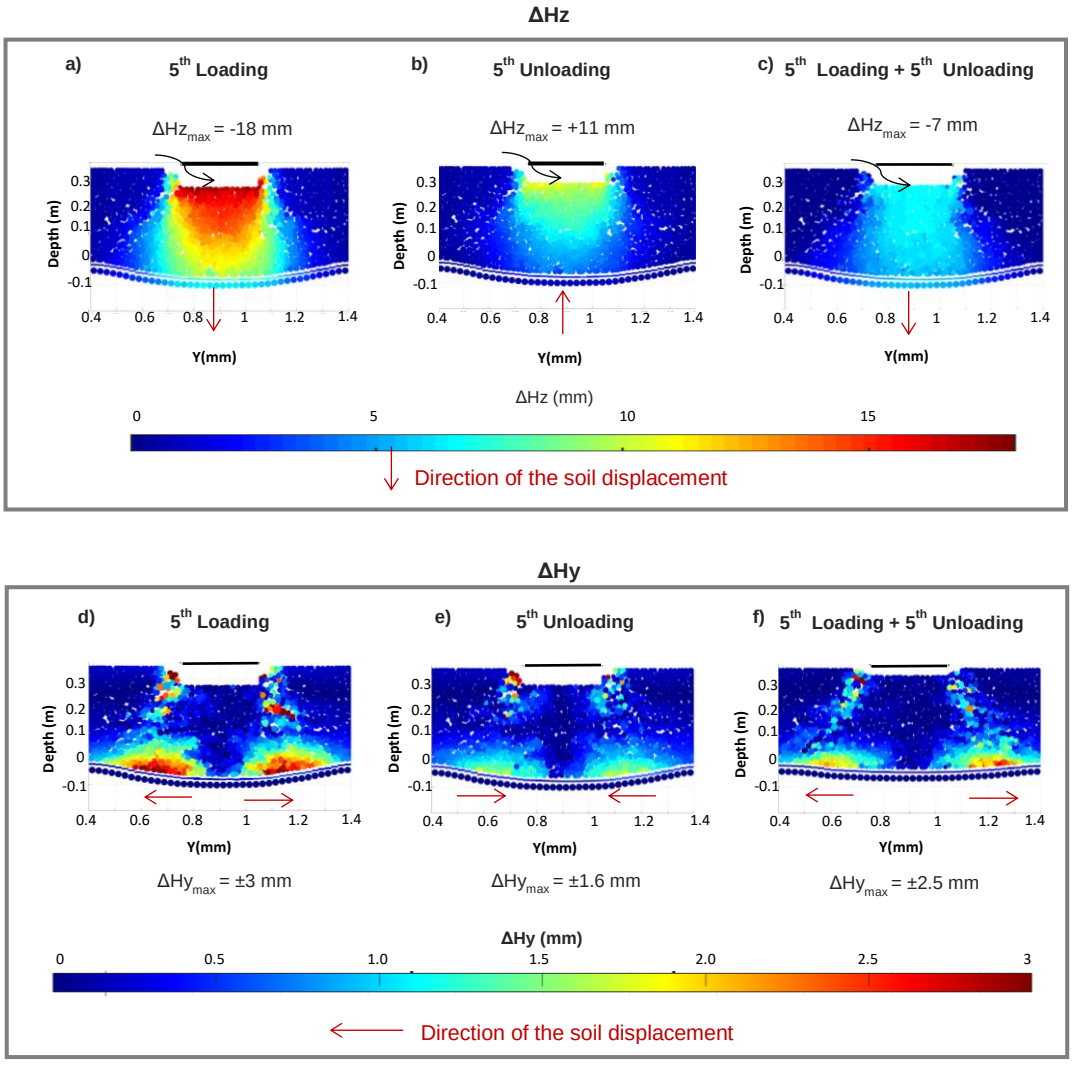

Figure 5-21: ΔHz due to the 5th loading cycle; b) ΔHz due to the 5th unloading cycle; c) ΔHz resultant of the 5th loading-unloading; e) ΔHy due to the 5th loading cycle; f) ΔHy due to the 5th unloading cycle; g) ΔHy resultant of the 5th loading-unloading

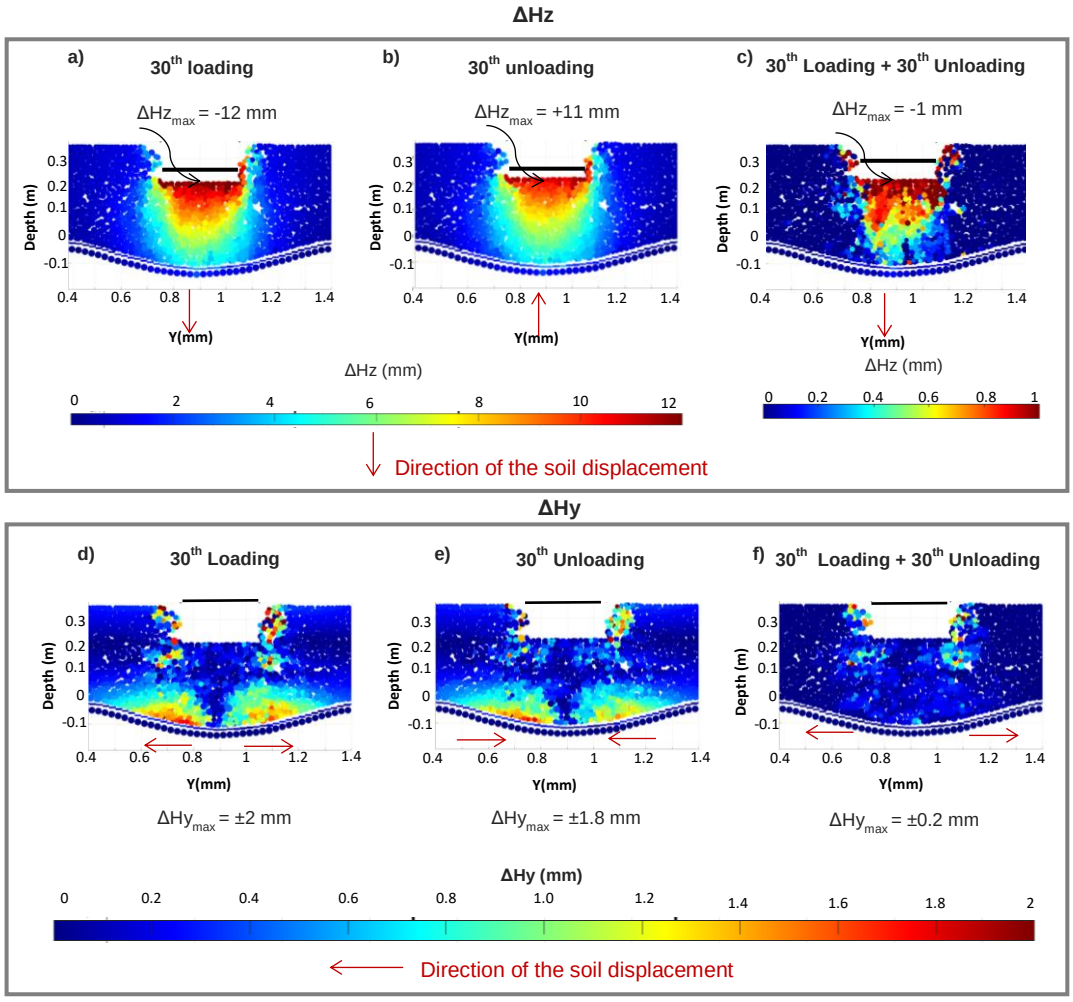

Figure 5-22: ΔHz due to the 30th loading cycle; b) ΔHz due to the 30th unloading cycle; c) ΔHz resultant of the 30th loading-unloading; e) ΔHy due to the 30th loading cycle; f) ΔHy due to the 30th unloading cycle; g) ΔHy resultant of the 30th loading-unloading

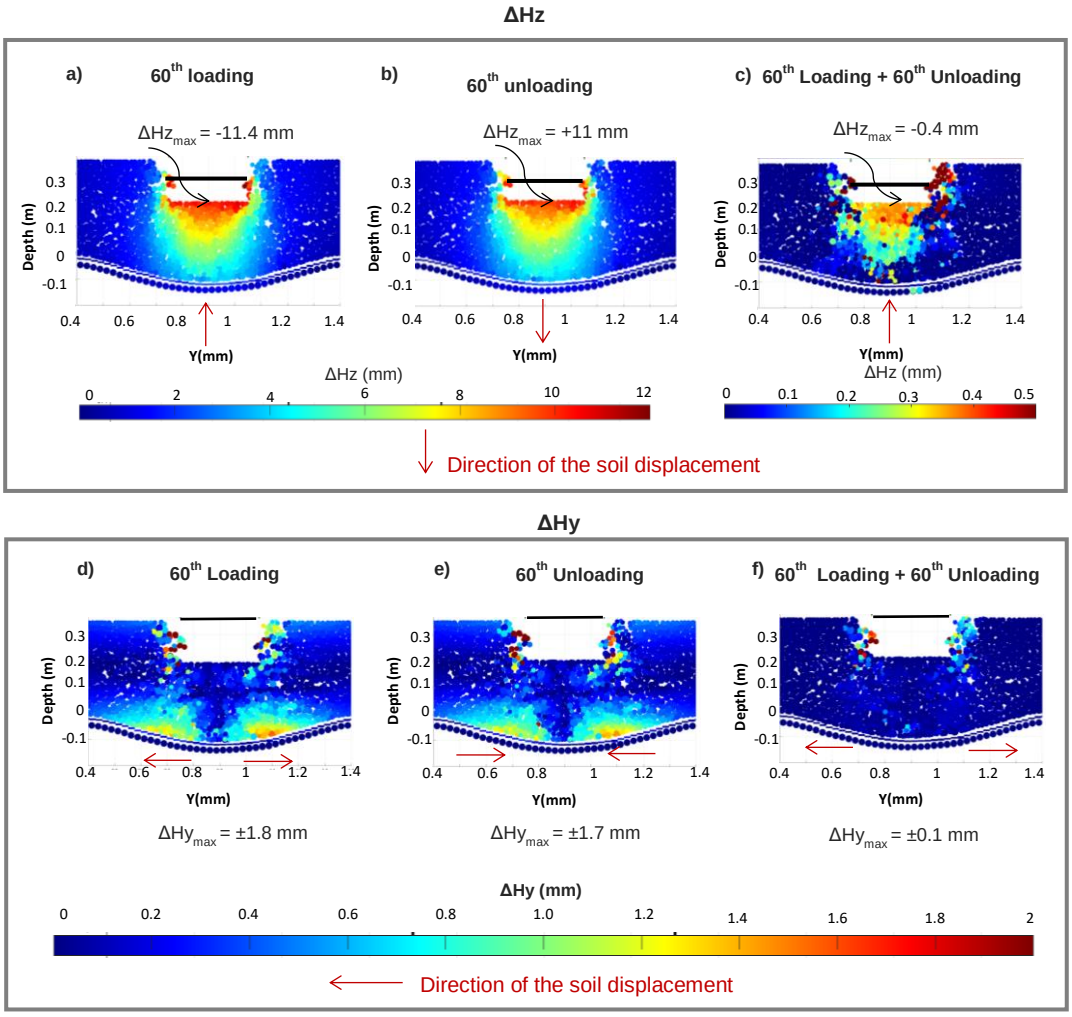

Figure 5-23: ΔHz due to the 60th loading cycle; b) ΔHz due to the 60th unloading cycle; c) ΔHz resultant of the 60th loading-unloading; e) ΔHy due to the 60th loading cycle; f) ΔHy due to the 60th unloading cycle; g) ΔHy resultant of the 60th loading-unloading

5.4.3 Force distribution within the granular mattress

The study investigates the contact forces *F* between clusters located in the vertical section beneath a loading plate, with a thickness of 72 mm (Figure 5-19). The analysis is performed after each loading and unloading cycle, specifically considering cycles 1 and 30.

The contact forces between the mattress grains are depicted using hyphens in Figure 5-24. When the self-weight of the model is applied, the maximum contact force intensity is around 23 N. This contact force intensity increases with depth indicates that the particles lower in the mattress bear the load of those above them. Moreover, it becomes apparent that the direction of force interaction is highly influenced by the arrangement of particles, with a predominant shift towards a vertical orientation as one delves deeper into the material, as visually presented in Figure 5-24.

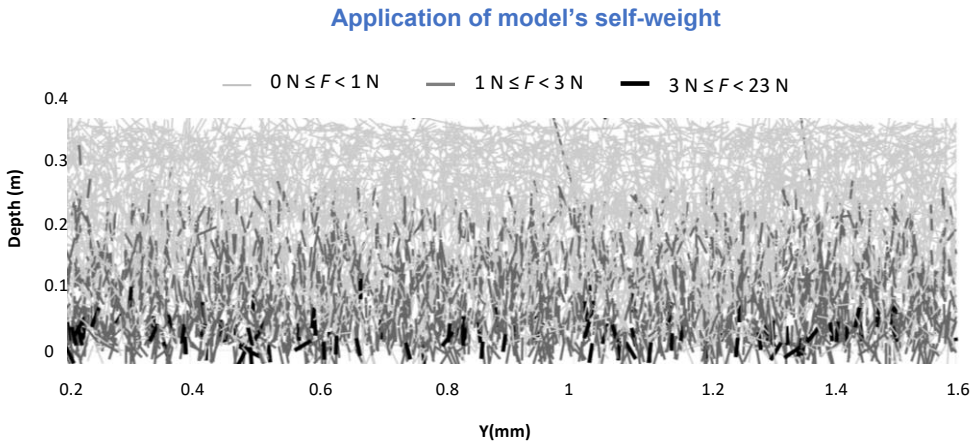

Figure 5-24: Contact force between clusters after the application of the model's self-weight

In Figure 5-25 the contact forces within the mattress during the loading and unloading cycles are visualized and categorized by their magnitudes. The contact force resulting from the application of the model's self-weight is again presented with a specific unified intensity scale, where all loads below 23 N are depicted in the same color (gray) to distinguish between the self-weight load and the applied loads during the loading and unloading cycles (Figure 5-25a).

Following the initial loading of 40 kN, high-intensity force chains emerge in the upper section of the conical zone directly beneath the plate load (Figure 5-25b). As depth increases, this force intensity gradually diminishes, while its impact extends over a broader area. Moreover, with further depth, a noteworthy change occurs: the direction of the contact force becomes increasingly oblique. This indicates that the loads are distributed form the semi cone zone to the neighbouring zones. Such a distribution aligns with predictions for a typical granular platform. During the initial unloading phase, transitioning from 40 kN to 1 kN (Figure 5-25c), the forces between particles undergo gradual relief due to the diminishing external load. This translates into an overall reduction in force magnitude. Forces redistribute across particles, causing the region located at the GTX interface beneath the plate to be less engaged in particle interactions compared to the areas on its left and right. These latter areas with the region directly beneath the plate in the mattress's upper section exhibit a tendency to restore their positions that existed prior to loading during the unloading phase.

Upon completing the 30th loading cycle, discernible shifts occur in the distribution of force chains (Figure 5-25d). Influenced by cyclic loading, a distinct realignment takes place, driven by particle repositioning and interlocking mechanisms. This realigned zone becomes narrower than the area affected during the first cycle (Figure 5-25b). Consequently, the force transmission pattern becomes less pronounced compared to the initial cycle. This is characterized by a heightened vertical alignment of contact forces within the mattress, contrasting with the initial cycle's oblique force direction. This realignment is accompanied by a prevalence of higher contact force magnitudes in contrast to the first loading cycle. This trend towards vertical alignment and increased force magnitudes, observed after thirty cycles, signifies a more focused and direct load transmission to the GTX sheet, rather than to the adjacent zones of the semi-cone, as seen in the first cycle.

Following the 30th unloading phase, as the platform undergoes relief, the intensity of force chains decreases due to load removal (Figure 5-25e). Interestingly, the internal zone of the semi-cone maintains higher force intensities compared to the semi-cone's extremities, in contrast with the behaviour observed during the 1st unloading cycle (Figure 5-25c). As consequence the internal zone of the semi-cone exhibit a tendency to restore their positions that existed prior to loading during the unloading phase.

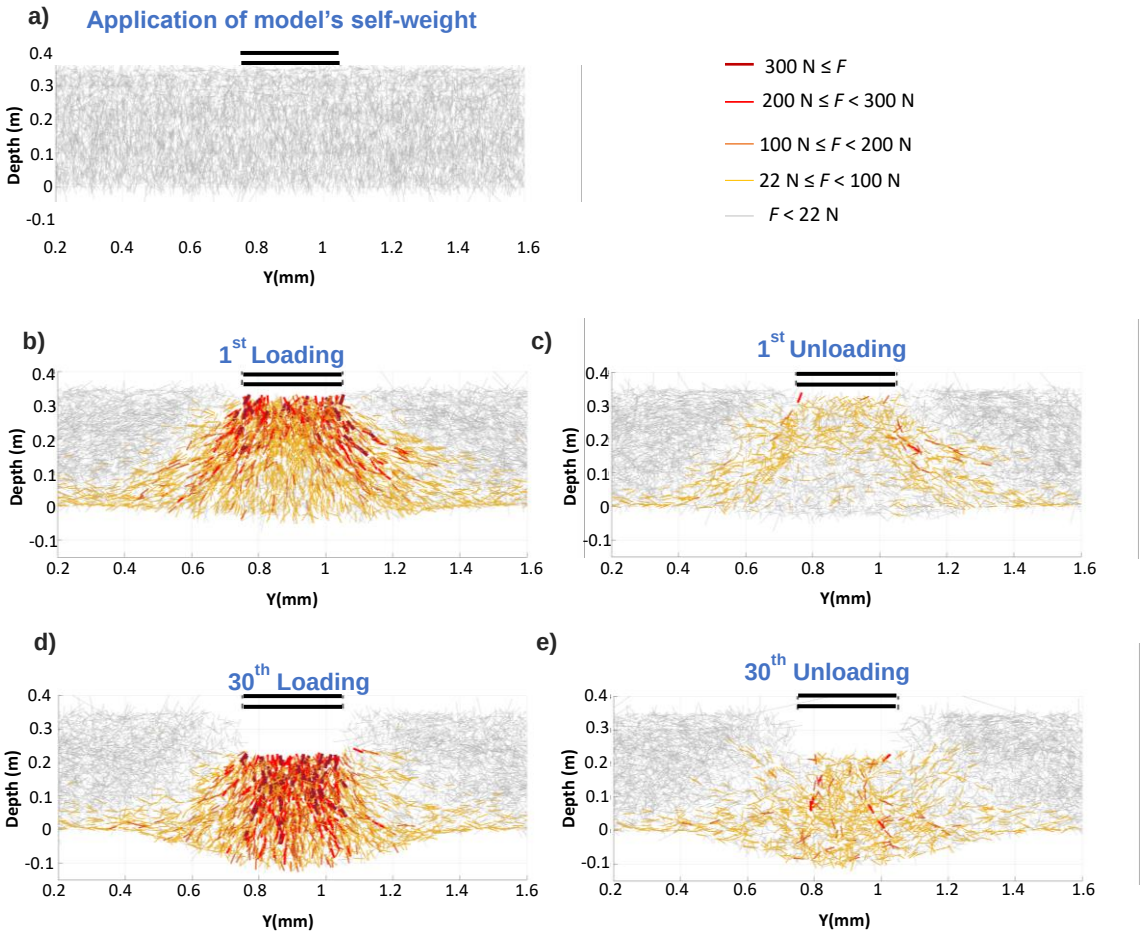

Figure 5-25: Contact force between clusters: a) before loading; b) 1st loading; c) 1st unloading; 30th loading; 30th unloading

5.4.4 Principal stress orientation

Figure 5-26 presents the principal stress orientations within the granular mattress subjected to cyclic vertical loading. The principal stress is calculated based on the application of Weber law in calculation spheres of diameter of 60 mm.

The main stress orientations shift from vertical during application of the model's self-weight to oblique after the 1st loading. Beneath the loading plate, major principal stresses take an oblique orientation towards the adjacent granular mattress zone. This implies cohesive functioning, effectively distributing loads from beneath the plate to neighbouring zones as seen with the contact force in Figure 5-25.

Upon load removal, principal stresses relax, reducing their magnitude (c) Particularly below the plate, principal stress realignment is noticeable as they tend to orient horizontally. The shift in the direction of principal stress from vertical to horizontal aligns with the observation in the contact force, indicating that zones surrounding the semi-cone tend to revert to their positions prior to loading during the unloading phase.

After the 30th loading principal stress orientations shift towards vertical alignment, emphasizing load transmission through the GTX as seen with the contact force (Figure 5-25). By the 30th unloading, particle

rearrangement again affects stress paths, introducing complexity and distinct stress responses compared to the 1st unloading (e). This could be attributed to the fatigue and the damage experienced by the mattress due to the repeated loading-unloading cycles.

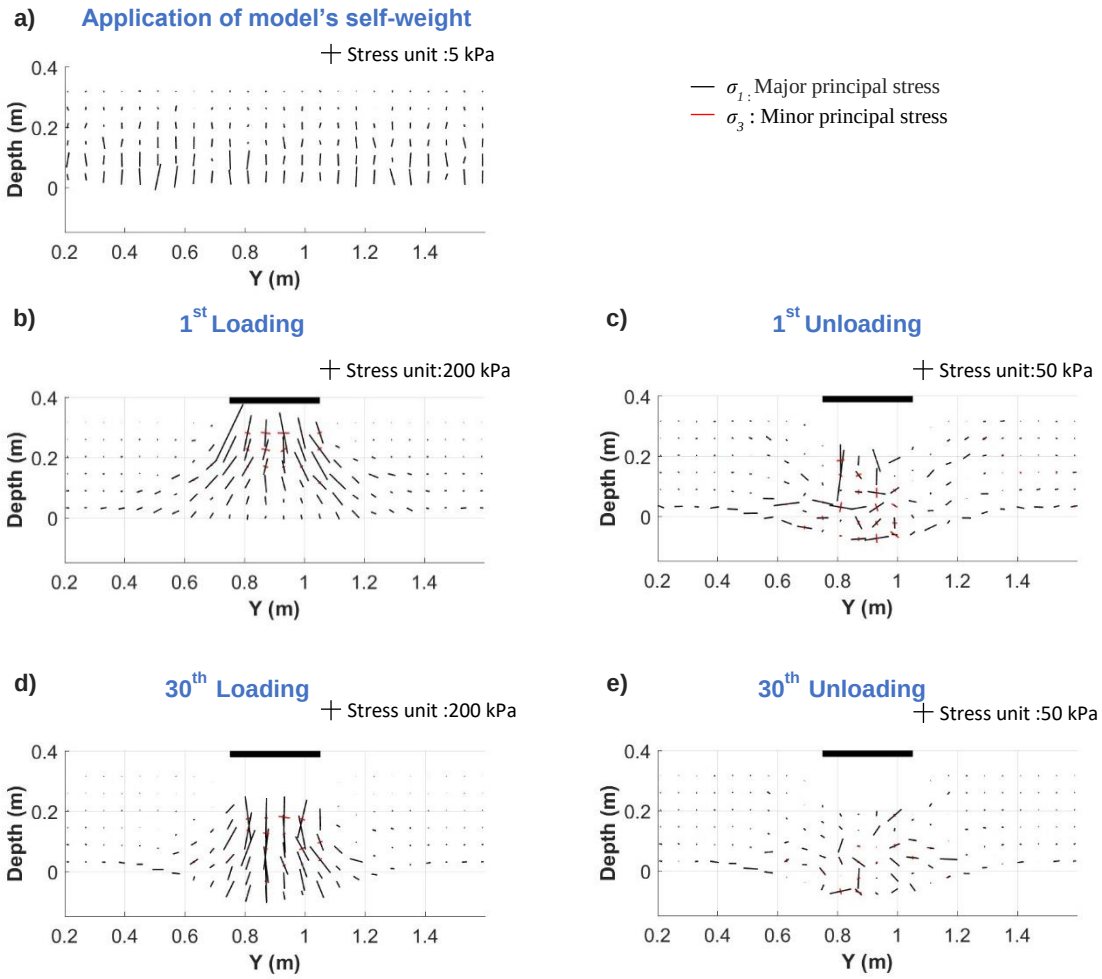

Figure 5-26: Principal stresses orientation within the granular mattress: a) before loading, b) after the 1st loading, c) after the 1st unloading, d) after the 30th loading and e) after the 30th unloading

5.4.5 Particle rearrangement

The observation pertains to the behavior of granular material within a mattress under various loading conditions and cycles. The relative density of the material (Dr) defined as the ratio of solid density after loading to the initial solid density serves as an indicator of densification or shear. The examination of relative density takes place within an elemental volume of fill with a diameter of 300 mm with 500 random points (see section 5.2.2.3). A value greater than 1 signifies compaction, while a value less than 1 suggests shear or decompaction.

The relative density is shown in Figure 5-27 for the mattress material after the 1st, 5th, and 30th loading cycles. After the initial loading the semi conical zone beneath the loading plate is formed. In this zone, the

granular material experiences disturbance. The upper part densifies due to significant force chains, while the lower part near the GTX experiences loosening due to horizontal displacement. Subsequent cycles (Cycle 5 in Figure 5-27b and Cycle 30 in Figure 5-27 c) show progressive disturbance in the conical zone without clear patterns of densification or loosening.

At the edge of the conical zone, shear zones emerge where material undergoes loosening (Figure 5-27). This phenomenon becomes more pronounced during Cycle 5 (Figure 5-27b) and Cycle 30 (Figure 5-27c). Additionally, zones along the model's edges experience slight disturbances. In Cycle 1, there's a trend towards densification more than loosening, which diminishes with cycles due to particle rearrangements caused by repetitive cyclic loading (Cycle 5 and Cycle 30).

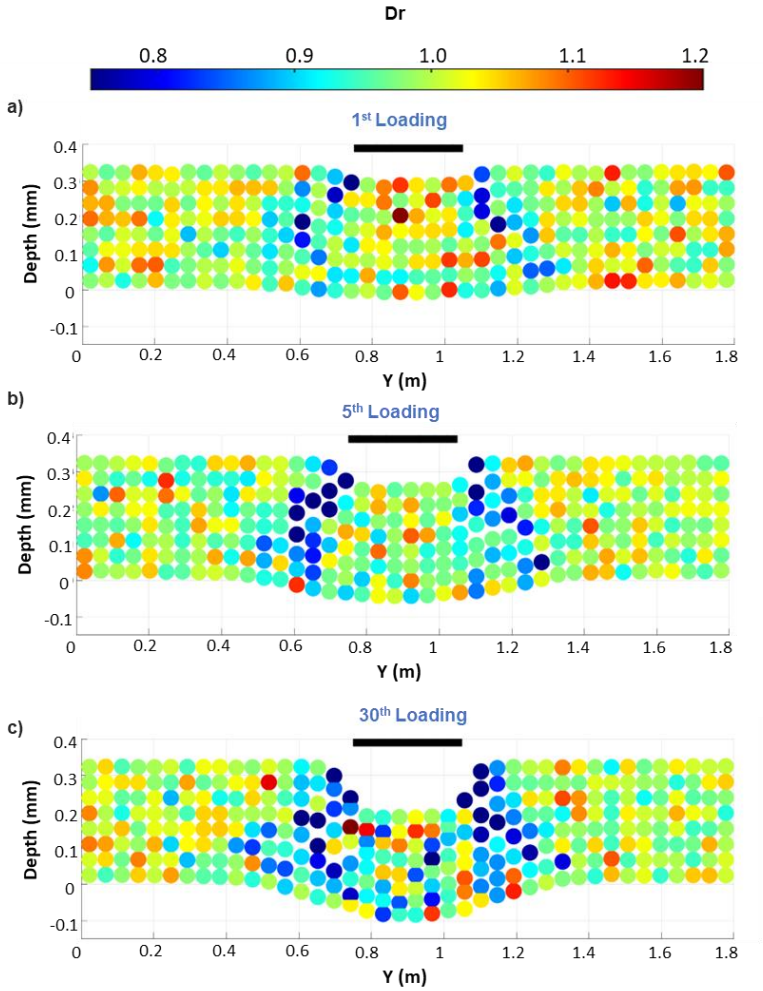

Figure 5-27: The relative density of the mattress material after the: a) the 1st loading, the 5tht loading, 30th loading

5.4.6 GTX displacement

This analysis focuses on the displacement of the GTX within the cross-section at the model's centerline (Figure 5-28) after the 1st, 5th, 30th and the 60th cycle.

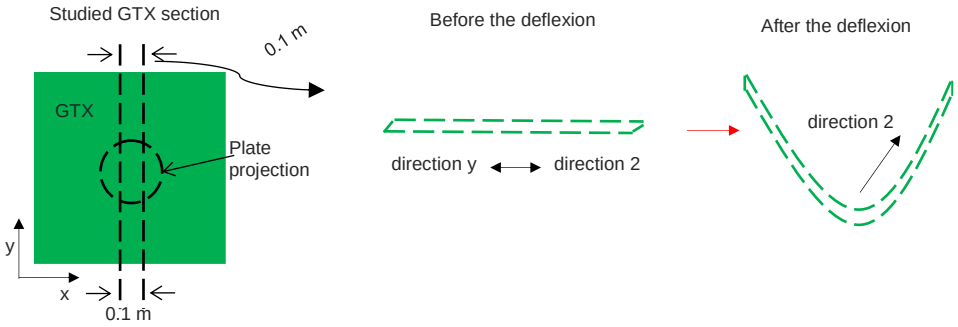

Figure 5-28: GTX studied section location

The deflection curve exhibits its maximum deflection directly beneath the center of the plate load (Figure 5-29a). This behavior aligns with expectations, as the highest deflection occurs where the load is most concentrated. As one moves outward from the plate's center towards the model's edges, the deflection gradually decreases and eventually reaches zero at the GTX's anchored zones. Furthermore, both the maximum deflection value and the overall deflection magnitude increase from cycle 1 to cycle 30.

Figure 5-29b presents the horizontal displacement profiles along the cross section. Negative horizontal displacement indicates that the GTX is pulled toward the two extremities of the section, while positive displacements indicate that the GTX is pushing toward the center of the section (the plate loading center). In the central zone (covering the plate zone and its immediate surroundings), the GTX is streched and moved to the extremities of the section. At the section's edges, the GTX is actively pulled toward the centre of the model in order mobilising the anchorage zones at 5^{th} and 30^{th} cycle. These two observations indicate that the GTX is not merely a passive element but actively participates in the model's behaviour. This engagement becomes more pronounced as we progress from cycle 1 to cycle 5 and, eventually, to cycle 30.

After 30 cycles, the increment in deflection and horizontal displacement level off, due to specific model conditions that prevent further subgrade settlement. This is illustrated by the overlap between the deflection profile (horizontal displacement profile) at cycle 30 and the deflection profile at cycle 60.

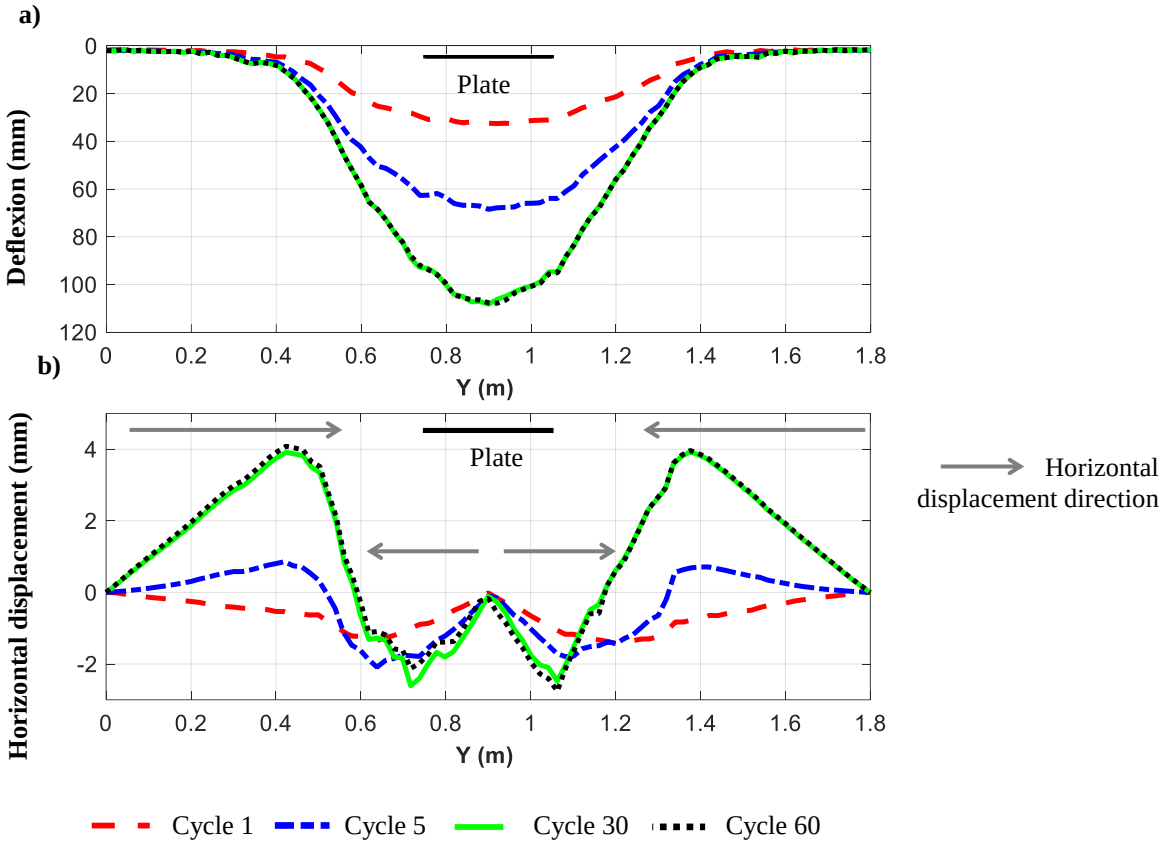

Figure 5-29: a) GTX deflection profiles after the 1st, 5th, 30th and 60th cycles, b) GTX horizontal displacement profiles after the 1st , 5th, 30th and 60th cycles

5.4.7 GTX strain

The study focuses on the strain of the GTX during the 1st, 5th, and 30th cycles, with particular attention to the central and anchored zones of the GTX sheet. The central zone encompasses the projection of the loading plate on the GTX and the surrounding circular region, while the anchored zones are situated at the sheet's edge. $\Delta\varepsilon_2$ is the strain increment in direction 2, corresponding to the deflected y-axis, originally parallel to the y-axis but altered due to deflection.

In the 1st loading-unloading cycle (Figure 5-30), two complementary effects are manifested. Post-unloading, elastic recovery occurs within the central zone previously subjected to elongation during the loading phase. Simultaneously, elongation is observed in the anchorage zone after unloading, which had earlier undergone elastic recovery during the loading phase. The net effect in the 1st cycle is stretching within the circular zone, resulting in a $\Delta\varepsilon_2$ of 0.2%. In the anchored zones, elongation offsets elastic recovery, yielding no net effect.

During the 5th loading cycle, the central zone continues to stretch, albeit in a smaller area and magnitude than in the initial loading due to increasing curvature and decreasing deflection rate over successive cycles. Like the 1st unloading, in the 5th unloading cycle, elastic recovery occurs in the central zone, while the anchored zones exhibit elongation with the same magnitude as in the 1st unloading. The net effect is a 1%

elongation in the central strip between the two parallel anchored zones, passing through the central zone (Figure 5-30f), indicating active engagement of the GTX within this central strip.
Throughout the 30th loading, the GTX central zone continues to stretch, undergoing elastic recovery during the 30th unloading. The combined effects of loading and unloading result in elastic recovery offsetting elongation in the same magnitude, resulting in no net effect.

Moreover, Figure 5-31 presents the strain ε_2 after various loading and unloading cycles, including the 1st loading, 1st unloading, 5th loading, 5th unloading, and 30th unloading. A comparison of the strain values between these corresponding loading and unloading cycles reaffirms the elastic recovery characteristics exhibited by the GTX sheet during unloading, as discussed earlier. Furthermore, Figure 5-31e reveals a progressive increase in strain values across these cycles, reaching 2% at the 30th cycle. This range aligns with typical strain values seen in similar applications, based on feedback.

In both graphs of the 1st cycle, the strain ε_2 displays a circular pattern concentrated at the central zone. Notably, this circular pattern transforms into an ovate (oval-like) shape in the 30th cycle, encompassing the centre of the model and the two parallel anchored zones. This change in shape signifies an increase in the mobilization of the GTX over cycles, indicating that the GSY sheet becomes progressively more engaged and responsive as the loading and unloading cycles advance.

It is important to note that the strain results ε_2 pertain to direction 2, which is a specific orientation, explaining the lack of symmetry in the strain patterns. The other dimension, direction 1 parallel to x, generates strain ε_1 similar to ε_2 but aligns with direction 1 rather than direction 2 of ε_2, ensuring a complementary pattern (Figure 5-32).

To supplement the available information regarding GTX strain, strain profiles ε_2 in the direction 2 of reinforcement are depicted in Figure 5-33. The shapes of the ε_2 strain curves are the same as those of the T_2 tension curves, due to the linear relationship in the behavior law connecting strain and tension, with a single stiffness value assigned to each fiber. The maximum values of strain and tension are found beneath the center of the plate. It is important to note that at the section's ends, which can be considered the anchorage zone, the values of strain and tension are not reduced to zero because of boundary conditions.

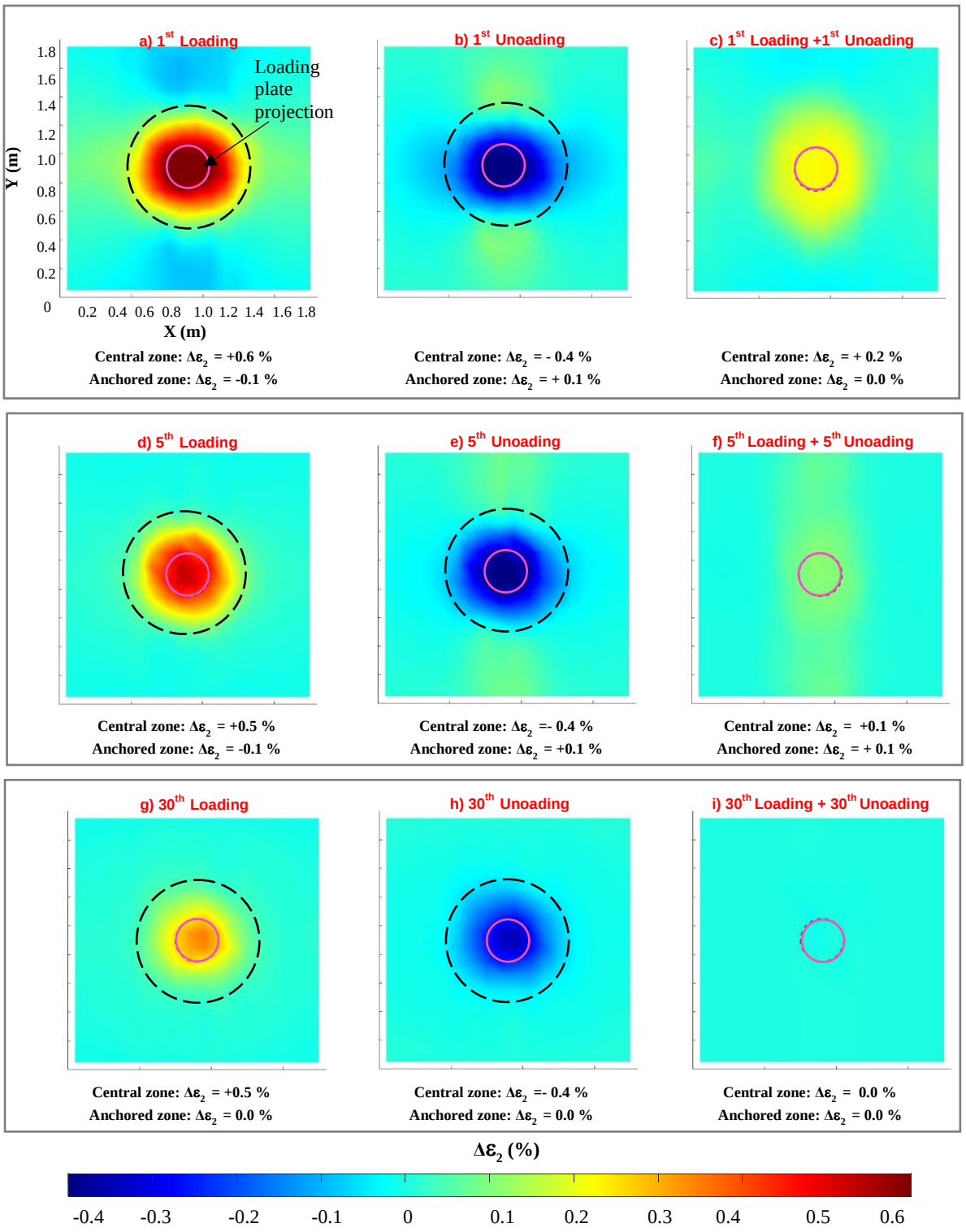

Figure 5-30: The GTX increment deformation due to loading, unloading and their resultant of: a) the 1st cycle, b) the 5th cycle and c) the 30th cycle

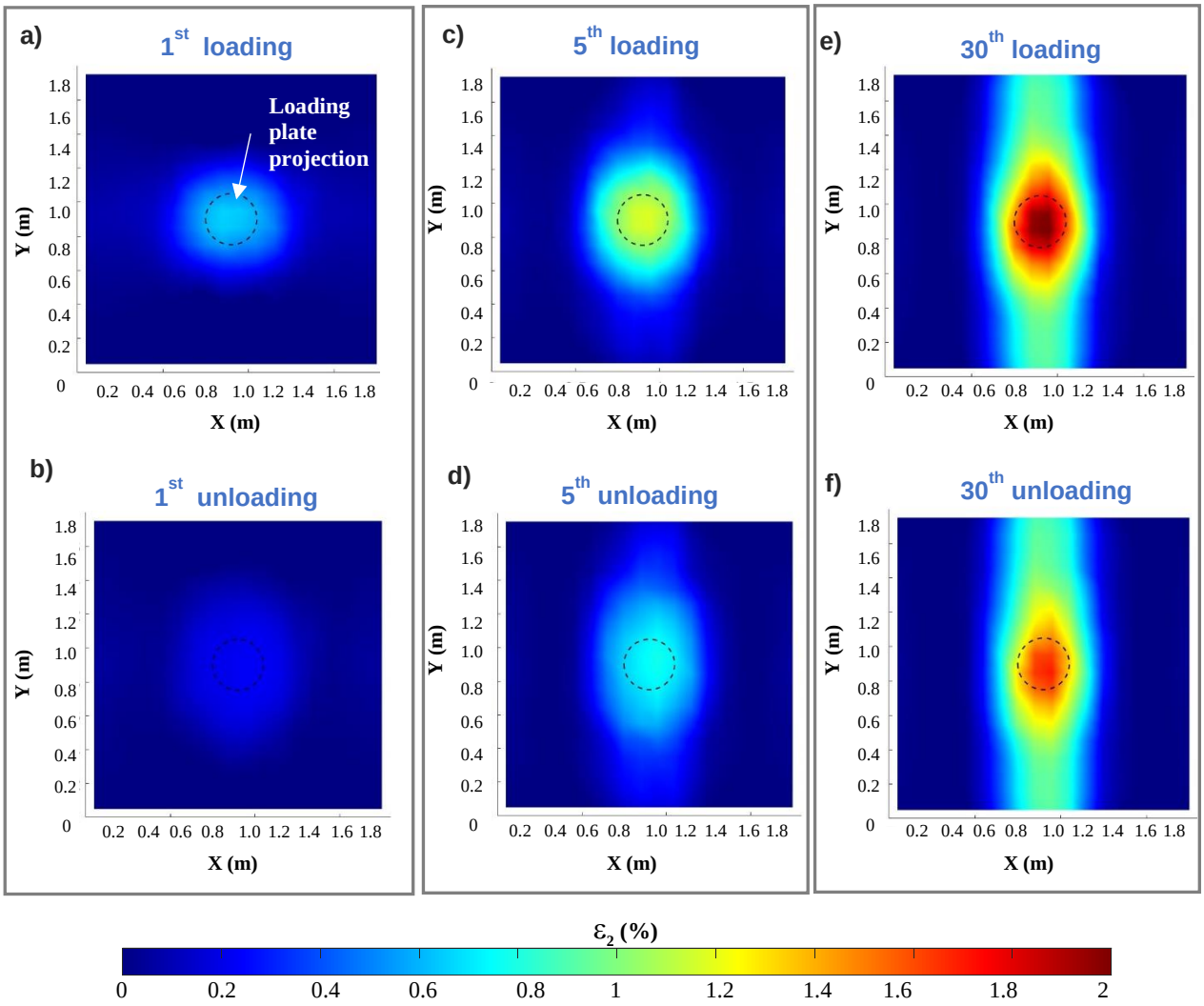

Figure 5-31: The GTX strain (ε_2) in the direction 2: a) the 1st loading; b) the 1st unloading; c) the 5th loading; d) the 5th unloading; e) the 30th loading and f) the 30th unloading

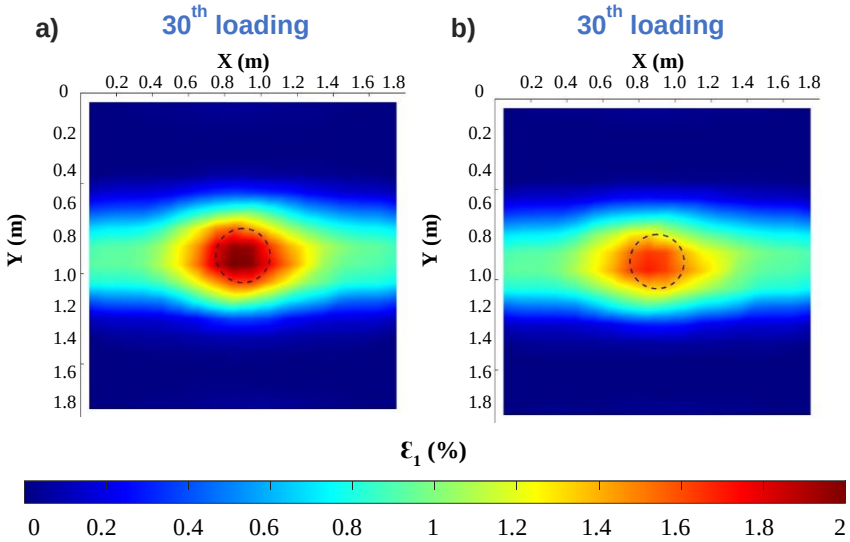

Figure 5-32: The GTX strain (ε_1) in the direction 1: a) the 30th loading and b) the 30th unloading

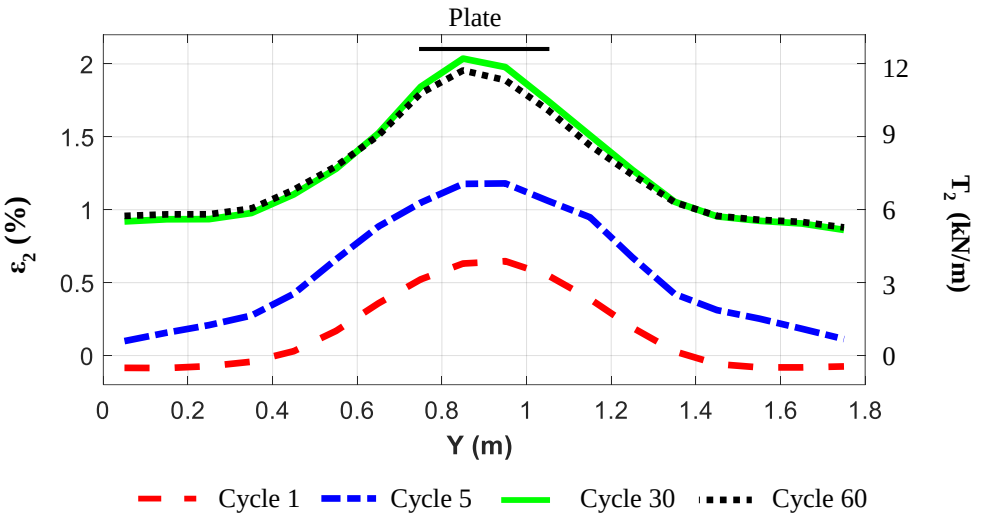

Figure 5-33: GTX strain / tension profiles after the 1st, 5th, 30th and 60th cycles in the direction 2

5.4.8 Involved mechanisms

In the context of a GTX-reinforced granular platform constructed over soft subgrade soil, several critical functions can fulfil by the GTX. These functions, including separation to prevent the mixing of granular materials with the underlying subgrade, stabilization through the frictional interaction between the GTX and soil grains, and reinforcement owing to the tensioned membrane effect imparted by the GTX, can be ensured by the GTX. Within the numerical model, access is granted to essential data regarding the tangential

forces (ft) between the granular mattress grains and the GTX, as well as the tensile forces within the GTX itself (T).

The studied section of the GTX has been centrally positioned in the model, aligned with direction 2 (Figure 5-34). The tangential forces between the mattress grains and the GTX at their interface in direction 2 are denoted as ft_2, while the tensile force in direction 2 is identified as T_2.

To clarify the process of determining ft_2 and T_2, a specific calculation is followed (Figure 5-34). For the calculation of ft_2, the strip section, measuring 0.1 m in width and 1.8 m in length is divided into 18 squares, each having a length of 0.1 m. In each square, ft_2 is computed by summing the tangential forces parallel to direction 2 (ft_{2i}) and then dividing this sum by the square's width. Similarly, for the calculation of linear tensile forces T_2, the same strip section is divided into 18 squares. Within each square, T_2 is determined by summing the tensile effort parallel to direction 2 and dividing this sum by the number of triangular elements considered.

The tensile effort evolves the sum of the frictional effort and the effort due to the tensioned membrane effect. Consequently, the effects attributed to the tensioned membrane can be quantified through the resultant between the tangential forces and the tensile forces within the GTX.

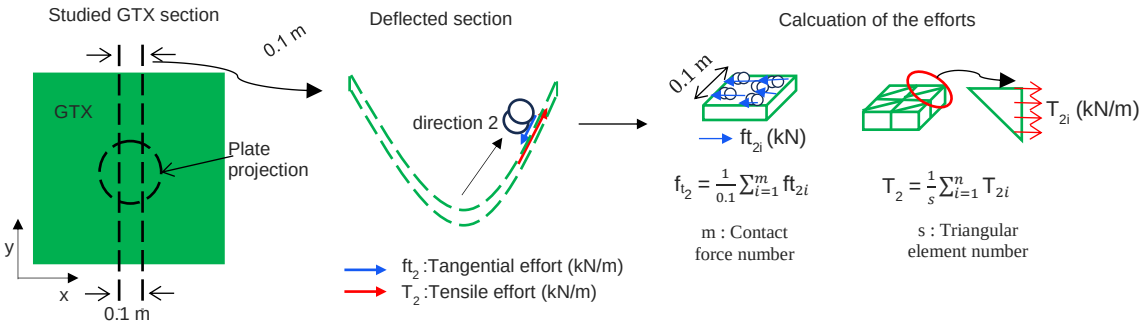

Figure 5-34: Representation of the studied section and the acting effort

After the 1st loading phase, the tensioned membrane effort profile shows a peak of 4 kN/m at the loading plate projection (Figure 5-35) with the GTX strain (ε_2) reaching its peak of 0.6% (Figure 5-33). Simultaneously, the frictional force profile exhibits two peaks of 2 kN/m in the vicinity the plate projection where the GTX strain is 0.3% (Figure 5-33). This is primarily due to the relative displacement between the granular soil and the GTX, emphasizing the significance of frictional effort in this zone. As consequence, the tensioned membrane effect prevails beneath the plate where the GTX strain is 0.6%, while friction dominates in the vicinity of the plate projection where the GTX strain is 0.3%.

Moreover, the frictional effort profiles across the 1st, 5th, 10th, and 30th loading cycles reveal a relative constancy across these cycles. Conversely, tensioned membrane effect effort progressively increases with each cycle, highlighting its growing significance. The initial cycle underscores the importance of the frictional effect, but as cycles advance and GTX strain and deflection increase, the tensioned membrane effect takes precedence, ultimately surpassing frictional effort across subsequent cycles.

It's important to note that after the 1st, 5th, 10th, and 30th unloading cycles, the tensile efforts decrease due to the relaxation of the GTX sheet. Furthermore, the frictional efforts approach zero, as the relative displacement between the GTX and the surrounding materials reverses with each loading/unloading cycle.

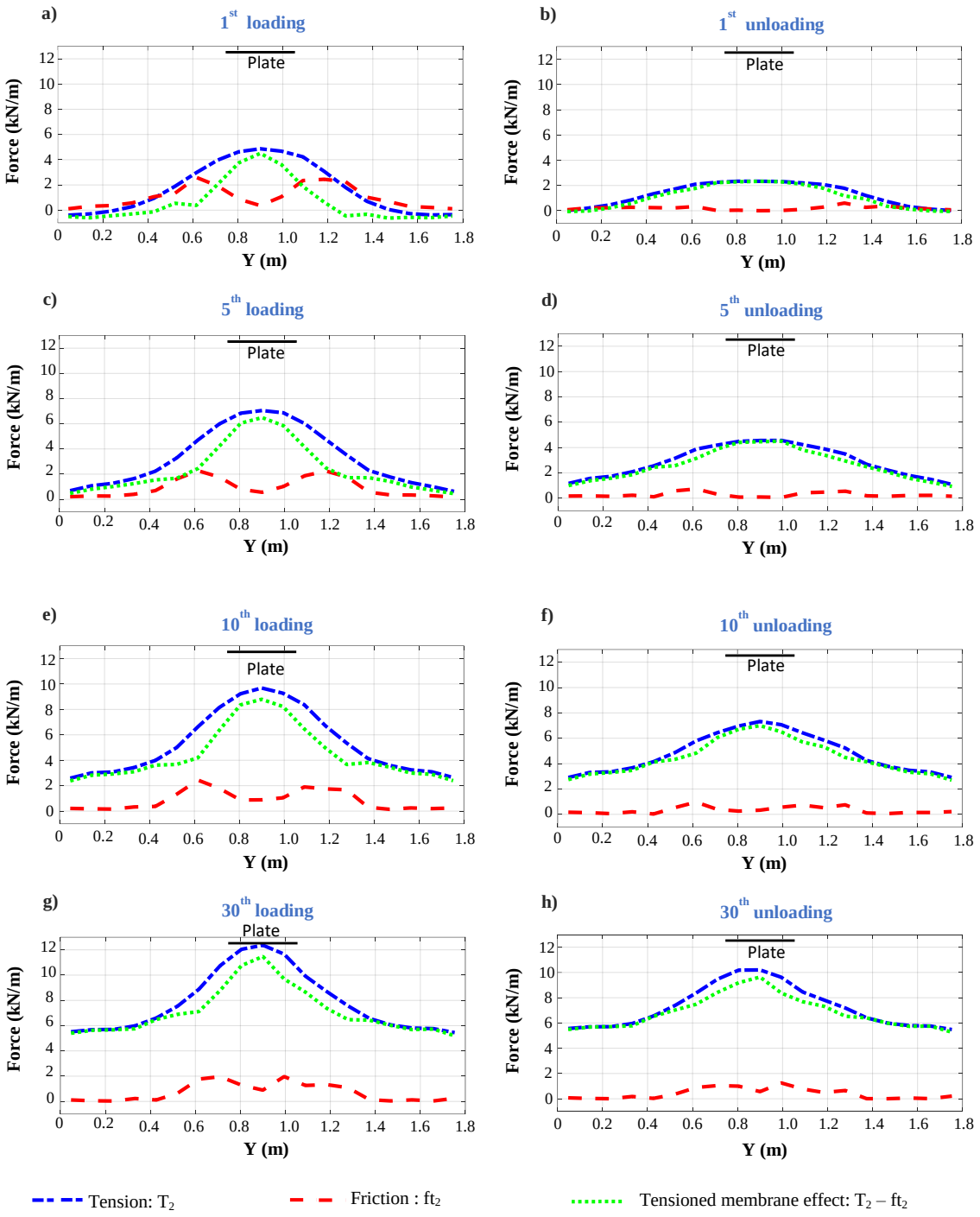

Figure 5-35: The frictional and the tensile efforts of the GTX: a) after the 1st loading; b) the 1st unloading; c) the 5th loading; d) the 5th unloading; e) the 10th loading; f) the 10th unloading; g) the 30th loading; h) the 30th unloading

5.4.9 Load Transfer through the GTX

The tensioned GTX, characterized by its curved shape and out-of-plane deformation, can transfer loads from the solicited zone to the anchored zone. The vertical stress acting on the upper part and on the lower part of the GTX within the central section (Figure 5-36) is shown in Figure 5-37. It's important to note that the sum of the vertical force acting on the upper face of the GTX is equal to that acting on its lower face. The vertical stress applied to the lower face of the GTX is lower than that experienced by the upper face within the region of the loading plate and its immediate surroundings, after the 1st (a), 5th (b), and 30th (c) loading. However, as moving away from the central zone, the vertical stress on the lower face of the GTX surpasses the vertical stress on the upper face especially after the 5th cycle (c) and the 30th cycle (d). This phenomenon signifies that the stress acting on the upper face of the GTX beneath the circular plate is not entirely transmitted vertically to the subgrade's surface; instead, a portion of it is redirected by the GTX towards the surrounding area (membrane effect).

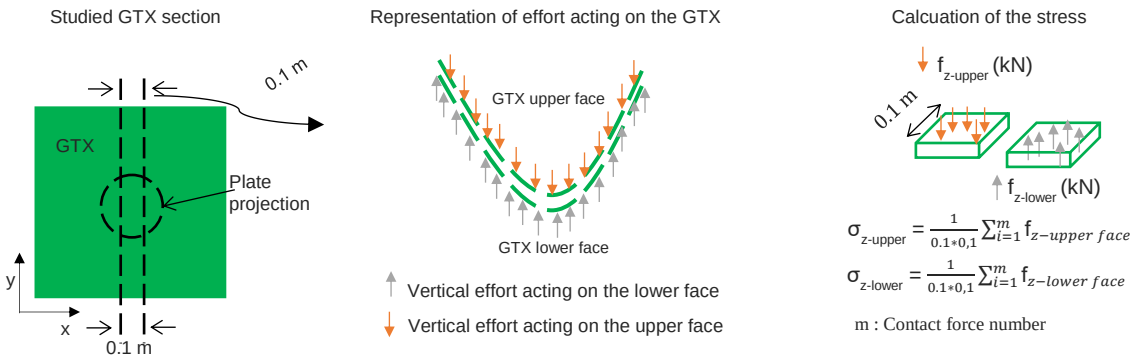

Figure 5-36: Representation of the studied section and the acting stresses

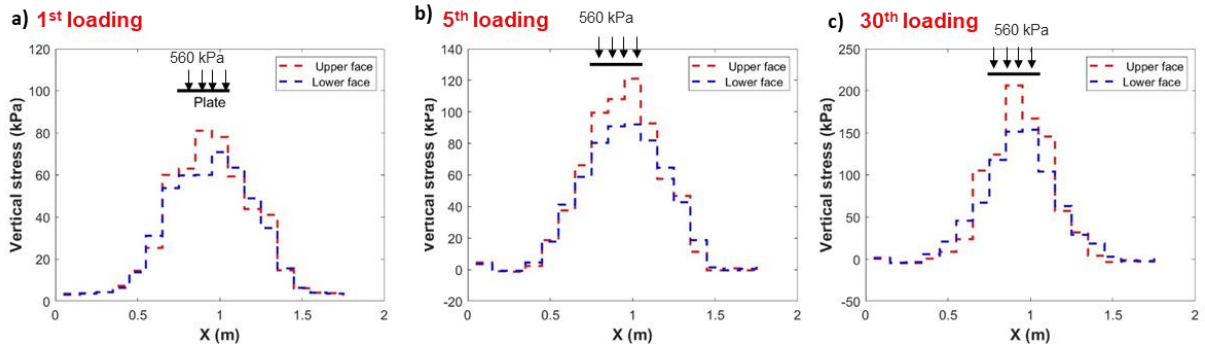

Figure 5-37: The vertical stress on the upper face of the GTX and on the lower face of the GTX: a) the illustration of the GTX; b) After the 1st loading; c) the 5th loading and d) the 30th loading

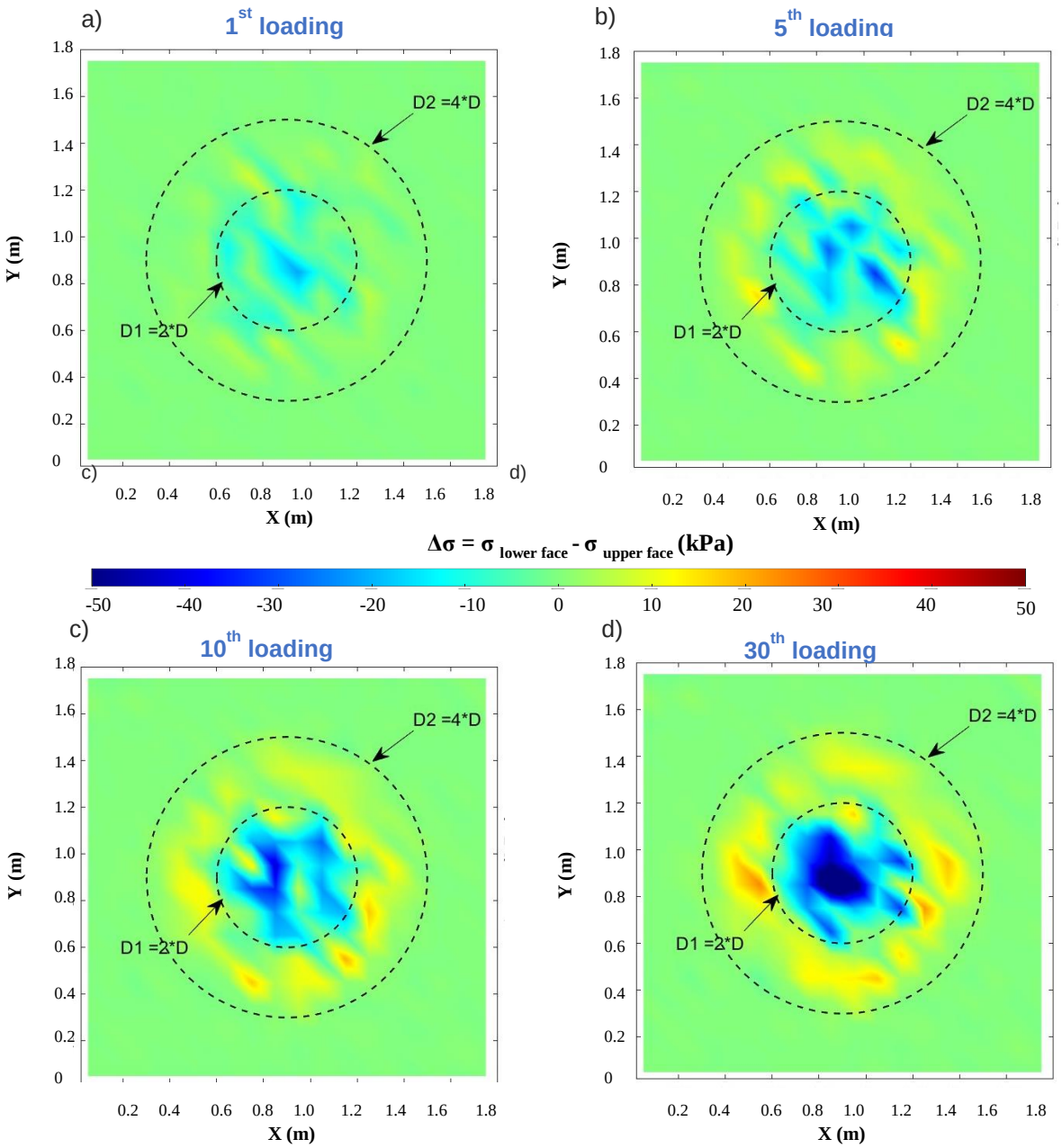

Figure 5-38: The resultant of the vertical stress acting on the lower face of the GTX subtracted from the vertical stress acting on the upper face of the GTX: a) after the 1st loading b) the 5th loading; c) the 10th loading and d) the 30th loading

Besides, Figure 5-38 depict the resultant of the vertical stress on the GTX upper face from the vertical stress on the GTX lower face. The result of subtracting the vertical stress acting on the upper face of the GTX from that on the lower face, denoted as ($\Delta\sigma$) (expressed in kPa) after the 1st, 5th, 10th, and 30th loading cycles, exhibits a negative value within a circular zone, centred at the loading plate's center, and with a

diameter D_1 equal to 2*D (Loading plate diameter = 0.3 m). Conversely, it shows a positive value in the area located between the circles with diameters D1=2D and D2=4D. This verify that a portion of the stress acting on the upper face of the GTX is directly transmitted to the subgrade, while another portion is transmitted by the GTX itself to the adjacent region (2D < diameter < 4D). Moreover, the comparison between the magnitudes of $\Delta\sigma$ for the 1^{st}, 5^{th}, 10^{th}, and 30^{th} loading cycles becomes increasingly significant as the loading cycles progress. This observation implies that the GTX becomes progressively more engaged in the load distribution by membrane effect with each cycle.

5.4.10 Conclusion on the Numerical Model's Representativeness

The performance of the numerical model in simulating a GTX-reinforced granular platform over soft subgrade soil was assessed through a comprehensive analysis. Several key insights were revealed.

Firstly, vertical displacements of the mattress particles were observed, with a semi-cone-shaped downward movement initiated by the first loading, followed by an upward movement during unloading. Horizontal displacement primarily occurred toward the model edges in the zone around the loading plate projection where the mattress grains interacted with the GTX. A reverse horizontal displacement in the same zones occurred after the unloading. As results permanent vertical and horizontal displacement were occurred after the 1^{st} cycle. The magnitude of permanent displacement decreased with each cycle due to an increase in subgrade rigidity.

Furthermore, the investigation delved into particle rearrangement, with patterns of densification observed under the loading plate and shear at the zones between the semi-cone and its surroundings.
In addition, changes in principal stress orientations within the granular mattress as loading cycles progressed were explored. Shifting patterns in force directions and intensities within the mattress were revealed, suggesting complex force transmission mechanisms.

GTX displacement, deflection, and strain were examined, emphasizing the active role of the GTX in the model and the activation of the two central strips parallel to 1 and 2 directions. Insights into load transfer through the GTX were provided, demonstrating its increasing engagement as loading cycles advanced. A comparison between the frictional forces acting on the GTX and the forces related to the tensioned membrane effect confirmed an increase in the latter as deflection increased with each cycle. The contribution of frictional forces remains relatively consistent during the loading cycles and tends to approach zero during unloading due to the GTX 's elastic behavior. Consequently, the dominance of the soil confinement mechanism, as observed in the first cycle, diminishes throughout subsequent cycles. Instead, it's the membrane effect that increasingly takes precedence across cycles, ultimately characterizing the reinforcement mechanism.

Collectively, these findings underscore the capability of the numerical model to accurately represent and simulate the complex behaviours and performance of GTX-reinforced structures. This reaffirms the valuable role of the model as a tool for comprehending how these applications are influenced under cyclic loading conditions.

5.5 Conclusion

The chapter begins by providing a comprehensive explanation of the FEM-DEM coupling method, initially introduced by Villard et al. in 2009. The numerical model is presented, characterized based on insights from laboratory experiments, material observations, and prior applications. A sensitivity analysis is conducted to determine crucial parameters, and the selected damping factor of 0.2 and load increment of 2N ensure model stability while minimizing dynamic effects.

The need for calibration arises as the purely frictional mattress proves inadequate to withstand applied loading. In addition to that, the need of reducing the calculation time by reducing the number of applied

cycles is the other need to calibrate the model. The calibration involves two key aspects: the introduction of adhesion between mattress grains to enhance resistance to external forces and refining the subgrade behavior law. The calibration ensures numerical models attained the range of the subgrade settlement of the experimental with reduced number of loading-unloading cycles compared to the experimental.

The comparison of numerical and experimental results focuses on the first cycle, last experimental cycle, last numerical cycle, and their evolution. Test T_5 is selected for comparison with two numerical models: M_1 (purely frictional mattress with (φ_{peak} = 41°, c = 0 kPa), M_2 (φ_{peak} = 37°, c = 17 kPa), and M_3 (φ_{peak} = 39°, c = 13.5 kPa). M_1 exhibits higher settlement and vertical stress levels, highlighting its inadequacy. In contrast, M_2 and M_3, with added adhesion between grains, closely match T_5 results, demonstrating effective calibration.

The chapter concludes with a detailed analysis of the numerical model's performance in simulating a GTX -reinforced granular platform over soft subgrade soil. Several key insights are revealed, including vertical and horizontal particle displacements, patterns of densification and shear, shifting principal stress orientations, and the active role of the GTX in load transfer mechanisms. The findings confirm the model's ability to accurately represent complex geotechnical behaviors under cyclic loading, providing valuable insights into such applications. This underscores the model's role as a powerful tool for understanding the performance of GTX -reinforced structures.

6. Chapter 6. Parametrical study

6.1 Introduction

This chapter delves into a comprehensive parametrical study through a series of numerical simulations with the overarching goals of aligning results with experimental and literature findings and scrutinizing parameters that have received limited attention. The key simulations and their main parameters are detailed in Table 6-1.

To enhance computational efficiency, the initial step involves a comparison between M_4 and M_5, where the cluster number in the mattress is halved from 72,000 to 36,000. This adjustment, accompanied by an increase in sphere diameter to maintain consistent model dimensions, reduces computational time from two weeks to one week per simulation. This flexibility allows for a choice between the 72,000-cluster model and the reduced-cluster model based on precision requirements.

The impact of subgrade softness on GTX effectiveness is a prominent topic in the literature. To investigate its influence on soil settlement reduction, six simulations (M_5 to M_{10}) with two different initial subgrade reactions and three different GTX stiffness values are examined. Similarly, the impact of GTX stiffness, a topic discussed in experimental and literature, is re-evaluated through a comparison of three simulations involving different GTX stiffness values.

Furthermore, the study addresses the often-overlooked friction angle at the granular mattress and the GTX interface ($\delta_{GTX\text{-}clumps}$). Simulations with a frictionless interface (M_{11}), an average friction angle of 38°(M_5), and a relatively high friction angle of 45°(M_{12}) enrich the understanding of its impact.

Moreover, the investigation expands its focus to the mattress by examining the influence of two crucial microscopic parameters: Φ_{int} (intergranular friction angle) and a (adhesion). During the calibration of the numerical model based on experimental results (as detailed in section 5.3), uncertainty arose regarding the inclusion of adhesion between grains. To elucidate its impact, the outcomes of two simulations, M_4 (a=25 kPa) and M_{14} (a=5 kPa) are compared. Concurrently, the effect of the friction angle is also scrutinized through comparisons between simulations M_4 (Φ_{int} =20°) and M_{13} (Φ_{int} =30°).

The comparative analysis spans various facets, encompassing particle displacement, contact forces between particles, the evolution of soil surface settlement, and the comparison of load transfer through the GSY. Additionally, the frictional efforts of the GTX are scrutinized to provide a comprehensive understanding of the model's behavior under varied conditions. For sake of clarity of the PHD report, only main results are presented in the following. Complementary results are given in the annexe.

Table 6-1: Simulations and parameters in the parametrical study

	k_1 (MPa/m)	J_x (kN/m)	J_y (kN/m)	$\delta_{clusters\text{-}GTX}$ (°)	Φ_{int} (°)	a (kPa)	φ_{peak} (°)	c (kPa)	Cluster Number
M_4	2	600	600	38	20	25	39	13.5	72,000
M_5	2	600	600	38	20	25	39	13.5	36,000
M_6	2	1,200	1,200	38	20	25	39	13.5	36,000
M_7	2	10	10	38	20	25	39	13.5	36,000
M_8	3	1,200	1,200	38	20	25	39	13.5	36,000
M_9	3	600	600	38	20	25	39	13.5	36,000
M_{10}	3	10	10	38	20	25	39	13.5	36,000
M_{11}	2	600	600	0	20	25	39	13.5	36,000
M_{12}	2	600	600	45	20	25	39	13.5	36,000
M_{13}	2	600	600	38	30	5	46	2	72,000
M_{14}	2	600	600	38	20	5	39	2	72,000

6.2 Impact of the number of particles comprising the mattress

6.2.1 Introduction

For the purpose of optimizing computational efficiency, Simulation M_5 was conducted, featuring a mattress comprising 36,000 clusters, which represents half the number of clusters found in Simulation M_4. This reduction in cluster number results in a significant reduction in calculation time compared to the M4 simulation (from 2 weeks to 1 week). The minimum ($l_{n\,min}$), maximum ($l_{n\text{-}max}$), and average ($l_{n\text{-}average}$) cluster lengths for both simulations M_4 and M_5 are showed in Table 6-2. It is worth noting that in the experiment, the gravel's largest diameter (D_{max}) was 0.031 m, smaller than the smallest length ($l_{n\,min}$). Selecting the same diameter distribution as the experiment is not the aim of this study because this would consume a lot of time; it was sufficient to attain the same macroscopic soil response when the experiment and the numerical were put in comparison.

Except for the cluster number, all the characteristic parameters of M_5 are identical to those used in the M_4 model (Table 6-1). In the forthcoming analysis, a comprehensive comparison will be carried out between specific outcomes of M_4 and M_5 to determine whether the reduction in cluster number by half yields similar behavioural patterns. This comparative analysis will encompass various aspects, including particle displacement and inter-particle contact forces, the evolution of soil surface settlement, GTX deflection, GTX displacement, and GTX strain. Additionally, a comparison will be made between the vertical stress applied to the upper face of the GTX in M_4 and M_5.

6.2.2 Particle displacement and contact force

The study on doubling cluster numbers' impact on vertical displacements compares M_4 (72,000) and M_5 (36,000) beneath the loading plate, specifically on the mattress and subgrade surfaces (Figure 6-1).

Throughout the initial 1st to 5th cycles, the vertical displacement evolution profiles for M_4 and M_5 exhibit overlap in the upper mattress. However, from the 5th cycle onward, these displacement profiles diverge, with the higher cluster number (M_4) displaying a steeper evolution rate, leading to greater settlement values. This disparity in top mattress displacement intensifies over cycles, resulting in a substantial 20 mm

difference between M_4 and M_5 by the 60th cycle. Despite this significant impact on the mattress, the influence of doubled cluster numbers on subgrade displacements remains minimal throughout the cycles. This suggests that local phenomena occur within the granular material, but the global mechanism of reinforcement is not substantially influenced by the number of particles.

Table 6-2: Cluster lengths for both simulations M_4 and M_5

	$l_{n\ min} = 2 * d_{n\ min}$ (m)	$l_{n\text{-}max} = 2 * d_{n\text{-}max}$ (m)	$l_{n\text{-}average} = 2 * d_{n\text{-}average}$ (m)
M_4	0.032	0.064	0.040
M_5	0.040	0.080	0.052

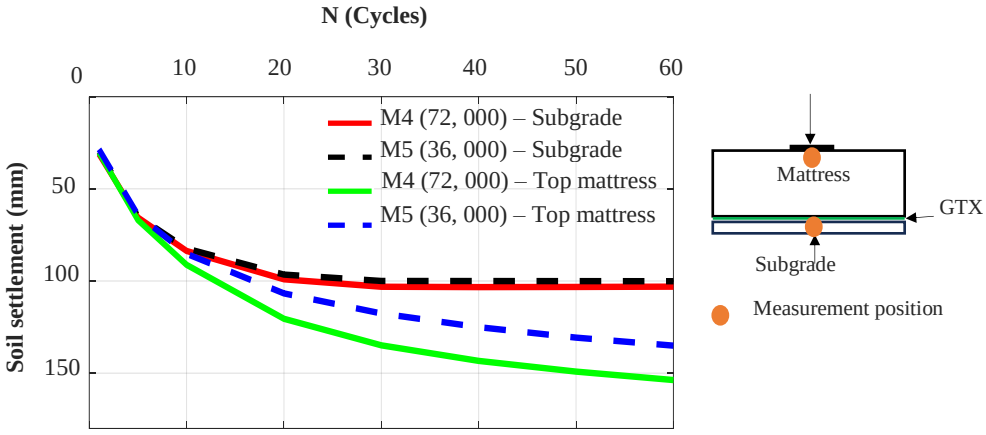

Figure 6-1: The evolution of the subgrade and the top mattress settlement across cycles of M_4 & M_5

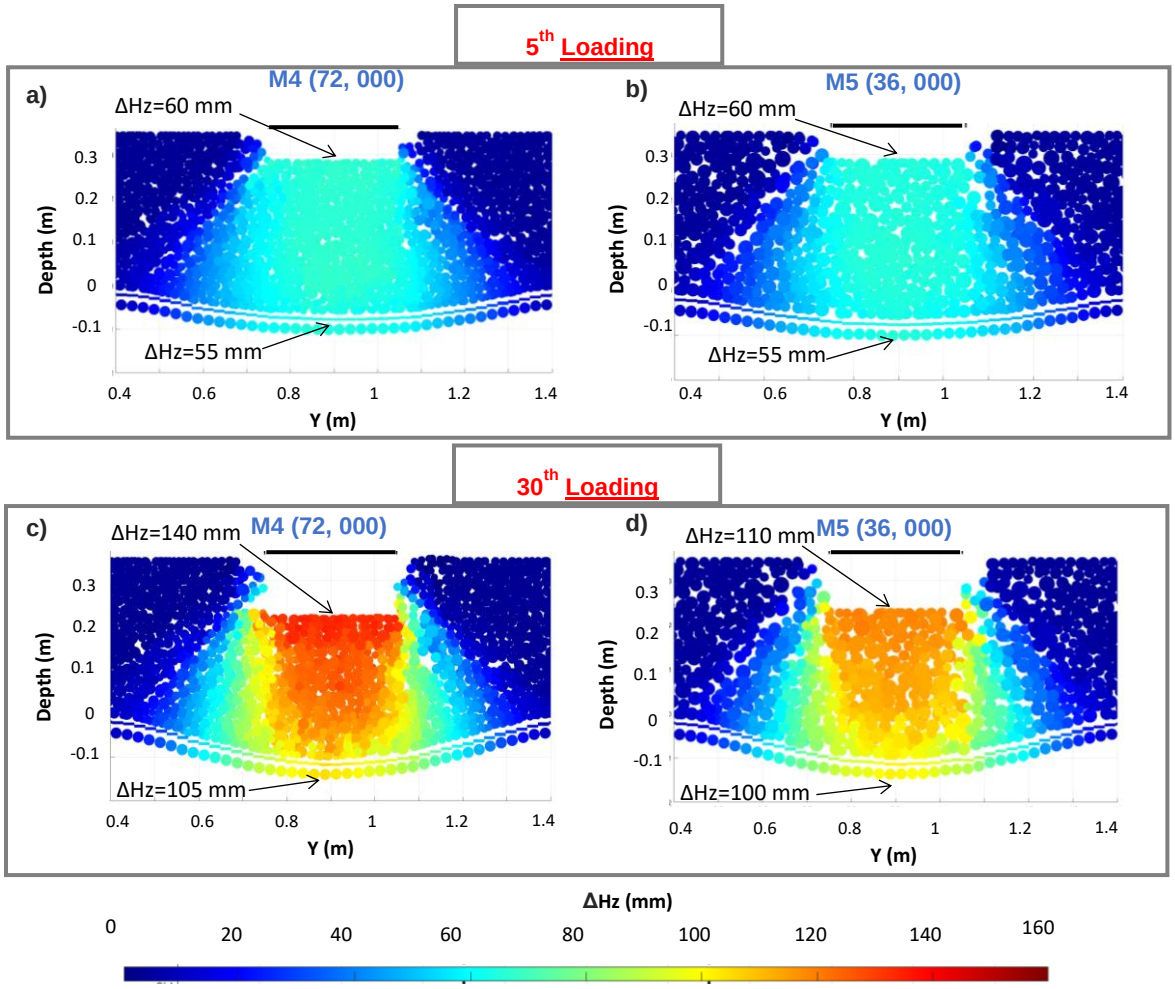

Figure 6-2: Comparison between the soil particles displacement of the two models: a) M_4 at the 5th cycle; b) M_5 at the 5th cycle; c) M_4 at the 30th cycle; d) M_5 at the 30th cycle

To support the findings presented earlier, the vertical displacement is graphically represented along a vertical section following the 5th and 30th loading cycles (Figure 6-2). Consistent with the previous observations, the doubling of cluster numbers from 36,000 to 72,000 manifests no significant impact on vertical displacements at the 5th cycle. Both models exhibit comparable displacement magnitudes within the mattress and subgrade. However, by the 30th cycle, doubling cluster numbers leads to larger displacement values beneath the loading plate, albeit with limited effects on subgrade displacements. Notably, the behavior of the shearing band within the granular material shows a slight influence based on the size of the discrete particles. This dynamic becomes more pronounced during cycles, resulting in increased displacements when reducing the size of clusters, particularly after the 5th cycle when damage occurs (ΔHz_{max} = 60 mm).

Expanding on this analysis (Figure 6-3), the doubling of cluster numbers results in denser configurations and an increased number of contact forces. Although the network of forces may vary between cases, the mechanisms facilitating the diffusion of forces toward the GSY reinforcement exhibit overall similar

intensities. This elucidates the minimal difference between subgrade displacements in the two numerical models throughout the cycles.

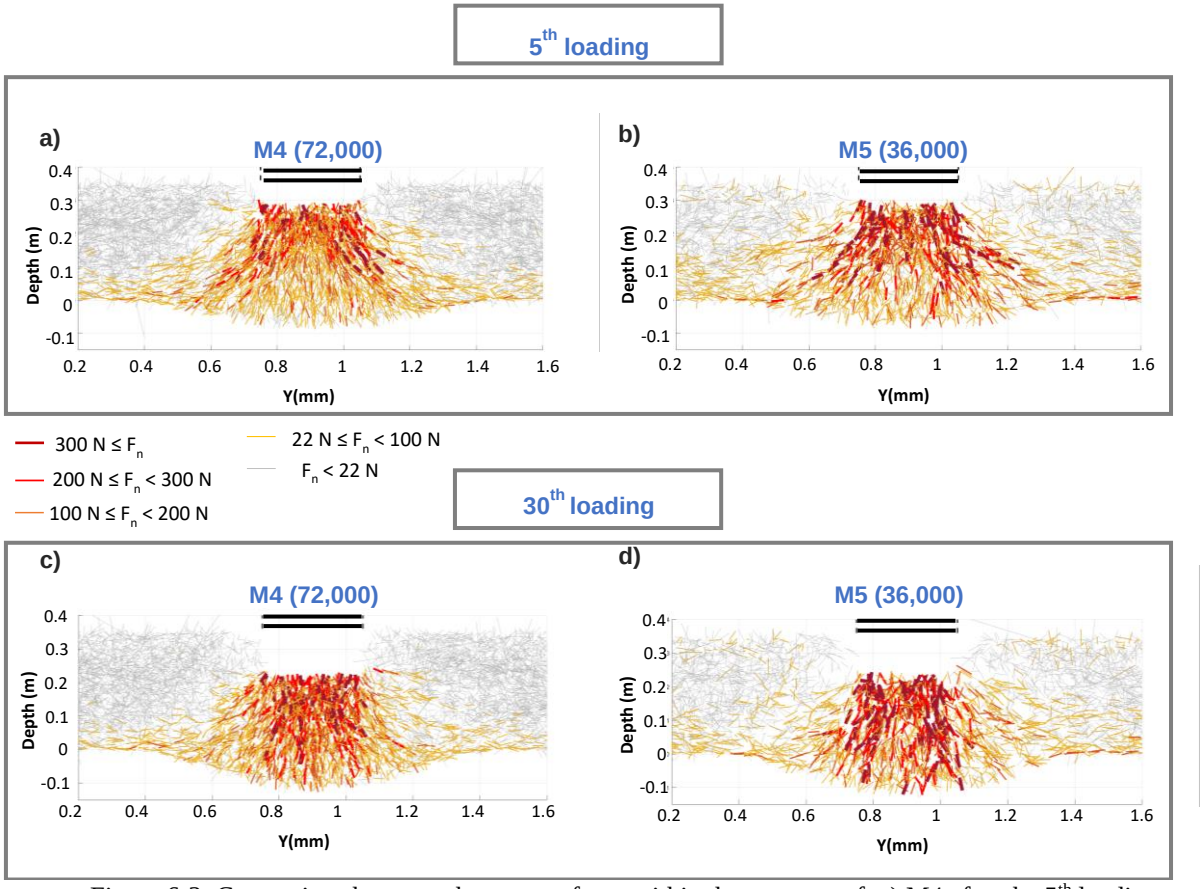

Figure 6-3: Comparison between the contact force within the mattress of: a) M4 after the 5th loading; b) M5 after the 5th loading; c) M4 after 30th loading; M5 after the 60th loading

6.2.3 GTX response

Following the 30th loading cycle, a comparison of the vertical stress on the GTX's upper and lower faces between M_4 and M_5 is presented in Figure 6-4. Doubling the cluster numbers in the mattress has a marginal effect on the solicited area and stress range on the GTX's upper face. Both M_4 and M_5 share similar shapes of solicited zones, displaying comparable magnitudes of vertical stress values, with a slight superiority in stress values for M_4 within the loading plate projection. This superiority is attributed to heightened force density and localized force distribution resulting from doubling the cluster numbers. Considering the vertical stress on the GTX's lower face after the 30th cycle in M_4 and M_5, the doubling of cluster numbers in the mattress has a marginal effect on the solicited area and stress range. M_4 and M_5 showcase similar shapes of solicited zones and comparable magnitudes of vertical stress values. Consequently, doubling cluster numbers under these model conditions does not significantly impact GTX strain, deflection, or horizontal displacement (see Figure 9-1 in the Annex).

Besides, in both M_4 and M_5, the GTX plays a crucial role in reducing stresses in the solicited zone. This is because the vertical stress transmitted to the GTX's lower face for both models is less significant than that acting on the GTX's upper face in the area of the loading plate's projection.

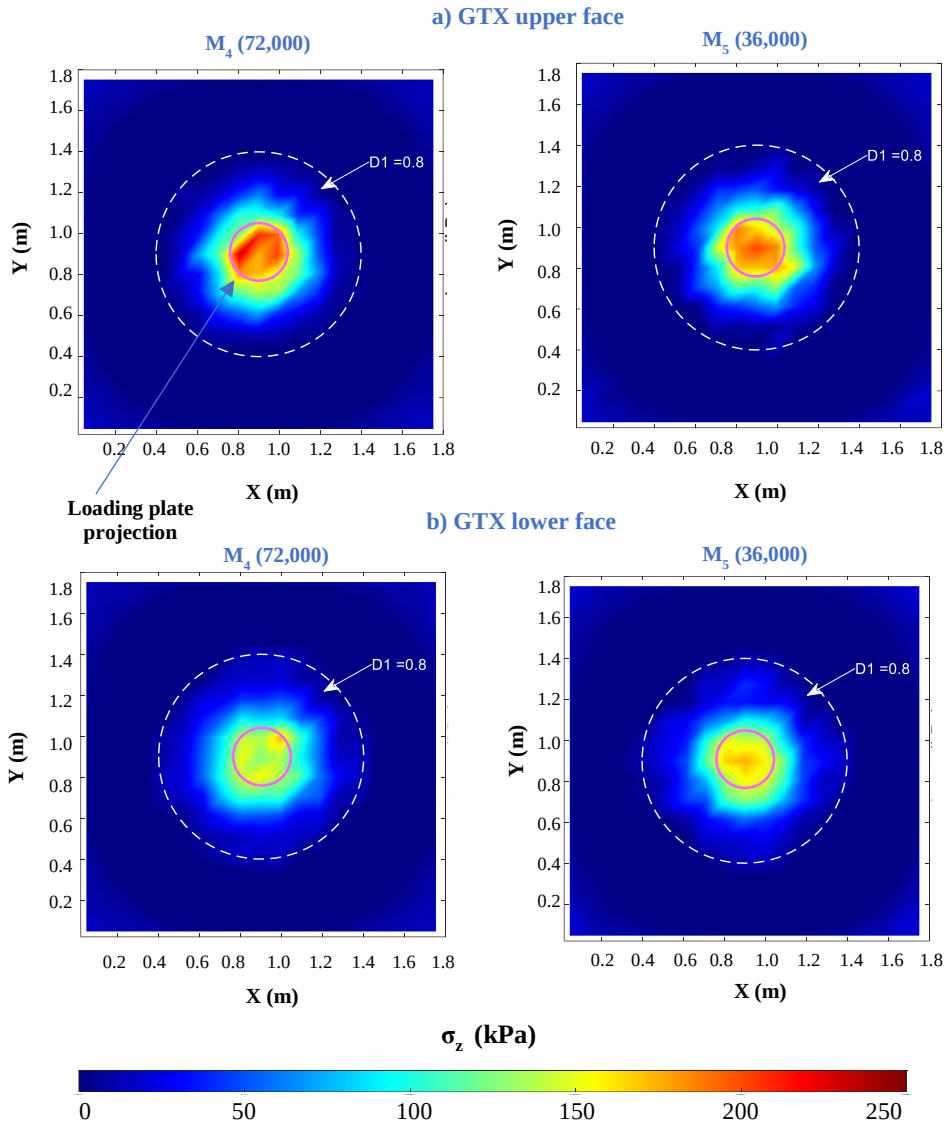

Figure 6-4: The vertical stress acting on: a) the GTX upper face and; b) the GTX lower face for M_4 and M_5

6.2.4 Conclusion

The impact of doubling the cluster numbers in the mattress on the model's behavior was investigated through a comparison of specific outcomes from M_4 (72,000) and M_5 (36,000). Doubling the clusters resulted in denser contact forces and localized deformation in the mattress, leading to more significant soil displacement throughout the cycles. However, subgrade displacements remained largely unaffected.

Examining the GTX response, including vertical stress on the GTX's upper and lower faces, deflection, horizontal displacement, and strain profiles, revealed minimal impact from doubling the cluster number. Therefore, M_4 and M_5 will serve as the foundational basis for our parametric study. When precision at the mattress level is crucial, M_4 is the preferred choice. However, for the majority of cases, M_5 will provide an adequate level of information.

6.3 Impact of the GTX stiffness and the subgrade softness

Both reinforced and non-reinforced platforms were tested in the experimentation (Chapter 4). In the reinforced sections, a GTX was utilized from a pair, each distinguished by distinct stiffness. To seamlessly align the experimental with numerical simulations and enhance our understanding of GTXs role within this application, six simulations were conducted. Valuable insights into the intricate interplay between GTX stiffness and subgrade rigidities were provided by these simulations. Specifically, three GTX stiffness categories—low, intermediate, and high stiffness—were tested in presence of two subgrade rigidities. The focus was centred on studying GTX effectiveness, subgrade rigidity impact, and GTX stiffness impact. The influence of subgrade rigidity and the GTX stiffness on reducing soil settlement and facilitating load transfer through tensioned membrane effects was delved into.

6.3.1 GTX effectiveness

Six simulations (M_5 to M_{10}) were conducted, considering two distinct initial subgrade reactions: k_1 = 2 MPa/m and k_1 = 3 MPa/m. For each subgrade reaction, three simulations were executed with GTX stiffness values in both machine and transverse directions: $J_x = J_y$ = 1200 kN/m (J_{1200}), $J_x = J_y$ = 600 kN/m (J_{600}), and $J_x = J_y$ = 10 kN/m (J_{10}). It is noteworthy that the latter stiffness value is considered low for a GTX intended for reinforcement, primarily designed for separation purposes.

The lower subgrade rigidity implies that the subgrade, and consequently the mattress positioned above it, is comparatively more deformable (Figure 6-5). This characteristic allows GTXs to exert a more pronounced influence on the reduction of settlements. With a subgrade of k_1=2 MPa/m, GTXs with appropriate stiffness values J_{600} and J_{1200} reduce soil settlement by 13% and 10%, respectively, compared to a GTX with low stiffness J_{10}. The level of load applied, and the relative low subgrade rigidity makes it possible to generate surface settlements of around 160 mm which are necessary for the mobilization of the reinforcement by membrane effect. Conversely, with a subgrade of k_1=3 MPa/m, GTXs with stiffness values J_{600} and J_{1200} reduce soil settlement by 6% and 3%, respectively, compared to a GTX with low stiffness J_{10}. Hence, the effectiveness of GTX in reducing settlements becomes more noticeable when the soil exhibits a lower modulus of reaction. This highlights the substantial dependence of GTX effectiveness on the properties of the underlying soil.

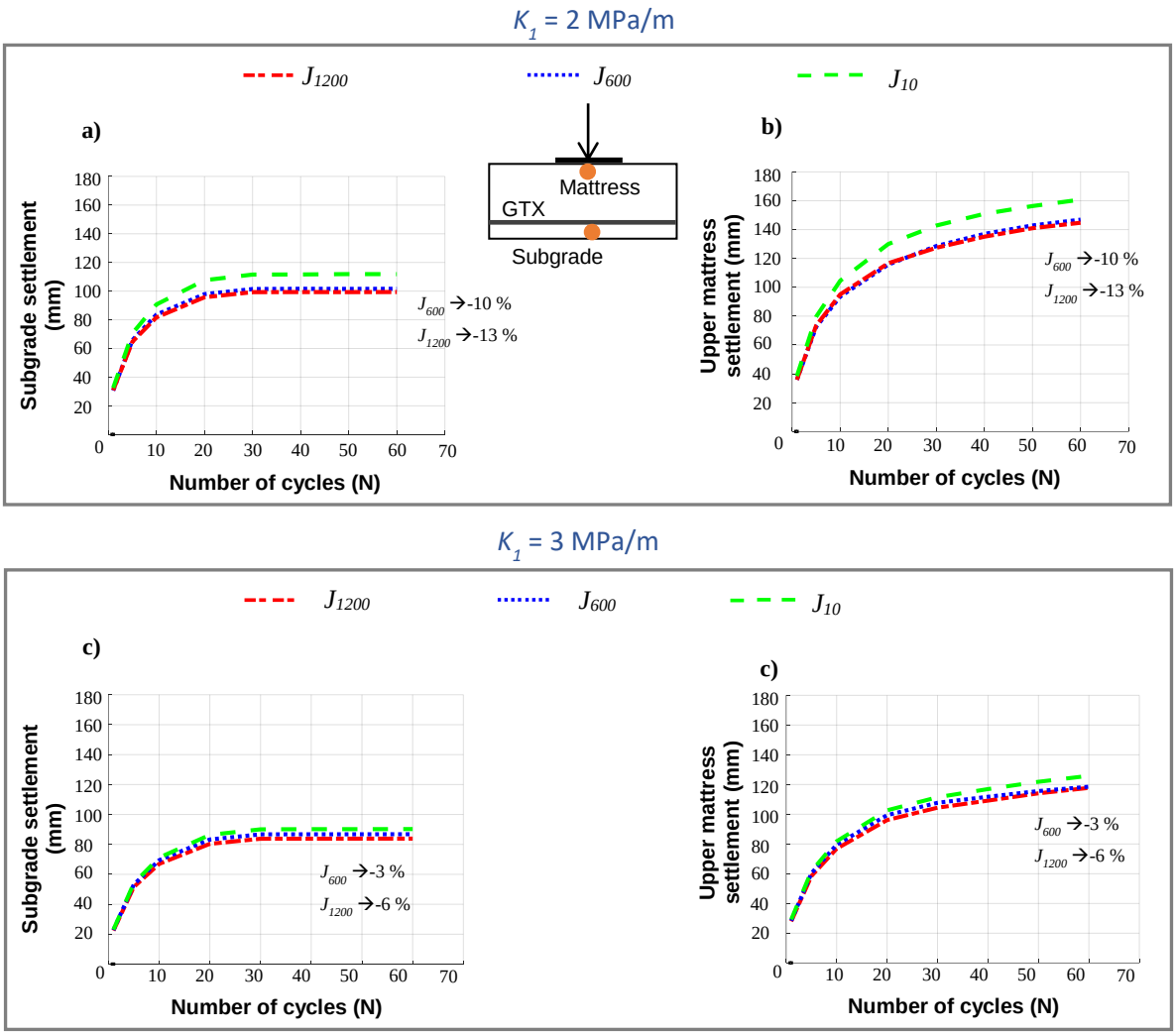

Figure 6-5: The evolution of soil settlement beneath the loading plate centre with an initial reaction modulus (k_1) equal to 2 MPa/m (a and b) and 3 MPa/m (c and d)

6.3.2 Subgrade rigidity impact

The influence of subgrade softness on the effectiveness of GTX in mitigating the load transferred to the subgrade within the solicited zone (the projection of the loading plate [D=0.3 m] and its surroundings) is investigated. This investigation is conducted through two simulations: M_5 with k_1 = 2 MPa/m and M_9 with k_1 = 3 MPa/m. It is noteworthy that the applied load on the circular plate is 40 kN, equivalent to 560 kPa.
A softer subgrade results in more pronounced soil settlement, as evidenced by the comparison of soil displacement evolution in both the subgrade and the overlying mattress throughout cycles (Figure 6-5). This phenomenon becomes more apparent when expanding the observation of soil displacement from localized points to the central vertical section during the 30th loading cycles (Figure 6-6).

Figure 6-7 illustrates the resultant vertical stress difference ($\Delta\sigma$) between the upper and lower faces of the GTX at the end of the 30th loading cycle. It is crucial to recall that a positive value of ($\Delta\sigma$) signifies an increase in the load transmitted to the subgrade soil, while a negative value indicates a decrease in the load transmitted to the subgrade soil. In the softer subgrade soil (k_1 = 2 MPa/m), the GTX shows a more significant role in stress distribution through membrane effects, transferring a greater stress from the

solicited area (D_1 = 2 D) to the less solicited surrounding area (2D < D_2 < 4D). This difference is attributed to the greater deflection and strain in the GTX when the subgrade is softer. Consequently, increased GTX deflection and strain enhance the efficiency of load transfer through the GTX.

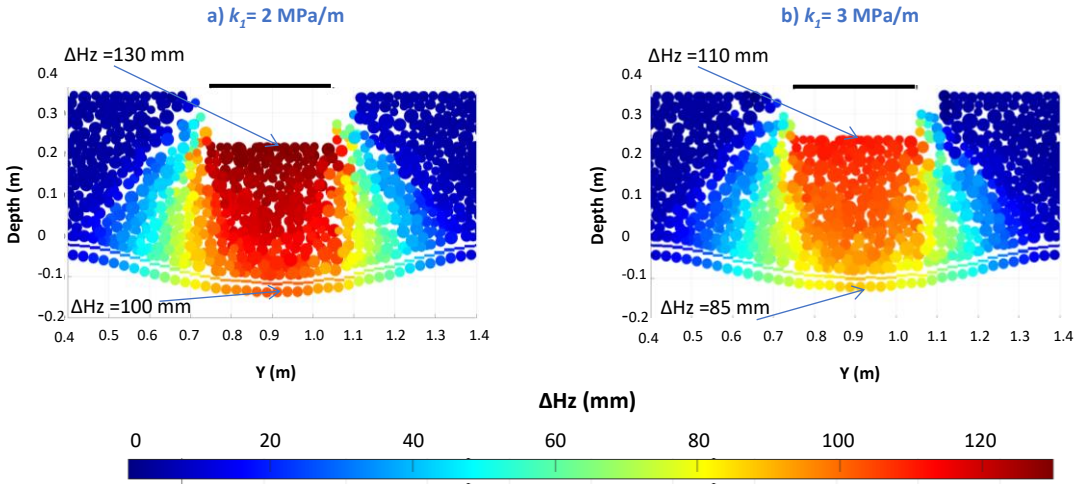

Figure 6-6: The vertical soil displacement at the end of the 30th loading cycle: a) for k_1 = 2 MPa/m; b) for k_1 = 3 MPa/m (J_{600})

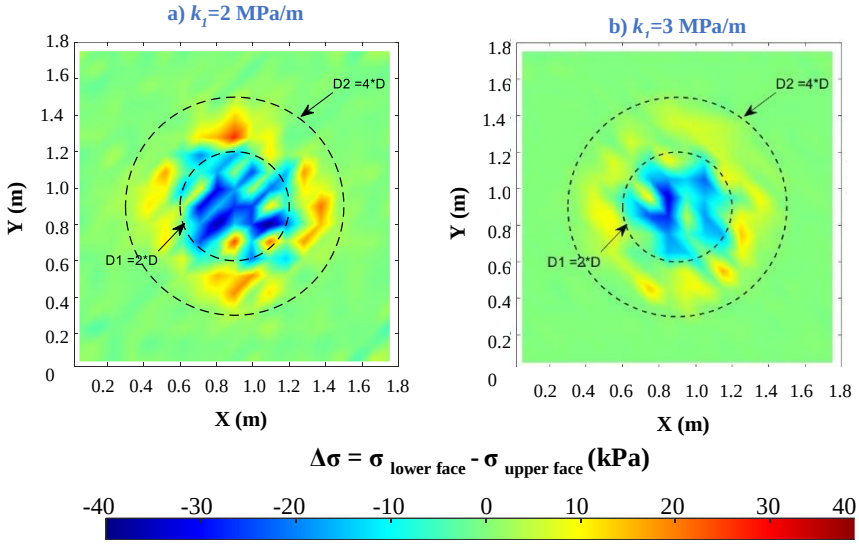

Figure 6-7: The resultant between the vertical stress on the upper face and the lower face of the GTX (J_{600}) at the end of 30th loading cycle: a) with k_1= 2 MPa/m; b) with k_1= 3 MPa/m

6.3.3 GTX stiffness impact

The study investigates the influence of GTX stiffness on its efficacy in reducing both the soil displacement and the load transmitted to the subgrade within the solicited zone encompassing the loading plate's

projection (D=0.3 m) and its adjacent area. Three simulations are compared (M_5 to M_7), each featuring an initial subgrade stiffness (k_1= 2 MPa/m) and varying GTX stiffness levels (J_{1200}, J_{600}, J_{10}). As previously, the applied load on the circular plate is 40 kN, equivalent to 560 kPa.

Figure 6-8 provides a visual representation of vertical soil displacement within the central section (0.87 m <x < 0.93 m and 0.4 m < y < 1.2 m) with subgrade rigidity k_1=2 MPa/m. The colour variation representing vertical displacement magnitude confirms that employing a GTX with appropriate rigidity (J_{600} (b) and J_{1200} (a)) reduces displacement compared to the GTX with low stiffness of 10 kN/m. Additionally, increasing the rigidity from 600 kN/m to 1,200 kN/m is not enough to reveal a significant impact on soil settlement reduction. This is primarily due to the substantial settlements observed in the subgrade soil (100 mm), which seems unable to more effectively mobilize tension in the GTX and contribute to an overall reduction in settlements. This is consistent with the experimental tests that show that the difference in soil settlement, comparing two GTXs with two different stiffnesses, was not significant when removing the compaction condition (section 4.4.3.3).

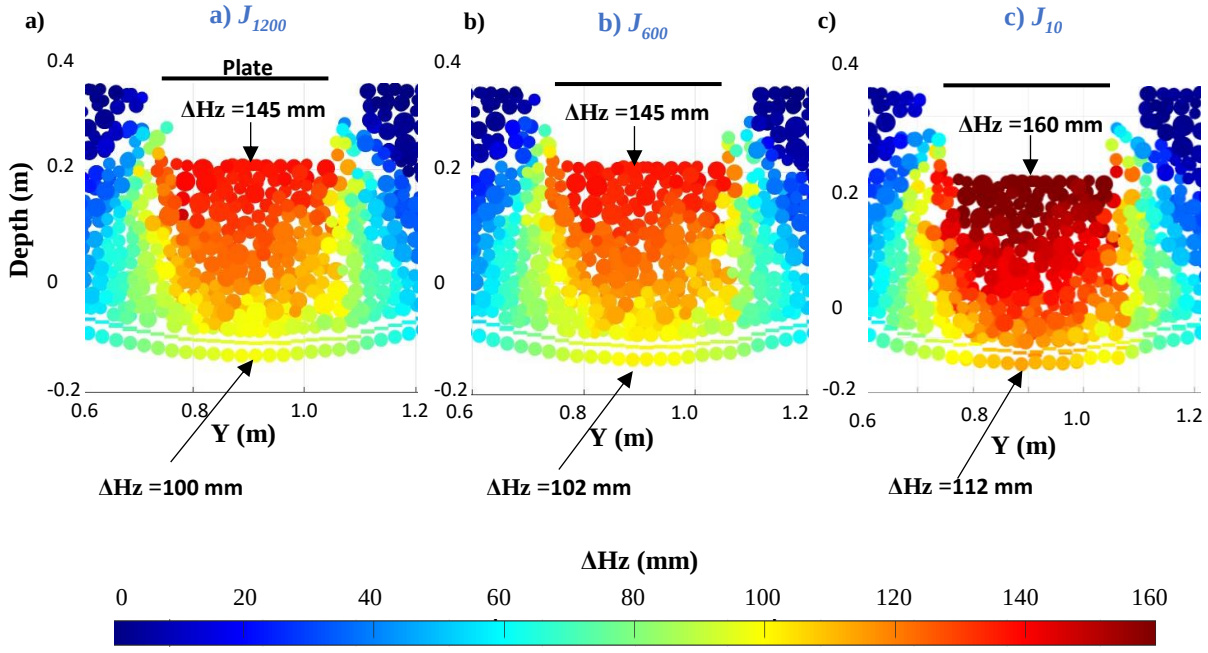

Figure 6-8: The vertical soil displacement due to the 30th loading cycle; a) for J_{1200} ; b) J_{600} ; c) J_{10}

Figure 6-9 shows the profiles of vertical stress on the upper and lower faces of the GTX at the end of the 1st, 5th, and 30th loading cycles within the central section. The vertical stress transferred to the GTX by the mattress are logically not influenced a lot by the different stiffness values of the GTX. Indeed, the vertical stress profiles on the upper face of the GTX are nearly superimposed. While, concerning the stress profiles on the lower face of the GTX, the stiffer the GTX generates the more pronounced the reduction in vertical transfer to the subgrade in the solicited zone. This behaviour is especially apparent during the 5th and 30th cycles when the GTX deflexion become sufficient to put it in tension.

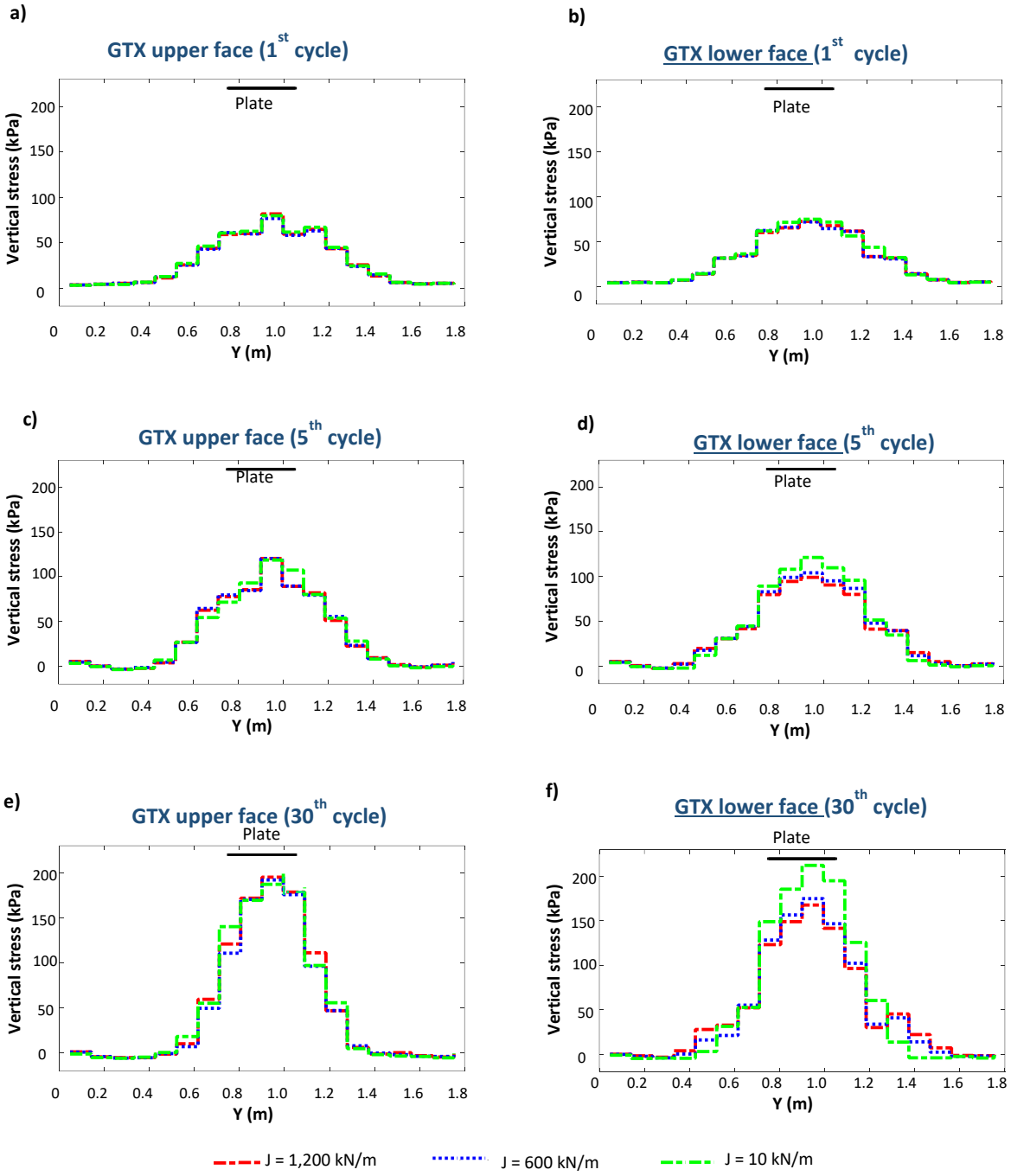

Figure 6-9: The vertical stress on the upper face of the GTX and on the lower face of the GTX: a) After the 1st loading; b) the 5th loading and c) the 30th loading

To further substantiate this analysis, Figure 6-10 illustrates the resultant vertical stress difference ($\Delta\sigma$) between the upper and lower faces of the GTX at the end of the 30th loading cycle. In the case of GTX with suitable stiffness (J_{600} and J_{1200}), a fraction of the load on the upper face is directly transmitted to the

subgrade, while another portion is transferred by the GTX itself to the adjacent region (where 2D < diameter < 4D). Conversely, the GTX with the lowest stiffness (J_{10}) does not contribute to load transfer toward adjacent areas.

Furthermore, comparing the magnitudes of Δσ between simulations with the highest stiffness J_{1200} and intermediate stiffness J_{600} reveals a substantial increase in Δσ with higher stiffness. This verifies that the GTX with the highest stiffness plays a role in load distribution through membrane effects. In the present study (subgrade rigidity k_1=2 MPa/m), this superiority in load transferring seems insufficient to reduce significantly the soil displacement. To ascertain the optimal improvement achievable through increased GTX rigidity, additional simulations with varying initial subgrade soil stiffness should be undertaken.

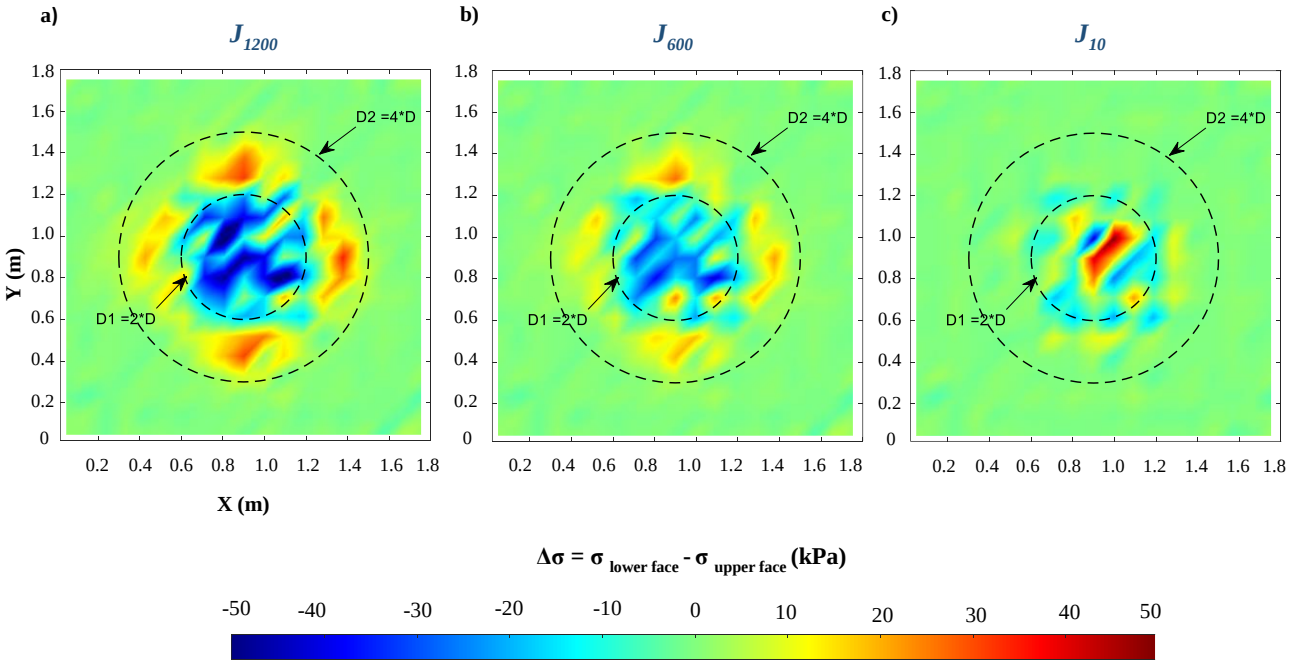

Figure 6-10: The resultant of the vertical stress acting on the lower face of the GTX subtracted from the vertical stress acting on the upper face of the GTX at the 30th loading cycle: a) with J_x= J_y =1,200 kN/m b) with J_x= J_y =600 kN/m and c) with J_x= J_y =10 kN/m

6.3.4 Conclusion

In summary, the examination of simulations incorporating three GTX rigidities (J_x= J_y =10 kN/m, J_x= J_y =600 kN/m, and J_x= J_y =1,200 kN/m) and two initial subgrade reaction moduli (k_1=2 MPa/m and k_1=3 MPa/m) has yielded notable findings. Firstly, the increase of GTX stiffness from low (10 kN/m) to intermediate (600 kN/m) values reduced the soil settlements, particularly prominent in subgrades with a lower modulus of reaction (k_1 = 2 MPa/m). However, the subsequent increase in GTX stiffness from intermediate (600 kN/m) to high (1,200 kN/m) displayed limited efficacy in reducing soil settlement, even when the subgrade reaction modulus was 2 MPa/m. This is consistent with experimental tests involving GTXs of varying stiffness values. Furthermore, the application of low GTX stiffness (10 kN/m) proved inadequate for significant contribution to load transfer through tensioned membrane effects. Conversely, GTXs with intermediate (600 kN/m) and high (1,200 kN/m) stiffness demonstrated their capacity for load transfer to adjacent areas through membrane effects, with the high-stiffness GTX showcasing superiority in transferring a higher magnitude of stress compared to the intermediate-stiffness counterpart.

Lastly, a decrease in the subgrade reaction modulus is correlated with increased soil settlement and an enhanced ability for load transfer through the GTX.

6.4 GTX - Mattress interface friction impact

To trigger the tensioned membrane effect mechanism, the GTX sheet must induce an out-plane displacement and strain. A minimal friction at the GTX-soil interface may be required for the GTX in the anchorage areas to effectively carry out its reinforcement role, but this parameter is often-overlooked. Moreover, the frictional forces acting at the soil/GTX interfaces could contribute in some cases to add some confining stresses to the granular mattress that leads to increase its bearing capacity. In this section the friction angle at the granular mattress is discussed. Three distinct simulations: one featuring a frictionless interface (M_{11}), another with an average friction angle of 38° (M_5), and a third with a relatively high friction angle of 45° (M_{12}). It is important to note that the friction angle at the subgrade/GTX interface remains constant in all three simulations, with a consistent value of 32°. The additional parameters for these simulations are detailed in Table 6-1. It's essential to acknowledge that, in practical terms, the interface between the GTX and the granular soil cannot be entirely frictionless (smooth), and assuming so may lead to exaggeration. A subsequent analysis must explore a scenario with a low friction interface angle, providing a more nuanced perspective on the interaction, and this will be undertaken in a later phase of the study.

6.4.1 Particle displacement

The horizontal displacement (ΔHy) and the vertical soil displacement (ΔHz) of the granular mattress particles within the central section (0.87 m < x < 0.93 m and 0.2 m < y < 1.4 m) at the end of the 30th loading cycle are presented in Figure 6-11 and Figure 6-12, respectively, for all three simulations.

As it can be seen on these figures, the heightened friction at the GTX-mattress interface obstructs the lateral movement of the granular particles within the interface zone. The increased friction serves as a deterrent, impeding the horizontal outward movement of clusters (Figure 6-11) and consequently resulting in a reduction in the settlement of the granular mattress both on its top or its bottom (Figure 6-12).

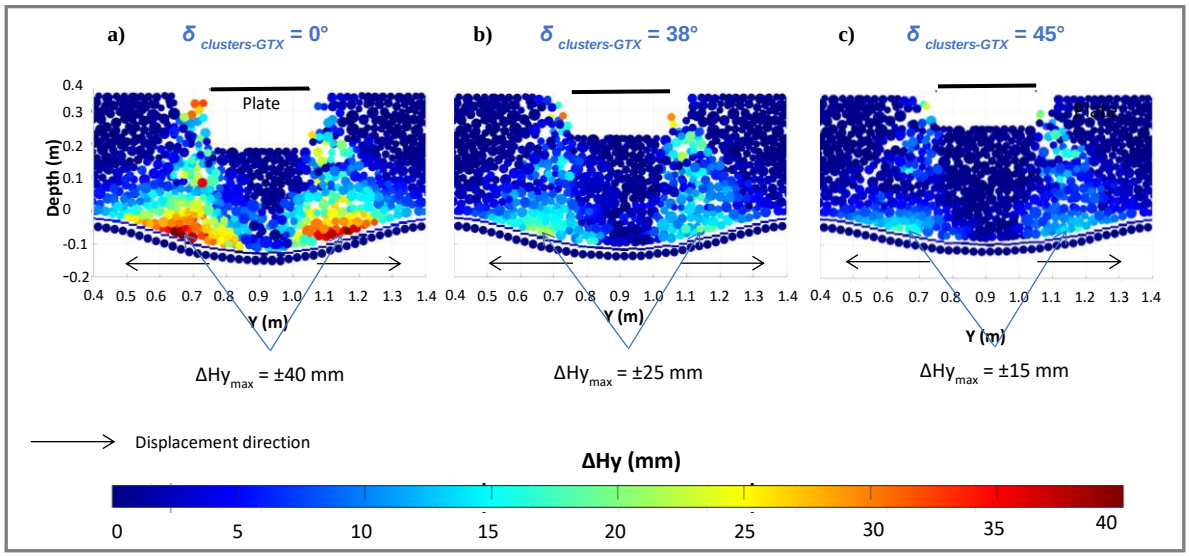

Figure 6-11: The horizontal soil displacement at the end of due to the 30th loading cycle; a) for $\delta_{Clusters\text{-}GTX}$ = 0°; b) for $\delta_{Clusters\text{-}GTX}$ = 38° and c) for $\delta_{Clusters\text{-}GTX}$ = 45°

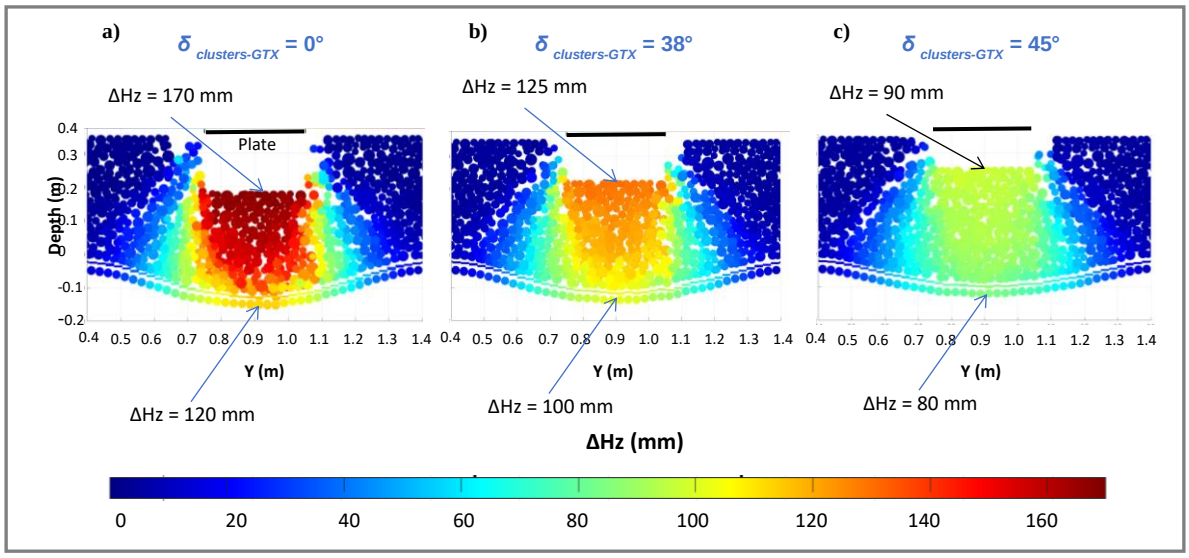

Figure 6-12: The vertical soil displacement at the end of due to the 30th loading cycle; a) for $\delta_{Clusters\text{-}GTX}$ = 0°; b) for $\delta_{Clusters\text{-}GTX}$ = 38° and c) for $\delta_{Clusters\text{-}GTX}$ = 45°

6.4.2 Friction effort

The tangential forces at the upper interface between mattress grains and the GTX (ft_2) in the central section, as illustrated in Figure 5-34 is studied. As the tangential force profile maintains a consistent value and allure across cycles (section 5.4.8), the presentation of the tangential force profile is limited to the 1st loading cycle.

In simulation M_{11}, where the interface is smooth ($\delta_{Clusters\text{-}GTX}$ = 0°), the tangential force between the GTX and the clusters of the mattress at the interface is null due to the inherent interconnection between these two factors. This correlation is vividly demonstrated in Figure 6-13 where the profiles of frictional forces (ft_2) consistently remain null throughout the 1st loading cycle.

As friction serves as a deterrent, impeding the outward motion of clusters, an increase in the friction angle ($\delta_{Clusters\text{-}GTX}$) from 38° to 45° results in an amplification of the tangential force exerted by the grains on the GTX (Figure 6-13). As it can be seen, due to the diffusion of the load under the plate, the main friction areas are located at the periphery of the loading plate. This intricate relationship between friction, grain movement, and tangential forces underscores the dynamic interplay within the system. It sheds light on the pivotal role of the friction angle in the lateral restraint mechanism, which contributes to the stabilization of the grains situated above the GTX.

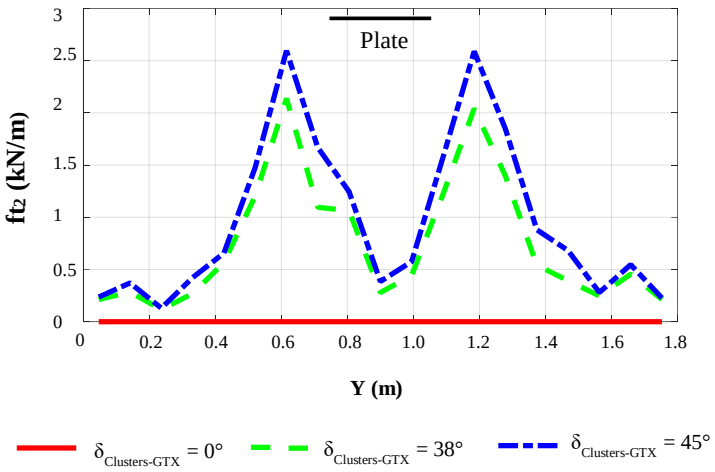

Figure 6-13: The tangential effort at the GTX- mattress interface with $\delta_{Clumps\text{-}GTX}$ = 0°, $\delta_{Clumps\text{-}GTX}$ = 38° and $\delta_{Clumps\text{-}GTX}$ =45° after the 1st loading

6.4.3 Load transfer through the GTX

The impact of friction at the GTX-mattress interface on the GTX's ability to reduce the stress transferred to the subgrade in the solicited zone by transferring a part of this stress to the less solicited zone by tensioned membrane effect is studied. It's worth noting that the surface pressure applied to the mattress surface of the model is 560 kPa by the loading plate (D=0.3 m).

The greater friction angle leads to a more effective in reducing stress transferred to the subgrade within the central zone (D_1= 2D), by transferring a portion of the stress less solicited area (2D<D2<4D). Figure 6-14 shows that the stress reduction in the central zone is more significant when $\delta_{Clumps\text{-}GTX}$ = 45° (50 kPa) compared to the observed stress reduction at $\delta_{Clumps\text{-}GTX}$ = 38° (30 kPa). Furthermore, the smooth GTX ($\delta_{Clumps\text{-}GTX}$ = 0°) logically does not show any contribution in the reduction of stress transferred to the subgrade.

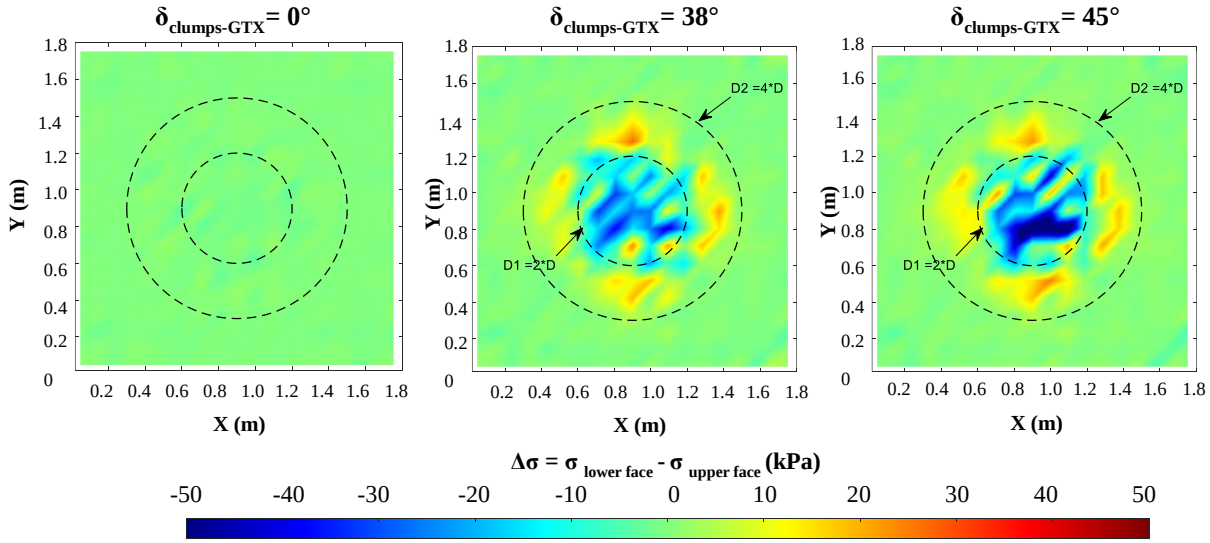

Figure 6-14: Δσ at the 30th loading cycle a) $\delta_{Clumps\text{-}GTX}$ = 0°; b) $\delta_{Clumps\text{-}GTX}$ = 35° and c) $\delta_{Clumps\text{-}GTX}$ = 45°

6.4.4 Conclusion

The investigation into the impact of friction at the GTX-mattress interface ($\delta_{Clumps\text{-}GTX}$) yields noteworthy insights. Firstly, heightened friction serves as a deterrent, restraining the outward motion of clusters and leading to an increase in the tangential force applied by the grains on the GTX. Additionally, a heightened friction angle significantly enhances the GTX's efficacy in transferring vertical stress from the central area to the surrounding region. These findings underscore the pivotal role of friction in influencing both local cluster dynamics and the broader load transferring within the system.

6.5 Mattress intergranular parameters

The selection of the intergranular parameters to give the required macroscopic parameters has been discussed in the calibration of the numerical model based on the experimental results (section 5.3). To shed the light into the influence of the two intergranular parameters: intergranular friction angle (Φ_{int}) and the grain adhesion (a) in the model three simulations M_4, M_{13} and M_{14} (Table 6-1) are studied. These intergranular parameters are related to the macroscopic factors among them: the cohesion (c) and the peak macroscopic angle (φ_{peak}). Simulations M_4 and M_{14} are examined to reveal the impact of varying grain adhesion (equivalent cohesion) from 25 kPa (13.5 kPa) to 5 kPa (2 kPa) while maintaining Φ_{int} (φ_{peak}) at 20° (39°). Similarly, the comparison between simulations M_{14} and M_{13} highlights the effect of Φ_{int} (φ_{peak}) varying from 20° (39°) to 30° (46°), with a constant adhesion (equivalent cohesion) at 5 kPa (2 kPa).

6.5.1 Particle displacement and principal stress orientation

In Figure 6-15 the horizontal displacement (ΔHy) is depicted for the central section of the mattress (0.87 m < x < 0.93 m and 0.4 m < y < 1.4 m) after the 5th loading. The figure also outlines the maximum vertical displacement (ΔHz_{max}) beneath the loading plate and the maximum horizontal displacement (ΔHy_{max}) at the GTX-mattress.

Increased soil cohesion contributes to a heightened soil load-bearing capacity and a reduction in soil displacement. This showed through the decrease in both horizontal and vertical displacement as cohesion increases from 2 kPa (M_{14}) to 13.5 kPa (M_4). Likewise, an elevated soil friction angle results in an enhanced soil load-bearing capacity and diminished soil displacement. This is demonstrated by the decrease in both horizontal and vertical displacement as the soil peak friction angle increases from 39° (M_{14}) to 46° (M_{13}). Furthermore, elevation in either the friction angle or cohesion induces a notable shift in the orientation of principal stresses. As the soil fortifies its resistance to horizontal deformation, there is a discernible inclination of the major principal stress (σ_1) away from the vertical direction. This inclination becomes more pronounced with the increasing of cohesion from 2 kPa (M_{14}) to 13.5 kPa (M_4), and with the augmentation of the friction angle 39° (M_{14}) to 46° (M_{13}) (Figure 6-16).

It's crucial to highlight that additional insights into displacement results are available in the annex (Figure 9-2 & Figure 9-3). The increase in either the friction angle or cohesion among soil grains significantly enhances the soil's resilience against repeated loading and unloading cycles. Notably, the vertical and horizontal displacements observed after the 5th loading with a cohesion value of 2 kPa (M_{13}) closely approximate those after the 60th loading with a cohesion value of 13.5 kPa (M_4). Similarly, the displacements following the 5th loading with a friction angle of 39° (M_4) are comparable to those after the 20th loading with a friction angle of 46° (M_{14}).

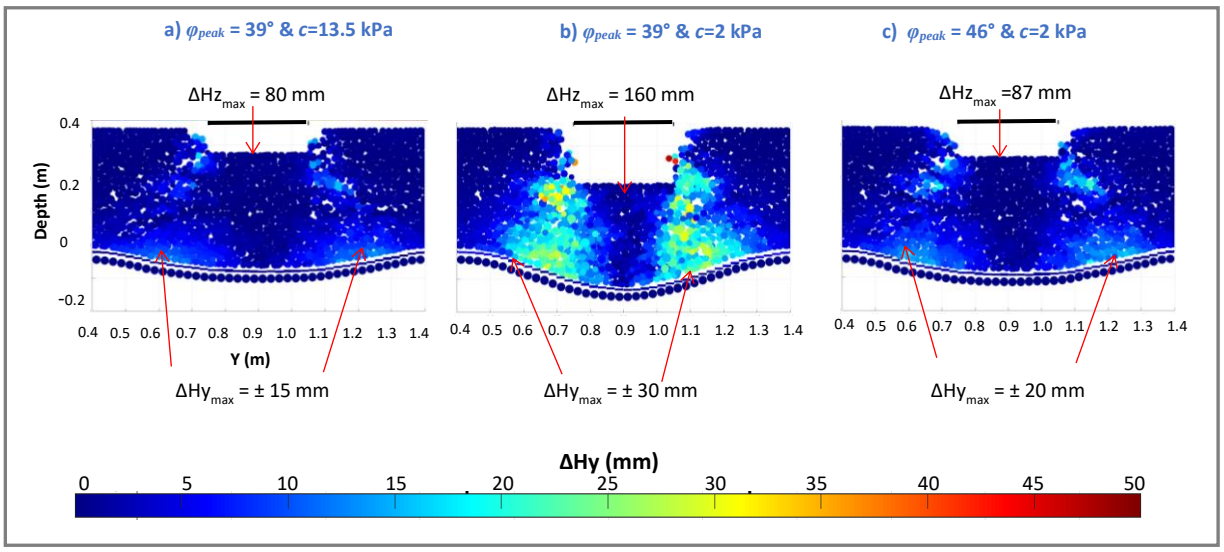

Figure 6-15: The horizontal soil displacement at the end of the 5th loading cycle: a) for M_4 (φ_{peak} = 39° and c = 13.5 kPa), for M_{13} (φ_{peak} = 39° and c = 2 kPa) and M_{14} (φ_{peak} = 46 and c = 2 kPa)

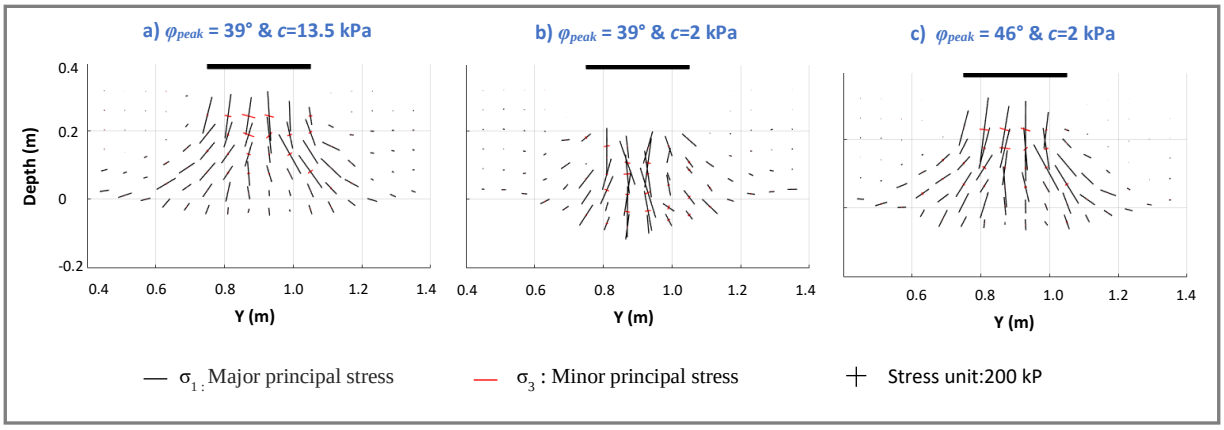

Figure 6-16: the principal stress orientation at the end of the 5th loading cycle: a) for M_4 (φ_{peak} = 39° and c = 13.5 kPa), for M_{13} (φ_{peak} = 39° and c = 2 kPa) and M_{14} (φ_{peak} = 46 and c = 2 kPa)

6.5.2 Load transfer through the GTX

The impact of peak friction angle (φ_{peak}) and cohesion (c) on the GTX's efficacy in mitigating vertical stresses transmitted to the subgrade within the area of the loading plate projection (D=0.3 m). As mentioned earlier the increase of φ_{peak} or cohesion (c) reduces the soil displacement. To ensure an equitable comparison among the three simulations, the soil displacement values are aligned to be approximately within the same range, effectively neutralizing the displacement factor. This alignment is achieved in M_4 (φ_{peak} = 39° and c = 13.5 kPa) at the 60th loading, M_{13} (φ_{peak} = 46° and c = 2 kPa) at the 20th loading, and M_{14} (φ_{peak} = 39° and c = 2 kPa) at the 5th loading.

Since the magnitudes of Δσ across the three cases are approximately equal (Figure 6-17), the intergranular parameters of the mattress have a minimal influence on the GTX's ability to reduce stress transmitted to the subgrade in the solicited area (D_1 = 2D) when soil displacement values are equal. Moreover, the vertical

stress transferred to the surrounding zone ($2D < D_2 < 4D$) remains consistently within similar ranges, supporting the idea that these parameters play a limited role in stress transmission when the soil displacement is aligned.

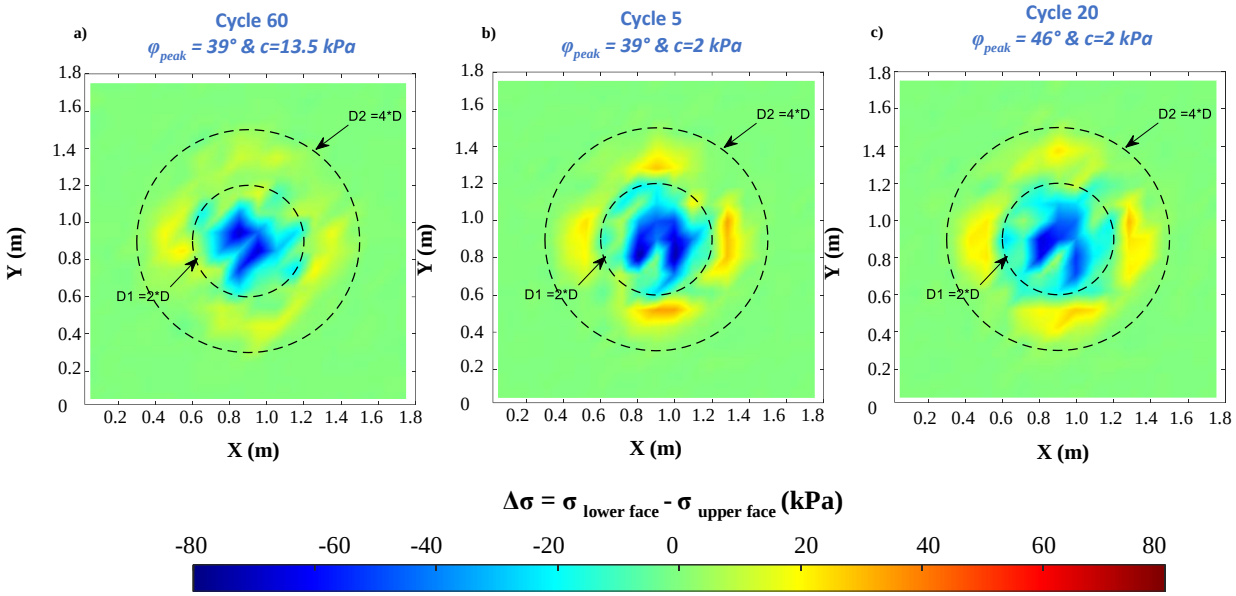

Figure 6-17: Δσ: a) with M_4 (φ_{peak} =39° and c=13.5 kPa) at 60th cycle; b) with M_{13} (φ_{peak} =46° and c =2 kPa) at 20th cycle; and c) with M_{14} (φ_{peak} =39° and c=2 kPa) at 5th cycle

6.5.3 Conclusion

This study delved into the influence of cohesion and friction angle, revealing significant findings:

1. Elevating either cohesion or the friction angle results an enhanced soil stiffness that reduce the particle displacement and shift in the orientation of the major principal stress away from the vertical direction.
2. Under equitable displacement conditions, the cohesion or the friction exert minimal influence on the GTX's efficacy in mitigating stress transferring from the solicited area to the surrounding area.

6.6 Conclusion

This chapter undertakes a comprehensive parametrical study through numerous numerical simulations, with the dual objectives of aligning results with experimental and literature findings and exploring parameters that are seldom addressed.

Increasing the cluster count from 36,000 to 72,000, while resulting in denser contact forces and localized deformation causing more substantial soil displacement within the mattress, had minimal impact on GTX response. The evaluation of vertical stress, deflection, horizontal displacement, and strain profiles revealed that the mattress with greater clusters is recommended for applications demanding high precision at the mattress level, while simulation with reduced clusters number is deemed suitable for most cases.

Examining the influence of GTX stiffness on soil settlement, the transition from low (10 kN/m) to intermediate (600 kN/m) stiffness notably reduced soil settlements, particularly in subgrades with a lower modulus of reaction (k1 = 2 MPa/m). However, further increases in GTX stiffness (from intermediate [600 kN/m] to high [1,200 kN/m]) showed, for the value of the stiffness subgrade retained, no effect on reducing soil settlement. In terms of the GTX's role in transferring load through tensioned membrane effects, low GTX stiffness proved insufficient, whereas GTXs with intermediate (600 kN/m) and high (1,200 kN/m) stiffness demonstrated their capacity for load transfer through membrane effects. Notably, the high-stiffness GTX showcased superiority in transferring a higher magnitude of stress compared to the intermediate-stiffness counterpart.

Furthermore, heightened friction at the GTX-mattress interface emerged as a significant deterrent, effectively restraining the outward motion of the granular particles of the mattress and markedly enhancing the GTX's capability to reduce vertical stress transmitted to the subgrade surface in the loading plate projection zone.

Additionally, an increase in cohesion and friction angle between the grains of the mattress was found to shift the orientation of the major principal stress away from the vertical direction, resulting in a notable reduction in particle displacement.

These multifaceted findings contribute to a nuanced understanding of the interplay of various parameters, offering valuable insights for geotechnical applications.

7. Chapter 7. General conclusions and perspectives

7.1 Conclusions

Unpaved roads encounter a pervasive challenge when constructed on subgrades with inferior quality. The introduction of GSYs has offered innovative solutions to tackle this issue. Despite decades of research in this field, there remains a knowledge gap in understanding GSY applications due to the diverse range of parameters influencing GSY reinforcement behavior.

This research project applied a protocol for the meticulous preparation and installation of an artificial soft soil and granular base course layers. The primary objective was to obtain specific characteristics of the soil layers that accurately reflect the conditions of an unpaved road built on soft soil on site, and to guarantee the reproducibility of the different sections of unpaved road built for testing. In fact, quality control tests played an essential role as an effective tool for controlling the properties of soft and granular soil layers. In addition, plate load repeatability tests were used to exert control over installation, instrumentation and test protocols. The results of the quality control tests indicated that the developed installation protocol facilitated the creation of a homogeneous subgrade layer throughout the depth. It was demonstrated that the targeted properties could be precisely achieved, with measured characteristics exhibiting consistency across all test sections. However, achieving uniform compaction of the granular platform, as observed on-site, posed challenges. The utilization of a heavy compactor was not feasible due to the constraints of the test box dimensions, and using such equipment risked depleting the compressibility of the soft soil entirely. Consequently, a less powerful compaction machine was employed for compacting the granular platform. Therefore, the granular platform attained a CBR (California Bearing Ratio) ranging between 10%-15% in all tests, falling short of the 20% recommended by FHWA (2008). Additionally, the repeatability plate load tests corroborated the efficiency of the protocol, producing consistent results across multiple tests.

In the specific conditions of the constructed unpaved road section, the cyclic plate load tests conducted on these sections unveiled certain key findings. The platform featuring a medium-thick base course (300 mm) experienced notable settlement reduction with the incorporation of woven GTXs. The woven GTX with the highest stiffness emerged as the most effective, demonstrating 55% reduction in settlement compared to the unreinforced platform after 1000 cycles. While the woven GTX exhibited a lower reduction of about 46%. Furthermore, the platform with a medium-thick base course (300 mm) reinforced by the woven GTX with the highest stiffness, a notable 25% reduction in settlement was observed compared to the unreinforced platform with a thicker base course (500 mm) after 10,000 cycles. However, the platform featuring a 500 mm base course, reinforced with the same highly stiff GTX, exhibited no reduction in settlement when compared to its unreinforced counterpart with the same thickness after the same number of cycles. This underscores a significant interplay between the influential factors: reinforcement and base course thickness. It is evident that, for the GTX to effectively fulfill its intended role, due consideration must be given to the base course thickness. This observation emphasizes the nuanced relationship between these parameters in achieving optimal performance in settlement reduction.

The validation of findings from the vertical plate load test under traffic loads has provided valuable insights into the performance of different configurations under diverse loading conditions. Notably, the reinforced 500 mm thick platform, reinforced with the GTX possessing the highest stiffness, demonstrated no improvement in settlement reduction compared to the unreinforced platform of the same thickness under traffic loads. This aligns consistently with the outcomes observed in the plate load test. Conversely, the 300 mm thick platform reinforced with the GTX featuring the highest stiffness exhibited a more rapid rate of settlement evolution and higher settlement values after 3000 cycles of traffic load when compared to the 500 mm thick unreinforced platform. This discrepancy contrasts with the results noted in the plate load test. These findings underscore the influence of the loading type on

the observed outcomes. Additionally, the lack of the GTX impact in the thick platform under both traffic load and vertical load may be attributed to insufficient deflection and the absence of anchoring.

The FEM-DEM coupled numerical model, calibrated to accurately simulate the GTX reinforced granular platform over soft subgrade soil, demonstrated capability in replicating the intricate behaviors observed under cyclic loading. The calibration procedure involved the introduction of adhesion between the clusters of the granular mat. Additionally, the behavior law of subgrade soil, derived from cyclic plate tests, was calibrated to attain the desired settlement within a reduced number of cycles, as compared to experimentation, aiming at the reduction of computation time. The calibrated model revealed valuable insights into load transfer through the GTX, showcasing its increasing engagement with cycles. Initially, frictional forces outweighed the tensioned membrane effect, but as deflection increased with cycles, the latter became more prominent. This dynamic highlighted a diminishing dominance of the soil confinement mechanism with cycles, giving way to the increasing significance of the membrane effect. Furthermore, the investigation extended to the response of the granular mattress, though constrained experimentally. Observations included particle rearrangement, densification beneath the loading plate, and shear at the zones between the semi-cone and its surroundings. Exploring changes in principal stress orientations within the granular mattress as loading cycles progressed unveiled shifting patterns, indicating intricate force transmission mechanisms at play.

A parametric study, conducted through many numerical simulations, aimed to align results with both experimental and literature findings while exploring often-neglected parameters. In investigating the impact of GTX stiffness on soil settlement, the shift from low to intermediate stiffness notably decreased settlements in subgrades with low modulus of reaction. However, further increases in GTX stiffness did not yield additional settlement reduction. The role of the GTX in load transfer through tensioned membrane effects was negligible at low stiffness but became apparent with intermediate and high stiffness. Moreover, increasing friction at the GTX-mattress interface emerged as a significant deterrent, effectively constraining outward motion of granular particles and significantly enhancing the GTX ability to reduce vertical stress transmitted to the subgrade surface. Additionally, an increase in cohesion and friction angle between mattress grains shifted the orientation of the major principal stress away from the vertical direction, leading to a notable reduction in particle displacement.

7.2 Perspectives

This research project has advanced the knowledge accumulated in this field over the past fifty years. However, certain limitations were identified in the anchorage of GTXs and the compaction of the base course. Notably, the experimental box has a width of 1.8 meters, making it challenging to properly anchor the GTX due to insufficient space. Proper anchoring is crucial as it allows the GTX to contribute early to the improvement of platform behavior by initiating the transfer of tensile forces from one location to another where the GSY is anchored. Additionally, compactor machine demonstrated its inability to meet the required CBR=20% for the base course, achieving an average between 10-15%. This compaction shortfall may also be attributed to the soft subgrade soil layer beneath. The weakness in the strength of the base course resulted in a significant uplifting effect of the aggregate around the wheel's centerline of the Simulator Accelerator of Traffic (SAT), causing rapid deformation of the base course thickness, exceeding in the first cycles the maximum allowable settlement acceptable for the SAT machine. After addressing these limitations, several test suggestions are proposed:

- Tests using different reinforcement products and manufacturing types, such as GTXs, GCE, extruded biaxial GGRs, and knitted GGRs with different aperture sizes.
- Tests employing two GSY layers, one placed at the interface and another placed within the base course.
- Further tests with the SAT machine using a dual wheel to increase the wheel contact area and applied load to 40 kN.
- Tests using subgrade soil with high water content to evaluate the efficiency of products designed for drainage function in conjunction with reinforcement or stabilization.

Moreover, a 3D FEM-DEM coupled numerical model was successfully calibrated in this study, proving its capability to simulate a granular platform reinforced by GTX over soft soil under cyclic vertical loading. One limitation, however, lies in the characterization of the mattress, specifically the comparison between the macroscopic friction angle obtained from experimental shear tests and the numerical triaxial tests for selecting microscopic parameters of mattress clusters. To overcome this constraint, we propose conducting triaxial tests on the base course using the recently acquired triaxial machine at the GEOMAS Laboratory, specifically designed to test particles with a larger diameter. Here, further simulations are recommended:

- Simulations using different GSYs with varying reinforcement directions, such as uniaxial and triaxial.
- Simulations employing two GSY layers, one at the interface and another within the mattress depth.
- Simulations using different base course thicknesses.
- Simulations involving clusters with more realistic shapes (by inceasing the number of overlapped spheres).
- Incorporating an advanced behavior law for the subgrade layer, allowing, for example, horizontal displacement of subgrade particles.
- Simulating traffic loading and conducting simulations with traffic loading.

8. Bibliography

AASHTO (1993). AASHTO Guide for design of pavement structures, pp. II–69.

AASHTO Committee 4E, Geosynthetic reinforcement of the aggregate base/subbase courses of pavement structures: Repord prepared by AASHTO Committee 4E (2000).

Abu-Farsakh, Murad Y., Akond, I. & Chen Q. (2016). Evaluating the performance of geosynthetic-reinforced unpaved roads using plate load tests. International Journal of Pavement Engineering, 17(10), pp.901-912.

Alkaissi Z.A & Al-Soud M. S. (2021). Effect of geogrid reinforcement on behavior of unpaved roads. IOP Conference Series: Earth and Environmental Science, 856 (1), 8p.

Akond I. (2012). Laboratory evaluation of geosynthetics to stabilize/reinforce the subgrade/base in Unpaved Roadways.

ASTM (1997). Standard test method for nonrepetitive static plate load tests of soils and flexible pavement components, for use in evaluation and design of airport and highway pavements. pp. 112-113.

Barenberg, E. J., Dowland, James H. Jr., and Hales & John H. (1975) Evaluation of Soil Aggregate Systems with Mirafi Fabric. Civil Engineering Studies, Department of Civil Engineering, University of Illinois, Report No UILU-ENG-75- 2020, pp. 52

Berg R. R. (2000). Geosynthetic reinforcement of the aggregate base/subbase courses of pavement structures.

Bhandari A. & Han J. (2010). Investigation of geotextile–soil interaction under a cyclic vertical load using the discrete element method. Geotextiles and geomembranes, 28(1), pp.33-43.

Bräu G. & Vogt S. (2018). Field and laboratory tests on the bearing behaviour of unpaved roads reinforced by different geosynthetics. Geotechnical Engineering Journal of the SEAGS & AGSSEA, 49 (4), pp. 115-123.

Briançon L. & Villard P. (2006). Dimensionnement des renforcements géosynthétiques de plates-formes sur cavités. Revue Française de Géotechnique, 117 (4), pp 51-62.

Calvarano L.S., Moraci N., Leonardi G. & Palamara R. (2016a). Reinforced unpaved roads: parametrical analysis of design procedures. 6th European Geosynthetics Congress Proceedings (EUROGEO 6), pp.1147-1155.

Calvarano L. S., Palamara R., Leonardi L. & Moraci N. (2016b). Unpaved road reinforced with geosynthetics. Procedia Engineering, 158, pp.296-301.

Calvarano L.S., Leonardi G. & Palamara R. (2017). Finite element modelling of unpaved road reinforced with geosynthetics. Procedia Engineering, 189, pp.99-104.

Chareyre, B., Briancon, L., & Villard, P. (2002). Theoretical versus experimental modeling of the anchorage capacity of geotextiles in trenches. Geosynthet. Int., 9 (2), pp.97–123.

Chareyre B. & Villard P. (2005). Dynamic spar elements and discrete element method in two dimensions for the modeling of soil-inclusion problems, Journal of Engineering Mechanics, 131 (7), pp.689-698.

Chen, Q., Abu-Farsakh M. & Sharma, R. (2009). Experimental and analytical studies of reinforced crushed limestone. Geotextiles and Geomembranes, 27(5), pp.357-367.

Chen C., McDowell G.R. & Thom N.H. (2012). Discrete element modeling of cyclic loads of geogrid reinforced ballast under confined and unconfined conditions, Geotextiles and Geomembranes, 35, pp. 76-86.

Cuelho E. & Perkins S. (2009). Field investigation of geosynthetics used for subgrade stabilization (No. FHWA/MT-09-003/8193). Montana. Dept. of Transportation. Research Programs.

Cuelho E., Perkins S. & Morris Z., (2014). Relative operational performance of geosynthetics used as subgrade stabilization. (No. FHWA/MT-14-002/7712-251). Western Transportation Institute Montana State University – Bozeman.

Cundal P.A. (1971). A computer model for simulating progressive large-scale movements in blocky rock systems, IRSM Symp., Nancy, France, Proc. 2, pp. 129-136.

Cundal P.A. & Strack O.D.L. (1979). A discrete numerical model for granular assemblies. Geotechnique 29 (1), pp. 47-65.

Demir A., Laman M., Yildiz A., & Ornek M. (2013). Large scale field tests on geogrid-reinforced granular fill underlain by clay soil. Geotextiles and Geomembranes, 38, pp.1-15.

Donzé F.V. & S.A. Magnier, (1997). Spherical Discrete Element Code. Discrete Element Project Report no. 2. GEOTOP, Universite du Quebec a Montreal.

FHWA, Federal Highway Administration (2008). Geosynthetic design and construction guidelines reference manual. FHWA NHI-07-092, U.S. Dept. of Transportation, Federal Highway Administration, Washington, DC.

Gabr M. (2001). Cyclic plate loading tests on geogrid reinforced roads. Research rep. To Tensar earth technologies, inc.

Gallage C., Jayakody S. & Wimalasena K. (2023). Use of geosynthetic to improve the bearing capacity of working platform constructed on soft subgrade. Proceedings of the 14th Australia and New Zealand Conference on Geomechanics (ANZ2023), 6p.

Ghosh C. & Madhav M. R. (1994). Reinforced granular fill-soft soil system: Membrane effect. Geotextiles and Geomembranes, 13(11), pp.743-759.

Giroud J. P. & Noiray L. (1981). Geotextile-reinforced unpaved road design. Journal of Geotechnical and Geoenvironmental Engineering, 107(ASCE 16489).

Giroud J. P. & Han J. (2004 a). Design method for geogrid-reinforced unpaved roads. I. Development of Design Method. Journal of Geotechnical and Geoenvironmental Engineering, 130(8), pp.775 - 786.

Giroud J. P. & Han J. (2004 b). Design method for geogrid-reinforced unpaved roads. II. Calibration and applications. Journal of Geotechnical and Geoenvironmental Engineering, 130(8), pp.787 - 797.

Giroud J.P., Han J., Tutumluer E. & Dobie M.J.D. (2023). Performance of composite geogrid reinforced unpaved pavements under cyclic loading. Geosynthetics International, 30 (1), pp. 47-80.

Hammitt G. M. & Iii W. A. (1970). Thickness requirements for unsurfaced roads and airfields. Bare Base Support (No. AEWES-TR-S-70-5). Army Engineer Waterways Experiment Station Vicksburg Miss.

Huckert A. (2014). Approches expérimentale et numérique du dimensionnement de renforcements géosynthétiques sur cavités et inclusions rigides. PHD theisis, Université Grenoble Alpes.

Hufenus R., Rueegger R., Banjac R., Mayor P., Springman S. M. & Brönnimann R. (2006). Full-scale field tests on geosynthetic reinforced unpaved roads on soft subgrade. Geotextiles and Geomembranes, 24(1), pp.21-37.

ISO TC221 WG6 N337 PG5 TR 18228-5 - 18 Dec 2019

Jayalath C., Gallage C., Wimalasena K., Lee J., & Ramanujam J. (2021). Performance of composite geogrid reinforced unpaved pavements under cyclic loading. Construction and Building Materials, 9, pp. 17-30.

Jean M., Moreau J. J. (1992). Unilaterality and granular friction in the dynamics of rigid body collections. Proceedings of the Contact Mechanics International Symposium, pp 31-48, 1992.

Jean M. (1999). The non-smooth contact dynamics method. Computer methods in applied mechanics engineering, 177, pp 235-257.

Khoueiry N. (2020). Study of granular platforms behaviour over soft subgrade reinforced by geosynthetics: experimental and numerical approaches. PhD Theisis. INSA Lyon. 202 p.

Kiptoo D., Aschrafi J., Kalumba D., Lehn J., Moormann C., & Zannoni E. (2017). Laboratory Investigation of a geosynthetic reinforced pavement under static and dynamic loading. Journal of Testing and Evaluation, 45 (1), 10 p.

Le Hello B. (2007). Renforcement par géosynthétiques des remblais sur inclusions rigides, étude expérimentale en vraie grandeur et analyse numérique, PHD thesis, Université Grenoble I - Joseph Fourier, 232 p.

Lekarp F., Isacsson U. & Dawson, A. (2000). State of the art. I: resilient response of unbound aggregates. Journal of Transportation Engineering 126 (1), 66–75.

Leng J. & Gabr M. A. (2006). Deformation–Resistance model for geogrid-reinforced unpaved road. Transportation research record, 1975(1), pp.146-154.

Leonardi G., Lo Bosco D., Palamara R. & Suraci F. (2020). Finite element analysis of geogrid-stabilized unpaved roads. Sustainability, 12 (5), 11p.

Palmeira E. M. & Antunes L. G. (2010). Large-scale tests on geosynthetic reinforced unpaved roads subjected to surface maintenance. Geotextiles and Geomembranes, 28(6), pp.547-558.

Palmeira E. M., & Gongora I. A. G., (2016). Assessing the influence of some soil–reinforcement interaction parameters on the performance of a low fill on compressible subgrade. Part I: Fill performance and relevance of interaction parameters. Int. J. of Geosynth. and Ground Eng., 2(1), 17p.

Perkins S. W. & Ismeik M. (1997). A synthesis and evaluation of geosynthetic-reinforced base layers in flexible pavements-part I. Geosynthetics International, 4(6), pp.549-604.

Pokharel, S.K., Han, J., Manandhar, C., Yang, X.M., Leshchinsky, D., Halahmi, I., & Parsons, R.L. (2011). Accelerated pavement testing of geocell-reinforced unpaved roads over weak subgrade. Transportation Research Record: Journal of the Transportation Research Board 2204, pp. 67-75.

Qian Y., Han J., Pokharel S. K. & Parsons R. L. (2011). Stress analysis on triangular-aperture geogrid-reinforced bases over weak subgrade under cyclic loading: An experimental study. Transportation research record, 2204(1), pp.83-91.

Qian Y., Han J., Pokharel S. K. & Parsons R. L. (2013). Performance of triangular aperture geogrid-reinforced base courses over weak subgrade under cyclic loading. Journal of Materials in Civil Engineering, 25(8), pp.1013-1021.

QDTMR, D. o. T. a. M. R., Queensland, Australia 2019, MRTS05 Unbound Pavements, Transport and Main Roads Specifications.

Salot C. (2007). Modélisation du comportement mécanique d'un matériau granulaire composite par la méthode des éléments discrets, PHD Theisis, Université Joseph Fourier (Grenoble).

Singh M., Trivedi A. & Shukla S.K. (2022). Evaluation of geosynthetic reinforcement in unpaved road using moving wheel load test. Geotextiles and Geomembranes, 50, pp. 581–589.

Skermer N.A. & Hillis S.F. (1970). Gradation and shear characteristics of four cohesionless soils. Canadian Geotechnical Journal 7 (1), 62–68.

Sun X., Han J., Kwon J., Parsons R. L. & Wayne M. H. (2015). Radial stresses and resilient deformations of geogrid-stabilized unpaved roads under cyclic plate loading tests. Geotextiles and Geomembranes, 43(5), pp.440-449.

Tang X., Abu-Farsakh M., Hanandeh S., & Chen Q. (2015). Performance of reinforced–stabilized unpaved test sections built over native soft soil under full-scale moving wheel loads. Transportation Research Record, 2511(1), pp.81-89.

TMR (Transport and Main Roads), Material Testing Manual, Test Method Q142A: Dry density-moisture relationship of soils and crushed rock - standard, Department of Transport and Main Roads, Queensland Government, Australia, Brisbane, 2020.

Tran V.D.H., Meguid M.A. & Chouinard L.E. (2013). A finite-discrete element framework for the 3D modeling of geogrid-soil interaction under pullout loading conditions. Geotextiles and Geomembranes, 37, pp. 1-9.

Villard P. & Giraud H. (1998). Three-Dimensional modelling of behaviour of geotextile sheets as Membrane. Textile Research Journal, 68, pp 797-806.

Villard P., Chevalier B., Le Hello B. & Combe G. (2009). Coupling between finite and discrete element

methods for the modelling of earth structures reinforced by geosynthetics. Computers and Geotechnics, 36, pp. 709-717.

Watts G. R. A., Blackman D. I. & Jenner C. G. (2004). The performance of reinforced unpaved sub-bases subjected to trafficking.

Weber J. (1966). Recherches concernant les contraintes intergranulaires dans les milieux pulvérulents, Bulletin de liaison des Ponts et Chaussées 20.

Webster, S. L., and Watkins, J. E. (1977). Investigation of Construction Techniques for Tactical Bridge Approach Roads Across Soft Ground, Technical Report S-77-1, United States Army Engineer Waterways Experiment Station, Vicksburg, Miss.

Wimalasena, K. and Gallage, C. and Jayalath, C. & Churchill, J. (2022). Monotonic Loading Test to Investigate the Benefits of Composite Geogrids for Subgrade Improvement. Road and Airfield Pavement Technology, 193, pp. 469-482.

Yang X., Han J., Pokharel S.K., Manandhar C., Parsons R.L., Leshchinsky D. & Halahmi I. (2012). Accelerated pavement testing of unpaved roads with geocell-reinforced sand bases. Geotextiles and Geomembranes, (32), pp. 95-103.

9. Annexe

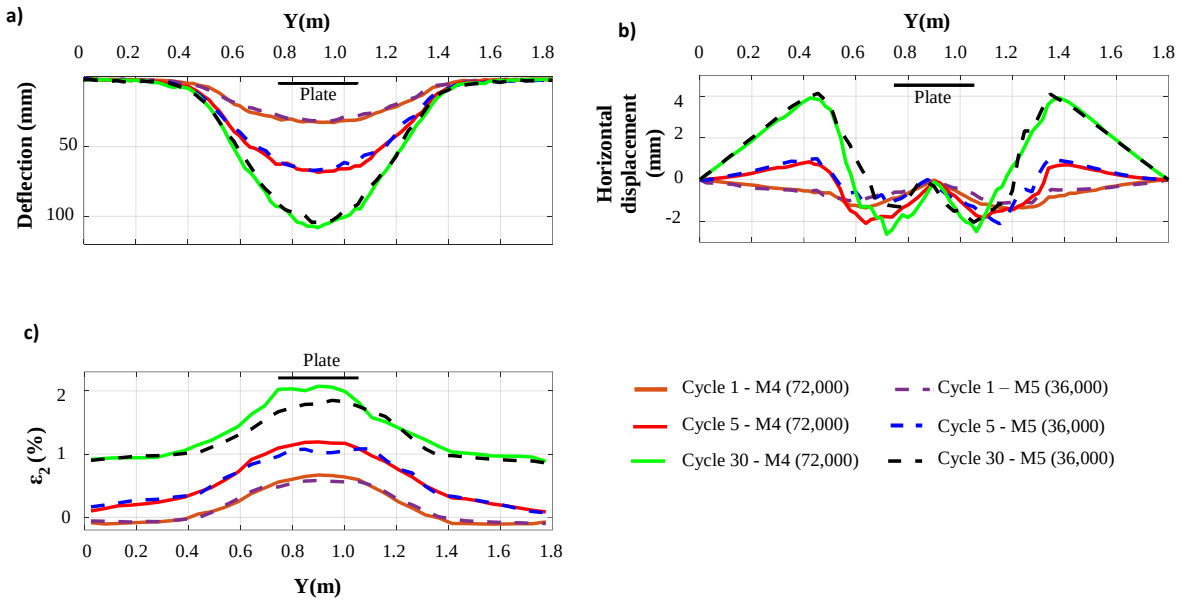

Figure 9-1: GTX response in the two compared models M4 (72,000) and M5 (36,000) at 1st loading, 10th loading and 30th loading: a) GTX deflection profiles; b) GTX horizontal displacement profiles; and c) GTX strain profiles

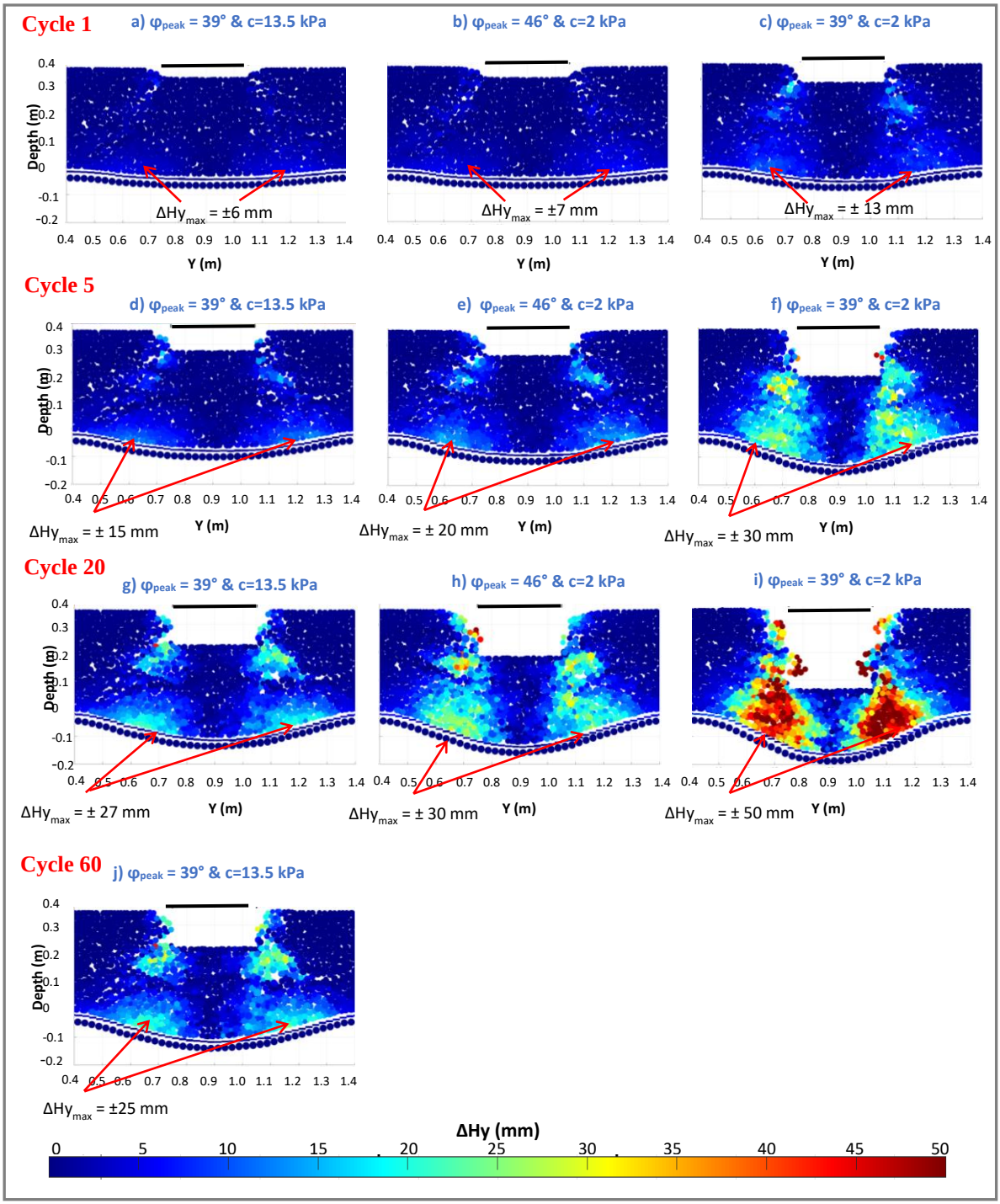

Figure 9-2: The horizontal soil displacement at the end of : the 1st loading cycle (a, b & c); the 5th loading cycle (d, e & f); the 20th loading cycle (g, h & i); the 60th loading cycle (j) for S1 (φ_{peak} =39° and c=13.5 kPa), for S2 (φ_{peak} =46° and c=2 kPa) and S3 (φ_{peak} =39 and c=2 kPa)

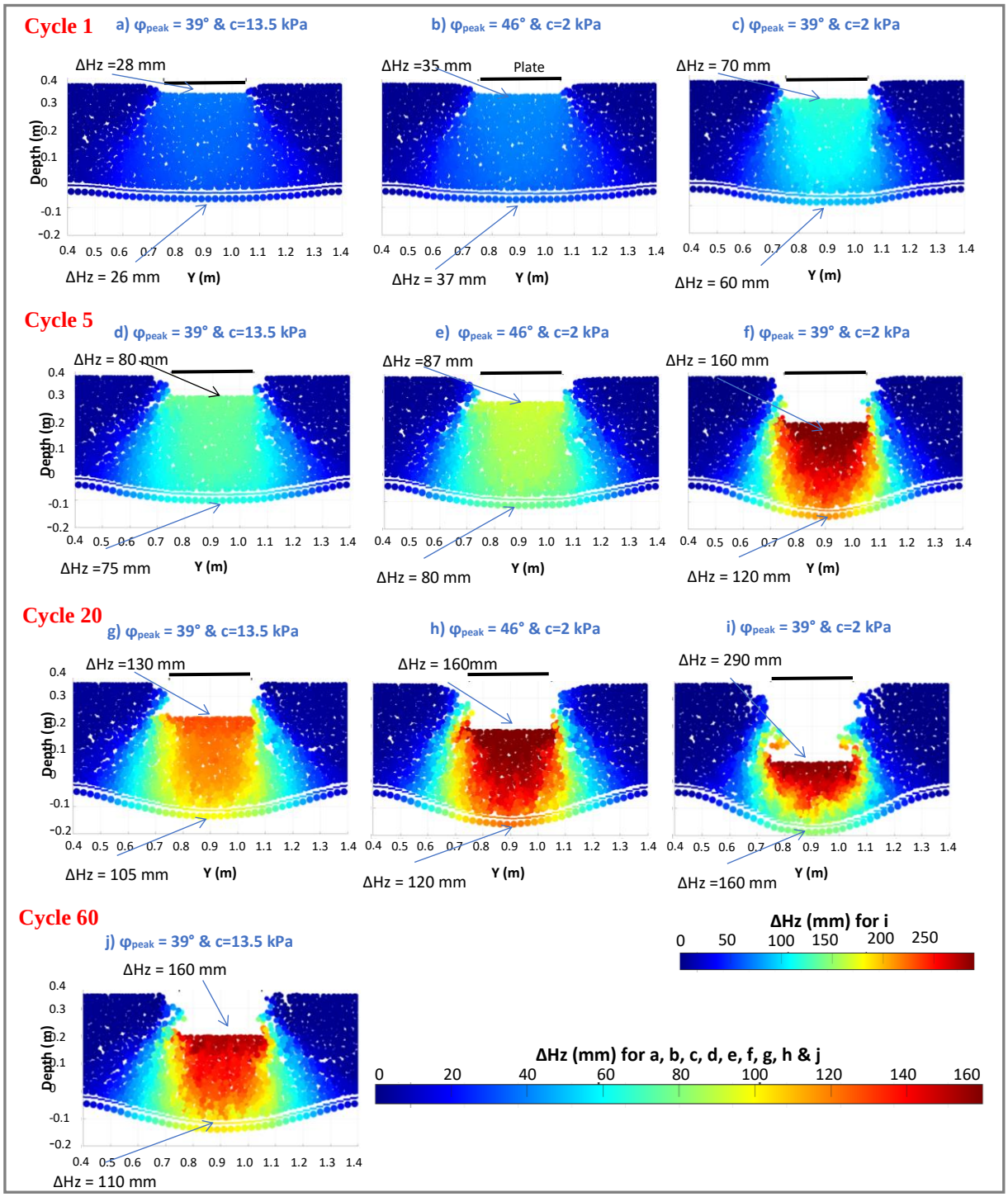

Figure 9-3: The vertical soil displacement at the end of : the 1st loading cycle (a, b & c); the 5th loading cycle (d, e & f); the 20th loading cycle (g, h & i); the 60th loading cycle (j) for S1 (φ_{peak}=39° and c=13.5 kPa), for S2 (φ_{peak} =46° and c=2 kPa) and S3 (φ_{peak} =39° and c=2 kPa)